BER the international journal of bridge engineering management and research

Editorial
Vol. 3, No. 3 (2026) Issue of International Journal of Bridge Engineering, Management and Research (IJBEMR)

Anil K. Agrawal, Dist. M. (ASCE), Ph.D., P.E.

Editor-in-chief, International Journal of Bridge Engineering, Management and Research,
Professor and Chair of Civil Engineering,
The City College of New York, New York, NY, 10031

Submitted: 07 July 2026 **Accepted:** 07 July 2026 **Publication date:** 10 July 2026

DOI: 10.70465/ber.v3i3.103

Abstract: The International Journal of Bridge Engineering, Management and Research (BER) is a fully open access online only journal. The journal serves as a forum for the publication of scientific and technical papers related to all aspects of bridge engineering and management, including structural, seismic, hydraulic and geotechnical risk analysis, structural health monitoring, static and dynamic assessments, structural retrofitting and resiliency enhancement. This issue of the journal presents six papers on artificial intelligence, low velocity impacts behavior of concrete, corrosion detection using Radar, load testing of bridges, prioritization of bridge interventions and chloride-induced corrosion initiation probability.

Issue Summary

It is my pleasure to publish the July issue (3rd issue) of Vol. 3 of the International Journal of Bridge Engineering, Management and Research. In this issue, we are pleased to bring to you six papers in innovative areas of bridge engineering.

As of 2022, there were 620,669 bridges in the United States. Each bridge is inspected according to the Federal Highway Administration's regulations to maintain safety and serviceability. These inspections are performed on varying schedules that are dependent on several factors. Over 100 types of characteristic data are collected during these inspections and are used to produce a structural evaluation rating (SER) for each bridge. These characteristics can include location, material, geometric features, and other types of information about a bridge. The paper entitled "**Use of Artificial Intelligence in Bridge Inspection and Management**" investigates the use of Pearson's correlations, decision trees, and random forest models to determine and show relationships between individual characteristics and the SER. These machine learning methods allow for fast and accurate predictions of the SER based on the selected individual characteristics over varying periods of time. These models also provide visual interpretations of the relationship information produced. Using these models in conjunction with current inspection scheduling methods may maximize efficiency and improve reliability. The models may also be useful for characteristic selection during the design process.

Reinforced concrete structures have been extensively investigated using ground penetrating radar (GPR) to qualitatively analyze corrosion-induced degradation. However, no reliable quantitative model exists for evaluating the corrosion of embedded steel rebars, which may significantly impact the strength, serviceability, and long-term durability of concrete structures. The paper entitled "**Experimental Detection of Embedded Rebar Corrosion in Concrete with Ground Penetrating Radar**" involved an experimental investigation to determine the relationship between the quantity of rebar corrosion and the maximum amplitude, as well as the two-way travel time (TWTT) of the GPR electromagnetic wave. A direct current was impressed into embedded steel rebars in concrete beams immersed in a 5% saltwater solution to induce accelerated corrosion. GPR data were collected before saline submersion and at 10-day intervals. The study proposed a multivariate linear regression model with high reliability to estimate corrosion-induced rebar mass loss.

Vehicle collisions subject reinforced concrete (RC) bridge piers to high strain-rate dynamic loads, producing complex material interactions and an apparent strength enhancement commonly quantified by the dynamic increase factor (DIF). During impact, the concrete cover, acting as a sacrificial layer, experiences initial damage during a car crash, subsequently transferring forces to the transverse

Discussion period open till six months from the publication date. Please submit separate discussion for each individual paper. This paper is a part of the Vol. 3 of the International Journal of Bridge Engineering, Management and Research (BER), ISSN 3065-0569.

reinforcement and altering the pier's axial and flexural behavior. The paper entitled "**Assessing Damage Behavior of Reinforced Concrete Bridge Piers under Low-Velocity Car Crashes: Experimental and Numerical Study**" presents an experimental investigation of low-velocity vehicular collisions involving sub-compact and sedan cars, with emphasis on cosmetic surface damage and global structural response. Finite element (FE) simulations developed in ANSYS are employed to reproduce the experimental behavior and to validate estimates of post-impact residual capacity. Damage levels are further quantified using a combined probabilistic and reliability-based framework to assess the likelihood and severity of cosmetic damage. The results offer valuable insights into impact-induced damage mechanisms, enable rational evaluation of residual structural capacity, and support informed decisions regarding repair or strengthening. Additionally, chaotic analysis has been further scrutinized in terms of chaotic risk amplification factor (CRAF) to reinforce the findings. This present study contributes to forensic assessments of RC bridge pier serviceability and resilience following vehicular impact events.

The paper entitled "**Load Testing and Rating of Prestressed Concrete Bridges Under Uncertainty**" introduces an approach for load testing and rating of prestressed concrete bridges when design information of the structure is not available. The paper uses testing of a bridge in New York for illustration of the proposed approach. The bridge was built in 1961 and consisted of five simply supported 70-ft-long post-tensioned bulb-T beams. No documents or plans for the structure were available at the time of the testing. In 1970, the structure was posted for 12 tons. Absence of the bridge plans coupled with the public's demand to accommodate school bus traffic on the bridge prompted the load testing and rating. A plan based on assumed design basis and investigation of bridge behavior under controlled truck loading was proposed to determine unknown design parameters and enable load rating of the structure. The bridge was then instrumented and load tested using trucks of known weights and configurations, positioned at specified locations on the deck to gradually increase their safe load effects on the structure. The results of the testing provided required information about the bridge and allowed for load rating of the structure.

The article entitled "**Theory and Application of a Method for Prioritizing Bridge Interventions**" presents a calculation method developed by the company Sina with the aim of establishing a priority ranking for interventions involving the improvement, upgrading, or demolition and reconstruction of a set of bridges. As a measure of the urgency of an intervention, the "cost of postponement" for the community is proposed, defined as the increased risk associated with maintaining the current state of the structure for one year. Following the standard logic of risk analysis, this cost is estimated by multiplying the probability of bridge collapse, calculated over a one-year period, by all the potential damage that such a collapse would cause. Although the calculation is affected by several sources of uncertainty, the proposed procedure, based on the collection of a few essential data points and a limited number of simple steps, allows for sufficiently reliable comparisons between bridges. It highlights which characteristics most significantly influence risk and which can reasonably be neglected.

Chloride-induced corrosion initiation is a major durability concern in reinforced concrete bridge infrastructure and can affect long-term structural performance. Reliable estimation of corrosion initiation probability is therefore important for durability assessment and maintenance planning. The article entitled "**Temporal Fusion Transformer Surrogate Modeling of Chloride-Induced Corrosion Initiation Probability in Reinforced Concrete Bridge Infrastructure**" investigates the time-dependent evolution of corrosion initiation probability under uncertain material, environmental, and geometric conditions, with particular attention to concrete cover depth. A diffusion-based stochastic reliability framework is used to generate simulator-derived corrosion initiation probability trajectories. Corrosion initiation is represented as a threshold-crossing event at the reinforcement depth, and population-level probability is estimated through stochastic simulation and ensemble aggregation. To reduce repeated simulation effort during inference, a temporal fusion transformer surrogate model is trained to reproduce simulator-derived probability trajectories from scenario variables and time. The results show that the surrogate closely follows the simulator-derived evolution of corrosion initiation probability within the sampled scenario space. The predicted trajectories preserve the expected influence of cover depth, with shallower cover associated with earlier initiation and higher probability levels. The model also provides low trajectory-level error relative to the probability scale and offers an inference-time alternative to repeated simulation-based evaluation. These findings indicate that simulation-trained sequence learning can provide a useful surrogate representation of time-dependent corrosion initiation probability under the assumed diffusion-threshold reliability framework. Further validation with field or experimental corrosion data is needed before practical implementation in reinforced concrete bridge infrastructure systems.

With this editorial note, it is also my pleasure to invite you to submit your papers addressing research with new and substantial contributions in bridge engineering to the International Journal of Bridge Engineering, Management and Research. The journal is committed to a prompt peer review process and the online publication of the paper within four weeks of acceptance. We are also committed to completing the peer review process within 90 days of paper submission. All accepted articles are generally published within three months of acceptance. You are invited to submit your papers to the next issue of the journal as soon as possible.

BER the international journal of bridge engineering management and research

Use of Machine Learning in Bridge Inspection and Management in Ohio

AKM Anwarul Islam[1,*] and Natalie Rose[2]

Submitted: 06 February 2026 **Accepted:** 24 June 2026 **Publication date:** 10 July 2026

DOI: 10.70465/ber.v3i3.80

Abstract: As of 2022, the United States had 620,669 bridges that required regular inspections to ensure their safety and serviceability. These inspections are conducted in accordance with Federal Highway Administration regulations and are scheduled based on bridge condition and mandated inspection intervals. During each inspection, more than 100 bridge characteristics, including location, material, geometric, and operational data, are collected and used to determine the Structural Evaluation Rating (SER), a key indicator of overall bridge condition. This study investigates the application of machine learning techniques, including Pearson's correlation, decision trees, and random forest models, to identify and visualize relationships between bridge characteristics and the SER. The proposed methods are expected to provide rapid and reliable predictions of bridge condition based on selected characteristics and historical inspection data. In addition to improving prediction accuracy, these models offer intuitive visual interpretations of the factors influencing bridge performance. When integrated with existing inspection scheduling practices, these techniques may support more efficient and data-driven bridge management and may also assist engineers in selecting design characteristics that enhance long-term bridge performance.

Author keywords: Bridge management; machine learning; Pearson's correlations; decision trees; supervised and unsupervised models

Background and Literature Review

The objective of this research is to develop and apply machine learning techniques to improve and optimize highway bridge inspection scheduling and management. The proposed methods identify relationships between bridge characteristics and inspection ratings, providing valuable insights for more effective bridge management. In addition, these methods offer an intuitive and visual representation of the factors influencing bridge condition ratings.

Although many bridge engineering principles have remained unchanged for decades, bridge inspection practices continue to evolve with advances in technology. Modern inspection technologies enable engineers to collect and process significantly larger volumes of data than ever before. However, managing and analyzing this increased amount of information can be time-consuming and challenging. The integration of machine learning techniques can help engineers and inspectors make more informed decisions, improve inspection efficiency, and better prioritize bridges for maintenance, repair, and rehabilitation.

Machine learning is a branch of artificial intelligence that uses statistical models and algorithms to identify patterns within datasets and uncover underlying relationships among variables. In this study, several machine learning methods were employed to examine the relationships between bridge characteristics and the Structural Evaluation Rating (SER). The SER is an overall bridge condition rating that ranges from 0 to 9 and is determined using the minimum value of the appraisal ratings. Bridges are classified according to their SER as follows: an SER $\geq$7 indicates a "Good" condition, an SER of 5–6 indicates a "Fair" condition, and an SER $\leq$4 indicates a "Poor" condition. Detailed descriptions of these classifications are provided in Table 1. The SER, together with key bridge characteristics, serves as a fundamental basis for bridge condition assessment and bridge management decision-making.

The methods investigated include Pearson's correlation (PC), K-means clustering, principal component analysis (PCA), decision tree (DT) modeling, and random forest (RF) modeling. These techniques were selected because of their ability to efficiently process and analyze large datasets. The visual representations generated by these methods help improve the interpretation of relationships among variables, supporting bridge ranking and prioritization efforts. They also provide structured workflows that can be applied to the evaluation of individual bridges. Alternative methods

*Corresponding Author: AKM Anwarul Islam.
Email: aaislam@ysu.edu
[1]Professor, Civil and Environmental Engineering, Youngstown State University, 1 Tressel Way, Youngstown, OH 44555
[2]Former Graduate Student, Civil and Environmental Engineering, Youngstown State University, Youngstown, OH 44555

Discussion period open till six months from the publication date. Please submit separate discussion for each individual paper. This paper is a part of the Vol. 3 of the International Journal of Bridge Engineering, Management and Research (© BER), ISSN 3065-0569.

Table 1. Item appraisal rating codes for SER

Code	Description
N	Not applicable
9	Superior to present desirable criteria
8	Equal to present desirable criteria
7	Better than present minimum criteria
6	Equal to present minimum criteria
5	Somewhat better than minimum adequacy to tolerate being left in place as is
4	Meets minimum tolerable limits to be left in place as is
3	Basically intolerable requiring high priority of corrective action
2	Basically intolerable requiring high priority of replacement
1	This value of rating code not used
0	Bridge closed

may require more extensive data preprocessing or greater computational resources.

Bridge inspection is a time-consuming process for engineers, inspectors, and motorists. By introducing new approaches to optimization and efficiency, transportation agencies and consulting firms can adopt methods that reduce computational errors and shorten the time bridges remain functionally obsolete. Identifying the characteristics that most strongly influence inspection ratings can also guide the design of future bridges to improve long-term performance. In addition, these relationships may be incorporated into new bridge rating systems or used to enhance existing evaluation programs.

In 2022, Ohio managed more than 27,000 bridges, the second-highest total among all U.S. states. Approximately 4.5% of Ohio's bridges were classified as poor, as shown in Fig. 1. The estimated cost to replace all poor-rated bridges exceeded $1 billion, while the estimated cost to rehabilitate them was more than $700 million.[1]

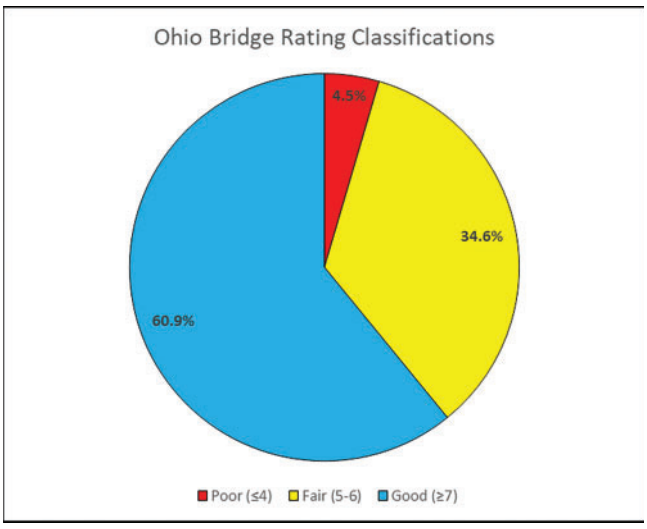

Figure 1. Structural evaluation rating classifications for all Ohio bridges

The Federal Highway Administration (FHWA) requires all states to comply with the National Bridge Inspection Standards (NBIS), which were first implemented in 1971.[2] These standards were established in response to the catastrophic collapse of the Silver Bridge over the Ohio River on December 15, 1967. The NBIS regulations define inspection procedures, inspector qualifications, and requirements for bridge inventories, reports, and condition ratings for all bridges within the public transportation network. This information is compiled in the National Bridge Inventory (NBI), a publicly accessible database containing annual bridge data for each state since 1992. The NBI supports public safety and enables transportation agencies to make informed decisions regarding the maintenance, preservation, and funding of the nation's transportation infrastructure.

Routine bridge inspections are conducted at intervals not exceeding 24 months, with approximately 83% of the nation's bridges inspected on this schedule.[3] State Departments of Transportation (DOTs) may require more frequent inspections than the federal minimum. Additional inspections may also be necessary when a bridge exhibits unexpected deterioration, damage, or other structural concerns. Inspections are performed visually and physically by teams of at least two inspectors. Bridges are accessed using snooper or bucket trucks, rappelling and climbing techniques, wading, or other terrain-navigation methods. Inspectors use hand tools, including scrapers, brushes, probing rods, and borers, to identify and measure defects. Bridge conditions and observations are documented on inspection forms and supported with photographic records. The Ohio Department of Transportation (ODOT) currently utilizes 14 inspection types with varying inspection frequencies, as summarized in Table 2.[4]

Since 2021, these inspection frequencies have outlined ODOT's prioritization using reliability-based inspection intervals.[4] This is performed using a bridge program called AssetWise, which tracks high-risk bridges by considering the following five critical features of a bridge.

Table 2. Ohio bridge inspection types and frequency

Inspection type	Frequency
Initial	Infrequent, performed and inventoried before the bridge is first opened to traffic or there is a change or update in inspection responsibility.
Routine	Performed at a maximum interval of 24 months based on reliability criteria.
In-depth	As-needed, generally for major or complex bridges often on a 60-month cycle or less.
Damage	As-needed.
Flood	As-needed.
Fracture critical	Not to exceed 24-months for structures that fit the rigid definition.
Underwater	Not to exceed 60-months.
Cross channel profile	As-needed.
Scour susceptibility inspection and evaluation	As-needed.
Special/interim	As-needed.
Safety (cursory)	
Quality assurance	A rolling sample set of field and office visits performed regularly by FHWA, ODOT Central Office, CEAO or initiated by any Control Authority or NBIS Program Manager to verify quality inspections.
Complex	Routine, with often a 60-month in-depth inspection cycle.

Note: CEAO—County Engineers Association of Ohio.

i. The presence of at least one fracture-critical member (FCM), which may occur in steel bridges and can result in a total loss of structural integrity if damaged.
ii. The susceptibility to scour, which occurs when water erodes or degrades streambeds beneath piers and abutments. Scour holes can occur more suddenly than other types of bridge deterioration and can affect the integrity and stability of the entire structure.
iii. The presence of a posted load or restriction on the bridge. Posted loads or restrictions are used when the capacity of the structure to carry its design or current legal load is reduced.
iv. The general appraisal or deck condition rating is less than seven.
v. If the bridge is a new construction or has had rehabilitation in the past three years. New construction or rehabilitation inspections are necessary to confirm that the design plans and requirements have all been met by the contractors.

Any defects or issues identified during these inspections can be addressed before the bridge is opened or reopened to traffic. This helps protect public safety while minimizing traffic disruptions and reducing delays caused by extended closures or detours. When any of these five critical features are identified during an inspection, AssetWise automatically adjusts the inspection interval. This adjustment increases the inspection frequency from the standard 24-month interval to a 12-month interval. Bridges that do not exhibit any of these critical features remain on the standard 24-month inspection schedule unless a non-routine inspection is warranted.

Bridge Inspection Technologies

Analysis of bridge condition ratings in Ohio indicates that the average SER for steel and concrete bridges increased by nearly one point in 30 years between 1992 and 2022, as shown in Fig. 2. However, this improvement should be interpreted with caution, as the construction of new bridges and the removal of poorly rated bridges may positively influence the statewide average. Several factors have likely contributed to this trend, including advances in design methodologies, construction practices, inspection technologies, rehabilitation techniques, material performance, and bridge replacement programs. Improved design approaches developed through research and lessons learned from structural failures have enhanced bridge safety and performance. For example, deficiencies in gusset plate design were identified as a contributing factor in the collapse of the I–35 W Bridge in 2007. Advances in materials and manufacturing processes have also improved durability, strength, and service life. In addition, emerging inspection technologies, such as ground-penetrating radar and ultrasonic surface wave testing, allow inspectors to evaluate internal conditions with minimal damage, cost, and disruption.[5]

Bridge deterioration results from a variety of factors, including accidental damage, material degradation, and environmental exposure. Unexpected events often require immediate attention to preserve structural integrity and public safety. In 2021, more than 13,000 vehicle–bridge collisions were reported in the United States.[6] Such impacts can damage columns, piers, girders, and other critical structural components, sometimes requiring bridge closure.

Environmental conditions also significantly influence bridge deterioration. While some effects, such as pavement

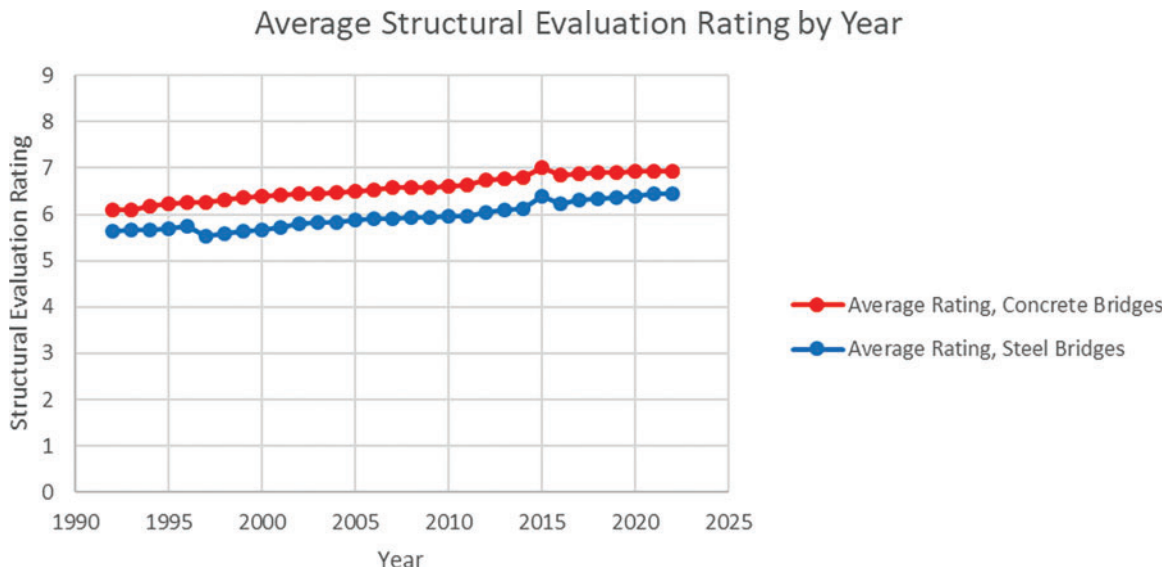

Figure 2. Average structure evaluation rating for Ohio bridges by year

potholes caused by seasonal weather changes, are easily observed, many forms of deterioration require detailed inspection to identify. Palu and Mahmoud[7] suggested that bridges in regions experiencing larger temperature fluctuations may face increased expansion-joint malfunctions as climate conditions evolve. In colder climates, repeated freeze-thaw cycles and the use of deicing salts can accelerate deterioration of concrete bridge decks and superstructures. Zhao et al.[8] found that concrete subjected to freeze-thaw damage experienced more severe deterioration when exposed to salt solutions similar to those used for winter maintenance. Bridge substructures located in waterways are particularly susceptible to scour and erosion caused by flowing water.

Technological advancements continue to improve the efficiency and accuracy of bridge inspections. Clarke-Sather et al.[9] identified report preparation and data compilation as among the most time-consuming aspects of the inspection process. Collecting and analyzing bridge data directly in the field can significantly reduce post-inspection processing time. Emerging technologies that integrate automation and machine learning may further streamline data management and decision-making. Abdallah et al.[10] provided a comprehensive review of current inspection technologies and proposed future frameworks for bridge assessment. One of the primary challenges identified was computational complexity. Machine learning methods that are both effective and interpretable can help address this challenge by enabling inspectors to implement advanced analytical tools with minimal training.

Recent research has also demonstrated the potential of robotic and remote inspection systems. Galdelli et al.[11] developed a robotic visual inspection platform equipped with multiple cameras capable of capturing high-quality images under a wide range of conditions. The system improved defect detection in areas that are difficult or hazardous for inspectors to access while reducing inspection time and cost. The authors also suggested that the data collected by such systems could support future machine-learning applications. Similarly, unmanned aerial vehicles (UAVs) have emerged as valuable tools for bridge inspections. UAVs can access areas that are difficult to reach using conventional methods, such as snooper trucks or rope access. Duque et al.[12] compared UAV-based damage assessments with traditional field measurements and found promising results. However, image quality remained sensitive to adverse weather and lighting conditions. Further research on the cost-effectiveness and reliability of UAVs under varying conditions could expand their role in bridge inspection programs.

Various machine learning methods have demonstrated significant value across a wide range of disciplines. In manufacturing, these methods are used to detect defects and optimize production processes. Altmann et al.[13] investigated supervised and unsupervised machine-learning techniques for defect classification in metal additive manufacturing. Using 635 processed micrographs, the researchers applied K-means clustering and RF models to identify and classify manufacturing defects. Among the methods evaluated, RF achieved the highest performance, exceeding 90% classification accuracy for all defect categories. In cybersecurity, machine learning has improved biometric authentication and network protection systems. Patro et al.[14] demonstrated that feature optimization techniques applied to electrocardiogram-based biometric data significantly improved recognition accuracy compared with existing classification approaches.

Armin and Hazem[15] used multi-target machine learning algorithms to simultaneously predict the condition of two core elements of the bridge, namely the deck and substructure. They used eXtreme Gradient Boosting (XGBoost) and RF models. For feature selection, the RF algorithm performed best on the training set, while the XGBoost performed best on the test set. For condition prediction, the

XGBoost achieved the highest accuracy on both the training and test sets.

Within bridge engineering, machine learning offers a practical, low-cost, and minimally invasive approach to structural health monitoring and damage detection. Luo et al.[16] reviewed computer-vision techniques for defect identification, vibration measurement, and parameter estimation. Li and Burgueño[17] evaluated five soft-computing methods, including support vector machines and fuzzy neural networks, for predicting deterioration in bridge abutment walls. Their results demonstrated that multiple modeling approaches can provide reliable predictions, allowing practitioners to select the method most appropriate for a specific application.

Ultimately, the most effective strategy for preserving the nation's bridge infrastructure is prevention. Early detection of defects provides agencies with greater flexibility and resources to implement corrective actions before conditions worsen. Routine inspections remain the cornerstone of this preventive approach. Advances in sensors, UAVs, robotic systems, and other inspection technologies have expanded engineers' ability to assess bridge components that were previously difficult to access or evaluate. The integration of machine learning into bridge inspection, health monitoring, and asset management represents another important advancement. The methods presented in this research offer practical and interpretable tools that have the potential to improve bridge management and contribute to the next generation of infrastructure assessment technologies.

Data Preprocessing

In this research, the term "bridge" is defined in accordance with FHWA guidelines as "a structure of more than 6.1 meters (20 ft) in length spanning an obstruction or depression".[18] The bridge data used in this study were obtained from the NBI repository, which provides annual inspection records for highway bridges throughout the United States and its territories. For each inspection year, the repository offers three data-access options: individual files for each of the 54 states and territories, a single file containing all bridges from all states and territories, and a file containing all records for that year. Each state is responsible for inspecting its public highway bridges and maintaining compliance with the NBIS. While all states must satisfy the minimum federal requirements, individual DOTs may adopt additional inspection procedures and regulations that are more stringent than those required by the FHWA.

This study focuses exclusively on bridges located in Ohio. Restricting the analysis to a single state provides greater consistency in inspection practices, reporting procedures, and regulatory requirements across all years of the dataset. Ohio was selected because it manages more than 27,000 bridges annually, providing a large and comprehensive dataset for analysis. Although all states follow FHWA inspection requirements, variations in state-specific regulations, inspection practices, climate conditions, population density, and infrastructure characteristics can introduce additional sources of variability. Limiting the study to Ohio reduces these external influences and improves the consistency of the analysis.

After selecting the state and inspection years, the raw NBI data were downloaded as delimited files and imported into a Microsoft Excel workbook containing 31 worksheets, representing each year from 1992 through 2022. Each worksheet was assigned a unique identifier based on the state abbreviation and the last two digits of the inspection year (e.g., "OH22" for Ohio bridge data from 2022).

The raw dataset contains up to 134 variables, each representing a specific bridge characteristic. Depending on the year, the dataset includes between 26,986 and 28,284 bridge records. Over time, bridges are constructed, rehabilitated, closed, or demolished; therefore, some bridges appear throughout the entire 31-year period, while others are present only for a portion of the study duration. Across all years, the dataset contains as many as 856,986 bridge records. Each record corresponds to a single bridge and includes all associated characteristics collected during the inspection. Bridges are uniquely identified by their structure number (SN), a numeric identifier used solely for identification purposes. To ensure consistency and facilitate data management, each worksheet was sorted by SN prior to analysis.

Characteristic Information

The characteristic columns provided in the raw datasets contain geospatial, physical, historical, and geometric information. Over the 31-year study period, new characteristics were added to inspection records, while others were removed as technologies and data collection practices evolved. To ensure consistency across the dataset, only characteristics that were available throughout the entire 31-year period were retained. This approach enables meaningful comparisons using both the raw data and the results of this study over any time span within the dataset.

Historical information, such as federal land designation, is primarily used to identify bridges for administrative or organizational purposes. Geospatial information, including location and latitude, provides reference data for locating bridges within Geographic Information Systems and other mapping frameworks. Although location data may assist in identifying environmental or climatic conditions, these characteristics are descriptive rather than causal and do not directly contribute to bridge deterioration. Therefore, historical and geospatial variables were excluded from the analysis.

Bridge geometry is highly variable and is directly related to the materials, loads, and service conditions experienced by a structure. Geometric configurations depend on the type of obstacle being crossed, operational requirements, and owner preferences. While design standards establish minimum requirements, many geometric characteristics are determined by engineers and bridge owners. To focus on the variables most relevant to bridge performance and condition

while simplifying data processing, only eight key characteristics directly associated with bridge health and management were selected for analysis.

Bridges are commonly constructed from concrete or steel, materials with substantially different mechanical properties and responses to environmental conditions. To account for these differences, the "structure kind" variable was retained initially and used to separate the dataset into steel and concrete bridge groups. Once the data were divided, this variable was no longer needed and was removed from the final workbooks.

Age was calculated as the difference between the inspection year and the value in the "year built" column. "Year built" is recorded as a four-digit code representing the year the bridge was completed or the best available estimate. Similarly, "age reconstructed" was calculated as the difference between the inspection year and the value in the "year reconstructed" column. This field is also recorded as a four-digit year, with bridges that have not been reconstructed coded as 0000.

Reconstruction refers to work that qualifies for Federal-aid funding and meets established eligibility requirements. A bridge component is considered reconstructed when the work substantially alters the bridge's geometry or load-carrying capacity. Temporary repairs intended only to maintain serviceability until a permanent solution is implemented are not classified as reconstruction. For example, resurfacing a bridge deck is considered a repair, whereas replacing a deck while modifying lane configurations or adding sidewalks constitutes reconstruction. Both bridge age and age since reconstruction may reflect material deterioration, changes in structural properties, and the cumulative effects of long-term loading.

"Average daily traffic" (ADT) represents the most recent measured or estimated traffic volume on the inventory route. It is recorded as a six-digit value representing up to one million vehicles per day. ADT serves as an indicator of the daily traffic demand placed on a bridge. Higher traffic volumes can increase wear on bridge components, potentially accelerating deterioration and reducing service life.

"Percent ADT truck" is a two-digit value representing the percentage of truck traffic within the ADT volume. This category excludes vans, pickup trucks, and other light-duty vehicles and may be estimated based on roadway classification. Because trucks generate larger and more concentrated loads than passenger vehicles, the percentage of truck traffic is an important consideration in bridge design and maintenance. Accurate estimates help engineers account for heavier loading demands and reduce stress-related deterioration over the bridge's service life.

"Main unit spans" is the number of spans within the bridge's primary structural unit. This generally includes all spans for most bridges, the principal unit of a large structure, or a section constructed using a different material or design than the approach spans. The value is recorded as a three-digit number. Bridges with multiple main spans may incorporate varying span lengths, beam configurations, or design features, which can influence both inspection procedures and the types of deterioration experienced.

"Maximum span length" is the length of the longest span within the bridge, measured along the centerline in metric units. Measurements may be taken from center-to-center bearing points or as the clear distance between piers, bents, or abutments. This value is recorded as a five-digit number. Longer spans generally experience greater deflections under load than shorter spans subjected to similar loading conditions. As a result, monitoring span behavior is particularly important for superstructures containing FCMs.

"Structure length" is the total length of the bridge roadway, measured from paving notch to paving notch or from the backwall of one abutment to the backwall of the opposite abutment. It is recorded in metric units using a six-digit code and measured to the nearest tenth. Unlike maximum span length, structure length represents the bridge as a whole and is useful for evaluating how loads are distributed throughout the entire structure and its support system.

"Deck width" is the out-to-out width of the bridge deck, measured either as the lateral clearance between superstructure members or as the actual deck width, depending on the bridge configuration. It is recorded in metric units using a four-digit code and measured to the nearest tenth. Deck width is largely determined by the transportation needs of the area served by the bridge. Wider decks can distribute vehicular and pedestrian loads across a larger area, reducing load concentration compared to narrower structures.

The "structural evaluation" column contains the SER value, which is the target variable of this research. After removing all other variables, the Steel Bridge Data and Concrete Bridge Data workbooks were finalized and prepared for analysis. Fig. 3 presents a sample of the final Steel Bridge Data workbook.

Complete Data and Materials

Some bridges did not contain a complete set of information for all characteristics. In some cases, a characteristic was not applicable to an individual bridge and was coded with an "N." To prevent the program from processing inapplicable information, any row containing an "N" was discarded. In other cases, no information was recorded for a characteristic. This was especially prevalent in earlier inspection years. This lack of information may have occurred because the bridge did not exhibit the characteristic, or the bridge element was not accessible during inspection, or because of inspector error. For ease of data processing, any rows containing blank cells were also discarded. This process was repeated for all 31 years of data. As a result, the remaining dataset included only bridges with complete sets of information, as shown in the example in Fig. 3.

After retaining only complete datasets, four copies of the consolidated workbook were created to allow comparisons between different bridge materials. The structure kind column identifies bridge material by code. Table 3 shows the bridge material classifications and their corresponding code numbers from this column.[18]

The first workbook (Concrete Bridge Data) contains bridges utilizing concrete, concrete continuous, prestressed

STRUCTURE_NUMBER	AGE	ADT	MAIN_UNIT_SPANS	MAX_SPAN_LEN	STRUCTURE_LENGTH	DECK_WIDTH	STRUCTURAL_EVAL	YEAR_RECONSTRUCTED	PERCENT_ADT_TRUCK
0100021	39	4627	3	21.9	58.3	12.8	6	0	13
0100048	39	4627	3	21.9	59.1	12.8	6	0	13
0100137	44	3881	3	28.7	73.8	12.2	6	0	19
0100145	44	3881	3	28.7	73.9	12.2	7	0	19
0100226	44	3881	3	38.4	97.7	12.3	7	0	19
0100234	44	3881	3	38.4	97.5	12.2	7	0	19
0100331	50	2888	3	16.5	44.2	12.8	7	0	20
0100366	50	2888	3	16.5	44.4	12.8	6	0	20
0100420	50	2888	3	22.9	61.4	12.2	8	0	20
0100455	50	2888	3	22.9	61.6	12.2	8	0	20
0101397	23	3612	3	40	105.1	14.1	7	0	8
0101842	24	3294	3	24.4	55.9	14.3	7	0	10
0101869	92	1108	3	30.8	77.8	12.2	5	1983	13

Figure 3. Final steel bridge data sample

Table 3. Main structure material and/or design based on NBI coding guide

Code	Name
1	Concrete
2	Concrete continuous
3	Steel
4	Steel continuous
5	Prestressed or Post-tensioned concrete
6	Prestressed or Post-tensioned concrete continuous
7	Wood or Timber
8	Masonry
9	Aluminum, Wrought Iron, or Cast Iron
0	Other

and post-tensioned concrete, and prestressed and post-tensioned concrete continuous spans. The second workbook (Steel Bridge Data) contained bridges with steel as the building material; these include steel and steel continuous spans. The third workbook (Steel and Concrete Bridge Data) contained both the steel and concrete spans together. The fourth workbook (Other Materials) contained bridges utilizing any other structural material, including wood or timber, aluminum, wrought iron, cast iron, or other spans. Steel and concrete bridges make up most of the remaining bridges, especially those located on the highway network. The third and fourth workbooks contain a small number of bridges and, therefore, were not considered for this analysis.

The Concrete Bridge Data and Steel Bridge Data workbooks are used for further analysis due to the ease of their year-to-year capabilities within the program. To run the DT and random forest (RF) models, copies of the workbooks were created and adjusted. In these copies, the data from each year was consolidated onto one sheet instead of 31 separate years. This was repeated to have one sheet of data for all 31 years, the last five years, and 2022 only. This was done for both concrete and steel bridge data. In total, six workbooks were created and used in this research. Table 4 provides the titles and descriptions of each workbook, while Table 5 indicates the final number of bridges considered for analysis within each data set per year.

Data Analysis and Modeling

The objective of this analysis is to determine the SER based on its relationship with selected bridge characteristics. Identifying the characteristics most strongly associated with deterioration may help prioritize bridges for more frequent inspections. Supervised machine learning models predict an output from labeled input data by learning patterns during training and are commonly used for regression and classification tasks. In contrast, unsupervised machine learning models analyze unlabeled data to identify underlying patterns, relationships, and structures through techniques, such as clustering, association analysis, and PCA. Both approaches were evaluated in this research for their pattern-recognition capabilities.

PC

PC measures the strength and direction of the linear relationship between two variables. The variables are plotted against each other, and a best-fit line is generated from the data points. The correlation coefficient, r, quantifies how closely the data points align with this line. Values of r range from −1 to 1. Negative values indicate an inverse relationship, while positive values indicate a direct relationship. A coefficient of zero indicates no linear relationship. Table 6 summarizes the ranges of r and their corresponding associations.

PC uses covariances and standard deviations to determine the relationship coefficient of two selected variables. The covariance (Covx,y) is a measure of variability between two

Table 4. Microsoft excel workbook summary

Excel workbook title	Bridge data included
2022 Concrete bridge data	Concrete bridges in 2022 only
2018–2022 Concrete bridge data	Concrete bridges from the last five years
1992–2022 Concrete bridge data	Concrete bridges for all years beginning in 1992
2022 Steel data bridge	Steel bridges in 2022 only
2018–2022 Steel data bridge	Steel bridges from the last five years
1992–2022 Steel bridge data	Steel bridges for all years beginning in 1992

Table 5. Final number of Ohio bridges considered every year

Year	Concrete bridges	Steel bridges
1992	7,829	10,746
1993	7,834	10,684
1994	8,135	10,590
1995	8,464	10,515
1996	8,567	10,404
1997	10,520	14,261
1998	10,750	14,099
1999	10,900	13,954
2000	11,271	13,810
2001	11,452	13,694
2002	11,682	13,381
2003	11,752	13,318
2004	11,873	13,194
2005	12,160	12,984
2006	12,287	12,816
2007	12,553	12,666
2008	12,770	12,553
2009	13,006	12,393
2010	13,087	12,241
2011	12,895	11,892
2012	12,857	11,707
2013	13,045	11,519
2014	13,170	11,398
2015	13,303	11,293
2016	14,118	11,432
2017	13,635	11,086
2018	13,711	10,977
2019	13,731	10,883
2020	13,719	10,798
2021	13,575	10,455
2022	13,621	10,383
Total	368,272	372,126

Table 6. Pearson's correlation coefficients association

Correlation coefficient (r)	Association
±1.0	Perfect positive or negative association
± 0.8 to 1.0	Strong positive or negative association
± 0.4 to 0.8	Moderate positive or negative association
± 0 to 0.4	Weak positive or negative association
0	No correlation

random variables and is calculated using Eq. (1).

$$Cov_{x,y} = \frac{\sum(x_i - \overline{x})(y_i - \overline{y})}{N - 1} \tag{1}$$

The standard deviation ($\sigma_{x,y}$) measures the dispersion of a dataset compared to the mean, calculated as the square root of the variance, as shown in Eq. (2).

$$\sigma_{x,y} = \sqrt{\frac{\sum(x_i - \mu)^2}{N}} \tag{2}$$

With this information, PC coefficient (r) can be determined using a ratio of the covariance and the product of the standard deviations, which is shown in Eq. (3).

$$r = \frac{Cov_{x,y}}{\sigma_x \sigma_y} \tag{3}$$

PC coefficients are calculated for each selected characteristic. Although these coefficients are produced in a tabular format, a heatmap can also be generated to provide an easily interpretable visual graphic. Coefficients and heatmaps were produced for each year from 1992 to 2022 for both steel and concrete bridges.

DT modeling

A DT is a supervised, non-parametric learning algorithm that classifies data and makes predictions using training subsets. It provides an interpretable, tree-structured model

in which rule-based branches guide data through decision nodes to possible outcomes while preserving key data characteristics.

The SER value is the target variable predicted using classes defined by the eight selected features. A random state is applied to ensure consistent data splitting across executions. The dataset is divided into training and test sets, with 80% used for training and 20% for testing and validation.

The DT algorithm is fitted to the training data. A fixed random state controls the estimator's random behavior during splitting, ensuring the tree structure remains consistent across runs. The trained model is then applied to the test set to predict SER values. Model performance is evaluated by comparing predicted and actual values.

The explained variance (r^2), or coefficient of determination, measures the proportion of variance in the dependent variable explained by the independent variables. It is calculated using the total sum of squares (TSS), which represents total variance, and the residual sum of squares (RSS), which represents unexplained variance after model fitting. The explained variance (r^2) is defined by Eq. (4):

$$r^2 = 1 - \frac{RSS}{TSS}. \tag{4}$$

The explained variance ranges from 0 to 1, with higher values indicating a better model fit.

The sum of squared errors (SSE) measures the discrepancy between actual (y) and predicted ($\hat{y}$) values. It is calculated as the sum of squared differences between them, with lower values indicating better performance. If predictions perfectly match observations, SSE equals zero. SSE is calculated using Eq. (5):

$$SSE = \sum (y - \hat{y})^2 \tag{5}$$

A DT is built branch by branch as rules are generated from the data. Each observation follows the applicable branches until it reaches a leaf node, which represents its final classification. The predicted SER is then compared with the actual value. A coefficient of determination is also calculated for each leaf to assess prediction accuracy within that node.

RF modeling

RF modeling is a supervised learning algorithm that improves prediction accuracy by combining multiple DTs. Rather than relying on a single tree, the model aggregates predictions from many independently trained trees, reducing overfitting and improving generalization. Each tree is built using a randomly selected subset of the data through a bagging process.

The RF models use the same dataset and Python libraries as the DT models. SER is the target variable, while the remaining features serve as predictors. A fixed random state ensures consistent data splitting and reproducible results.

An RF classifier containing 100 trees is trained and evaluated using classification accuracy. An RF regressor with 100 trees predicts SER values and is assessed using the R^2 score. Combined tree outputs produce a single generalized prediction.

Selection of Analysis Methods

Three analytical methods were selected to evaluate relationships between SER and the chosen characteristics: PC, DT, and RF modeling. Although DT and RF models operate under similar principles, they differ in how training data are processed. Applying both methods enables comparison of their strengths and limitations for predicting bridge health and supporting management decisions.

Other techniques, including K-means clustering and PCA, were considered but not used. These methods offer limited advantages when working with categorical data because measuring distances between categories is difficult. While the characteristics analyzed in this study are discrete or continuous, future bridge inspection data may include categorical or ordinal variables. To maintain flexibility for analyzing a broader range of characteristics, methods better suited to mixed data types were selected. Table 7 summarizes the analytical methods used.

Results and Discussions

Both steel and reinforced concrete bridges undergo deterioration from fatigue, freeze-thaw cycles, corrosion, vehicular loads, and other environmental distresses. However, the

Table 7. Summary of supervised and unsupervised learning methods

Learning method	Method type	Summary
K-means clustering	Unsupervised	Clusters data based on similar features
Principal component analysis	Unsupervised	Transforms data into lower dimensional forms
Pearson's correlation	Statistical	Measures linear correlation between two sets of data
Decision tree modeling	Supervised	Categorizes data based on training information to make predictions
Random forest modeling	Supervised	Categorizes data based on multiple randomized training information to make predictions

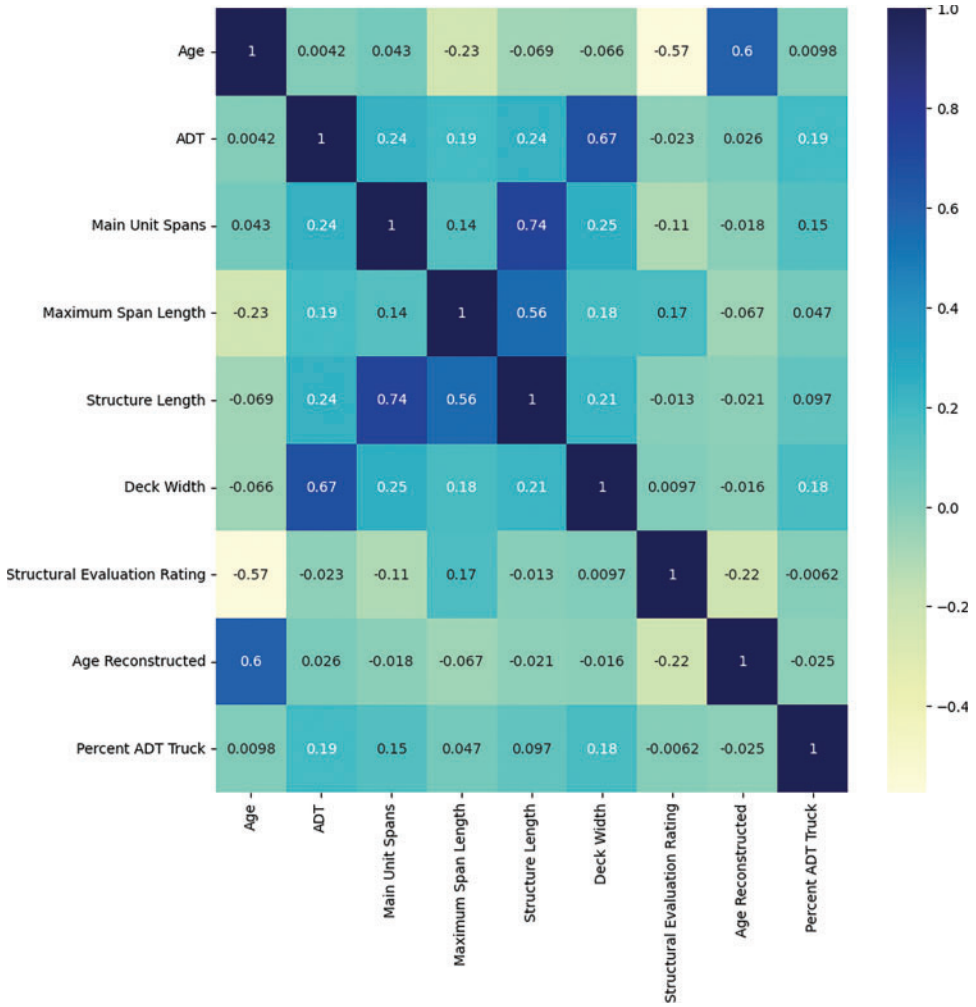

Figure 4. Pearson's correlation heatmap for 2022 concrete bridge data

average SER has been increasing instead of decreasing in both bridge types over time. This can be attributed to more efficient and precise design methods, better inspection tools and techniques, and preventative maintenance. The SER may also be dependent on the inspectors, with 95% of condition ratings varying by two points and 68% varying within one point for each element.[19] Utilizing machine learning becomes valuable for predicting the SER by removing inspector bias and only considering the raw data.

PC results

PC coefficients were calculated for each characteristic annually. Fig. 4 presents the correlation matrix for the 2022 Concrete Bridge dataset. The heatmap uses colors and numerical values to visualize the strength and direction of correlations between characteristics. A characteristic correlated with itself has a coefficient of 1, indicating a perfect relationship, while a coefficient of 0 indicates no relationship.

Although the matrix displays relationships among all characteristics, this study focuses only on correlations with SER. Correlation matrices provide a clear and interpretable way to examine relationships within each year, offering greater visual insight than tabulated results alone. Heatmaps were generated for both Concrete Bridge and Steel Bridge datasets from 1992 to 2022, resulting in 31 annual correlation matrices for each bridge type.

PC coefficients were calculated for all 31 years of data. To identify long-term trends, the average coefficient for each characteristic was determined across the entire study period. While these averages provide an overall measure of relationship strength, they may mask temporal changes in importance. Examining shorter periods, such as individual years or rolling five-year averages, can reveal shifts caused by evolving design practices, technologies, or maintenance strategies. Considering multiple timeframes provides complementary perspectives for decision-making and facilitates comparison between concrete and steel bridges.

Table 8 presents the average correlation coefficients for each characteristic, while Fig. 5 compares these values by bridge material. This comparison highlights characteristics with differing relationships to SER and provides a visual assessment of their relative importance. In six of the eight characteristics, the correlation sign was consistent across both materials. However, ADT and main unit spans showed negative correlations for concrete bridges and positive correlations for steel bridges. Such differences may result from

Table 8. Characteristics average 31-year Pearson's correlation coefficient by material

	Average correlation	
Characteristic	Concrete bridges	Steel bridges
Age	−0.5806	−0.4594
ADT	−0.0433	0.1585
Main unit spans	−0.0772	0.1336
Maximum span length	0.2110	0.1384
Structure length	0.0202	0.1189
Deck width	0.0123	0.2847
Age reconstructed	−0.1871	−0.2163
Percent ADT truck	0.0096	0.1816

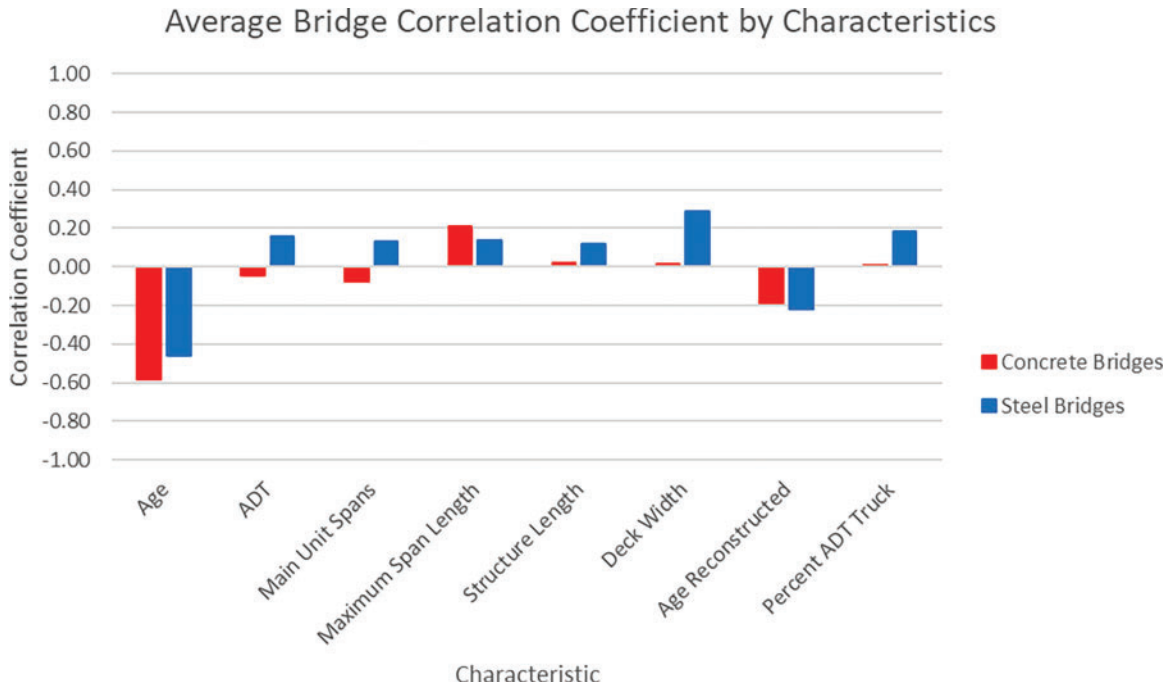

Figure 5. Average of 31-year Pearson's correlation coefficients based on the material of construction

unaccounted factors influencing bridge performance. Correlations near zero are also more likely to change sign than stronger positive or negative relationships because only small numerical shifts are required.

Averaging correlation coefficients across 31 years could produce unrepresentative results if coefficient signs changed over time. However, although these two characteristics exhibited weak relationships, their coefficient signs remained consistent throughout the study period. This indicates that the long-term averages accurately reflect their overall relationships and are not artifacts of temporal variation.

Figs. 6 and 7 illustrate annual fluctuations in correlation coefficients, making it easy to identify positive, negative, and near-zero relationships. These visualizations provide a clearer comparison of bridge materials and characteristics than tables alone. They also help reveal the effects of changes in specifications, inspection practices, environmental events, or data collection methods. For example, the introduction of new technologies may create trends in subsequent years. Analyzing specific time periods can further isolate such effects and support targeted engineering decisions.

Age and age reconstructed consistently showed negative correlations with SER for both bridge materials over 31 years. Age had the strongest, though only moderate, relationship with SER, while age reconstructed ranked third overall but remained weak. As bridges age, exposure to weather, chemicals, impacts, and repeated loading reduces conditions reflected in negative coefficients. Early inspections can identify deterioration, enabling component replacement or full reconstruction. LeBeau and Wadia-Fascetti[20] highlighted the importance of early inspection for detecting corrosion in strands and rebars. Prior work by Agrawal et al.[21] did not account for abrupt changes, such as rehabilitation or data

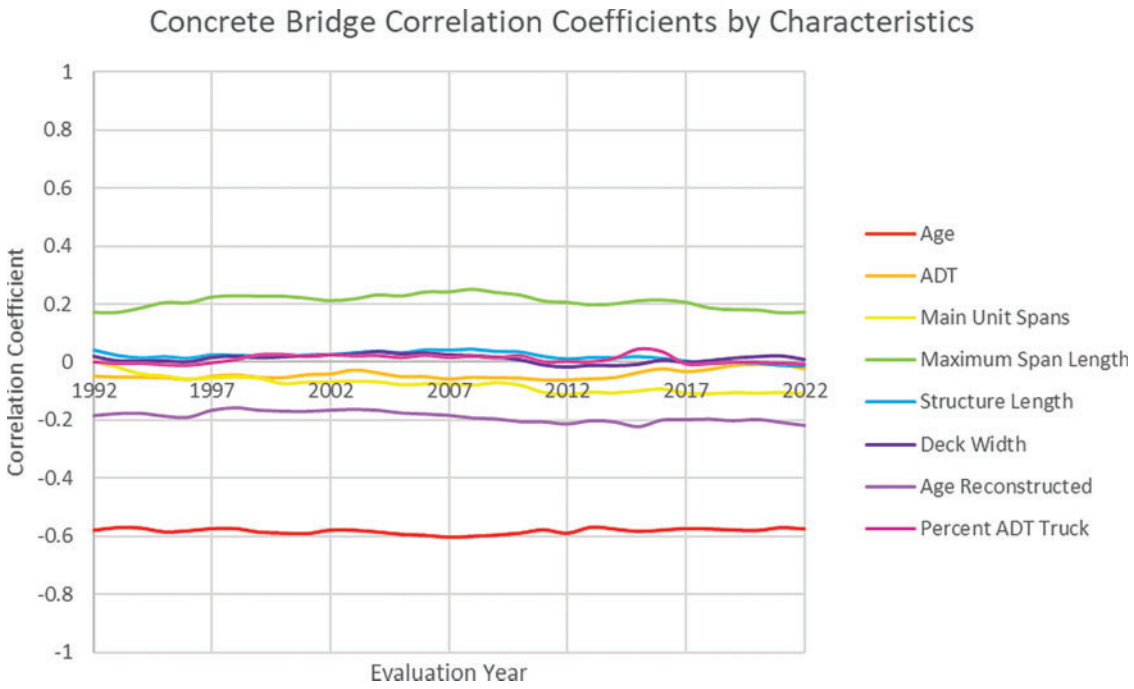

Figure 6. Pearson's correlation coefficients over time for concrete bridges

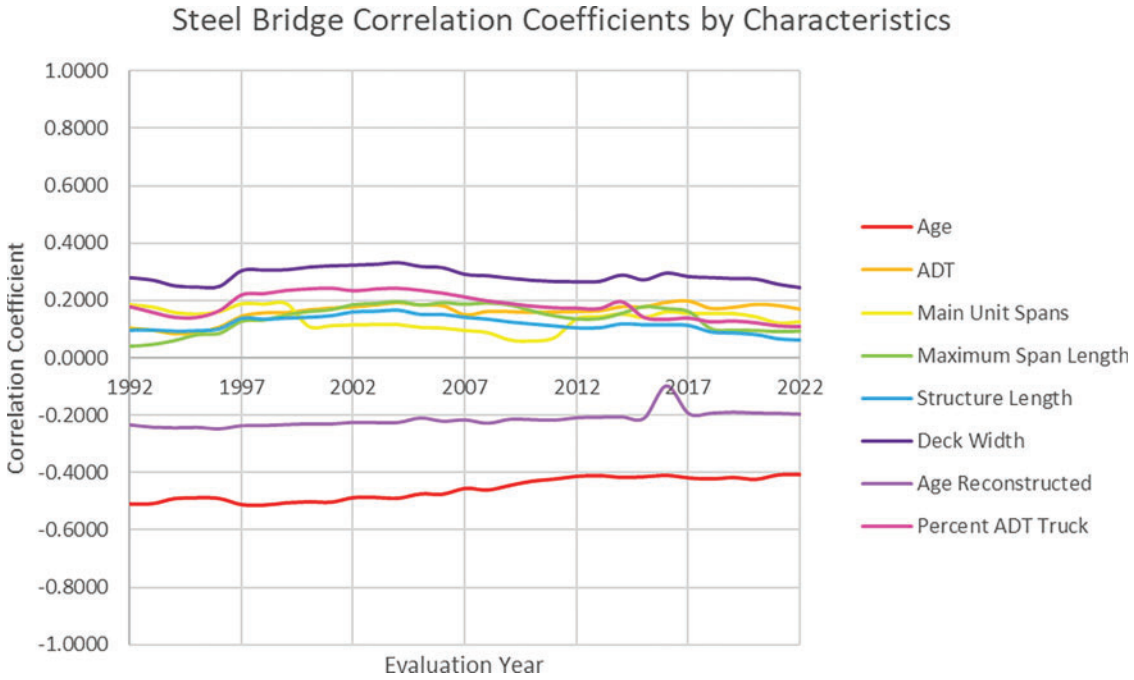

Figure 7. Pearson's correlation coefficients over time for steel bridges

errors. Reconstruction resets bridge age by replacing most components.

Except for age, all variables exhibited weak or negligible correlations with SER. Although these relationships were weak, they can still be ranked relative to one another. For both steel and concrete bridges, ADT showed the fifth-strongest correlation with SER. However, the correlation was positive for steel bridges and negative for concrete bridges. ADT reflects repeated traffic loading, which has been linked to increased bridge deterioration through more frequent load cycles, greater use of deicing agents, and fatigue damage.[22,23] Despite these effects, ADT demonstrated only weak or no correlation with SER in either bridge type.

The number of main unit spans exhibited the fourth-strongest relationship with SER for concrete bridges and the seventh-strongest for steel bridges. Maximum span length ranked second for concrete bridges and sixth for steel bridges. Although load distribution patterns may be similar between long and short spans on the same bridge, longer

spans carry greater total loads due to increased self-weight and vehicular loading. These loads result in larger midspan deflections and higher internal stresses, which could accelerate deterioration.

Structure length ranked sixth for concrete bridges and eighth for steel bridges. Because structure length only measures the distance between paving notches, it does not account for the number of supports, span configurations, or individual span lengths. Consequently, it may not accurately represent the forces, moments, and stresses experienced by the bridge. Longer bridges often require additional structural components, such as larger decks, more girders and piers, and greater superstructure anchorage. While these features may increase potential deterioration points, both concrete bridges and steel bridges exhibited only weak correlations between structure length and SER. This suggests that structure length alone is insufficient to explain SER variation and that its influence may depend on interactions with other characteristics.

Deck width ranked second for concrete bridges and seventh for steel bridges, yet both bridge types showed only weak positive correlations with SER. Bridge decks are directly exposed to traffic loads, weather, and deicing agents, making them particularly susceptible to deterioration. Deck width is largely determined by functional requirements, including the number of traffic lanes, shoulders, bicycle lanes, sidewalks, and safety barriers. These design elements vary according to traffic demand, site conditions, and owner requirements. Although wider decks may present more potential deterioration areas, they can also distribute loads more effectively. For example, bridges with wider shoulders or pedestrian facilities may experience lower live-load demands than bridges of equal width carrying only vehicular traffic. This may help explain the observed positive relationship between Deck width and SER.

Aside from age and age reconstructed, the ranking of bridge characteristics differed between concrete bridges and steel bridges. Many observed correlations were weaker or differed from expected trends, and the small differences between coefficient values make rankings sensitive to minor fluctuations. Overall, the analysis indicates that geometry alone has limited influence on SER. Nevertheless, PC analysis remains valuable for identifying trends, guiding further investigation, and highlighting age as the most influential factor affecting bridge condition and long-term performance. These findings underscore the importance of preventive maintenance and comprehensive inspection records in managing aging infrastructure effectively.

DT and RF model results

Using DT and RF modeling, it was possible to associate the selected characteristics with the correct SER reliably for both bridge types. Two timespans were processed: all recorded years from 1992 to 2022 and the last five recorded years from 2018 to 2022. The corresponding accuracy scores are shown in Table 9.

Model performance was similar for both Concrete Bridge and Steel Bridge datasets, with the largest difference in accuracy being 2.5% in the five-year DT model. This suggests that both DT and RF models can effectively predict SER regardless of bridge material, despite the datasets differing by approximately 4,000 bridges. Model performance was also consistent across timeframes. The largest accuracy difference between the 1992–2022 and 2018–2022 Concrete Bridge datasets was 2.9%, occurring in the DT model. Across all datasets, both model types achieved accuracies above 79%. The explained variances are presented in Table 10.

Explained variance ranges from 0 to 1, with values closer to 1 indicating a better model fit. The 31-year datasets produced the highest explained variances for both bridge

Table 9. Decision tree and random forest model accuracy percentage by material

		Concrete bridges	Steel bridges
1992–2022	Decision tree	82.1%	82.9%
	Random forest	87.9%	86.2%
2018–2022	Decision tree	79.2%	81.7%
	Random forest	88.0%	88.5%

Table 10. Decision tree and random forest model explained variances by material

		Concrete bridges	Steel bridges
1992–2022	Decision tree	0.786	0.809
	Random forest	0.877	0.881
2018–2022	Decision tree	0.705	0.740
	Random forest	0.838	0.861

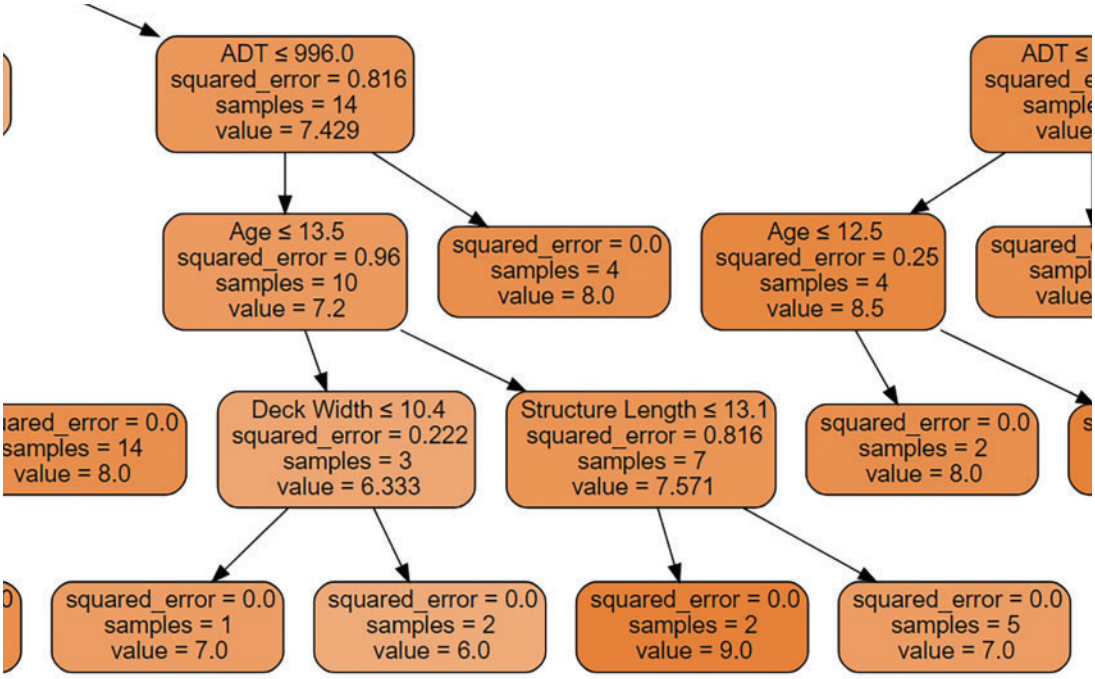

Figure 8. A partial representation of the decision tree model for 1992–2022 concrete bridge data

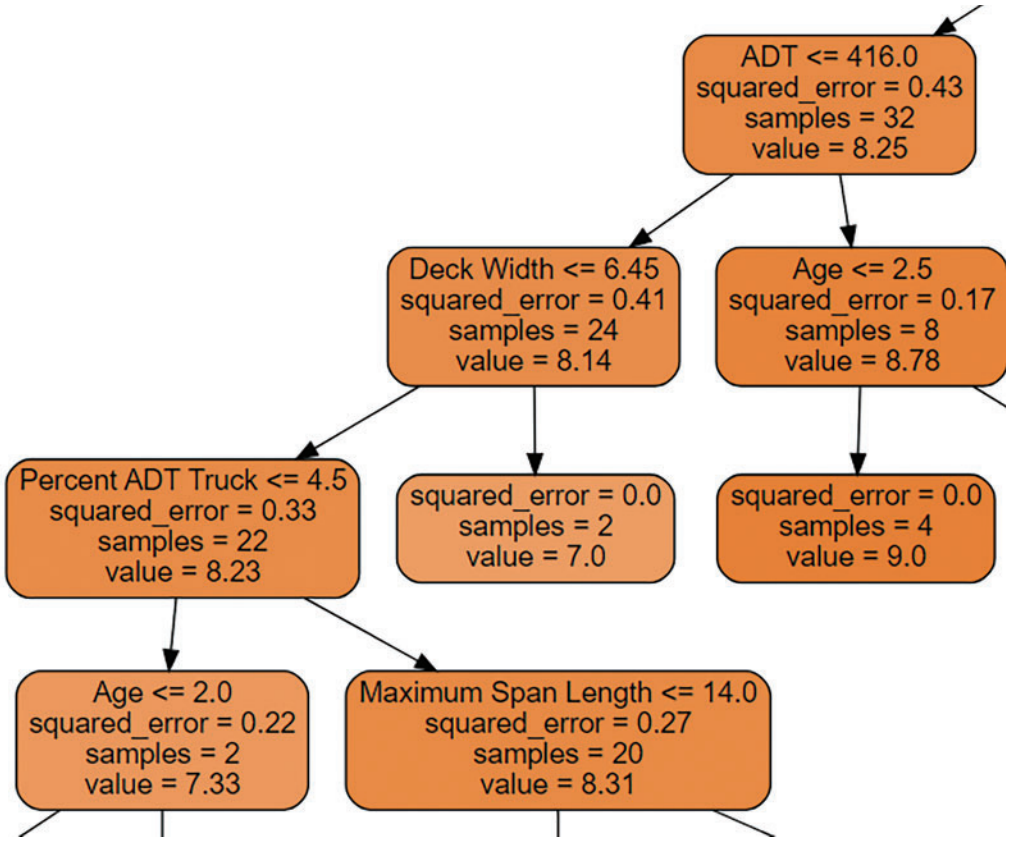

Figure 9. A partial representation of the RF model for 2018–2022 concrete bridge data

materials and model types, while the five-year datasets showed only slight reductions; all values remained above 0.70. The larger dataset, which included over 740,000 bridge records, benefited from repeated observations of the same bridges over time, capturing changes in condition, rehabilitation activities, and characteristics, such as ADT. Although some records were excluded during preprocessing due to incomplete data, the longitudinal nature of the dataset likely improved model performance.

In all cases, the RF model outperformed the DT model. By averaging the outputs of 100 randomized DTs, RF models reduce variance and noise, resulting in more robust predictions. Overall, the RF models trained on the 1992–2022 Concrete Bridge and Steel Bridge datasets achieved the strongest performance. As additional inspection data become available, model accuracy may further improve through continued integration of historical and future records.

Figs. 8 and 9 present sample outputs from the DT and RF models of the Concrete Bridge datasets. Three node types are shown: root, internal, and leaf nodes. The root node is the starting point of the tree from which all branches originate. Internal nodes split into additional nodes based on decision criteria, forming the structure of the tree. Leaf nodes are the terminal nodes and represent the final prediction outcomes, with no further branching.

The DT models can be followed by tracing the characteristic thresholds used at each split. Because most variables in this analysis are quantitative, nodes divide the data using conditions based on values greater than or less than a specified threshold. If the characteristics of a bridge are known, its predicted SER can be determined by following the appropriate path to a leaf node.

Each node contains four key pieces of information. The first row identifies the characteristic and threshold used for the split. The second row shows the squared error, with values closer to zero indicating a more accurate fit. The third row reports the number of bridge samples within the node. This sample size decreases with each split until a leaf node is reached. The fourth row provides the average SER of the bridges contained within that node.

The full DT and RF models generated in this study are too large to display effectively on a single page. To improve interpretability and reduce overfitting, tree size can be controlled through pruning, which removes or prevents splits that do not meet specified criteria, such as a minimum sample size. Tree depth may also be limited. Depth refers to the number of levels between the root and leaf nodes. While deeper trees can improve classification accuracy by capturing more detailed patterns, they also increase the risk of overfitting. Effective model development, therefore, requires balancing predictive performance and generalization.

Both DT and RF models identify patterns in bridge characteristics that predict SER. Each branch represents a sequence of conditions leading to a predicted SER value. For example, in Fig. 8, the root node first splits bridges according to ADT. Subsequent nodes continue to divide the data until groups of bridges with highly similar characteristics remain. The resulting leaf node provides the predicted SER based on the average value of the bridges within that subset. Although RF models consistently outperformed DT models, both demonstrated strong potential as decision-support tools for bridge management.

Because RF visualizations are particularly large, representative paths for concrete bridge and steel bridge models are summarized in Tables 11 and 12, respectively. In the 2022 Concrete Bridge Data model, a sample path begins with a split at bridge age $\leq$31.5 years, containing 6,896 bridges with a squared error of 1.64 and an average SER of 6.94. Moving down the branch by to the left, or the "True" option, the next node was a decision between an age less than to equal to 12.5 years. Here, 3,270 samples were included with a squared error of 1.04 and an average SER of 7.64. Following subsequent age-based splits eventually leads to a leaf node containing five bridges with identical characteristic paths. This node has a squared error of 0.0 and an average SER of 8. Along the path, squared error decreases as additional information is incorporated, indicating improved predictive certainty, while the sample size declines as bridges are partitioned into increasingly specific groups.

The selected path in the 2022 Steel Bridge Data RF model began with a split on deck width $\leq$7.25 m, containing 5,264 bridges with a squared error of 1.81 and an average SER of 6.42. Following the branch for deck widths greater than 7.25 m led to an age-based split, where 4,247 bridges with ages $\leq$19.5 years remained. This node had a squared error of 1.42 and an average SER of 6.68. After ten successive decisions, the path reached a leaf node containing a single bridge with a predicted SER of 8.0.

Table 11. Random forest branch sample information for 2022 concrete bridge data

Characteristic boundary	Boundary decision	Squared error	Sample	Value
Age $\leq$31.5		1.64	6,896	6.94
Age $\leq$12.5	True	1.04	3,270	7.64
Age $\leq$21.5	False	0.92	2,325	7.34
Deck width $\leq$9.05	False	0.97	1,325	7.19
Structure length $\leq$11.5	True	0.91	632	7.36
Deck width $\leq$6.3	True	1.18	226	7.13
Age $\leq$25.5	True	0.76	20	7.67
ADT $\leq$272.0	False	0.43	9	8.20
Structure length $\leq$7.9	True	0.16	7	7.80
ADT $\leq$26.5	False	0.1	6	7.89
	False	0.0	5	8.00

Table 12. Random forest branch sample information for 2022 steel bridge data

Characteristic boundary	Boundary decision	Squared error	Sample	Value
Deck width ≤7.25		1.81	5,264	6.42
Age ≤19.5	False	1.42	4,247	6.68
Age ≤8.5	True	0.74	405	8.04
Structure length ≤199.2	True	0.47	149	8.53
ADT ≤880.0	True	0.42	145	8.56
Deck width ≤10.0	False	0.49	90	8.42
Percent ADT truck ≤6.0	True	1.01	12	7.79
Main unit spans ≤2.0	True	0.96	5	7.2
Percent ADT truck ≤1.5	True	0.4	3	8.0
ADT ≤4080.5	False	0.19	2	7.75
	False	0.0	1	8.0

Similar to the concrete bridge example, the squared error generally decreased as the path progressed toward the leaf node, indicating improved prediction accuracy as additional information became available. Although some nodes exhibited higher squared errors, these deviations may be attributable to limited data for less common characteristics, such as percent ADT truck. The sample size consistently decreased at each split until a single bridge with a unique combination of characteristics remained. Unlike the concrete bridge example, the average SER did not exhibit a consistent trend along this path.

A key advantage of DT and RF models is their ability to clearly visualize how bridges are distributed across characteristic subsets. The paths presented in Tables 11 and 12 represent only two examples from many possible combinations. Every bridge in the dataset is represented within the trees, allowing engineers to explore how specific design or operational characteristics influence predicted SER values. For example, during bridge design, engineers can evaluate how choices, such as the number of main unit spans, may affect the predicted SER.

These models also facilitate the identification of decision points where substantial changes in average SER occur, providing valuable information for inspection planning. Unlike ODOT's AssetWise system, which primarily uses conditional statements based on individual characteristics, RF models evaluate multiple characteristics simultaneously. This capability enables the identification of bridge groups with similar deterioration risks and SER predictions, potentially supporting more targeted inspection intervals.

Effective bridge management depends on both comprehensive documentation and informed decision-making. The proposed models provide engineers with accessible, data-driven insights to support maintenance and rehabilitation decisions. They can function either as standalone screening tools or as enhancements to existing bridge management practices.

Conclusion

This study utilized NBI data for Ohio bridges collected between 1992 and 2022 to develop statistical and supervised machine learning models for predicting the SER. Raw NBI data were imported into Microsoft Excel, where records were organized, cleaned, and filtered. Bridges with incomplete inspection records or inapplicable information were removed. Eight physical and geometric bridge characteristics were selected for analysis, while other variables were excluded and may be investigated in further studies. The remaining data were separated by bridge material into concrete, steel, combined concrete and steel, and other bridge categories. Due to their larger sample sizes, only the Concrete Bridge and Steel Bridge datasets were analyzed, resulting in more than 700,000 usable records. Separate datasets were then created representing the full 31-year period, the most recent five years, and the most recent year.

Data processing and model development were performed using Jupyter Notebook. Three analytical approaches were evaluated: PC, DT, and RF models. PCs quantified the relationships between individual bridge characteristics and SER across the 31-year dataset. Bridge age consistently demonstrated the strongest relationship with SER for both concrete and steel bridges, whereas most other characteristics exhibited weak or negligible correlations. Several results differed from expected trends, and although varying the analysis timeframe affected model performance slightly, it had little influence on the observed correlations.

DT and RF models provided both visual representations of characteristic interactions and accurate SER predictions. The strongest predictive performance was achieved using the complete 31-year datasets, emphasizing the value of comprehensive historical inspection records. Among the machine learning approaches, RF models consistently outperformed DT models while maintaining strong interpretability.

The findings demonstrate the usefulness of all three methods for supporting bridge management decisions. PCs help identify characteristics most closely associated with bridge

condition, while DT and RF models reveal how combinations of characteristics influence SER. These tools could support future bridge inspection programs by identifying bridges that warrant increased monitoring. Unlike traditional screening methods that rely on individual criteria, machine learning models can evaluate multiple characteristics simultaneously, improving the precision of bridge selection. Integrating these models with existing systems, such as AssetWise, could help prioritize the most critical bridges within already-flagged populations. As bridge infrastructure continues to age, data-driven tools can enhance inspection planning, maintenance prioritization, and rehabilitation strategies, ultimately improving public safety and the long-term management of transportation assets.

Data Availability Statement

All data related to this research are available upon request.

References

[1] Federal Highway Administration (FHWA). *Bridge Replacement Unit Costs 2022*. Washington DC, USA: Bridges and Structures; 2022. https://www.fhwa.dot.gov/bridge/nbi/sd2022.cfm#c.

[2] Hartmann J, Weingroff R. *Highway History*. Washington DC, USA: Federal Highway Administration; June 2021. https://www.fhwa.dot.gov/highwayhistory/national_bridge_inspection_standards.cfm#:~:text=The%20modern%20highway%20bridge%20safety,and%20unsafe%20bridges%20are%20.

[3] Gee K, Henderson G. *Highway Bridge Inspections*. Washington DC, USA: U.S. Department of Transportation; 2007. https://www.transportation.gov/testimony/highway-bridge-inspections.

[4] Ohio Department of Transportation (ODOT) Office of Structural Engineering. Columbus, Ohio, USA: Reliability Based Inspection (RBI) Implementation Procedure; 2021. https://www.transportation.ohio.gov/business/engineering/structural.

[5] Federal Highway Administration (FHWA). Nondestructive evaluation and structural health monitoring. In: *Nondestructive Evaluation and Structural Health Monitoring*. FHWA; 2021. https://highways.dot.gov/research/long-term-infrastructure-erformance/ltbp/nondestructive-evaluation-structural-health-monitoring#tools.

[6] National Highway Traffic Safety Administration (NHTSA). *Traffic Safety Facts 2021: A Compilation of Motor Vehicle*. Washington DC, USA: Federal Highway Administration; 2023. https://crashstats.nhtsa.dot.gov/Api/Public/ViewPublication/813527.

[7] Palu S, Mahmoud H. Impact of climate change on the integrity of the superstructure of deteriorated U.S. bridges. *PLoS One*. 2019;14(10). doi:10.1371/journal.pone.0223307.

[8] Zhao R, Shi C, Zhang R, Wang W, Zhu H, Luo J. Study on the freeze-thaw resistance of concrete pavements in seasonally frozen regions. *Materials*. 2024;17(8):1902. doi:10.3390/ma17081902.

[9] Clarke-Sather AR, McConnell JR, Masoud E. Application of lean engineering to bridge inspection. *J Bridge Eng*. 2021;26(2). doi:10.1061/(asce)be.1943-5592.0001657.

[10] Abdallah AM, Atadero RA, Ozbek ME. A state-of-the-art review of bridge inspection planning: current situation and future needs. *J Bridge Eng*. 2022;27(2). doi:10.1061/(asce)be.1943-5592.0001812.

[11] Galdelli A, D'Imperio M, Marchello G, Mancini A, Scaccia M, Sasso M, Frontoni E, Cannella F. A novel remote visual inspection system for bridge predictive maintenance. *Remote Sens*. 2022;14(9):2248. doi:10.3390/rs14092248.

[12] Duque L, Seo J, Wacker J. Bridge deterioration quantification protocol using UAV. *J Bridge Eng*. 2018;23(10). doi:10.1061/(asce)be.1943-5592.0001289.

[13] Altmann ML, Benthien T, Ellendt N, Toenjes A. Defect classification for additive manufacturing with machine learning. *Materials*. 2023;16(18):6242. doi:10.3390/ma16186242.

[14] Patro KK, Jaya Prakash A, Jayamanmadha Rao M, Rajesh Kumar P. An efficient optimized feature selection with machine learning approach for ECG biometric recognition. *IETE J Res*. 2020;68(4):2743–2754. doi:10.1080/03772063.2020.1725663.

[15] Armin RN, Hazem E. Predicting Ohio bridges' conditions using multi-target machine learning algorithms. *Proceedings of the International Conference on Transportation and Development 2024*. Reston, VA: American Society of Civil Engineers; 2024. doi:10.1061/9780784485538.055.

[16] Luo K, Kong X, Zhang J, Hu J, Li J, Tang H. Computer vision-based bridge inspection and monitoring: a review. *Sensors*. 2023;23(18):7863. doi:10.3390/s23187863.

[17] Li Z, Burgueño R. Using soft computing to analyze inspection results for bridge evaluation and management. *J Bridge Eng*. 2010;15(4):430–438. doi:10.1061/(asce)be.1943-5592.0000072.

[18] Federal Highway Administration (FHWA). *Recording and Coding Guide of the Structure Inventory and Appraisal of the Nation's Bridges*. Washington DC, USA; 1995. https://www.fhwa.dot.gov/bridge/mtguide.pdf.

[19] Phares BM, Washer GA, Rolander DD, Graybeal BA, Moore M. Routine highway bridge inspection condition documentation accuracy and reliability. *J Bridge Eng*. 2004;9(4):403–413. doi:10.1061/(asce)1084-0702(2004)9:.

[20] LeBeau K, Wadia-Fascetti S. Predictive and diagnostic load rating model of a prestressed concrete bridge. *J Bridge Eng*. 2010;15(4):399–407. doi:10.1061/(asce)be.1943-5592.0000073.

[21] Agrawal AK, Kawaguchi A, Chen Z. Deterioration rates of typical bridge elements in New York. *J Bridge Eng*. 2010;15(4):419–429. doi:10.1061/(asce)be.1943-5592.0000123.

[22] Tabatabai H, Tabatabai M, Lee C-W. Reliability of bridge decks in Wisconsin. *J Bridge Eng*. 2011; 16(1):53–62. doi:10.1061/(asce)be.1943-5592.0000133.

[23] Saberi MR, Rahai AR, Sanayei M, Vogel RM. Bridge fatigue service-life estimation using operational strain measurements. *J Bridge Eng*. 2016;21(5). doi:10.1061/(asce)be.1943-5592.0000860.

BER the international journal of bridge engineering management and research

Assessing Damage Behavior of Reinforced Concrete Bridge Piers under Low-Velocity Car Crashes: Experimental and Numerical Study

Suman Roy*

Submitted: 12 April 2026 **Accepted:** 24 June 2026 **Publication date:** 10 July 2026

DOI: 10.70465/ber.v3i3.90

Abstract: Vehicle collisions subject reinforced concrete (RC) bridge piers to high strain-rate dynamic loads, producing complex material interactions and an apparent strength enhancement commonly quantified by the dynamic increase factor (DIF). During impact, the concrete cover, acting as a sacrificial layer, experiences initial damage due to the car crash, subsequently transferring forces to the transverse reinforcement and altering the pier's axial and flexural behavior. This study presents an experimental investigation of low-velocity vehicular collisions involving subcompact and sedan cars, with emphasis on cosmetic surface damage and global structural response. Finite element simulations developed in ANSYS are employed to reproduce the experimental behavior and to validate estimates of post-impact residual capacity. Damage levels are further quantified using a combined probabilistic and reliability-based framework to assess the likelihood and severity of cosmetic damage. The results offer valuable insights into impact-induced damage mechanisms, enable rational evaluation of residual structural capacity, and support informed decisions regarding repair or strengthening. Additionally, chaotic analysis has been further scrutinized in terms of chaotic risk amplification factor (CRAF) to reinforce the findings. This present study contributes to forensic assessments of RC bridge piers' serviceability and resilience following vehicular impact events.

Author keywords: Representative prototype RC bridge piers; low-velocity car crashes; Finite Element (FE) simulations; determination of cosmetic damage; validation of experimental results; and validation of experimental results

Introduction

Bridge piers are subjected to highly dynamic actions arising from seismic events, blasts, and vehicular collisions. These actions may induce damage ranging from superficial surface deterioration to severe structural degradation, potentially leading to collapse. While the seismic performance of reinforced concrete (RC) piers has been extensively investigated, the effects of low-velocity vehicular impacts, particularly those resulting in minor or cosmetic damage, remain inadequately understood.

In practice, RC piers experiencing low-velocity vehicular collisions are often left unrepaired because the observed damage is perceived as non-structural. However, even minor impact-induced damage may compromise stiffness, alter load paths, and reduce residual capacity over time. At present, there is no reliable framework for quantifying capacity degradation associated with such damage, raising concerns regarding the safety and serviceability of impacted piers when subjected to subsequent loading, including earthquakes, blasts, or additional collisions. This deficiency highlights the need for systematic investigation into the cumulative effects of cosmetic damage and its potential role in progressive or catastrophic failure.

Existing design codes provide limited guidance for RC piers subjected to high strain-rate loading and are particularly inadequate in addressing post-impact deformation and residual capacity following low-severity vehicular collisions. Although dynamic impact scenarios, including vehicle crashes and blast loading, have been studied, the specific response of RC bridge piers under low-velocity vehicular impacts remains largely unexplored. This limitation is critical given that vehicular collisions represent one of the most frequent impact hazards for bridge substructures, a risk amplified by increasing traffic volumes.[1]

This study addresses the identified knowledge gap by investigating the structural performance of RC bridge piers subjected to low-velocity vehicular impact. The objectives are to characterize cosmetic damage, identify dominant failure mechanisms, and quantify residual load-carrying capacity. An experimental program consisting of pendulum impact tests on four half-scale RC pier specimens was conducted to simulate realistic low-speed vehicle collisions. The

*Corresponding Author: Suman Roy.
Email: sumanroy74@gmail.com
Department of Civil and Environmental Engineering, Utah State University, Logan, Utah 84322 U.S.A

Discussion period open till six months from the publication date. Please submit separate discussion for each individual paper. This paper is a part of the Vol. 3 of the International Journal of Bridge Engineering, Management and Research (© BER), ISSN 3065-0569.

experimental results provide insight into damage evolution, energy dissipation, and post-impact serviceability.

Previous studies have identified shear failure and overturning moments at the column base as dominant failure modes in RC columns subjected to impact loading.[2,3] Investigations involving sequential loading scenarios, such as blast followed by vehicular impact, have further demonstrated the influence of column diameter, longitudinal reinforcement ratio, and transverse reinforcement on structural reliability.[4] Increasing column stiffness and modifying pier geometry have been proposed as effective strategies to enhance resistance to low-velocity dynamic impacts through improved energy dissipation.[5]

Despite these advances, the influence of cosmetic damage caused by low-velocity vehicular impacts on residual capacity remains largely unquantified. To address this gap, experimental findings are used to define post-impact performance levels, which are subsequently validated and extended through finite element modeling (FEM). The numerical models simulate quasi-static low-speed impact conditions, enabling replication of realistic vehicle–pier interaction and identification of critical failure mechanisms. Stress concentration and plastic hinge formation are consistently observed near the column–foundation interface, which governs energy dissipation through crack initiation and propagation.[6]

To replicate in-service conditions, axial preloading was applied to the pier specimens prior to impact, and corresponding FEM simulations were developed for numerical validation. The interaction between axial compression and lateral impact forces was analyzed to characterize stress, strain, and deformation behavior in the vicinity of the column base. Uniaxial material constitutive models have been adopted to capture localized damage with sufficient accuracy, supporting a comprehensive assessment of post-impact structural performance.

Furthermore, the circular geometry of RC piers, commonly adopted to enhance short-duration impact performance, has been re-examined in the context of vehicular collision loading.[7] Detailed assessment of cosmetic damage at both material and member levels has been employed to evaluate complex existing load-transfer mechanisms and identify key considerations for post-impact inspection and decision-making prior to returning piers to service.[8]

A key contribution of this research is the integrated experimental–numerical framework developed to investigate the nonlinear response of RC bridge piers subjected to low-velocity vehicular impacts. Realistic crash scenarios based on Class-I vehicle parameters are considered to quantify residual capacity following impact. In addition, probabilistic reliability analyses are conducted to account for uncertainties associated with damage progression and failure risk, providing a rational basis for post-impact assessment and design recommendations.

The findings offer critical insights into low-velocity impact behavior, addressing current gaps in design provisions and highlighting the need for revised evaluation criteria. Through detailed parametric and push-over analyses, this study informs future efforts to develop robust assessment methods and enhance the safety and longevity of bridge infrastructure. In conclusion, this research provides a foundational framework for understanding and assessing the post-impact performance of RC bridge piers as follows:

- This study presents a comprehensive investigation into the post-impact performance of RC bridge piers subjected to short-duration, low-velocity vehicular collisions. Such impacts, though often considered minor, can cause significant cosmetic and structural damage that compromises long-term performance. By examining damage propagation, energy dissipation, and changes in load-bearing behavior, the study seeks to better understand the implications of seemingly low-severity collisions on the structural integrity and residual capacity of bridge piers.
- To strengthen and validate the experimental findings, a series of detailed FEM simulations were performed. These simulations closely replicate the experimental conditions with trivial deviation and provide deeper insights into failure mechanisms, such as shear cracking, localized plastic deformation, and stress redistribution. The numerical analyses serve not only to confirm the experimental observations but also to extend the investigation to a broader range of impact scenarios and structural configurations.
- Recognizing the need for practical assessment tools, the study also incorporates reliability-based analysis to develop a holistic framework for evaluating post-impact damage severity. This framework quantifies reductions in structural capacity by considering uncertainties in material properties, geometry, and loading conditions. The aim is to support engineers in reaching informed decisions about serviceability and repair strategies for impacted piers without relying solely on traditional visual inspections or conservative assumptions.
- In pursuit of a non-destructive alternative to damage assessment, the study proposes a methodology that simulates extreme load events to estimate performance deterioration. This approach enables the evaluation of damage levels and failure risk without the need for full-scale destructive testing, offering a more efficient and cost-effective path toward ensuring structural safety and operational continuity.
- In short, the findings of this research contribute to a more nuanced understanding of RC pier performance under vehicular impact, particularly in the context of low-velocity collisions. By highlighting the influence of uncertainty in design parameters and post-impact conditions, the study lays the groundwork for improving both design practices and evaluation protocols. This ensures better preparedness for real-world impact scenarios, helping to enhance the resilience and longevity of bridge infrastructure.

Methodology

In this study, the performance of a prototypical traditional half-sized RC bridge pier is assessed under low-velocity vehicular impact loading through a combination of experimental testing and validated by numerical analysis using FEM. The investigation focuses on impacts from Class-I vehicles, specifically subcompact and mid-sized sedans, to evaluate the pier's residual capacity following such collisions and its ability to withstand subsequent events like earthquakes. Pendulum impact tests have been conducted to simulate vehicle crashes. These controlled low-speed impacts are intended to replicate cosmetic damage typical of real-world minor crashes. After impact, the specimens are closely delved to identify damage patterns and assess the reduction in structural capacity. The post-impact behavior has been analyzed to estimate the probability of failure (P_f) to determine the reliability index (β) under additional loading, offering insight into the resilience of RC bridge piers exposed to low-level vehicular collisions.

In the numerical investigation, the RC bridge pier model has been subjected to axial preloading to replicate in-service compressive forces and simulate equivalent nonlinear loading conditions induced by low-velocity vehicle impacts. The performance assessment focused on material properties, post-impact behavior, and cosmetic damage levels. FE simulations were conducted using the commercial software ANSYS, with input parameters derived from experimental testing, published literature, and manufacturer data.[9] Static numerical simulations have been performed to evaluate the short-duration post-impact response of the pier, including deformation patterns and failure mechanisms. These simulations are validated against experimental results for similarly configured RC piers under identical loading conditions, ensuring model accuracy and relevance.

The numerical model represented the RC pier as a composite structure, incorporating different materials modeled with non-separable contact definitions to closely capture real-world behavior under impact. For each crash scenario, detailed results were obtained, including deformation profiles, Von Mises stress and strain distributions, shear stress, maximum strain energy, and stress intensity. Beyond deterministic analysis, probabilistic methods are applied to account for uncertainties in material behavior and loading conditions.

The post-impact performance results obtained from FE simulations are utilized to assess the damage severity and determine the residual load-carrying capacity of the RC pier under subsequent cyclic loading. Reliability analyses are conducted for both the impact scenarios to estimate the P_f and corresponding β under low-velocity impact scenarios, supporting the validation of experimental findings and offering a robust framework for quantifying structural risk and residual performance under minor vehicular collisions.

Furthermore, the study offers a practical framework for evaluating whether traditionally designed RC bridge piers impacted by minor vehicular collisions can remain in service. By integrating experimental data with numerical simulations, the research captures the extent of damage and quantifies the performance of the impacted piers under sequential loading scenarios. The results demonstrate the feasibility of continuing service for such structures when the damage remains within cosmetic or non-critical limits. Overall, the findings present an effective tool for infrastructure managers and engineers to justify post-impact serviceability decisions, enhancing the safety and sustainability of aging bridge infrastructure.

Representative RC Pier

Material and geometric properties of RC pier

In this study, a circular RC pier section is selected as the representative model for analysis, with its geometric and material properties shown in Fig. 1. The pier is designed to emulate realistic bridge substructure conditions and has an unrestrained height of 8.4 feet (2.54 m), reflecting typical above-ground lengths used in practice. The cross-section of the pier is solid and circular, with an outer diameter (overall) of 20 in (0.51 m) and an inner diameter (core concrete) of 17 in (0.43 m). This hollow-core design helps reduce weight while maintaining sufficient strength and stiffness. The concrete used in the pier has a compressive strength of 7 ksi (48.26 MPa), a value commonly used for structural

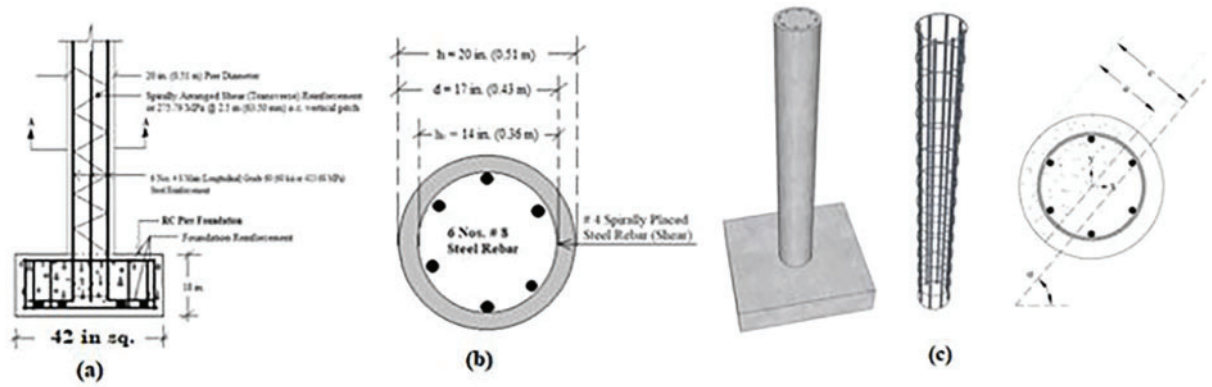

Figure 1. Reinforcement detailing of RC pier. (a) Sectional elevation, (b) Pier cross-section, and (c) 3D detailing. 3D, three dimensional

elements requiring high durability and load resistance. The reinforcing steel is specified as ASTM A706 Grade 60 with a yield strength of 60 ksi (413.68 MPa), selected for its superior ductility and weldability, which are crucial for seismic applications.

The pier's reinforcement configuration includes six longitudinal #8 bars placed symmetrically around the inner core to provide resistance against bending and axial loads. These bars extend fully into the foundation with a development length of 8 in (0.203 m), ensuring proper anchorage and load transfer. To resist shear forces and enhance ductility, #4 steel rebars with a yield strength of 40 ksi (275.79 MPa) are arranged in a spiral configuration at a center-to-center spacing (pitch) of 2.5 in (63.5 mm). This spiral arrangement conforms to the minimum shear reinforcement requirements outlined in ACI 318-11 and supports adequate confinement of the concrete core, which is essential for maintaining strength and energy dissipation capacity under cyclic and impact loading. Furthermore, the detailing complies with the recommendations by Furlong,[10] ensuring that both rebar diameter and spiral pitch meet established safety and performance criteria. This reinforcement layout enables the pier to develop sufficient ductile behavior and structural resilience under multiple loading conditions, including seismic and vehicular impacts.

The details of the representative RC pier are further shown in Table 1.

Table 1 summarizes the key geometric and material properties of the representative circular RC pier section used in this study. The symbol h denotes the outer diameter of the pier, while d represents the inner diameter as stated, defining the uniform circular section. The gross cross-sectional area of the pier is given as A_g, while A_{st} indicates the total area of the main (longitudinal) reinforcing steel bars embedded in the pier section. The net cross-sectional area, denoted by A_{net}, refers to the effective concrete area available for axial and flexural resistance.

The material strengths are represented by f_c' for the compressive strength of concrete and f_y for the yield strength of the reinforcing steel. Additionally, the reinforcement ratios are expressed as ρ_l and ρ_t, representing the longitudinal (main) and transverse (spiral) steel ratios, respectively. These parameters provide a comprehensive understanding of the pier's reinforcement layout and material capacity, serving as critical inputs for both the experimental evaluation and numerical simulations conducted in the study.

Experimental Program of Test Pier Specimens

In analyzing and determining the post-impact residual capacity of the RC pier in the test program, five prototype pier specimens with circular cross-sections were considered and tested. The specifications for the RC bridge pier were taken from a standardized state department of transportation detail.[11] The representative pier is modeled as having a uniform solid circular cross-section with a constant overall diameter of 20 in. (50.80 cm) throughout its length. The unrestrained length of the pier is 8 feet 4 in (2.54 m). A concrete cover of 1.5 in. (3.81 cm) is provided as per standard specifications. The boundary conditions for the pier are such that the bottom end is fixed, restraining displacement and rotation in all directions, while the top end is also fixed, preventing displacement and rotation, as shown in Figs. 3a and 3b. A schematic diagram illustrating these end conditions is provided in Fig. 3b.

For each representative RC pier, a square foundation has been designed in accordance with established design procedures to resist both static and dynamic impact loads. The foundation has a square plan measuring 3 ft 6 in. × 3 ft 6 in.

Table 1. Details of the representative pier

h (in.) (cm)	d (in.) (cm)	A_g (in.^{2}) (cm^2)	A_{st} (in.^{2}) (cm^2)	A_{net} (in.^{2}) (cm^2)	ρ_l (%)	ρ_t (%)	f'_c (ksi) (MPa)	f_y (ksi) (MPa)
20 (50.80)	17 (43.18)	314.28 (2027.60)	4.74 (30.58)	309.54 (1997.02)	1.5	0.06	7.00 (48.26)	60 (413.68)

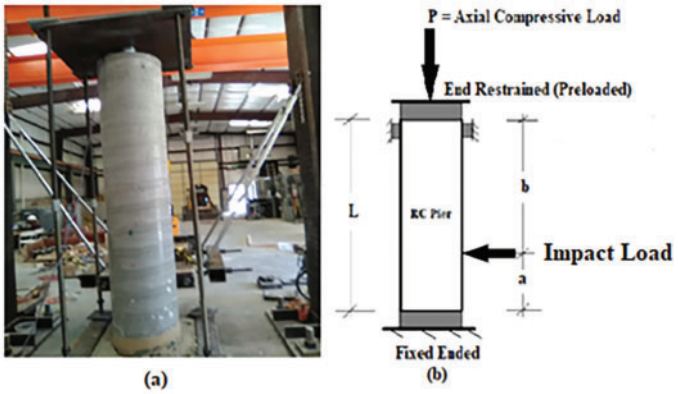

Figure 2. (a) Test specimen, and (b) schematic diagram of pier end conditions

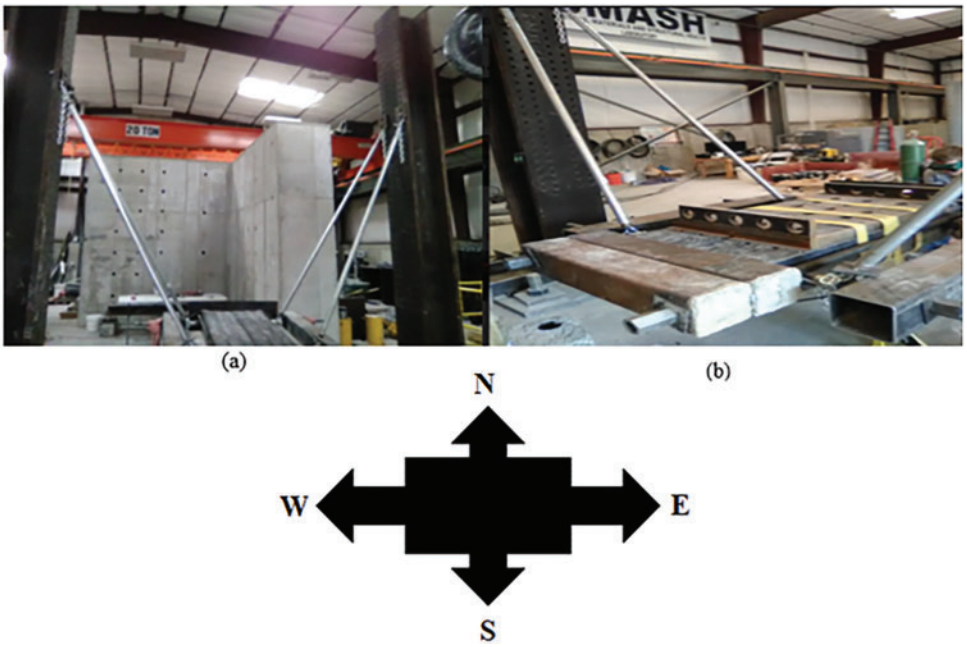

Figure 3. Pendulum impactor with weights. (a) 17.50 kips and (b) 22.50 kips

(106.68 cm × 106.68 cm) with a thickness of 1 ft 8 in. (53.34 cm), as shown in Fig. 1. Each foundation was fabricated to anchor the pier to the strong floor using 4 in (≈100 mm) diameter and 16 ft (≈4.87 m) long high-strength anchor bolts, thereby replicating a fixed-base boundary condition. At the opposite end, the pier was provided with a pinned boundary condition, as shown in Fig. 2, and axial preloading was imposed to simulate realistic support conditions.

To evaluate the serviceability and post-impact response of circular RC bridge piers subjected to vehicular collisions, representative prototype pier specimens (depicted in Figs. 2a and 2b) are analyzed. The pier's design specifications are based on experimental data obtained from tests conducted at the high-precision "Structural Laboratory" at Utah State University, Logan, Utah, USA. The pier is modeled with a uniform circular cross-section throughout its entire height to accurately reflect its structural behavior. Regarding the boundary conditions, the top end of the pier is modeled as a hinged (pinned) support. Translational displacement is permitted only in the direction of the applied impact force, while translational movements in all other directions are restrained. Rotational degrees of freedom are left unrestrained. The bottom end of the pier, representing the foundation interface, is fully fixed, preventing any displacement or rotation, as illustrated in Fig. 2.

Test setup for pendulum impact test

The pendulum system is supported by four arms and anchored to rigid steel columns, enabling free swing through a calibrated quick-release mechanism. The detailed configuration of the pendulum impact test setup is presented in Fig. 3.

Pendulum-based impact testing is widely employed to simulate vehicle–bridge pier collision scenarios and to investigate the associated dynamic response characteristics and damage mechanisms.[12] In the present study, the impact energy imparted to the pier resulted in deformations that have been observed to be negligible within the measurement limits.

A schematic representation of the pendulum system, including the direction of load application and the overall experimental arrangement, is shown in Fig. 3.

Determination of pendulum weights

In-built pendulums have been used in the experimental program to replicate the impact energy imparted to the pier by representative Class-I vehicles. Vehicle weights of 3.36 kips (14.95 kN) for a mid-sized sedan and 2.51 kips (11.14 kN) for a subcompact car are adopted based on the data reported by Thomas et al. (2018). Corresponding impact velocities of 22.87 mph (33.54 ft/s or 36.80 km/h) and 21.38 mph (32.83 ft/s or 36.02 km/h) were reproduced using the pendulum system, thereby simulating realistic vehicle–pier collision conditions.

The impact energy (E) imparted by these collisions is calculated from the kinetic energy (KE) using the standard equation shown in Eq. (1).[13] This calculation is essential to quantify the energy absorbed by the pier during impact, allowing for a precise assessment of its structural response under these controlled yet realistic conditions

$$E = 0.5 * M_{veh} * V_I^2 \tag{1}$$

where E is the total impact energy, M_{veh} designates the vehicle masses (Class-I), and V_I is the impacting velocity of the car.

As the total impacting energy does not get transformed into crash energy due to dissipation caused by column stiffness,[4] as well as the frontal stiffness and recoiling action of the impacting body.[4,14] To conduct the experimental methods and extracting results into real crash scenarios, the energy dissipation ratio (k) is considered as 0.72.[15] Thus, the effective energy ratio can be considered as (1 – k). The effective energy (E_{Eff}) can be estimated by using the Eq. (2).

$$E_{Eff} = (1 - k) \cdot E \tag{2}$$

where E_{Eff} is the effective energy causing damage to the column, k is the dissipation ratio, and E represents the energy incurred and transmitted from vehicle impact.

In order to reproduce a similar impact scenario, pendulum weights (W) used in the experiment can be computed from Eq. (3)

$$W = \frac{E_{Eff}}{g_{altitude} \cdot (h)} \tag{3}$$

where $g_{altitude}$ is the acceleration due to gravity (ft/s^2) considered as 32.16 ft/sec^2 (9.8 m/s^2) at a high altitude of 4,777 feet (1456.03 m), and h is the height of fall for pendulum, which is considered as 7 feet (2.438 m).

From the above Eqs. (1) through (3), weights of the pendulum are computed as 1.75 kips (7.78 kN) and 2.25 kips (10.01 kN), respectively, in order to reproduce the vehicle impacts caused by Class-I category of vehicles.

Test procedure

Pendulum impact experiments were conducted on a series of RC pier specimens, designated P1 and P2, using custom-fabricated pendulums with weights of 1.75 kips (7.78 kN) and 2.25 kips (10.00 kN). The pendulums were designed and assembled in such a manner that they can deliver controlled impact forces, as shown in Fig. 3. The pier specimens were subjected to impact loading generated by a pendulum released from a drop height of 7 ft (2.13 m). A schematic of the experimental setup, along with the step-by-step testing procedure, is presented in Fig. 4, providing an incisive representation of the test configuration and methodology.

Fig. 4 provides a schematic representation of the structural system and pendulum assembly. The test column of height H = 8.4 ft (2.56 m) supports a horizontal beam at elevation h = 7.0 ft (2.13 m). A pendulum of weight W is suspended from the beam, forming an angle θ with the vertical, as shown. The applied lateral load from the swung pendulum at the column base is denoted by P.

To determine the equivalent impacting vehicle velocities corresponding to lower vehicle weights, as presented in Table 3, two representative vehicle classes were selected to simulate low-impact collision conditions: a subcompact car (2.51 kips or 11.14 kN) and a mid-sized sedan (3.36 kips or 14.95 kN).[16] These vehicles were chosen due to their prevalence in urban traffic environments and their relatively lower weights, which reduce KE during collisions compared with heavier vehicle types. This selection allows for a more accurate assessment of short-duration impact energy transfer and structural response under low-to-moderate and cosmetic collision scenarios.

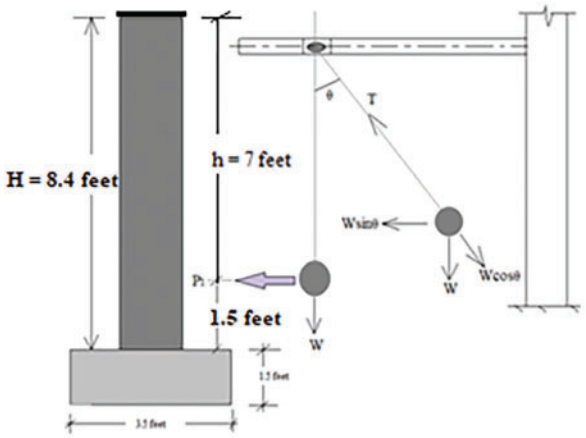

Figure 4. Schematic diagram for pendulum impact experiment

The impacting vehicle velocities (V_I) are estimated assuming approximately 72% energy dissipation, following the methodology proposed by Li et al.,[15] as expressed in Eq. (4).[17] This dissipation factor reflects the proportion of KE absorbed by vehicle deformation, frictional losses, and restitution during impact, providing a more realistic representation of actual crash dynamics. Incorporating this energy loss into the velocity computation ensures that the equivalent velocities derived more accurately capture the mechanical behavior of real-world collisions rather than idealized, perfectly elastic impacts

$$V_I = \sqrt{\frac{W..g_{altitude} \cdot h_I}{0.14 \cdot (M_{veh})}} \tag{4}$$

Rearranging Eq. (4), the final expression for determining the vehicle impacting speed is shown in Eq. (5).[17]

$$V_I = 2.67\sqrt{\left(\frac{W}{M_{veh}}\right) \cdot (g_{altitude}) \cdot (h_I)} \tag{5}$$

where W, M_{veh}, $g_{altitude}$, and h_I represent pendulum weight, weight of the impacting vehicle, acceleration due to gravity at specific altitude as already mentioned, and height of fall for impact. The impacting velocities are given in Table 2.

FEM

In this study, a detailed FEM of the RC test pier specimen was developed to simulate and analyze its behavior under low-velocity car crashes. The FEM was specifically designed to capture the nonlinear response of the pier during low-velocity car crash events, enabling accurate prediction of the post-impact structural performance and residual capacity. To validate and complement the experimental results, two pier models subjected to higher preload conditions, reflective of those applied during physical testing, were investigated. These preload levels are critical for simulating the in-service stresses and boundary constraints the piers experience prior to impact. The pier geometry employed in the simulations

Table 2. Equivalent car impacting velocities

Car type	Picture	Car weights in kips (kN)	Pendulum weights in kips (kN)	Height of fall in ft (m)	Car impacting velocities in ft/sec (m/s)	Car impacting velocities in mph (kmph)
Subcompact car		2.51 (11.14)	1.75 (7.78)	7 (2.13)	33.54 (10.22)	22.87 (40.46)
Mid-sized sedan car		3.36 (14.95)	2.25 (10.00)	7 (2.13)	32.83 (10.00)	22.38 (43.53)

replicates the physical specimens exactly, as shown in Fig. 5, ensuring consistency between experimental and numerical analyses.

The modeled piers were subjected to impacts from Class-I vehicle types, which correspond to commonly encountered vehicles in typical collision scenarios and are frequently used as standard references in impact testing. The detailed specifications of these vehicles, including weight, size, and impact velocity, are outlined in Table 3, ensuring that the simulation parameters closely mimic real-world conditions. By accurately representing these vehicle characteristics and their interaction with the pier, the numerical model provides a comprehensive insight into the pier's dynamic response, including stress distribution, damage initiation, and energy absorption mechanisms. This realistic simulation framework is crucial for evaluating the pier's post-impact durability and structural integrity, ultimately aiding in the design of safer and more resilient infrastructure capable of withstanding vehicle collisions.

Figure 5. FE model of test pier specimen

Loading conditions of the representative RC pier

Low-velocity car impact

Traditionally, bridge piers have been designed primarily to withstand static loads, such as axial forces, shear stresses, bending moments, bond stresses, and ensuring adequate development length for reinforcement. These static considerations have formed the basis for most design codes and practices due to their predictability and relative simplicity. However, in recent years, the importance of dynamic loading conditions has gained greater recognition, especially in the context of extreme events such as vehicle impacts, blasts, and earthquakes. Unlike static loads, dynamic loads introduce time-dependent forces that can cause rapid changes in stress and strain, leading to complex structural responses including vibrations, localized damage, and sometimes catastrophic failure modes up to complete collapse.

To effectively evaluate the effects of impact loads on RC piers, engineers often convert the dynamic impact forces into an equivalent static force. This simplification allows for practical design and analysis by approximating the maximum effects of dynamic loading through a static load case that represents the peak force during impact. Although this method does not capture the full time-history response of the structure, it provides a conservative and computationally efficient means to assess structural safety under impact scenarios. The specific loading conditions applied to the prototype RC bridge pier in this study are illustrated in Fig. 6, highlighting how the forces are assumed to act on the pier during impact. This representation aids in bridging the gap between complex dynamic behavior and practical engineering design, ensuring that the pier's resilience and performance under impact conditions can be reliably assessed and improved.

In this study, the equivalent car (Class-I) impact results are replicated. The impact duration considered for these analyses is 0.21 s, which is appropriate for the quasi-static impact and the corresponding results are utilized to determine low-velocity impacts using Eq. (6)

$$I_F = (M_{veh} * V_{veh})/t \tag{6}$$

where M_{veh} represents the weight of the impacting vehicle, V_{veh} is the frontal impact velocity of the vehicle causing

Table 3. Car crash data

Car type	M_{veh} (kips)	V (feet/sec)	T (sec)	I_F (kips)	Preload (kips)
Subcompact	2.505	33.54	0.207	405.88	50
Mid-sized sedan	3.361	32.83	0.207	533.05	75

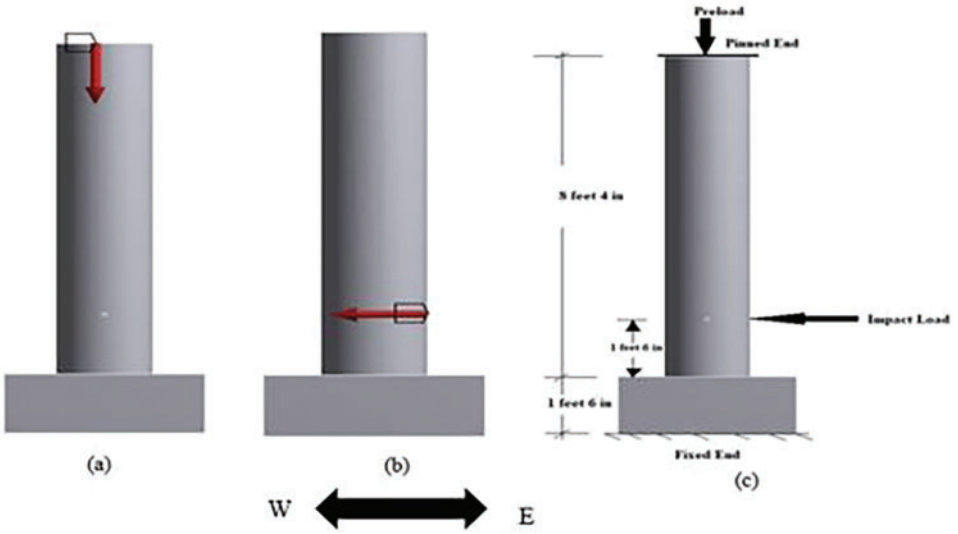

Figure 6. Pier for (a) preloading, (b) car impact loading, and (c) combined loading scenario

instability of the column, and t is the duration of impact. Impact duration for heavy to mid-sized cars may vary from a very short duration of 40 ms[14] to 0.21 s for quasi-static to dynamic strain rate loading (Roy et al., 2021). In this study, impact duration is considered as 0.21 s because of the quasi-static short-duration impact. However, the car crash data, as applied on the prototyped representative RC bridge pier along with the applied preloading, are shown in detail in Table 3.

Material properties

The FE analyses (FEA) have been carried out using models that precisely replicate the actual geometrical configurations, material properties, and boundary conditions of the tested RC piers. This high-fidelity modeling approach enables a realistic simulation of the piers' structural behavior under diverse loading scenarios, ensuring that the numerical outcomes are consistent with experimental observations. By carefully defining each geometric and material parameter, the FE models can accurately capture stress distributions, deformation patterns, and local failure modes, thereby enhancing the reliability of the analytical outcomes.

Table 4 summarizes the key input parameters, including the compressive strength of concrete, mechanical properties of the reinforcing steel, and other critical material characteristics that govern the nonlinear response of the structure. These parameters play a vital role in simulating complex behaviors such as cracking, yielding, and energy dissipation during impact loading. Incorporating these detailed material definitions allows the FE model to reproduce the progression of damage and the post-impact residual capacity of the piers, providing valuable insights into their performance and resilience under extreme loading conditions.

For all material interfaces within the FEM, a non-separable contact condition is applied to accurately represent the interaction between different components, such as concrete and reinforcing steel. This ensures that the elements remain bonded during the analysis and that no relative motion occurs at the interfaces, which is critical for simulating realistic stress transfer and failure mechanisms. In terms of boundary conditions, the external peripheral surface of the column is considered free, allowing natural deformation, while the top face of the column is modeled as pinned, restraining translational movement but allowing rotation. The foundation base is modeled as fully fixed, preventing any displacement or rotation to replicate the actual test setup and anchorage conditions.

A detailed three-dimensional (3D) FE model of the RC pier has been developed, incorporating accurate geometry, material properties, and boundary conditions. Non-separable contacts ensured proper interaction between materials, while the top of the pier was modeled as pinned and the foundation as fixed. This model, shown in Fig. 7, served as the basis for simulating the structural response under impact loading.

Mesh and boundary conditions for FE model

A comprehensive mesh-independence study has been performed to determine the optimal mesh size for the FE

Table 4. Material properties

Materials	Material properties and respective values	
Concrete	Modulus of elasticity (psi) (MPa)	$3.6 * 10^6$ ($2.48 * 10^4$)
	Poisson's ratio	0.18
	Open shear transfer coefficient	0.3
	Closed shear transfer coefficient	1
Reinforcing steel (main)	Modulus of elasticity (psi) (MPa)	$2.9 * 10^7$ ($1.9 * 10^5$)
	Poisson's ratio	0.3
	Yield stress (psi) (MPa)	60000 (413.68)
	Tangent modulus (psi) (MPa)	2900 (19.995)
Reinforcing steel (transverse)	Modulus of elasticity (psi) (MPa)	$2.9 * 10^7$ ($1.9 * 10^5$)
	Poisson's ratio	0.3
	Yield stress (psi) (MPa)	40000 (275.79)
	Tangent modulus (psi) (MPa)	2900 (19.995)

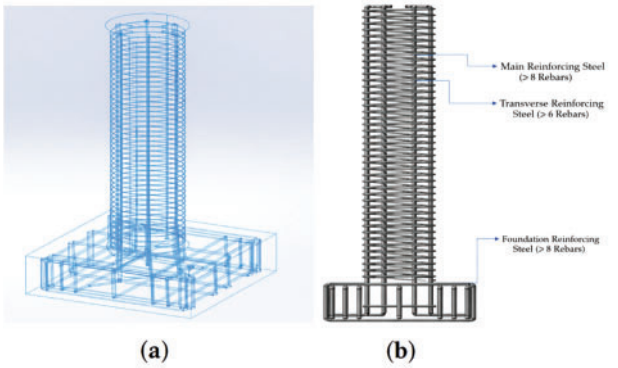

Figure 7. (a) Three-dimensional (3D) reinforcement using solid works and (b) 2D reinforcement detailing

simulations, ensuring a balance between computational efficiency and numerical accuracy. Through multiple refinement trials, the mesh was optimized to capture localized stress concentrations and potential failure regions without excessive computational cost. Non-separable contact definitions were implemented for all materials listed in Table 4, allowing for realistic interaction and load transfer between the concrete, longitudinal, and spiral reinforcements. A smooth transition between mesh densities was achieved using a transition ratio of 0.272, resulting in a total of 1,345,129 elements and 3,736,988 nodes, parameters that collectively guarantee stable convergence and physically consistent results.

The selected mesh sizes of 4.0 in. (101.60 mm) for concrete, 0.25 in. (6.35 mm) for longitudinal reinforcement, and 0.125 in. (3.175 mm) for spiral reinforcement have been chosen based on the structural significance of each component and their associated yield strengths of 60 ksi (413.68 MPa) and 40 ksi (275.79 MPa), respectively. The boundary conditions are configured to simulate the experimental setup accurately, with the pier's top fixed against displacement and rotation, while the foundation base has been fully restrained in all directions, as illustrated in Fig. 5. The meshing configuration shown in Fig. 8 demonstrates the fine discretization

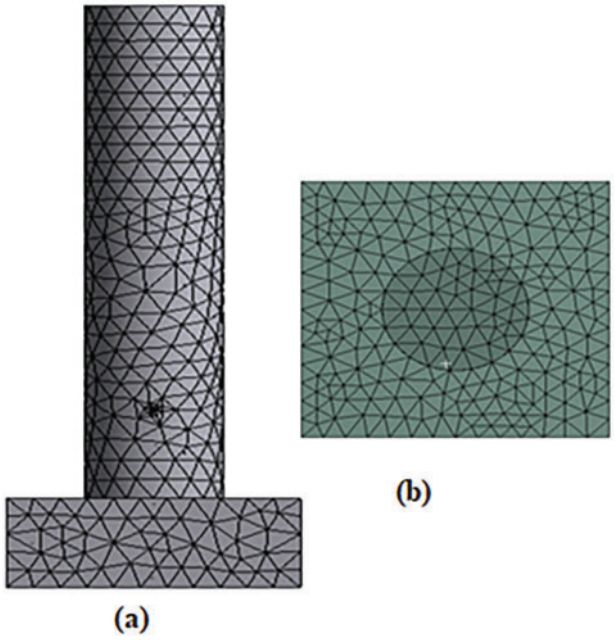

Figure 8. Meshing of FEM for (a) Combined mesh model with impacting point and (b) plan of concrete element

in critical regions and the smooth transitions that minimize numerical artifacts, ensuring reliable simulation of stress propagation and deformation behavior under applied loads.

Impact Damage Assessment Using Reliability Analyses

In this research, a probabilistic framework is adopted to evaluate the structural performance of RC piers subjected to low-velocity car crashes as already discussed. Specifically, reliability analysis is employed to quantify the likelihood of structural failure and assess the extent of damage. The analysis follows the resistance–load approach, wherein

uncertainties in both structural capacity (resistance) and external demands (impact loads) are considered. To evaluate post-impact performance, the resistance reduction method (RRM) is used, which involves reducing the pier's resistance incrementally and computing the corresponding probability of failure (P_f). This method enables a detailed understanding of how impact-induced damage affects the residual strength of the pier. The test pier is thus assessed not only in terms of whether it fails under impact but also to evaluate its reduced load-carrying capacity diminishes, providing a comprehensive insight into its post-collision structural reliability.

Pier resistance

Prior to computing the residual capacities, the design capacities in axial and shear for the representative RC pier are computed as specified in ACI.[18]

The design axial capacity ($P_{N,design}$) is computed as shown in Eq. (7)[19]

$$P_{N,design} = 0.85 * f_c' * \left(A_g - A_s\right) + \sigma_y * A_s \tag{7}$$

where f_c' is the 28-day compressive strength of concrete, f_y is the yield strength of steel, and A_g and A_{st} are the gross cross-sectional area of concrete and total cross-sectional area of longitudinal steel, respectively. $P_{N,design}$ is computed as 2126.16 kips (11,034.61 kN) and shown in Table 5. The axial load (preloading) applied on each test specimen was initially considered as 80% of the axial capacity and are as shown in the Table 3. The detailed considered preloading estimated from design strength is as shown in Table 5.

The design shear capacity of the RC bridge pier is determined using Eq. (8)[20]

$$V_{N,design} = V_c + V_s \tag{8}$$

where V_c is the shear strength carried by the concrete and V_s is the transverse shear capacity.

The shear strength, V_c, is computed as shown in Eq. (9)[21]

$$V_c = \nu_b[1 + 3P_{N,design}/f_c' \cdot A_g] \cdot A_e \tag{9}$$

where A_g represents the gross cross-sectional area of the concrete in the pier and A_e is 80% of A_g, i.e., $A_e = 0.8 * A_g$, and ν_b is the shear constant.

The shear constant (ν_b) is determined using Eq. (10)[21]

$$\nu_b = [0.0096 + 1.45\rho_t] \cdot \left(f_c'\right)^{1/2} \leq 0.03\left(f_c'\right)^{1/2} ksi \tag{10}$$

where ρ_t is the longitudinal steel ratio and $P_{N,design}$ represents the axial load capacity of the RC pier.

The transversal shear capacity, V_s, is computed using Eq. (11)[21]

$$V_s = (\pi/2)(A_h\sigma_{yh}) \cdot (D'/s) \tag{11}$$

where A_h is the area of a single hoop or spiral, D' is the spiral or hoop diameter, s denotes the pitch of the helix, and σ_{yh} represents the yield stress of transverse reinforcing steel.

Load

The equivalent Class-I vehicle impact responses have been replicated from the pendulum impact experiments to establish representative loading conditions. The resulting impact parameters are subsequently incorporated into Eqs. (1)–(4) to evaluate the corresponding low-velocity impact effects. The computed results derived from this procedure are presented in Table 6.

Determination of post-impact damage

In this study, post-impact cosmetic damage to the RC pier is evaluated through a reliability-based assessment by determining the probability of failure under specific low-velocity impact scenarios. In the first stage, the reduction in structural resistance resulting from vehicle impact is estimated using the RRM, implemented through Monte Carlo (MC) simulations. This method allows for the incorporation of variability in material properties, loading conditions, and damage extent. Given the inherent uncertainty in quantifying residual capacity following low-impact events, deterministic analysis alone may not reliably capture the true probability of failure. Therefore, a probabilistic approach is employed to provide a more robust estimate of the

Table 5. Estimated preloading

$P_{N,design}$ (kips) (kN)	Preloading (kips) (kN)	Percent preload (Initial)
2126.16 (9457.63)	1063.08 (4728.81)	50

Table 6. Equivalent car impacting velocities[22]

Car type	Picture	M_{veh} in kips (kN)	V in feet/sec (km/hr)
Subcompact car		2.51 (11.14)	33.54 (36.80)
Mid-sized sedan car		3.36 (14.95)	32.83 (36.02)

post-impact performance, focusing particularly on cosmetic damage levels that may not lead to structural failure but still affect serviceability and safety perception.

LSE analysis method

Using Eqs. (11) through (14) and Eq. (16), it is evident that the load model is governed by the dynamic impact force, while the resistance model is characterized by the dynamic shear capacity of the pier. Both models incorporate parameters treated as random variables to reflect the inherent uncertainties in material properties, loading conditions, and structural response. A random variable is typically defined by its mean, standard deviation, and probability distribution, statistical descriptors that capture the variability and unpredictability associated with real-world conditions. Therefore, replacing nominal design values with their corresponding means and standard deviations allows for a more realistic representation of uncertainty in the probabilistic framework. This approach ensures that the reliability analysis captures the true variability in both loading and resistance, as recommended in Roy.[9]

However, structural serviceability for the limit state function (G_i) comprises the performance not exceeding the permissible function as shown in the Eq. (12). This shows the limit state equation (LSE) satisfying the serviceability criteria.[9]

$$G_I = 1 - \lambda = 1 - \frac{I_{dyn}}{V_{dyn}} \tag{12}$$

where G_I is the limit state function, I_{dyn} is the peak vehicle dynamic impacted force, and V_{dyn} indicates the dynamic shear effect on concrete as mentioned in the Section 3.3.

Nominally, the probability of failure (P_f) is determined by integrating the limit state function over the region where the limit state function is less than or equal to zero, as expressed in Eq. (13)[23]

$$P_f = \int_{Z=-\infty}^{Z\leq 0} f_x\,(x_1, x_2, \ldots, x_n)\,dx_1 dx_2 dx_3 \ldots\ldots\ldots dx_n \tag{13}$$

where f_x is the joint PDF of the random vector $\boldsymbol{X} = \{x_1, x_2, \ldots, x_n\}$, *and* $Z = g(x) < 0$; that is the region of failure. This is further illustrated within the region, $-\infty = Z \leq 0$, where the failure of the RC bridge pier due to vehicle impact is expected to occur.

Determining P_f by directly evaluating the integral in Eq. (16) is analytically complex due to the nonlinear nature of the limit state function and the presence of multiple random variables. As an alternative, structural reliability can be assessed using the β, which provides a simplified yet effective measure of safety. Unlike the probability of failure, which quantifies the likelihood of failure directly, the reliability index serves as a standardized metric that reflects the margin of safety while accounting for the inherent uncertainties in model parameters.[24] Various reliability methods have been developed to compute P_f and, consequently, estimate the corresponding β. However, β can also be determined from different simulations.

In this study, MC simulations are used to evaluate the P_f under low-velocity impact conditions, particularly focusing on cosmetic damage levels that may not result in structural collapse but still impact serviceability. While different reliability methods may yield slight variations in β and P_f, they offer consistent insight into the overall structural performance. In its most basic form, the reliability index is calculated using the mean and standard deviation of the load and resistance variables, as outlined in Eq. (14)[25]

$$\beta = \frac{\mu}{SD} \tag{14}$$

where μ is the mean of the LSE and SD is the standard deviation of the limit state equation.

However, computing μ and SD of the LSE is often impractical especially when the limit state is a nonlinear function. Also, it presents problems in dealing with limit state equations where the probability distribution is not normal. As a result, an alternate method of computing the β involves using MC simulations. This method involves simulating the LSE a number of times with changing design variables. These design variables are developed using the uncertainty parameters and randomly generated numbers as shown in Eqs. (15) and (16)[25]

$$x_i = \mu_x + z_i \sigma_x \tag{15}$$

$$z_i = \Phi^{-1}(u_i) \tag{16}$$

where x_i is the computed variable, z_i is standard normal variable, u_i are uniformly distributed random variables between 0 and 1, and Φ^{-1} is the inverse of the standard normal cumulative distribution function (CDF).

The LSE defines the boundary between safe and failure conditions for the structure, where a value less than zero indicates failure. To assess the P_f, this equation is iterated multiple times using randomly generated input variables, which represent the inherent uncertainties in material properties, loading, and geometry. These variables are typically sampled from uniform or other relevant probability distributions to cover a broad spectrum of realistic scenarios. By running thousands, or even millions of such simulations, the analysis captures the variability and randomness present in real-world conditions.

The P_f is then estimated as the ratio of the number of simulations in which the LSE yields a negative value (indicating failure) to the total number of simulations performed. This MC-based approach provides a statistically robust measure of risk without relying on overly simplistic assumptions. Once the probability of failure is obtained, the β can be estimated using established mathematical relationships (as shown in Eqs. (17) and (18)). The β essentially translates the P_f into a standardized safety metric, reflecting the number of SDs the system's performance is from the failure threshold. This allows engineers to quantify safety margins and make informed decisions regarding design and maintenance

$$P_f = \frac{n}{N} \tag{17}$$

$$\beta = -\Phi^{-1}\left(P_f\right) \tag{18}$$

where n is the number of times the limit state was exceeded ($g(x) < 0$), and N is the total number of simulations undertaken.

A recently developed method that addresses some of the challenges associated with traditional fault tree analysis is the RRM.[17] Fault tree analysis often struggles with capturing the nuanced degradation of structural capacity following impact events, especially at low velocities where damage may be subtle yet significant. The RRM overcomes this by focusing directly on the residual capacity of the structural member after the loading event. It does so by quantifying the P_f that arises due to impact-induced damage, thereby providing a probabilistic measure of how the structure's ability to carry loads has diminished.

Using this probabilistic framework, the method computes a resistance reduction factor, denoted as ζ_P, which is defined as the complement of the P_f. This factor serves as a scaling coefficient applied to the original, undamaged structural capacity, effectively adjusting it to reflect the reduced capacity after impact. The calculation of ζ_P is shown in Eq. (19) (Roy[9]; ASCE).[4,5] By integrating uncertainty and variability in damage assessment, the RRM provides a more realistic and reliable means of updating structural capacity post-impact, enhancing both safety evaluations and maintenance decision-making

$$\zeta_P = 1 - P_f \tag{19}$$

where ζ_P is the resistance reduction factor and P_f has already been explained.

Reliability analysis requires that design parameters be treated as random variables characterized by their statistical properties μ and SD, and probability distributions, which are essential inputs for calculating the β. Table 4 summarizes the random variables considered in this study along with their associated probability distributions. The geometric dimensions and material properties used as parameters are sourced from established literature,[25] ensuring that the analysis is grounded in validated data. Vehicle mass parameters are derived from weigh-in-motion data collected in Utah,[26] while vehicle speed parameters are taken from Hwang and Nowak's study,[27] reflecting realistic loading conditions. Notably, the pitch of the transverse reinforcement is assumed constant and thus excluded as a random variable in this analysis. A comprehensive list of design variables and their uncertainty parameters is presented in Table 7, providing a detailed overview of the factors influencing the reliability assessment.

Similar to the damage index (λ), the ζ_P provides a practical means to adjust the original design capacity of the pier to reflect its residual strength after impact damage. By multiplying the design capacity by this factor, the method explicitly accounts for the degradation caused by the collision, effectively reflecting the reduced capacity to a level that represents the pier's post-impact performance. This probabilistically derived reduced capacity offers a more realistic assessment of the structure's remaining load-carrying ability. The calculation for the reduced capacity using this approach is expressed in Eq. (20)

$$L_{Reduced} = \zeta_P * L_{Design} \tag{20}$$

where ζ_P is the resistance reduction factor evaluated via a probabilistic approach, L_{Design} is the design capacity, and $L_{Reduced}$ is the reduced capacity of the impacted pier at specific loading event.

The evaluation of $L_{Reduced}$ is essential for understanding the pier's residual strength and for assessing structural safety after extreme events. It enables engineers to identify critical damage thresholds, evaluate the need for repair or replacement, and improve design strategies for impact-resistant structures. In numerical and experimental analyses, this parameter serves as a key performance indicator that bridges observed damage patterns with quantitative measures of strength degradation, supporting data-driven decision-making in structural resilience assessment.

In this study, a total of ten thousand (10,000) MC simulations have been performed on the limit state function to evaluate the reduced structural capacity corresponding to a target P_f. The simulations are carried out by repeatedly sampling the input variables and evaluating the limit state function for each realization. The selected number of simulations was sufficient to ensure statistical convergence of the results, as confirmed by the stabilization of the estimated mean and standard deviation of the response parameters.

Random numbers required for the MC simulations have been generated using the *RAND* function in Microsoft Excel,[28] enabling the stochastic representation of uncertainties associated with material properties, loading conditions, and geometric parameters. The design variables considered in the analysis, along with their corresponding statistical properties and probability distributions, are summarized in Table 4.

Results

Experimental

This section presents results primarily focused on detecting cosmetic damage and structural collapse through push-over experiments. Observations of damage include the development of localized cracks, spalling, and concrete delamination, which serve as key indicators of the pier's post-impact condition.

The observed results document the progression and severity of damage sustained by the test specimens during impact, specifically highlighting localized cracks, spalling of the concrete surface, and internal delamination. These damage modes are critical indicators of structural distress and energy dissipation mechanisms under dynamic impact loading as shown in Fig. 9. Impact damages combined with preloading conditions are detailed in Table 8. A detailed summary of these observations is encapsulated in Table 8, offering a comparative view of the extent and type of damage across different specimens and impact scenarios.

FEM

Comprehensive structural analyses were performed on the representative RC pier to assess its post-impact performance under low-velocity collision conditions. Damage quantification was achieved by evaluating key numerical indicators such as deformation, equivalent static strain and stress

Table 7. Design variables and their uncertainty parameters

No.	Variables	Distribution	Mean	CoV	St. Dev.	Units
1	Diameter of pier (h)	Normal	20.00 (0.51)	–	0.25 (0.006)	in. (m)
2	Height of pier (L)	Normal	100.06 (2.54)	–	0.25 (0.006)	in. (m)
3	Vehicle weight (M_{veh})	Normal	Varying	0.235	–	kip (kN)
4	Vehicle velocity (V)	Lognormal	Varying	0.165	–	ft/s (m/s)
5	Core concrete diameter (d_c)	Normal	17.00 (0.43)		0.25 (0.006)	inches (m)
6	Yield strength of transverse Reinforcement (σ_{yt})	Lognormal	40770 (280.62)	0.116	4729.32 (32.55)	psi (MPa)
7	Compressive strength of concrete (f'_c)	Normal	Varying	0.18	–	psi (MPa)
8	Diameter of longitudinal reinforcement (d_l)	Normal	0.855 (0.021)	–	0.365 (0.009)	in. (m)
9	Yield strength of longitudinal reinforcement (σ_y)	Lognormal	67500 (465.40)	0.098	6615 (45.61)	psi (MPa)
10	Diameter of transverse reinforcement (d_t)	Normal	0.56 (0.014)	–	0.365 (0.009)	in. (m)
11	Confined hoop diameter	Normal	17.355(0.44)	–	0.365(0.009)	inches (m)
12	Stiffness (k)	Normal	1713045 (300.00)	0.2	342609 (60.00)	kip/in. (kN/m)
13	Pitch (s)	Deterministic	2.5 (0.06)	–	–	in. (m)

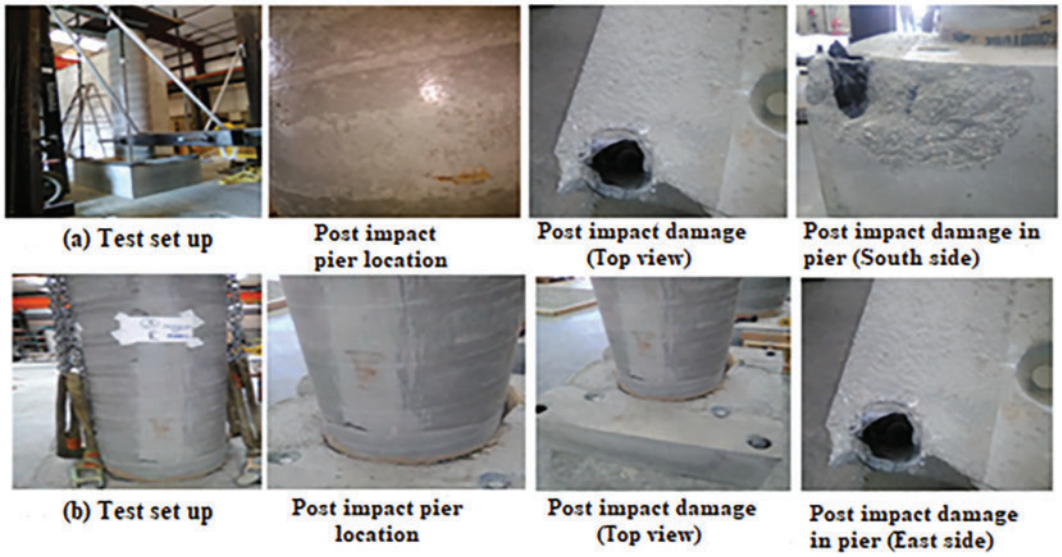

Figure 9. Pre-impact test setup and post-impacted pier damage for (a) P1 and (b) P2

(both based on the Von Mises criterion), shear stress, maximum strain energy, and stress intensity. These results are systematically presented in Figs. 10 and 11. Furthermore, high-resolution directional strain data were captured to provide a nuanced understanding of strain distribution patterns throughout the pier, with detailed visualizations shown in Figs. 12 and 13.

FE results of model for impacting subcompact car

The crash behavior of the representative RC pier specimen was simulated using a detailed FEM developed to capture the pier's response under impact loading. The FEM incorporated appropriate material models for concrete and reinforcement, realistic geometric details, and boundary conditions consistent with the experimental setup. The analysis captured the evolution of deformation and stress distribution throughout the pier during the impact event. The key results are presented in Fig. 10, which illustrates the deformation patterns and stress concentrations observed in the simulation. The simulation results show good agreement with the experimental observations, including the overall deflection shape and locations of maximum stress, indicating

Table 8. Results of pendulum impact testing

Column specimens	Preloading (kips)	Pendulum weights (kips)	Damage assessment			
			Damage location		Observations	Damage type
			Element type	Side		
P1	52	1.75	Foundation	South	Foundation damage	Spalling cracks along with delamination and edge cracking at the foundation concrete
P2	75	2.25	Foundation	East	Foundation damage	Spalling cracks along with delamination and edge cracking at the foundation concrete

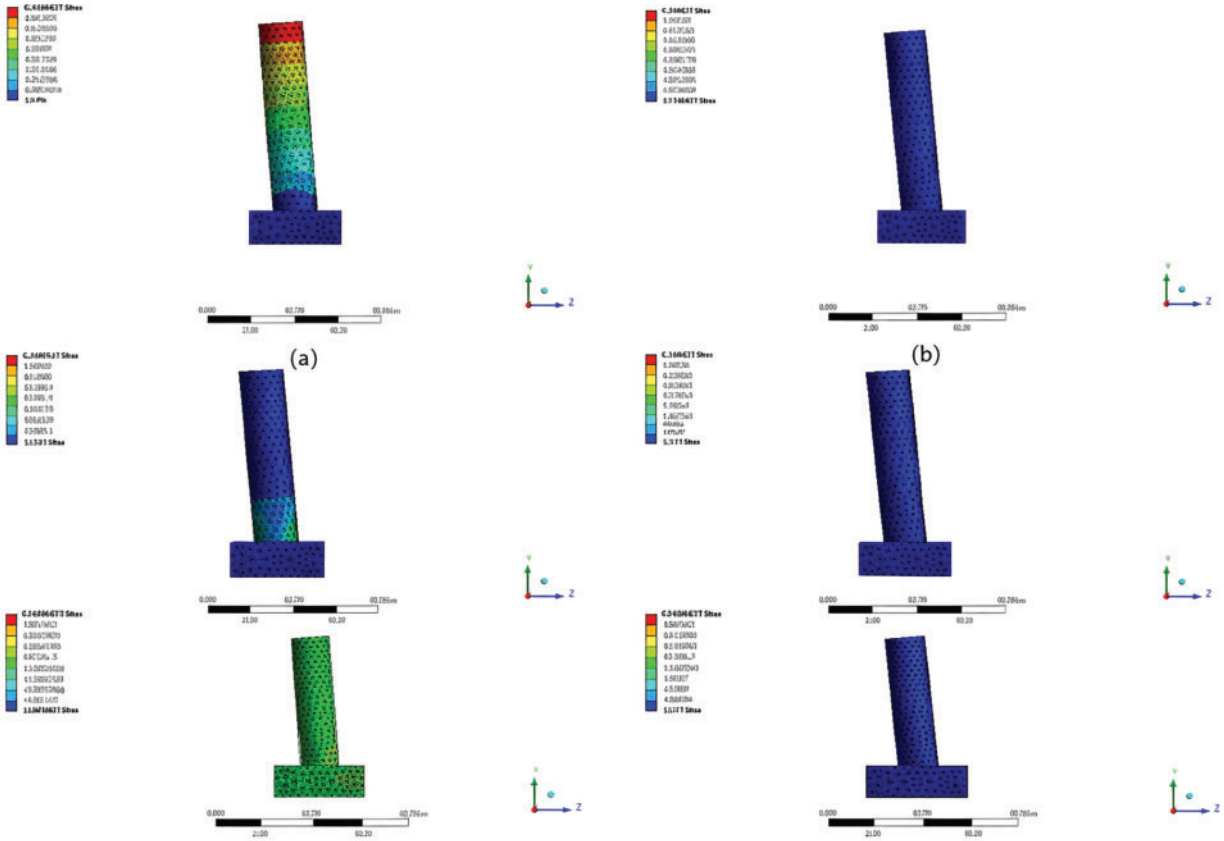

Figure 10. Subcompact impact results for (a) deformation, (b) Von Mises strain, (c) Von Mises stress, (d) Maximum Shear stress, (e) Maximum strain energy, and (f) Stress intensity

that the model provides a reliable representation of the pier's crash behavior.

FE results of model for impacting mid-sized sedan car

The impact response of the representative RC pier was simulated using a detailed FEM, with the results presented in Fig. 11. The simulation captures the dynamic interaction between the impacting body and the pier, revealing stress concentrations, crack initiation, and progressive damage throughout the structure. These results provide insight into the pier's deformation patterns, energy absorption capacity, and overall structural performance under impact loading. By highlighting the regions of maximum stress and localized failure, the FE analysis not only validates the accuracy of the

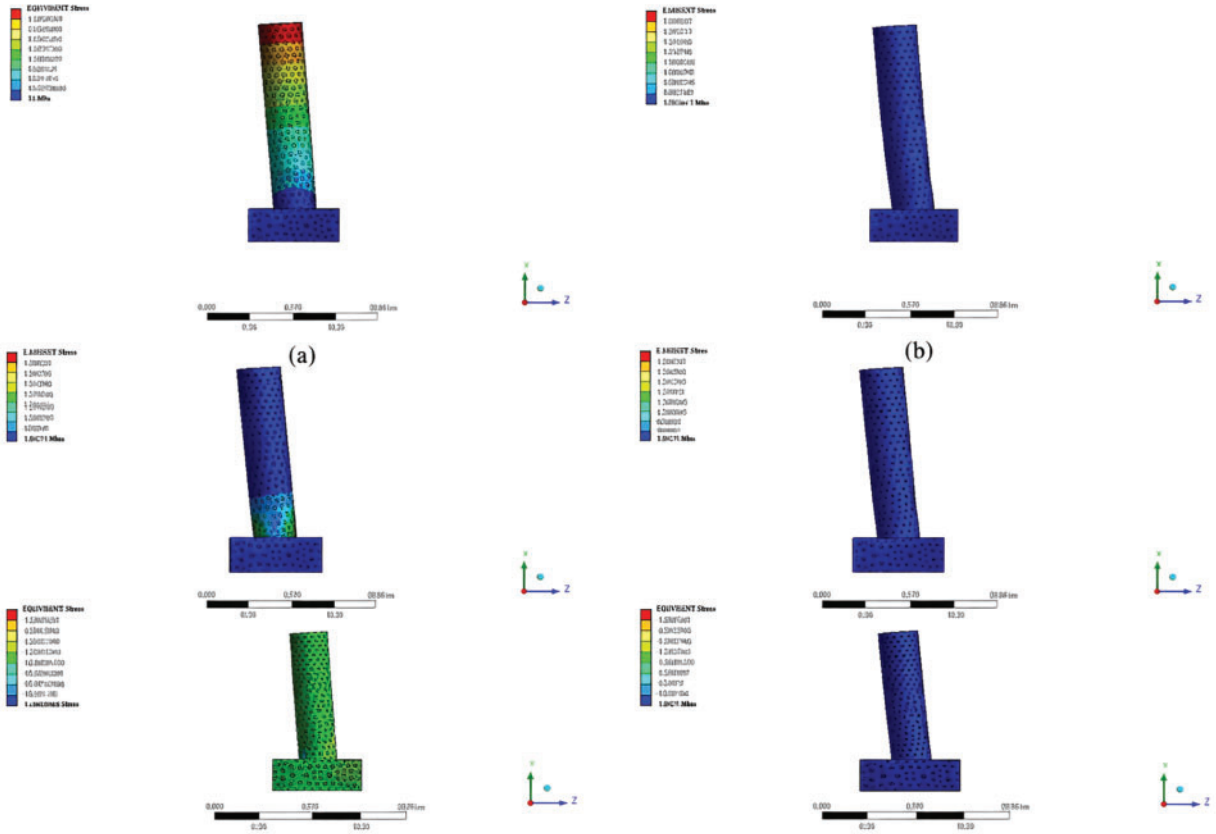

Figure 11. Subcompact impact results for (a) deformation, (b) Von Mises strain, (c) Von Mises stress, (d) maximum shear stress, (e) maximum strain energy, and (f) stress intensity

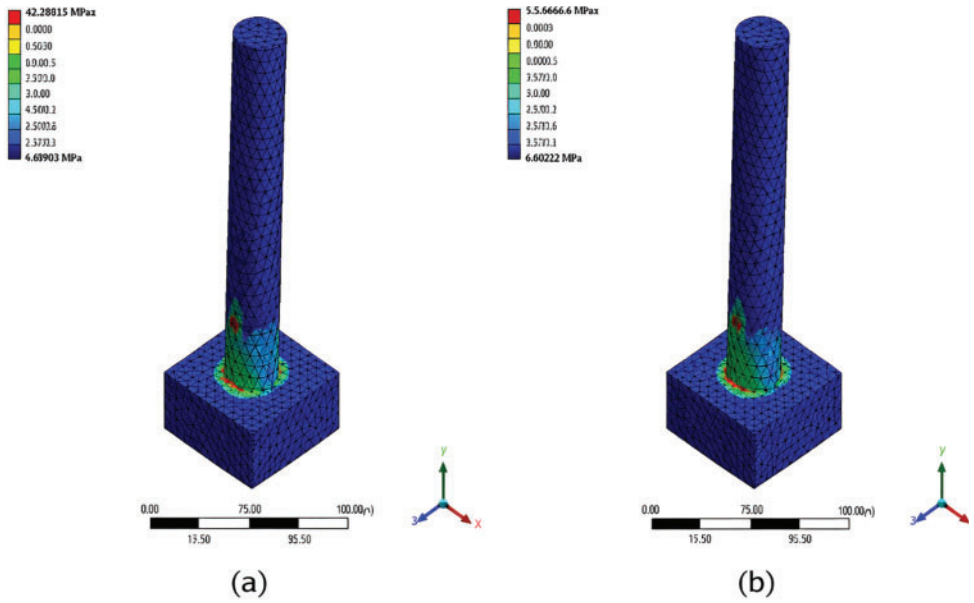

Figure 12. Three-dimensional view of high-precision stress concentration results due to impact from (a) Subcompact car and (b) Mid-sized sedan car

modeling approach but also offers a quantitative basis for assessing residual strength, performance degradation, and the effectiveness of design parameters in mitigating impact-induced damage.

Maximum stress concentrations and deformations were observed at the junction between the pier base and the foundation, as illustrated in Figs. 11 and 12. To better understand the failure mechanisms, high-precision stress concentration

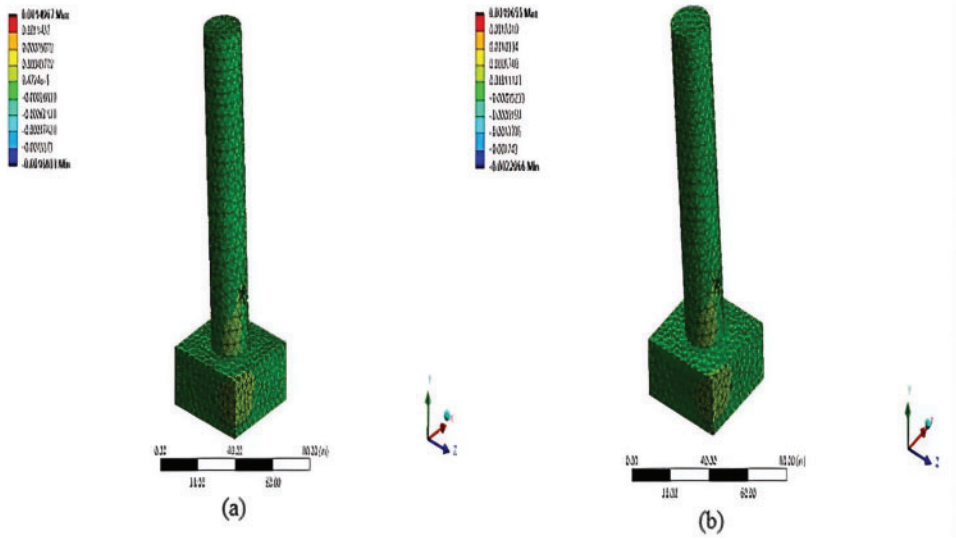

Figure 13. Three-dimensional view of high-precision directional deformation results due to impact from (a) subcompact car and (b) mid-sized sedan car

Table 9. Results from FEM

Pier specimens	Preloading (kips)	Pendulum weights (kips)	Damage assessment			
			Damage location		Observations	Damage type
			Element type	Position		
P1	52	1.75	Foundation and pier–foundation	Foundation edge and corners	Pier and foundation are highly stressed and deformed	Highly stressed zones are pier–foundation junction and foundation edge
P2	75	2.25	Foundation and pier–foundation	Foundation edge and corners	Pier and foundation are highly stressed and deformed	Highly stressed zones are pier–foundation junction and foundation edge

data were rescaled and compared in Fig. 12, which highlights the critical damage patterns in this region. The results indicate that the pier–foundation interface is the most vulnerable location under vehicle impact loading, where stress accumulation and structural deformation are most pronounced.

Variations in the simulation results reflect the inherent complexities involved in accurately modeling material behavior under post-impact conditions resulting from vehicle collisions. Despite these uncertainties, the analysis clearly shows that increasing impact loads significantly intensify the extent of structural damage. This trend is further supported by the directional deformation results presented in Fig. 13, where higher impact forces correspond to larger deformation magnitudes, confirming the direct relationship between impact intensity and structural response.

Results captured and extracted from FEA, summarized in Table 9, offer valuable insights into the structural response of the RC pier under impact loading. The simulations reveal pronounced stress concentrations, particularly at the pier–foundation interface and along the periphery of the foundation. Potential load transmittance paths followed by stress concentration-induced cracks are observed. These zones of elevated stress are critical, as they mark potential sites for the initiation and propagation of complex damage mechanisms such as cracking, spalling, or even localized structural failure.

The identification of these stress hotspots highlights inherent weaknesses in the structural system, emphasizing the need for careful design attention and potential reinforcement at these critical junctions. By pinpointing the most vulnerable areas, the FEM analysis not only aids in anticipating failure modes but also supports the development of targeted retrofitting and strengthening strategies to improve impact resilience. Overall, these findings demonstrate the indispensable role of detailed numerical modeling in capturing complex stress distributions, insights that are often missed by conventional or simplified design approaches.

Model validation

The developed FEM demonstrates a strong compatibility in predicting the post-impact behavior of the test pier, closely mirroring the physical damage observed during experimental testing. In particular, the model successfully captures critical failure modes, such as corner cracking and localized deformation, by analyzing directional displacement patterns. This precise replication of failure mechanisms not only confirms the model's accuracy but also provides valuable insight into stress concentrations and material responses at vulnerable locations. The consistency between the simulated deformation and the experimentally observed crack propagation, as illustrated in Fig. 14, validates the FE model as a reliable tool for assessing structural performance under impact loading, thereby supporting its use in design evaluation and damage mitigation strategies.

Although the car crash occurred at a relatively low velocity, Fig. 14 reveals that significant cracking developed at the foundation corners, warranting load transmittance path. These cracks propagate vertically along the anticipated load transfer paths, suggesting that even under modest impact energy, localized stress concentrations can be sufficient to initiate damage. This phenomenon indicates that the corners of the foundation act as critical stress increment locations where structural discontinuities or geometric features lead to an intensification of stress. The vertical crack propagation aligns with the direction of force transmission, implying a brittle or quasi-brittle failure mode typical of materials like concrete under tension.

The FE simulations, shown in Fig. 14, model pendulum impacts of 1.75 and 2.25 kips to represent the sequential increase in loading conditions. These simulations effectively replicate the experimentally observed patterns of crack initiation and growth, demonstrating the model's sensitivity to incremental damage development. The FE model captures both the spatial location and directionality of the cracks, indicating a high fidelity in stress distribution and fracture prediction. This strong correlation between simulated and experimental results not only validates the accuracy of the FE model but also reinforces its capability to simulate progressive damage mechanisms under repeated or escalating impact loads, a critical consideration for evaluating structural resilience in real-world crash scenarios.

Reliability analyses

A rigorously undertaken MC simulation involving 10,000 iterations has been performed on the LS function (g_i), with statistical parameters such as the mean and standard deviation converging at this sample size to ensure reliable results. The outcomes are presented in terms of the inverse CDF of the probability of failure (P_i), denoted as $\Phi^{-1}(P_i)$, under high strain-rate loading conditions. The simulation results are illustrated in Figs. 16a and 16b, while the corresponding plots of Pi and $\Phi^{-1}(P_i)$ are shown in Figs. 15a and 15b, respectively. These graphical representations provide a comprehensive understanding of the failure probabilities and their statistical distribution, facilitating an in-depth assessment of structural reliability and post-impact reduced resilience under low velocity car crashes.

The P_f quantifies the likelihood that the pier will not perform adequately under the specified impact conditions. A P_f of 0.21 means there is a 21% chance of failure, while 0.39 indicates a 39% chance, both significant risks, with the latter showing a notably higher vulnerability.

The residual index (ζ_P) is a complementary measure that represents the remaining structural capacity of the pier after the impact, expressed as a fraction of its original capacity. For example, a ζ_P of 0.79 suggests the pier retains 79% of its initial strength post-impact, while 0.61 indicates a more substantial reduction, retaining only 61%.

These values help engineers understand not only how likely the structure is to fail but also the extent to which its load-bearing capacity is diminished after an impact. This dual insight is critical for assessing safety, planning repairs, or deciding on strengthening protocols following a low velocity collision event.

Deterministic analysis using λ is employed to assess low to moderate damage levels and to estimate the residual capacities of the impacted pier. This approach evaluates the extent of damage caused by low-velocity vehicle impacts. A representative prototype RC pier is examined to understand

Figure 14. Resulting cracks for (a) experimental and (b) FEM

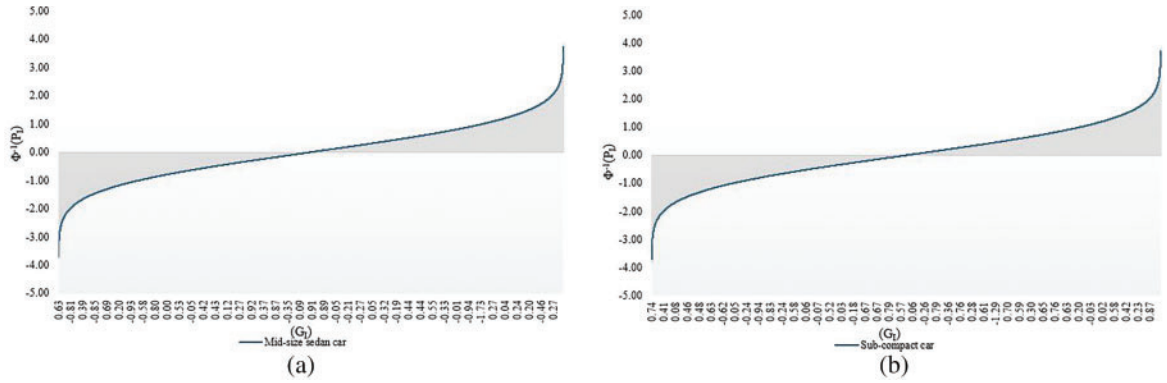

Figure 15. MC simulation impact results for (a) subcompact and (b) mid-sized sedan cars

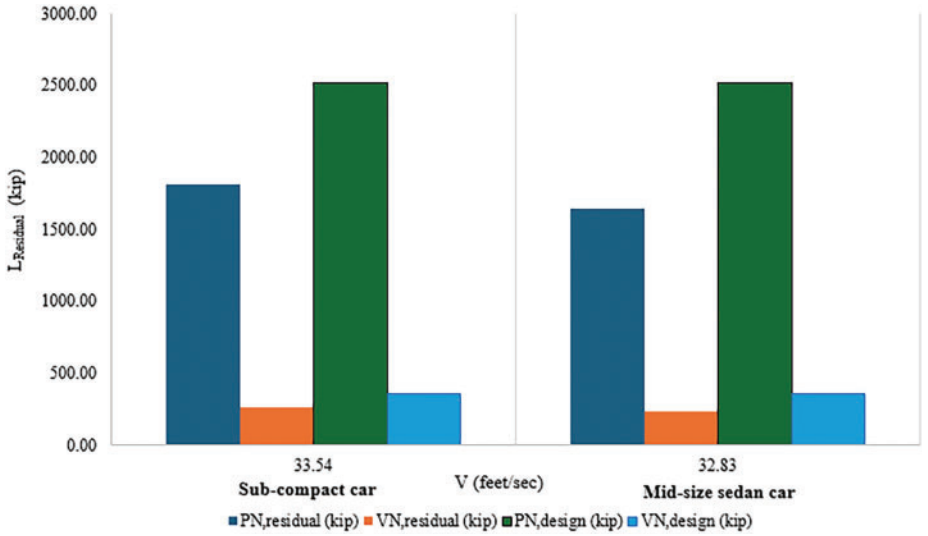

Figure 16. Residual capacities of RC pier impacted at a specific vehicle weight at specific impacting speed

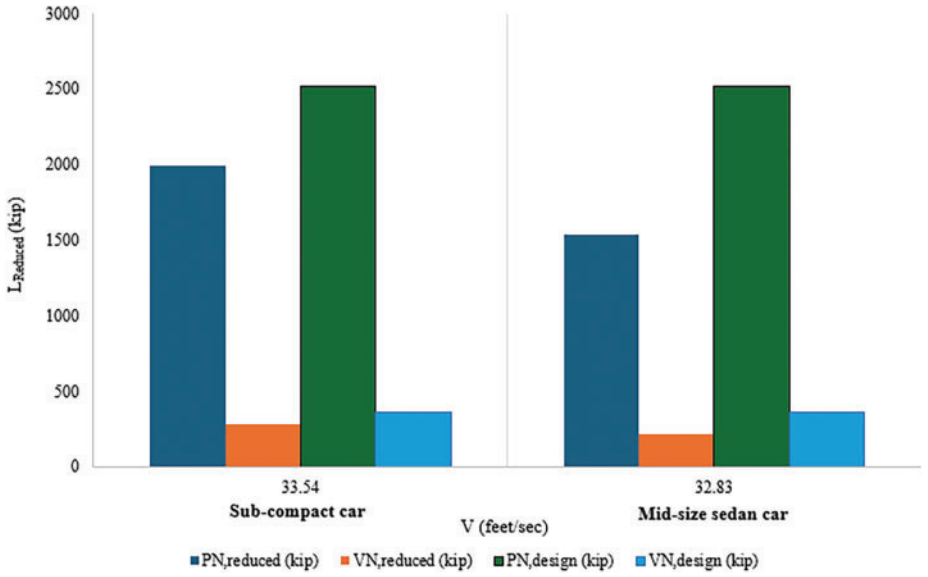

Figure 17. Residual capacities of RC pier impacted at a specific vehicle weight at specific impacting speed

its post-impact behavior, focusing on residual axial and shear capacities under specific vehicle weights and impact speeds. The resulting performance levels of the pier after impact are compared and illustrated in Fig. 16.

The probability of failure (P_f) values extracted from Figs. 15 and 16 showing 0.21 and 0.39, respectively, indicate varying levels of risk under different loading scenarios. Applying Eqs. (17) and (18), the P_f and the associated β are computed as 0.81 and 0.28. These metrics reveal a marked decline in structural reliability, emphasizing the heightened vulnerability of the system under increased impact demands. Furthermore, the ζ_P values, calculated as 0.79 and 0.61 via Eq. (19), quantify the degradation in structural performance, reflecting reduced safety margins.

The subsequent evaluation of reduced capacities through Eq. (20), with results presented in Fig. 17, provides critical insight into how impact loading compromises the load-bearing ability of the RC pier. This probabilistic assessment not only highlights key thresholds where failure becomes more probable but also underscores the importance of incorporating reliability-based approaches in design and retrofitting strategies. Ultimately, these findings advance a more nuanced understanding of structural resilience, enabling engineers to make informed, and risk-aware decisions to enhance infrastructure safety.

Determination of normalized β

From Figs. 15 and 16, the determined P_f at the respective impact conditions is determined as 0.21 and 0.39, indicating a moderate increase in failure likelihood with higher impact levels. Using Eqs. (17) and (18), the estimated P_f and the corresponding β are determined as 0.81 and 0.28, respectively. These values highlight the reduced safety margin under more severe loading, emphasizing the sensitivity of the system to variations in impact conditions. The ζ_P values, evaluated from Eq. (19), are found to be 0.79 and 0.61, further confirming the decline in reliability under increased stress levels. The corresponding reduced capacities, determined using Eq. (20), are presented in Fig. 17, showing a clear decrease in structural capacity with increasing impact intensity.

By further analyzing the results in Figs. 16 and 17, a normalized β is derived to account for variations in structural response across different crash scenarios. This normalized β\betaβ is used to calculate an overall standardized metric representing the behavior of a representative pier subjected to specific low-velocity vehicle impacts. Fig. 18 illustrates a comprehensive methodology that integrates experimental data, normalization procedures, and standardization techniques to provide a consistent and quantitative assessment of pier performance at specific strain rate impact loads. By systematically incorporating variations in impact intensity, pier properties, and observed responses, this approach enables more reliable comparisons and enhances predictive modeling for low-velocity crash scenarios, corroborating both structural design evaluation and safety assessment.

For specific low-velocity crash conditions applied to a half-sized traditional RC bridge pier, the normalized β values have been plotted against the corresponding P_f values. Using Eq. (18), a nonlinear trend of β is identified, showing an exponential relationship with P_f. This trend indicates that small increases in impact force produce progressively larger changes in the β response, reflecting the pier's nonlinear deformation and energy-absorption behavior under impact.

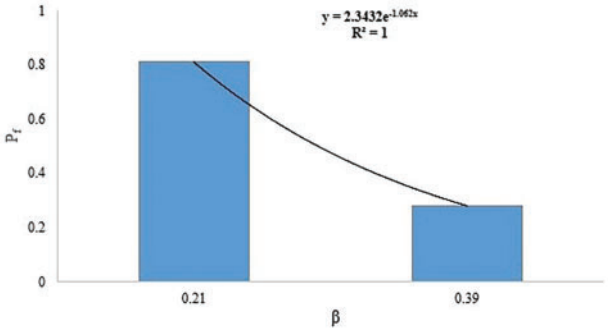

Figure 18. Normalized β and P_f

The model achieves an R^2 value of 1.0, demonstrating that the exponential relationship accurately captures the pier's response across the tested scenarios. This provides both a precise predictive tool and a meaningful physical interpretation of how low-velocity crashes influence the pier's structural behavior, where a gradual exponential decrement occurs as shown in Eq. (21)

$$P_f = 2.34 * e^{-1.062\beta} \tag{21}$$

where P_f and β are already explained.

Calibration formalism

In this study, a representative prototype RC pier is evaluated under a range of impact conditions, using vehicle weight and velocity parameters that simulate realistic collision scenarios. The objective is to assess how such impacts affect the pier's residual strength, predict its post-impact behavior, and propose a calibration process).[22,29] This deterministic analysis provides critical insights into the pier's remaining serviceability and its capacity to withstand additional loading after damage.[30] Comparative results are presented in Fig. 16, and offering a clear visual summary of the pier's performance across varying impact severities as illustrated in Table 10.

The present study investigates the impact response of a representative RC pier under realistic vehicle collision scenarios defined by weight and velocity, emphasizing residual strength and post-impact performance as shown in Table 11. Deterministic analysis captures the pier's remaining serviceability, while probabilistic evaluation predicts an 8.68% higher capacity for subcompact and a 6.86% lower capacity for mid-sized sedan impacts. The findings underscore the influence of input uncertainties and demonstrate the complementary value of deterministic and probabilistic approaches in evaluating post-impact structural resilience.

The results can be further interpreted by introducing a safety factor (η), defined as the ratio of the post-impact capacities predicted using the probabilistic framework to those obtained from the deterministic methodology. By expressing the relative capacities in this manner, η provides a direct and quantitatively robust indicator of the degree of discrepancy between the two evaluation procedures. This, in turn, facilitates a more comprehensive assessment of whether either method exhibits systematic conservativeness or permissiveness under varying impact conditions. The

Table 10. Failure evaluation

	Experimental		Deterministic		Probabilistic	
Car type	P_f	ζ_E	P_f	ζ_P	P_f	ζ_P
Subcompact	0.15	0.75	0.28	0.72	0.21	0.79
Mid-sized sedan	0.21	0.79	0.35	0.65	0.39	0.61

Table 11. Factors estimating residual capacities

	Deterministic		Probabilistic		Percent difference	
Car type	λ	ζ_D	P_f	ζ_P	Axial	Shear
Subcompact	0.28	0.72	0.21	0.79	8.68	8.68
Mid-sized sedan	0.35	0.65	0.39	0.61	6.86	6.86

formal definition of η is presented in Eq. (22), and the corresponding values derived from the dataset are compiled in Table 11.[27]

$$\eta = \frac{\zeta_P}{\zeta_D} \tag{22}$$

where η represents the calibrated safety factor, and ζ_P and ζ_D are the factors utilized to determine specific low–velocity, post-vehicle impacted residual capacities estimated, respectively, by using respective probabilistic and deterministic approaches.

Bayesian-chaotic-risk analysis

Bayesian-chaotic-risk analysis of Eq. (22) is crucial to be investigated for estimating single impact risk in terms of failure, as shown in Eq. (23)

$$P_f = \int P(y < 0|\theta)\, p(\theta|D)\, d\theta \tag{23}$$

where P_f has been explained, y is denoted as $ln(\zeta_D/\zeta_P)$, and $p(\theta|D)$ is the posterior distribution of parameters after observing crash data D and shall be estimated using Baye's theorem as shown in Eq. (24)[31]

$$p(\theta|D) = \frac{p(D)\, \mathrm{p}(\mathrm{D}|\theta)}{\mathrm{p}(\theta)} \tag{24}$$

Eq. (25) can capture epistemic uncertainty triggering limited number of crash tests, model uncertainty, measurement error, and chaotic amplification uncertainty.

Failure is shown when Eq. (25) is used, utilizing Eqs. (23) through (24)

$$g < 0 \Longleftrightarrow \eta < 1 \tag{25}$$

where η signifies calibration and equals to ζ_D/ζ_P, which is already explained in Eq. (22), and y is as shown in Eq. (23) is given by $ln(\eta)$ and equals to $ln(\zeta_D/\zeta_P)$.

Failure can be more precisely captured when η is further defined as shown in Eq. (26)

$$\eta < 0 \Longleftrightarrow \eta < 1 \tag{26}$$

Therefore, the analytical interpretation suggests that deterministic capacity remains below probabilistic capacity, indicating that safe calibration has been achieved. This condition is best understood by evaluating chaotic risk, which functions as the key diagnostic measure for identifying the potential onset of unstable and unpredictable system behavior.

This effect is conceptualized as the chaotic risk amplification factor (CRAF), a parameter that quantifies how marginal disturbances can amplify within the system and potentially trigger chaotic risk dynamics. CRAF is a metric that quantifies how much structural failure risk is increased due to chaotic effects and deep uncertainty in system behavior. It is the ratio between the failure probability obtained under chaotic, fully Bayesian calibration and the failure probability estimated using conventional or deterministic assumptions. In essence, CRAF captures the degree to which sensitive dependence on initial conditions, nonlinear interactions, and model uncertainty amplify the assessed risk of estimating η, providing a clear and meaningful indicator of how much unassessed or underestimated risk emerges when chaotic dynamics are rigorously accounted for.

In this study, this has been insightfully utilized to illustrate risk through using CRAF, which is defined in Eq. (27)

$$CRAF = \frac{Var_{chaotic}(\eta)}{Var_{gaussian}(\eta)} \tag{27}$$

where *Var* signifies *variance* of the statistical analysis of crash data, $Var_{chaotic}$ is the variance estimated using Bayesian calibration that accounts for nonlinear sensitivity, parameter uncertainty, and model-form uncertainty under low-velocity impact loading, and $Var_{gaussian}$ represents the gaussian variance from a conventional gaussian deterministic or single-model calibrated analysis.

In this specific scenario, CRAF ≈ 1, indicates the system is relatively stable to uncertainty, but the structure exhibits strong sensitivity to small variations in impact parameters.

Table 12. Conversion chart for the US customary to the equivalent SI units. SI, standard international

US customary	SI unit
1 ksi 1 psi	6.89 MPa (kN/mm^2) 0.00689 Mpa (kN/mm^2)
1 kip-in	0.113 kN-m
1 kip	4.45 kN
1 lbs	0.00445 kN
1 mph	1.61 km/hr
1 ft-lb/sec	0.00136 kN-m/sec (1.36 N-m/sec)

Discussions of Results

Deterministic analysis based on the λ approach is used to assess the extent of structural degradation in RC piers subjected to low-velocity vehicle impacts. The damage index quantifies the severity of damage by correlating it with reductions in the pier's load-carrying capacity. This approach is especially valuable for detecting low to moderate levels of damage that may not be visually obvious but can significantly compromise structural performance. By capturing indicators such as cracking, spalling, and internal stress redistribution, the λ method enables engineers to estimate residual axial and shear capacities with a reasonable degree of accuracy.

- The P_f quantifies the likelihood that a pier will not perform adequately under the specified impact conditions. A P_f of 0.21 corresponds to a 21% probability of failure, whereas a P_f of 0.39 indicates a substantially higher risk, highlighting increased vulnerability under more severe impact scenarios.
- The residual index represents the remaining structural capacity of the pier after impact, expressed as a fraction of its original strength. For example, a ζ_P of 0.79 suggests that the pier retains 79% of its initial capacity, whereas a ζ_P of 0.61 reflects a more pronounced reduction, indicating significant post-impact strength loss.
- Post-impact performance of RC bridge piers was evaluated through experimental testing and FEM simulations, considering axial compression combined with low-velocity vehicular impacts. Reliability analysis provided a probabilistic measure of post-damage safety, integrating structural performance and uncertainty.
- Despite conservative fixed-base assumptions, FEM models closely reproduced experimental deformations, effectively capturing stress concentrations at critical regions such as the pier base and foundation corners, precisely capturing the load transmittance path, which are particularly susceptible to spalling and splitting.
- Simulations identified peak stress concentrations at the pier base–foundation interface under subcompact and mid-sized sedan impacts. Predicted crack initiation zones closely matched experimental observations, with deviations limited to within 5%, demonstrating the model's predictive accuracy.
- Comparison with published data confirmed strong agreement in deformation patterns, stress magnitudes, and crack initiation locations, which accurately corroborates load transmittance path. This alignment further validated the slightly conservative FEM model, reinforcing confidence in its predictive reliability.

Conclusions

RC bridge piers, often positioned in exposed locations such as highway medians or bridge approaches, are especially susceptible to vehicular collisions due to their slender geometry and limited lateral resistance. Despite their critical structural role, the dynamic impact response and damage mechanisms of RC piers under sudden vehicle loads remain inadequately understood. Such knowledge gaps warrant the development of effective design strategies and protective measures aimed at improving pier resilience and ensuring overall structural safety protocol following the specific impact events.

To address this limitation, the present study employs an integrated approach that combines analytical modeling, FEM simulations, and experimental validation. This comprehensive framework enables the investigation of both the immediate impact response and the subsequent residual capacity of RC piers after collision. By correlating numerical predictions with empirical data, the study provides deeper insights into damage progression, energy dissipation mechanisms, and post-impact load-bearing behavior. Ultimately, the outcomes contribute to more accurate performance prediction models and inform the design of more robust RC piers capable of withstanding realistic vehicular impact scenarios.

(1) Performance-based studies of the impacted pier are investigated and presented for short-duration impacts to capture the low to cosmetic damages of the representative piers.
(2) This research is an attempt to investigate the material requirements for enhancing resistance. Additionally, this instills an insightful idea and realistic correlation between experimental and numerical simulations.[32,33]
(3) Simulations accurately identify critical damage in RC piers and foundations under low-velocity impacts.

Using a conservative resistance–reduction method, post-impact failure is probabilistically assessed, providing insights into material behavior and impact performance for future calibration without destructive testing.

(4) However, before making cognitive conclusions regarding cosmetic damage and developing methods for re-strengthening and enhancing resilience, it is recommended to conduct high-precision experimental studies encompassing a variety of geometries, material properties, and impact scenarios.

(5) The validated FEM framework accurately predicted residual capacity and observed damage patterns, demonstrating its effectiveness as a reliable predictive tool for evaluating the post-impact resilience of RC bridge piers. By closely replicating experimental behavior and capturing key nonlinear damage mechanisms under impact loading, the model provides practicing structural engineers with a robust methodology for assessing probabilistic post-damage performance and making informed structural safety decisions regarding the resilience and reliability of damaged bridge infrastructure.

(6) Such dual insights, quantifying both residual capacity and failure probability, seems essential for informed decision-making regarding pier safety, enabling engineers to accurately evaluate structural integrity, prioritize interventions, and optimize resource allocation. By integrating deterministic capacity assessment with probabilistic risk evaluation, the study provides a comprehensive basis for planning repairs, designing strengthening measures, and ensuring the continued safety and serviceability of bridge piers following a specific collision event.

(7) The final intuitive explanation is that P_f represents the average probability of failure, weighted by how plausible each competing model is. Rather than relying on a single "best" model, it incorporates uncertainty across all candidate models, giving greater influence to those better supported by the evidence. Thus, P_f provides the most complete probabilistic statement of structural risk under Bayesian chaotic calibration, integrating both model and parameter uncertainty into a unified and balanced assessment of failure risk.

(8) Practically, the study complies with the fact that columns with higher CRAF values may appear safe under mean-value analysis but show elevated failure probability when uncertainty is rigorously propagated. This affects predictions of local damage extent, global instability risk, and post-impact residual strength. In design and assessment, a high CRAF signals the need for conservative safety margins, impact-resistant detailing (e.g., confinement reinforcement), or strengthening measures, while a low CRAF suggests the column's response is relatively stable and less vulnerable to uncertainty assessment.

In summary, this study provides a critical step toward enhancing the safety and longevity of RC bridge piers exposed to vehicle impacts, combining rigorous simulation and validation efforts with practical recommendations for future research and infrastructure resilience.

Table 12 provides a comprehensive conversion chart for accurately translating measurements between U.S. Customary Units and the Standard International System of Units. As a key reference, the chart ensures consistency and precision in unit conversions, supporting uniform calculations and analysis throughout the article. By offering reliable conversion factors, it facilitates seamless cross-referencing and comparison of data across different measurement systems, thereby enhancing the clarity and applicability of the presented information.

Competing Interests

The authors declare that there are no competing interests.

Data Availability Statement

Some or all data, models, or code that support the findings of this study are available from the corresponding author upon reasonable request.

Funding

This research is funded by the Department of Civil and Environmental Engineering, Utah State University, Logan, Utah 84322, USA.

References

[1] Sharma H, Gardoni P, Hurlebaus S. Performance-Based probabilistic capacity models and fragility estimates for RC columns subject to vehicle collision. *Comput-Aid Civil Infrast Eng*. 2015;30(7):555–569. doi:10.1111/mice.12135.

[2] El-Tawil S, Severino E, Fonseca P. Vehicle collision with bridge piers. *J Bridge Eng*. 2005;10(3):345–353. doi:10.1061/(asce)1084-0702(2005)10:3(345).

[3] Thilakarathna HMI, Thambiratnam DP, Dhanasekar M, Perera N. Numerical simulation of axially loaded concrete columns under transverse impact and vulnerability assessment. *Int J Impact Eng, Pergamon*. 2010;37(11):1100–1112. doi:10.1016/j.ijimpeng.2010.06.003.

[4] Roy S. Precision assessment of reinforced concrete RC bridge pier resilience under high-velocity vehicle impact using an energy-based analytical model. *Int J Bridge Eng, ManagRes, BER*. 2025a;2(3). Publication date: July 10, 2025. doi:10.70465/ber.v2i3.40.

[5] Roy S. Stochastic modeling of vehicle impact on reinforced concrete bridge piers: assessment of structural reliability and resilience. *Recent Prog Sci*. 2025b;2(1):013. doi:10.70462/rps.2025.2.013.

[6] Ebrahimpour A, Earles BE, Maskey S, Tangarife M, Sorensen AD. *Seismic Performance of Columns with Grouted Couplers in Idaho Accelerated Bridge Construction Applications*. Idaho: Transportation Dept.

[7] Tazarv M, Saiidi MS. Seismic design of bridge columns incorporating mechanical bar splices in plastic hinge

regions. *Eng Struct, Elsevier*. 2016;124(2):507–520. doi:10.1016/j.engstruct.2016.06.041.
[8] Zhou D, Li R, Wang J, Guo C. Study on impact behavior and impact force of bridge pier subjected to vehicle collision. *Shock Vibrat*. 2017;2017(18):1–12. doi:10.1155/2017/7085392.
[9] Roy, S. Sustainability and resiliency investigation of grouted coupler embedded in RC ABC bridge pier at vehicle impact. *Eng Appl Sci*. 2024;9:14–33.
[10] Furlong RW, Ferguson PM, Ma JS. *Shear and Anchorage Study of Reinforcement in Inverted T-Beam Bent Cap Girders*. Project No. 3-5-68-113. Austin, TX: Center for Highway Research, Univ. of Texas at Austin; 1971.
[11] Ameli MJ, Pantelides CP. Seismic analysis of precast concrete bridge columns connected with grouted splice sleeve connectors. *J Struct Eng, American Soc Civil Eng*. 2017;143(2):4016176.
[12] Sun X, Bi Y, Zhou R, et al. *Experimental Study on the Damage of Bridge Pier under the Impact of Rockfall*. 2021.
[13] Li RW, Zhou DY, Wu H. Experimental and numerical study on impact resistance of RC bridge piers under lateral impact loading. *Eng Fail Anal, Pergamon*. 2020b;109(1):104319. doi:10.1016/j.engfailanal.2019.104319.
[14] Feyerabend M. *Hard Transverse Impacts on Steel Beams and Reinforced Concrete Beams*. Germany: University of Karlsruhe (TH); 1988.
[15] Li RW, Wu H, Yang QT, Wang DF. Vehicular impact resistance of seismic designed RC bridge piers. *Eng Struc, Elsevier*. 2020a;220(8):111015. doi:10.1016/j.engstruct.2020.111015.
[16] Jack. "How Much Does A Car Weigh?" *Auto Shop Accessories*; 2019. https://www.drivinggeeks.com/average-weight-car/. January 21, 2022.
[17] Roy S. Reliability analysis and uncertainty evaluation for assessing low velocity car impacted cosmetic damage of prototyped RC bridge pier. *J Ins-Civil Eng*. September 29, 2024;7(1):1. doi:10.18282/ice.v7i1.623.
[18] Standard AA. *Building Code Requirements for Structural Concrete (ACI 318-11)*. American Concrete Institute; 2011 August. Vol. 680, 681.
[19] American Society of Civil Engineers. *Minimum Design Loads and Associated Criteria for Buildings and Other Structures (ASCE/SEI 7-16)*. American Society of Civil Engineers; 2017. doi:10.1061/9780784414248.
[20] AASHTO. *Guide Specifications for LRFD Seismic Bridge Design*. 2nd Edition. Washington, DC: American Association of State Highway and Transportation Officials; 2011.
[21] AASHTO, M. *145–91. Classification of Soils and Soil-Aggregate Mixtures for Highway Construction Purposes*. Washington, DC: AASHTO DESIGNATION, American Association of State Highway and Transportation Officials; 1993, 122–126.
[22] Wiacek C, Nagabhushana V, Rockwell T, Summers S, Zhao L, Collins LA. Evaluation of frontal crash stiffness measures from the US New car assessment program. *ESV Conference*, Seoul, South Korea.
[23] Ayyub BM, McCuen RH. *Probability, statistics, and reliability for engineers and scientists*. CRC press; 2025.
[24] Der Kiureghian A. Analysis of structural reliability under parameter uncertainties. *Probab Eng Mech*. 2008;23(4):351–358. doi:10.1016/j.probengmech.2007.10.011.
[25] Nowak AS, Collins KR. *Reliability of Structures*. 2nd ed. CRC Press; 2012.
[26] Seegmiller LW. *Utah Commercial Motor Vehicle Weigh-in-Motion Data Analysis and Calibration Methodology*. Brigham Young University; 2006.
[27] Hwang E, Nowak AS. Simulation of dynamic load for bridges. *J Struct Eng*. 1991;117(5):1413–1434. doi:10.1061/(asce)0733-9445(1991)117:5(1413).
[28] Roy S, Majumdar BB. Predictive assessment of crack behavior in RC bridge piers under vehicle impact: a reliability and resilience-based approach. *Innov Infrastruct Solut*. 2025;10(12):586.
[29] Ameli MJ, Brown DN, Parks JE, Pantelides CP. Seismic column-to-footing connections using grouted splice sleeves. *ACI Struct J, American Conc Inst*. 2016;113(5):1021–1030. doi:10.14359/51688755.
[30] Girão Coelho AM, Simão PD, Bijlaard FSK. Guidance for the design of spliced columns. *J Struct Eng, American Soc Civil Eng*. 2012;138(9):1079–1088. doi:10.1061/(asce)st.1943-541x.0000546.
[31] Navidi WC. *Statistics for Engineers and Scientists*. vol. 2. New York: McGraw-Hill; 2006. ISBN 978-0-07-340133-1.
[32] Jacob GC, Fellers JF, Starbuck JM, Simunovic S. Crashworthiness of automotive composite material systems. *J Appl Polym Sci* 2004;92(5):3218–3225. doi:10.1002/app.20336.
[33] Pantelides CP, Ameli MJ, Parks JE, Brown DN. *Seismic Evaluation of Grouted Splice Sleeve Connections for Precast Rc Bridge Piers in Accelerated Bridge Construction (ABC) (Report No. UT-14.09)*. Utah Department of Transportation, Research Division; 2014.

BER the international journal of bridge engineering management and research

Experimental Detection of Embedded Rebar Corrosion in Concrete with Ground Penetrating Radar

Khadiza Binte Jalal[1,*]; Nur Yazdani[2]; Eyosias Beneberu[3] and Mohd Mezanur Rahman[4]

Submitted: 07 April 2026 **Accepted:** 24 June 2026 **Publication date:** 10 July 2026

DOI: 10.70465/ber.v3i3.89

Abstract: Reinforced concrete structures have been extensively investigated using ground-penetrating radar (GPR) to analyze corrosion-induced degradation qualitatively. However, no accurate quantitative model exists for evaluating the corrosion of embedded steel rebars, which may significantly impact the strength, serviceability, and long-term durability of concrete structures. This study involved an experimental investigation to determine the relationship between the quantity of rebar corrosion and the maximum amplitude, as well as the two-way travel time of the GPR electromagnetic wave. A direct current was impressed on embedded steel rebars in concrete beams immersed in a 5% saltwater solution to induce accelerated corrosion. GPR data were collected before saline submersion and at 10-day intervals. The study proposed a multivariate linear regression model with high reliability to estimate corrosion-induced rebar mass loss.

Author keywords: Accelerated corrosion; amplitude; ground-penetrating radar; multivariate regression model; reinforced concrete structures corrosion

Introduction

Embedded steel rebar corrosion in concrete is a time-dependent electromagnetic phenomenon and is one of the major causes of structural deterioration. It occurs due to carbon dioxide and chlorine infiltration through the protective concrete cover. Any loss of protective cover can lead to rebar corrosion and concrete deterioration, such as cracking, spalling, and debonding. Consequently, structural capacity deteriorates, and the service life could be compromised.[1] Many previous catastrophic collapses of concrete structures were due to a lack of knowledge on the extent of embedded rebar corrosion.[2] According to the National Association of Corrosion Engineers report, approximately 1% to 5% of the USA Gross Domestic Product (GDP) is allocated to repairing and rehabilitating structures with corrosion damage.[3] Developing an accurate monitoring and condition assessment methodology for affected concrete structures is essential to make informed decisions on the extent of rebar corrosion, any effect on structural safety and serviceability, and to effectively reduce the maintenance/rehabilitation budget.

Early-stage rebar corrosion is difficult to detect through visual inspection because corrosion damage may not be visible until cracking, staining, or spalling has occurred. In general, non-destructive evaluation (NDE) is considered a more accurate method than visual inspection. Electrochemical methods such as half-cell potential (HCP), linear polarization resistance (LPR), and X-ray computed tomography (XCT) have been widely used for the condition assessment of corroded concrete structures. However, these methods have certain limitations. The HCP and LPR are semi-destructive methods requiring physical contact with embedded rebars, and they only detect instantaneous corrosion activity. The XCT is unsuitable for on-site measurements due to its large size and transportation challenges.[1] Corrosion assessment methods may be broadly classified as qualitative or quantitative. Qualitative approaches, such as visual inspection, HCP, and many conventional GPR applications, indicate the presence, location, or likelihood of corrosion but do not directly estimate reinforcement section loss. Quantitative approaches aim to estimate corrosion severity, such as corrosion rate or percentage mass loss; however, methods such as LPR, XCT, and gravimetric measurement are often semi-destructive, laboratory-based, or difficult to apply efficiently at field scale.

Apart from the methods mentioned above, ground-penetrating radar (GPR) is another NDE technique to determine reinforcement cover, concrete thickness, rebar location and spacing, localization of voids and cracks, and concrete deterioration mapping.[4–6] Most previous GPR studies have focused on qualitative corrosion detection

*Corresponding Author: Khadiza Binte Jalal.
Email: khadiza.binte.jalal@gmail.com
[1]Bridge Engineer, HNTB, Plano, TX 75024
[2]Department of Civil Engineering, University of Texas at Arlington, Arlington, TX 76019
[3]Bridge Engineer, Bridgefarmer & Associates, Inc., Dallas, TX 75234
[4]Bridge Engineer, Consor Engineers, Farmers Branch, TX 75244

Discussion period open till six months from the publication date. Please submit separate discussion for each individual paper. This paper is a part of the Vol. 3 of the International Journal of Bridge Engineering, Management and Research (© BER), ISSN 3065-0569.

through changes in reflected amplitude, travel time, or frequency characteristics. While these approaches can identify areas potentially affected by corrosion, relatively few studies have attempted to directly quantify corrosion-induced reinforcement mass loss. Narayanan, et al.[7] found that reflected GPR amplitude can indicate possible corrosion in steel rebars. Hubbard, et al.[8] investigated the difference between GPR signals collected before and after accelerated rebar corrosion for 10 days. It was found that the GPR amplitude was affected, and the two-way travel time (TWTT) was influenced by the moisture introduced during the accelerated corrosion process. Zaki, et al.[2] used GPR for corrosion detection in accelerated corroded rebars in a slab and deduced that the reflected wave amplitude was reduced due to corrosion. Lai, et al.[9] also monitored the accelerated corrosion of concrete specimens with GPR and observed amplitude reduction as the corrosion level increased. This agreed with the findings from Hong et al.[10] and Hong et al.[11] In addition, Lai et al.[12] proposed a new corrosion evaluation approach using GPR, employing changes in lapsed travel time, amplitudes, and peak frequencies. The maximum positive amplitude of the reflected wave was found to change at different phases of corrosion, and the reflected amplitude decreased with an increase in travel time. Zhan et al.[13] investigated the changes in GPR parameters during accelerated corrosion. A reduction in TWTT and an increase in the reflected wave amplitude with an increase in corrosion rate were found. Liu et al.[14] proposed a hybrid-polarized GPR system for early-stage rebar corrosion detection rather than using a traditional GPR system, single polarized signals.

Hasan and Yazdani[5] corroded three steel rebars with accelerated corrosion and then placed them at different depths under materials with known dielectric constants to simulate concrete embedment. The rebars were then scanned using a GPR, which showed an increase in TWTT and a decrease in amplitude, agreeing with the findings from other researchers: Raju et al.,[15] Sossa et al.,[16] and Senin et al.[17] Moreover, Faris et al.[18] concluded that corrosion increases the reflected wave amplitude by spreading rust into concrete cracks. However, the simultaneous presence of chloride and moisture significantly attenuates both the amplitude and frequency of electromagnetic waves.

Actually, rebar corrosion in real life is often a slow process, and waiting a long time to measure the corrosion extent is not practical. Hence, accelerated corrosion through impressed-current techniques is a suitable solution to induce rebar corrosion in a relatively short time. In addition to saving time, it is cost-effective, and the corrosion rate can be controlled as needed, as shown by Ahmad.[19] Several previous accelerated corrosion studies were conducted using the impressed-current technique.[20–22] Impressed-current techniques are also known as galvanostatic methods, which use a direct current (DC) from an external power source to corrode steel embedded in the concrete.

Although previous studies have demonstrated that GPR signal characteristics, including reflected amplitude, travel time, and frequency response, are sensitive to corrosion-induced changes in reinforced concrete, several important limitations remain. Moreover, published articles often focus on qualitative corrosion detection, monitoring corrosion progression under a limited set of conditions, or establishing relationships between individual GPR parameters and corrosion activity. In practical applications, however, GPR responses are influenced not only by corrosion level but also by rebar diameter, concrete cover depth, concrete quality, moisture condition, chloride contamination, and signal propagation characteristics. The combined influence of these parameters on corrosion quantification has received limited attention in the literature. Furthermore, few studies have attempted to integrate structural parameters and GPR measurements into a unified framework for estimating actual corrosion-induced mass loss. To address this gap, the present study experimentally investigates the effects of rebar diameter, concrete cover, concrete compressive strength, and corrosion duration on GPR amplitude and TWTT using a controlled accelerated corrosion program. Based on these results, a multivariate regression model is proposed to estimate corrosion mass loss from both GPR-derived and structural parameters. The study, therefore, contributes toward the development of a more comprehensive and practically applicable framework for quantitative corrosion assessment of reinforced concrete structures.

Methodology

Experimental design

The factorial design method was used in the current study to determine the number of samples considering rebar diameter, concrete strength, concrete cover, and corrosion period as parameters.[23] The Minitab statistical software was utilized for this purpose, employing three degrees of freedom.[24] The first degree expressed two levels of concrete strength: 1. normal strength concrete (NSC) with low porosity and 2. low strength concrete (LSC) with high porosity. The compressive strength for NSC ranges from 20 to 40 MPa, whereas any concrete strength below that is considered LSC. ACI[25] prescribes minimum concrete covers between 19 and 76 mm for embedded rebars. Thus, the second degree considered 38-, 50-, and 75-mm covers. The third degree was used for different corrosion exposure periods. The experimental design is shown in Table 1. Two samples were fabricated for each criterion, employing 10-, 22-, and 32-mm rebar diameters, yielding a total of 36 specimens.

Preparation

A total of 36 rectangular beams, measuring 910 × 380 × 200 mm, were prepared. The dimensions were chosen to account for the GPR antenna footprint, ensuring that reflections were free of interference from the edges and the bottom. Thus, the GPR waveforms contained two genuine signals: the direct wave propagating from the transmitter to the receiver and the signals reflected from the steel rebars.

The LSC and NSC mixtures were designed to achieve 28-day cylinder compressive strengths of 19 and 47 MPa, respectively. Table 2 shows the concrete mix designs. Concrete compressive strength and fresh concrete air content,

Table 1. Experimental design

Criteria no.	Accelerated corrosion period (days)	Concrete strength (MPa)	Concrete porosity (% air content)	Concrete cover (mm)	Rebar diameter (mm)	No. of samples
1	30	47	1.5	50	10, 22, 32	2
2	20	47	1.5	50	10, 22, 32	2
3	10	47	1.5	75	10, 22, 32	2
4	10	19	4.5	38	10, 22, 32	2
5	10	47	1.5	50	10, 22, 32	2
6	30	19	4.5	50	10, 22, 32	2
7	20	19	4.5	38	10, 22, 32	2
8	20	47	1.5	75	10, 22, 32	2
9	20	47	1.5	38	10, 22, 32	2
10	20	19	4.5	75	10, 22, 32	2
11	30	47	1.5	38	10, 22, 32	2
12	10	19	4.5	50	10, 22, 32	2
13	30	19	4.5	75	10, 22, 32	2
14	30	19	4.5	38	10, 22, 32	2
15	10	19	4.5	75	10, 22, 32	2
16	30	47	1.5	75	10, 22, 32	2
17	20	19	4.5	50	10, 22, 32	2
18	10	47	1.5	38	10, 22, 32	2
						Total = **36**

Table 2. Concrete mix designs

LSC		NSC	
Material	Weight per m^3	Material	Weight per m^3
Cement (Type I/II)	268 kg	Cement (Type I/II)	346 kg
Fly Ash	67 kg	Fly Ash	87 kg
Coarse Aggregate	606 kg	Coarse Aggregate	1,098 kg
Fine Aggregate	872 kg	Fine Aggregate	743 kg
Water-Reducing Admixture	1,465 g	High-Range Water-Reducing Admixture	1,891 g
Air-Entraining Admixture	105 g	Viscosity-Modifying Admixture	812 g
Water	143 kg	Water	153 kg
Air Void	0.035 m^3	Air Void	0.012 m^3

measured in accordance with ASTM C231 and C39,[26] were selected as primary parameters in this study. Although fresh concrete air content is not equivalent to hardened concrete porosity, it provides an indirect indication of the relative pore structure and permeability characteristics of the concrete mixtures. These characteristics influence moisture transport, chloride ingress, and the dielectric properties governing GPR signal propagation. Therefore, air content was used as a practical mixture parameter rather than a direct measure of hardened concrete porosity.

Each specimen contained six steel rebars with diameters of 10, 22, and 32 mm (#3, #7, and #10), out of which three were Grade 60 type and the remaining three were Type 304 stainless steel. The rebars were placed at 100-mm center-to-center spacing. Grade 60 rebars were used as anodes, and Type 304 stainless-steel rebars were used as cathodes during the impressed-current accelerated corrosion process. No visual rust was observed while embedding the rebars into the concrete.

Plywood and lumber were used to make the formwork (Fig. 1). Holes were drilled in the plywood to extend the rebars for the impressed-current connections. Rope anchors were placed in the formwork to facilitate the moving of the beams. The formwork was sealed with silicone caulking. The specimens were compacted and troweled during casting to ensure proper consolidation and finish as per ASTM.[27] Twelve concrete cylinders (six each for NSC and

LSC) were made to verify the target compressive strengths. A curing compound was applied to the exposed surfaces of the beams and the cylinders to facilitate curing. The specimens were covered with polythene sheets, and the formwork was removed after 4 days.

Figure 1. Sample preparation: formwork

Accelerated corrosion

Accelerated corrosion was induced in all 36 specimens by immersion in a 5% (50,000 ppm) NaCl solution, as used by Raju et al.[15] and Abouhussien, et al.[28] Per ASTM,[29] the Grade 60 (A572) rebar was used as the anode, and the Type 304 stainless steel rebar was used as the cathode during the impressed-current technique, as shown in Fig. 2. Each beam specimen contained three cathodic (stainless steel) rebars and three anodic Grade 60 rebars, placed in an alternating pattern with 100-mm center-to-center spacing. This configuration ensured that the anodic rebars were adequately surrounded by cathodic elements, promoting a uniform distribution of the electrical field and simulating realistic corrosion initiation across the rebar surface. The choice of Type 304 stainless steel was based on its high corrosion resistance and electrochemical stability, which ensured that the cathode remained inert throughout the testing period and did not undergo self-corrosion or interfere with the anodic corrosion process. El Maaddawy et al.[30] used an impressed-current system for laboratory corrosion studies due to its passive behavior in chloride-rich environments. Grade 60 rebars were chosen intentionally as anodes in the accelerated corrosion setup due to their widespread use in reinforced concrete structures in the United States.

Prior to immersion, one end of the wire was connected to the extended portions of the anode and the cathode in the form of a coil and then wrapped with white Teflon tape (Fig. 3a). This prevented corrosion of the extended portions of the rebars. The other end of the wire was soldered to size 35-mm alligator clips that were subsequently connected to the main circuit board. The specimens were immersed in 1143 × 965 × 965-mm plastic totes containing an NaCl electrolyte solution, and finally, a power supply was connected to the circuit board (Fig. 3b). A current of 0.65 A was used since a prior study found an acceptable current range of 0.1–2 A.[30] A parallel connection scheme was used for the specimens to ensure an uninterrupted current supply in case of connection failure. The corrosion due to the impressed-current method is different from natural corrosion. Natural corrosion is governed by chloride diffusion, moisture availability, oxygen transport, temperature variation, and wet–dry exposure cycles, whereas impressed-current corrosion accelerates the electrochemical reaction through an externally applied current.

There are no existing guidelines for accurately time-scaling the accelerated corrosion period to the equivalent in situ corrosion period. Most prior investigations employed current levels three to 100 times larger than the highest observed in field studies.[31] Malumbela et al.[32] stated that the degree of damage produced by a current density of 3 $\mu A/cm^2$ in 1 year could be attained in two hours by utilizing a current density of 10400 $\mu A/cm^2$. There is currently no universally accepted methodology for directly converting accelerated corrosion duration into an equivalent natural corrosion age. Previous studies have used current–density scaling relationships to provide approximate comparisons between laboratory-induced corrosion and field exposure conditions.[31,32] Based on these relationships, the corrosion levels achieved after 10, 20, and 30 days of accelerated testing may be broadly comparable to those developed over substantially longer field exposure periods. However, these values should be interpreted only as theoretical approximations rather than direct service-life equivalents.

Although Faraday's Law is widely used for estimating theoretical corrosion mass loss, it assumes ideal conditions (100% current efficiency, uniform corrosion) that are rarely met in concrete. To obtain more realistic and field-representative data, this study employed direct gravimetric measurement per ASTM G1-03[33] of rebar mass loss, which captures both electrochemical and mechanical deterioration. This approach aligns with the study's objective of correlating GPR parameters with actual corrosion rather than theoretical predictions, thereby enhancing model reliability for practical applications.

Determination of rebar mass loss

Following the accelerated corrosion and scanning, the corroded rebars were extracted from the specimens using a jackhammer and cleaned per ASTM G1-03[33] standard. The reinforcement percentage mass loss was then calculated by comparing the initial (new) rebar weight before corrosion and the final rebar weight after the corrosion, extraction, and cleaning processes.

GPR Scanning

The GPR scans were performed using a 2.6-GHz antenna connected to a data-acquisition system. This antenna can provide a high-resolution concrete scan up to a depth of 250 mm. To partially prevent interference from salt water, the samples were removed from the saline, and their top surfaces were dried for a day before scanning. Eight scans

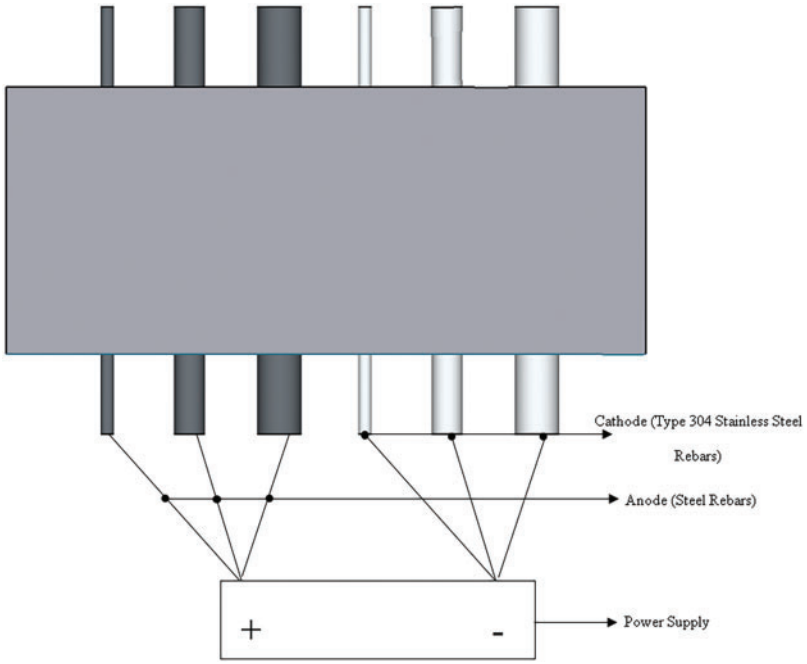

Figure 2. Accelerated corrosion process, schematic diagram

(a) Accelerated corrosion process

(b) Schematic diagram

Figure 3. Accelerated corrosion: (a) anode–cathode wiring connection; (b) power supply to the submerged specimens

were recorded for each sample in the following sequence: before the saline submersion, at 10-day intervals during saline submersion, and at the end of a predetermined corrosion level. Fig. 4 displays a sample during scanning. The first five scans were conducted normal to the embedded rebars, while the remaining three scans were made along the lengths of the rebars. Waveforms, frequency, and amplitudes were recorded during the scanning process. The scans were analyzed using GPR-SLICE Software GPR-SLICE,[34] considering filters such as background-noise removal and time-zero cancellation. The exported results were calibrated according to the positioning of the rebars during sample casting.

Figure 4. GPR scanning

Results and Discussions

The amplitude and TWTT of the GPR waveforms changed throughout the corrosion process due to the evolving physical and electromagnetic properties of the concrete–rebar system. The observed response can be interpreted by considering three distinct stages of deterioration: (1) chloride contamination and moisture ingress; (2) corrosion initiation and propagation; and (3) advanced corrosion with microcracking and corrosion-product accumulation.

During the early chloride contamination stage, the saline solution penetrated the concrete cover and chloride ions accumulated around the embedded reinforcement. At this

stage, the dominant effect was an increase in moisture content and ionic conductivity within the concrete pores. The elevated conductivity increased electromagnetic attenuation, causing a reduction in the reflected GPR amplitude. Simultaneously, the changing dielectric properties of the concrete influenced signal propagation and resulted in a slight reduction in the measured TWTT. Therefore, the early-stage GPR response was primarily governed by moisture- and chloride-induced attenuation rather than by corrosion products.

As chloride ions progressively disrupted the passive layer surrounding the reinforcement, corrosion initiation occurred and corrosion products began to form at the steel–concrete interface. During this intermediate stage, rust accumulation altered the local dielectric properties of the concrete and created additional interfaces between steel, corrosion products, and surrounding concrete. The resulting dielectric discontinuities enhanced the reflection of the electromagnetic wave and partially compensated for the attenuation effects observed during the initial contamination stage. Consequently, the reflected amplitude gradually increased while the TWTT began to recover toward its original value.

During the advanced corrosion stage, the accumulation and expansion of corrosion products generated localized microcracking, debonding, and damage within the concrete cover. These defects introduced additional dielectric discontinuities and increased the electromagnetic contrast at the steel–concrete interface. As a result, stronger reflections were produced, leading to higher reflected amplitudes. At the same time, moisture retention, corrosion products, and deterioration of the surrounding concrete increased the effective dielectric constant of the medium, slowing the propagation of the radar wave and increasing the TWTT. Therefore, the amplitude increase observed during the later stages of the accelerated corrosion process is attributed primarily to corrosion-product accumulation and corrosion-induced damage rather than to chloride contamination alone.

The evolution of GPR amplitude is not necessarily monotonic. Depending on the relative influence of moisture content, chloride concentration, corrosion-product accumulation, and cracking, either amplitude reduction or amplitude increase may be observed. Consequently, GPR amplitude should be interpreted together with TWTT and other material parameters when evaluating corrosion severity.

Fig. 5 presents representative amplitude contour maps for NSC specimens with a 50-mm concrete cover. For all rebar sizes, a general increase in the maximum reflected amplitude was observed with increasing corrosion duration, indicating that the corrosion-product accumulation and damage mechanisms dominated over attenuation effects during the later stages of the experimental program. The increased dielectric contrast at the corroded steel–concrete interface enhanced the reflection coefficient and produced stronger reflected signals. In addition, corrosion-induced microcracking and localized moisture accumulation likely contributed to the observed amplitude enhancement.

The amplitude contour patterns were generally symmetric for the 22-mm rebar but appeared asymmetric for the 10- and 32-mm rebars. Although chloride-induced pitting corrosion is inherently localized and nonuniform, the observed asymmetry is likely influenced by several additional factors, including antenna alignment, scanning direction, rebar size, local variations in chloride penetration, moisture distribution, and microcrack development. Furthermore, post-processing procedures such as background-noise removal and time-zero correction may influence the apparent contour geometry. Therefore, the observed asymmetry should be interpreted as the combined result of corrosion morphology, specimen characteristics, and signal-processing effects.

The contour plots corresponding to the 10-mm rebar exhibited a nonlinear response to corrosion progression. While substantial changes were observed after 10 days of accelerated corrosion, the contour patterns at 20 and 30 days became less pronounced and partially resembled the pre-corrosion condition. This behavior may be attributed to the redistribution of moisture and corrosion products within the concrete pore structure, resulting in localized changes in dielectric contrast. These observations suggest that the GPR response does not necessarily scale linearly with corrosion duration and is controlled by evolving interactions among moisture content, chloride contamination, corrosion products, and damage development.

Although the cover-to-diameter ratio (c/d) is widely used to characterize corrosion-related behavior and corrosion-induced cracking in reinforced concrete,[35,36] the present study considered cover depth and rebar diameter separately because they influence GPR measurements through different physical mechanisms. Cover depth primarily governs electromagnetic wave attenuation and travel time,[37,38] whereas rebar diameter influences the size of the reflecting target and the resulting signal amplitude.[39,40]

Influence of parameters on amplitude

Fig. 6 shows changes in maximum positive GPR amplitude with increasing rebar diameter and the effect of concrete strength on the GPR amplitude. A clear trend emerges in which specimens containing larger-diameter rebars, specifically the 32 mm (#10), exhibit higher reflected GPR amplitudes compared to smaller-diameter rebars such as the 22 mm (#7) and 10 mm (#3). A clear trend emerges in which specimens containing larger-diameter rebars exhibit higher reflected GPR amplitudes than smaller-diameter rebars. This behavior is primarily attributed to the larger geometric target presented to the electromagnetic wave. Larger rebars provide a greater reflective surface area and stronger electromagnetic contrast with the surrounding concrete, resulting in increased reflection strength. Although smaller rebars experienced a higher percentage mass loss, the larger physical dimensions of the 32-mm rebars produced stronger baseline reflections and more pronounced amplitude responses throughout the corrosion process.

In addition to rebar diameter, concrete strength also plays a significant role in influencing GPR amplitude. Across all stages of accelerated corrosion, the amplitudes recorded from LSC specimens generally exhibited higher reflected amplitudes than NSC specimens throughout the testing

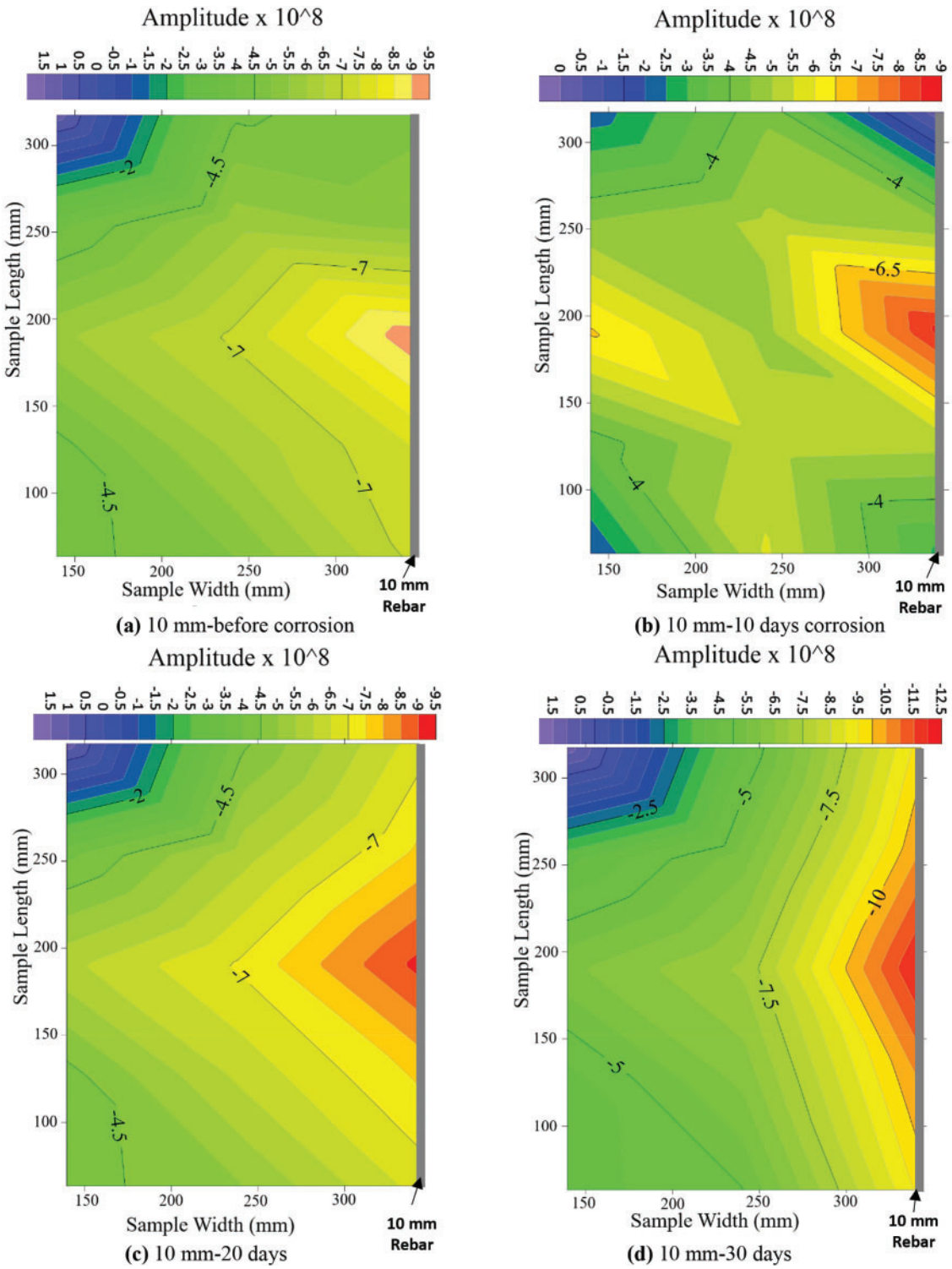

Figure 5. (Continued)

period. This difference is primarily due to the higher air content or porosity inherent in the former. Air has a significantly lower dielectric constant compared to concrete, which means that it absorbs less electromagnetic energy from the GPR wave. As a result, the radar signal experiences less attenuation when passing through LSC, leading to stronger reflections and higher measured amplitudes. Furthermore, the porous nature of LSC promotes easier ingress of chlorides and moisture, which accelerates corrosion and amplifies the electromagnetic response captured by the GPR system.

Fig. 7 illustrates the effect of concrete cover depth on the reflected GPR amplitude. It is evident that specimens with 75- and 50-mm cover depths exhibited lower amplitudes compared to those with a 38-mm cover. This is primarily due to the increased travel distance of the radar wave through

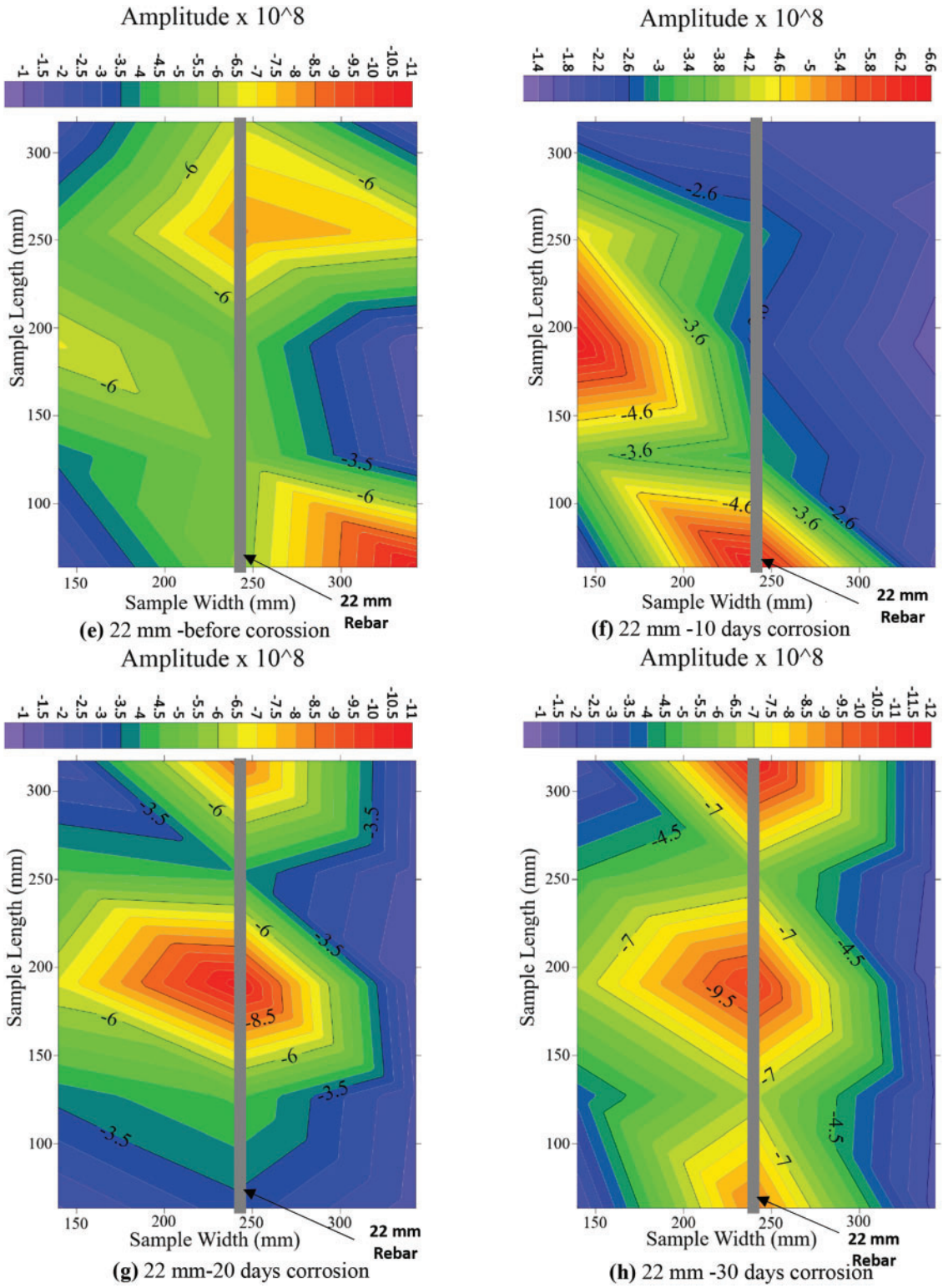

Figure 5. (Continued)

the concrete, which results in greater attenuation and energy loss before the wave reaches the rebar and returns to the receiver. As the cover depth increases, more of the radar energy is absorbed or scattered within the concrete matrix—especially in higher-porosity mixes—leading to a diminished signal strength. Consequently, deeper covers produce weaker reflections and lower amplitudes, reinforcing the known inverse relationship between wave travel distance and signal strength in GPR applications. It should be noted that the amplitude trends discussed herein correspond primarily to the intermediate and advanced stages of corrosion, where the influence of corrosion products and corrosion-induced damage exceeded the attenuation effects associated with the initial chloride contamination phase.

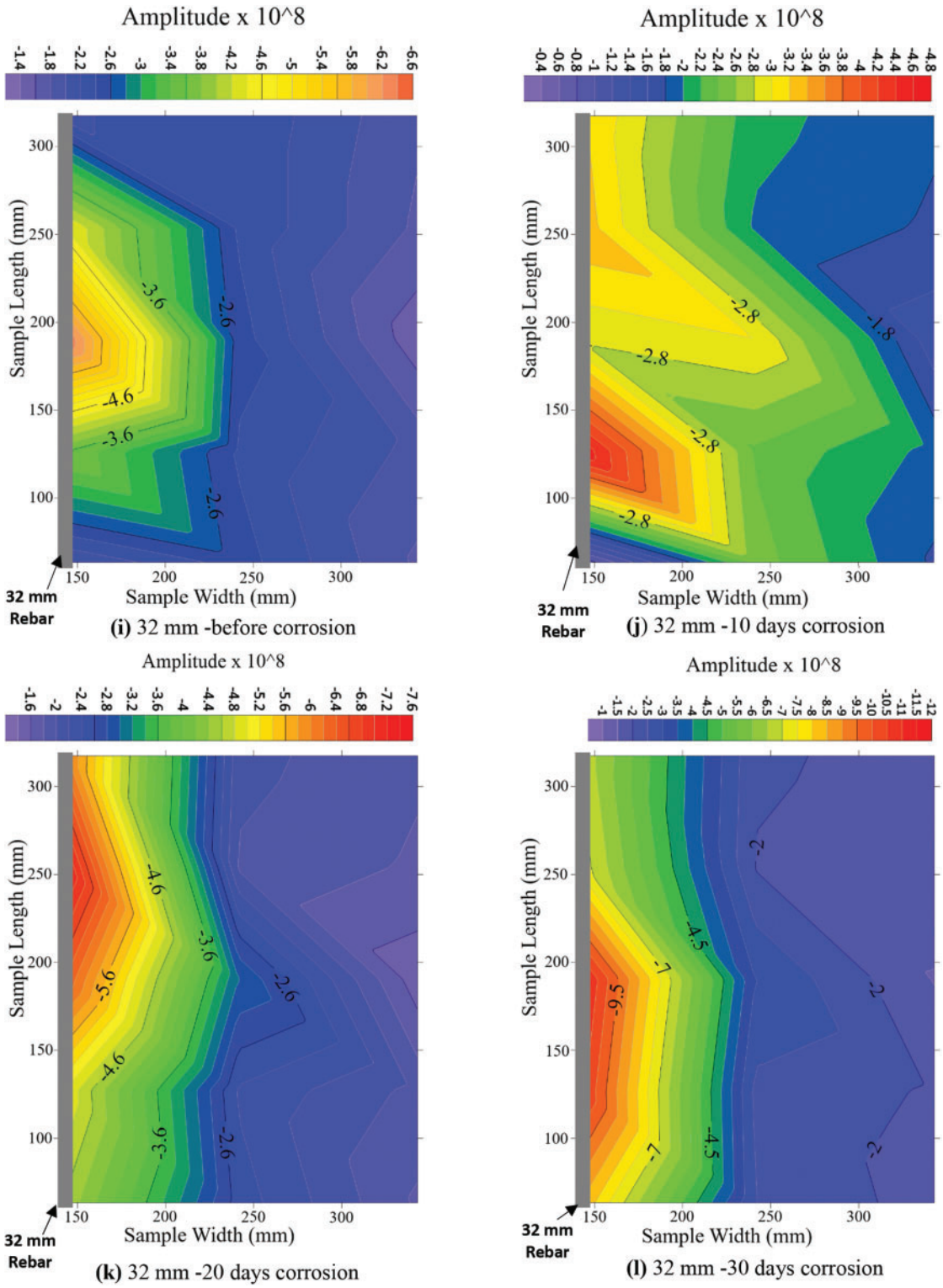

Figure 5. GPR amplitude contours for NSC specimens with 50-mm cover at different corrosion durations and rebar diameters. GPR, ground-penetrating radar; NSC, normal strength concrete

Influence of parameters on TWTT

The TWTT of the reflected GPR waveforms at different corrosion levels was evaluated for varying rebar diameters, concrete strengths, and concrete cover depths, as shown in Figs. 8 and 9. In general, the TWTT exhibited a non-monotonic response throughout the corrosion process. During the early stages of chloride contamination, a slight reduction in TWTT was observed. This behavior is attributed to the ingress of chloride ions and moisture into the concrete pore structure, which altered the electromagnetic properties of the concrete surrounding the

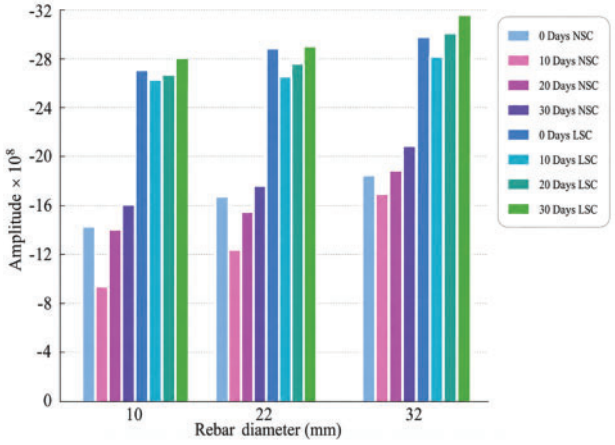

Figure 6. GPR amplitude variations with concrete type and rebar diameter

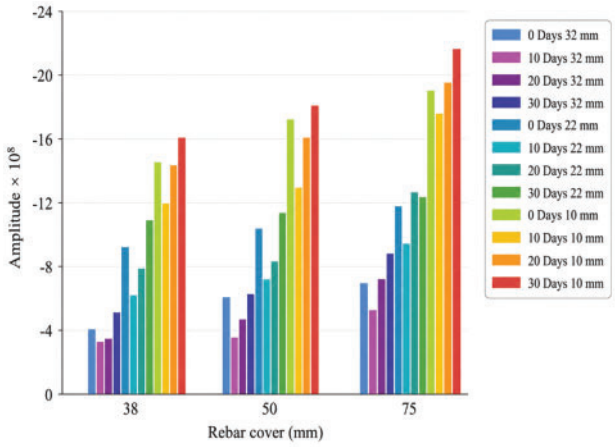

Figure 7. GPR amplitude variation with cover depth and rebar diameter

reinforcement. Similar observations have been reported in previous accelerated corrosion studies.

As corrosion progressed, the TWTT gradually increased. This increase is attributed to the accumulation of corrosion products, increased moisture retention, and the development of localized microcracking near the steel–concrete interface. These changes increase the effective dielectric constant and heterogeneity of the surrounding medium, resulting in slower electromagnetic wave propagation and longer travel times. Consequently, the reflected signal required a longer time to travel between the antenna and the embedded reinforcement, producing increased TWTT values during the later stages of corrosion.

Unlike amplitude, which may either increase or decrease depending on the balance between attenuation and reflection mechanisms, the TWTT exhibited a more consistent relationship with corrosion progression. The increase in TWTT observed during advanced corrosion stages is primarily associated with changes in dielectric properties caused by corrosion products, moisture redistribution, and concrete deterioration.

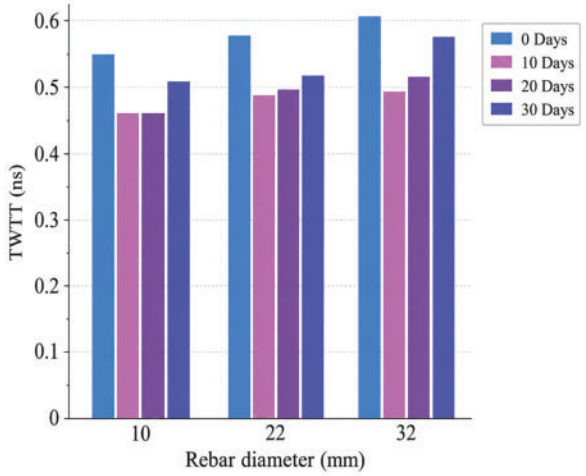

(a) NSC-38 mm cover

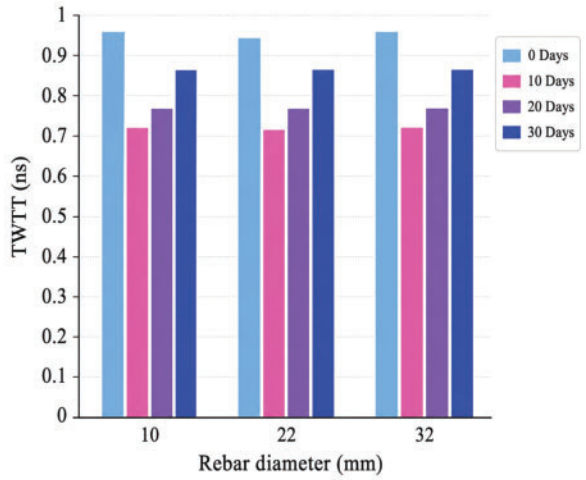

(b) NSC-50 mm cover

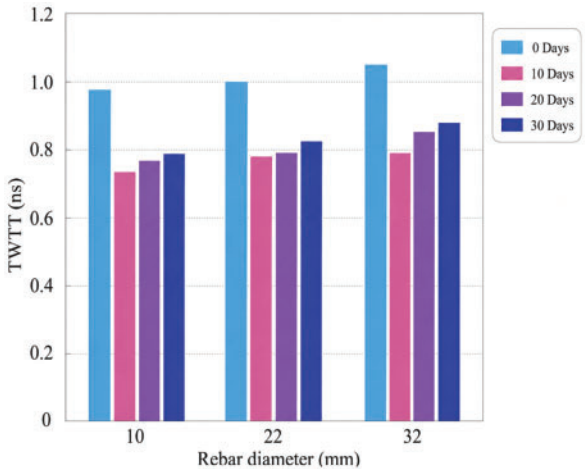

(c) NSC-75 mm cover

Figure 8. Variation of TWTT: (a) NSC with 38-mm cover; (b) NSC with 50-mm cover; and (c) NSC with 75-mm cover

The influence of rebar diameter on TWTT was relatively small compared with the influence of concrete cover depth. While slight variations were observed among the different

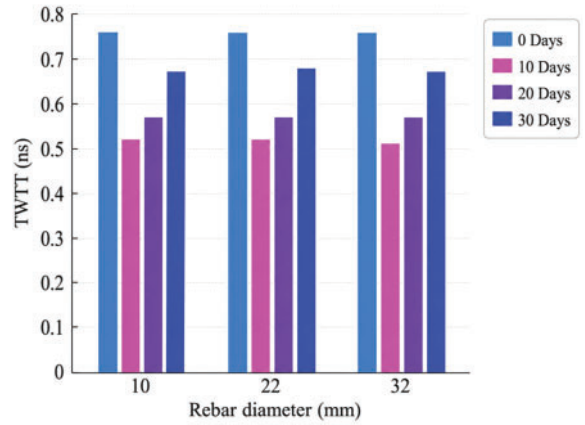

(a) LSC-38 mm cover

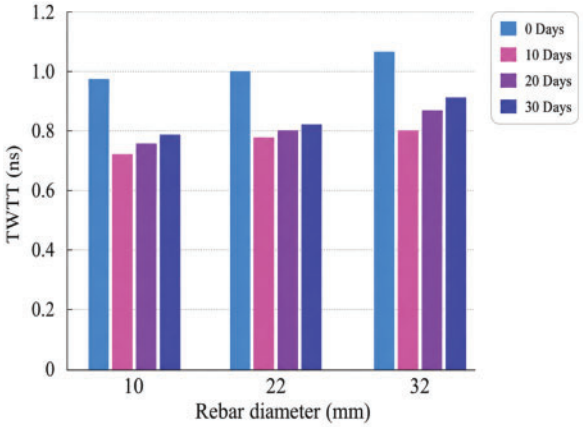

(b) LSC-50 mm cover

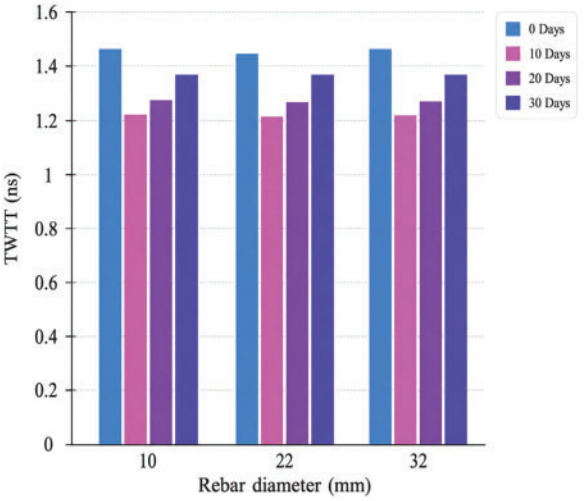

(c) LSC with 75 mm cover

Figure 9. Variation of TWTT: (a) LSC with 38-mm cover; (b) LSC with 50-mm; and (c) LSC with 75-mm cover

rebar sizes, the dominant parameter affecting TWTT was the travel distance through the concrete. Specimens with larger concrete covers consistently exhibited greater TWTT values because the radar wave traveled a longer path before reaching the reinforcement and returning to the receiver.

Concrete quality also affected the measured TWTT. For all cover depths and corrosion durations, LSC specimens generally exhibited higher TWTT values than NSC specimens. The higher air content and more porous microstructure of LSC facilitated greater moisture ingress and chloride penetration, resulting in larger changes in dielectric properties during the corrosion process. Consequently, electromagnetic wave propagation was slower in LSC specimens, leading to increased travel times compared with NSC specimens.

Figs. 8 and 9 demonstrate that the combined effects of concrete cover depth, concrete quality, and corrosion progression have a greater influence on TWTT than rebar diameter. The results suggest that TWTT may provide a useful supplementary indicator of corrosion-related deterioration when interpreted together with reflected amplitude and other structural parameters.

Rebar mass loss

Although all specimens were subjected to the same impressed-current level, chloride concentration, and corrosion duration, the resulting corrosion mass loss was not identical among the reinforcing bars. Variations in corrosion development are expected due to differences in rebar diameter, concrete cover depth, concrete quality, moisture transport characteristics, and local electrical resistance within the concrete. Consequently, the rebar mass loss was directly related to the corrosion levels. As shown in Fig. 10, the percentage of rebar mass loss was the highest for LSC specimens with the smallest rebar diameter and clear cover, and subjected to the longest corrosion duration. For instance, smaller-diameter rebars have a higher surface-area-to-volume ratio, making them more susceptible to corrosion. At the same time, a smaller cover means that the rebar is closer to the surface, allowing corrosive agents to reach it more quickly and in higher concentrations. Furthermore, prolonged exposure to corrosive conditions results in more extensive corrosion and mass loss. The different sizes of circles in Fig. 10 represent the remaining parameters. For example, in Fig. 10a, with the rebar diameter shown on the x-axis, the circle sizes indicate concrete cover, and each 10-day result included six brown circles, three representing LSC and NSC each.

In calculating the rebar mass loss, the length of the rebars extending outside the concrete specimens for making electrical connections was not included. This ensures that mass loss measurement accurately reflects the corrosion occurring within the concrete.

Quantitative relationships

A multivariate linear regression equation (Eq. (1)) was generated using Python Software Foundation[41] as a quantitative relationship between rebar corrosion mass loss and related parameters. Linear regression is a basic and extensively used type of predictive analysis that works with continuous data. Multivariate linear regression allows researchers to predict or explain criterion variable scores based on scores on two

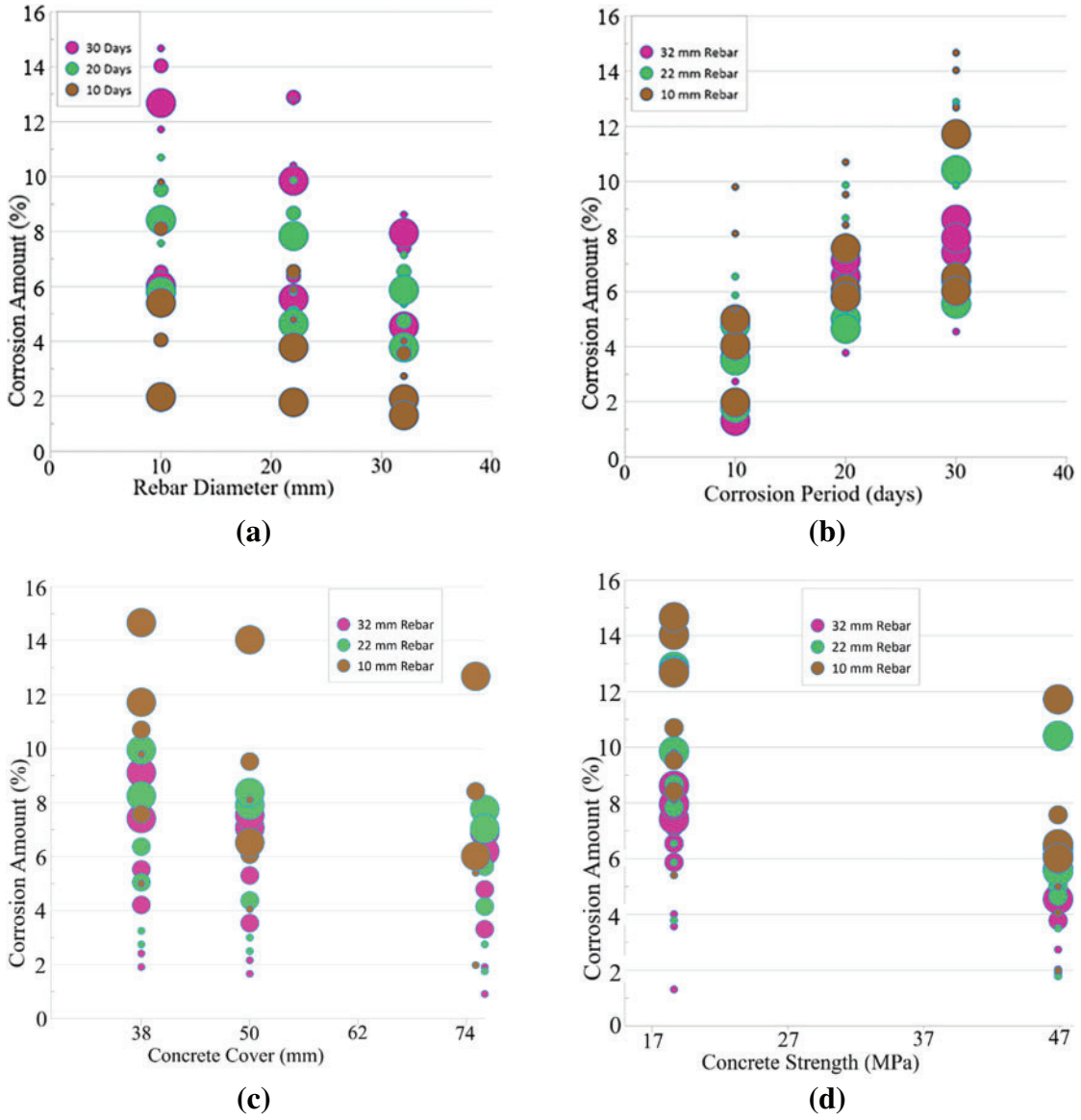

Figure 10. Change in percentage of corrosion with: (a) rebar diameter; (b) corrosion period; (c) concrete cover; and (d) concrete strength

or more predictor factors and knowledge of the relationships between them. The approach was to determine how much each predictor variable contributes to explaining the criterion variable by providing a regression or beta coefficient, which indicates how much each predictor variable contributes to explaining the criterion variable scores while controlling for the other predictor variables.[42]

The coefficient of determination, R^2, was 0.84 as determined from the IBM Corp.[43] software, implying that the model's inputs can explain around 84% of the observed variation.

$$Cr = 5.095 + 0.122T_c - 0.012fc' - 0.183d_b - 1.208t_{TWTT} + 0.016c - 2.8 \times 10 - 10A_{GPR} \quad (1)$$

where

T_c is the corrosion exposure duration (years),
f_c' is the concrete compressive strength (MPa),
d_b is the initial rebar diameter (mm),
t_{TWTT} is the two-way travel time (ns),
c is the concretecover depth (mm), and
A_{GPR} is the maximum reflected GPR amplitude.

The factors included in Eq. (1) were selected based on their theoretical and empirical impact on GPR wave amplitude. Each factor, such as rebar diameter, concrete cover, and corrosion level, was shown in previous studies to influence the amplitude of GPR signals.[44] Rebar diameter and concrete cover affect the reflection and attenuation of GPR waves, while corrosion impacts the material's dielectric properties and, consequently, the signal amplitude.

It is important to note that the regression coefficients in Eq. (1) reflect both the statistical weight and the scale of the respective input variables within the experimental dataset. The relatively large negative coefficient for rebar diameter (−0.183) indicates that smaller-diameter rebars

experienced higher corrosion percentages under the same exposure conditions, likely due to their higher surface area-to-volume ratio and lower residual cross-sectional area. This trend is consistent with prior studies[5,22] on accelerated corrosion behavior. The coefficient for GPR amplitude appears small (-2.8×10^{-10}) due to the large numerical scale of the amplitude values (in the range of thousands). Although the amplitude coefficient is small in magnitude, it captures subtle variations in signal intensity that are relevant to the progression of corrosion. The role of GPR amplitude should therefore be interpreted in the context of signal scaling and system sensitivity, and its generalizability is discussed further in the conclusions section.

In evaluating existing structures, the concrete strength, cover, and rebar diameter may be found from as-built drawings and in-situ or laboratory testing. The GPR amplitude and TWTT can be obtained from the GPR scanning. In the absence of initial parameters for the equation input, normalization can be performed by back-calculating the GPR amplitude collected from a corrosion-free section from the same structure (where $Cr = 0\%$), followed by inspection and exposing a portion of the rebar. If it is not possible to identify a corrosion-free section, then calibration with respect to the least corroded sample could be an option. Based on this, the residual rebar area can be estimated by deducting the corrosion percentage from the uncorroded rebar area, which may be used to compute the remaining capacity of reinforced concrete structures. Knowing the residual capacity of a member can aid engineers and owners in making an informed decision to retrofit or replace building or bridge structural components.

Model validation (case study)

The proposed model was validated by comparing it with the corrosion rate of a rebar retrieved during the demolition of a 32-year-old bridge deck on IH-30 in Dallas, Texas (Fig. 11). The compressive strength of the deck concrete was 20.7 MPa. The retrieved sample had corroded rebars measuring 203 mm in length and 12.7 mm (#4) in diameter, embedded in 50-mm-thick concrete. A GPR scan was conducted on the sample. The collected data were post-processed following the same procedure used for the laboratory specimens, including background removal, time-zero correction, and signal interpretation. The resulting GPR waveform is presented in Fig. 12. Analysis of the processed waveform yielded an average reflected amplitude of 5,758 and a TWTT of 0.9 ns. Employing the proposed Eq. (1), a 6.14% corrosion rate was predicted for the rebar. The corroded rebar was extracted from the concrete sample, cleaned per ASTM G1-03,[33] and then weighed to determine the mass loss owing to natural corrosion. A mass loss of 6.3% was determined, considering the masses of the extracted rebar and uncorroded rebar with the same length and diameter. Thus, the corrosion rate from the proposed equation was around 0.16% lower than the actual value, which is a satisfactory match.

Figure 11. Specimen obtained from the IH-30 bridge deck

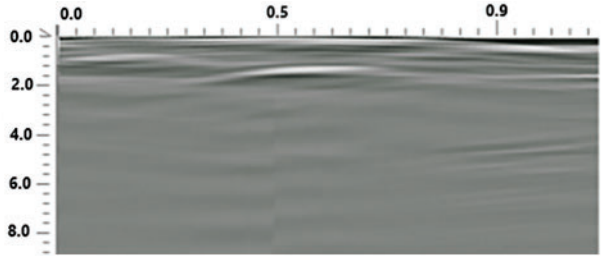

Figure 12. GPR waveform for 12.7-mm (#4) rebar

Conclusions and Recommendations

The following conclusions and recommendations may be made based on the findings from this study:

1. The present study successfully quantified the amount of steel rebar corrosion in concrete beams using GPR scanning. The research involved fabricating reinforced concrete beam specimens, exposing the beams to accelerated corrosion, scanning samples utilizing a 2.6-GHz frequency GPR, analyzing the data, and developing a multivariate regression equation.
2. Larger rebar sizes underwent more corrosion than smaller rebars due to the additional surface area and corrosion potential. As a result, the GPR reflected wave amplitudes also increased.
3. The reflected GPR amplitudes from LSC specimens were greater than those from NSC specimens for all corrosion durations. LSC has a higher air content than NSC, and the dielectric constant of air is lower than that of concrete. Air absorbs less radar radiation, resulting in higher amplitudes for LSC.
4. Larger concrete covers for rebars resulted in smaller reflected GPR wave amplitudes. This is because the radar waves travel longer distances for larger cover depths, causing most of the radar energy to be absorbed by the concrete.
5. It was found that the corrosion stages on the embedded rebars had a significant impact on the maximum amplitude and the TWTT of the GPR signal. For a given cover depth, rebar diameter, and concrete strength, the amplitude remained constant prior to corrosion commencement. The reflected amplitude

decreased at the commencement of the accelerated corrosion but increased after a specific period. This may be attributed to increased corrosion within the concrete pores with time. Restoration of the original TWTT and increased value were noticed at the latter stages due to corrosion product dispersion inside the concrete pores, suggesting an increase in the concrete dielectric property.

6. The available chloride ions, water content, and current flow were kept constant throughout the accelerated corrosion process. Therefore, the rebar corrosion mass loss was directly related to the corrosion levels. The mass loss was highest in LSC samples with the smallest rebar diameter and cover, and under the longest corrosion duration.
7. An experimentally calibrated multivariate linear regression model was developed to determine the corrosion amount in consideration of the parametric effects. A user-friendly step-by-step approach is presented for estimating or finding the various input parameters, such as concrete strength, concrete cover, rebar diameter, and GPR amplitude and TWTT.
8. The proposed regression model was validated by comparing it with the actual corrosion rate of an embedded rebar retrieved during the demolition of an old concrete bridge deck in Dallas, TX. The model's corrosion percent output was only 0.16% lower than the actual rebar mass loss. Since the IH-30 bridge calibration is an independent case study comparison to demonstrate the practical applicability of the proposed framework, it is recommended that future research validates the model with a large field data set and additional real-life samples to increase confidence in the model.
9. Accelerated corrosion of steel rebars in concrete over a condensed period results in increased corrosion product concentrations around the rebars and diffusion of these products into the pores[30]. However, the extent of this activity within the concrete cover is minimal. As a result, the properties of the concrete around the rebars remain unchanged. When natural corrosion occurs over a longer time, corrosion products infiltrate more deeply into the surrounding concrete pores, resulting in a significant variation in the concrete property. The current study considered concrete compressive strength and measured fresh concrete air content as parameters influencing the GPR response. Although air content provides an indirect indication of the pore structure, it does not directly quantify hardened concrete porosity. Future studies should incorporate direct measurements of hardened concrete porosity and moisture distribution to further improve the predictive capability of GPR-based corrosion assessment models.
10. GPR wave amplitude can vary significantly across different GPR systems due to differences in hardware and signal processing techniques. This current study used only one GPR system, which could limit the generalizability of the regression model. Future studies could use an amplitude conversion approach[45] to address this harmonization issue. On top of that, it is recommended to incorporate quantified moisture profiles and relative humidity monitoring during corrosion testing. This will help account for the influence of moisture on dielectric properties and improve the predictive capability and generalizability of GPR-based corrosion models. Moreover, temperature effects were not explicitly investigated in this study.
11. The accelerated corrosion program enabled the development of measurable corrosion levels within a practical testing period; however, it may not fully reproduce the corrosion morphology, moisture distribution, chloride transport mechanisms, and corrosion-product accumulation observed in naturally corroded structures. Future studies should incorporate additional field-corroded specimens and long-term exposure tests to further assess the applicability and transferability of the proposed GPR-based corrosion assessment framework under real-world conditions.
12. Cross-validation and optimization of the regression model are recommended to enhance its generalizability and broader applicability. Additionally, cracking was not considered in this study, as the corrosion process was controlled to prevent visible damage. However, cracking can significantly affect chloride transport, corrosion development, and GPR signal response. Future research should incorporate cracked specimens to better reflect real-world conditions and enhance the model's applicability. Moreover, the experimental program included two replicate specimens for each test condition. While this level of replication was sufficient to observe general trends in GPR response and corrosion mass loss, it limits the statistical confidence of the results and prevents a comprehensive assessment of variability.

Data Availability Statement

The datasets used and/or analyzed during the current study are available from the corresponding author on reasonable request.

Acknowledegments

The study was performed under a grant from the Texas Department of Transportation (TxDOT).

Disclaimer

The authors declare that they have no competing interests as defined by Springer or other interests that might be perceived to influence the results and/or discussion reported in this paper.

Supplemental Materials

The author has declared that there are no supplemental materials associated with this manuscript.

References

[1] Hong S, Chen D, Dong B. Numerical simulation and mechanism analysis of GPR-based reinforcement corrosion detection. *Constr Build Mater*. 2022;317(4–5):125913. doi:10.1016/j.conbuildmat.2021.125913.

[2] Zaki A, Johari MM, Hussin WW, Jusman Y. Experimental assessment of rebar corrosion in concrete slab using ground penetrating radar (GPR). *Int J Corros*. 2018;2018(283):1–10. doi:10.1155/2018/5389829.

[3] Koch G, Varney J, Thompson N, Moghissi O, Gould M, Payer J, International measures of prevention, application, and economics of corrosion technologies study. In: *Report No. OAPUS310GKOCH (AP110272)*. Houston: NACE International; 2016.

[4] Rahman MM, Yazdani N, Beneberu E, Jalal KB. Evaluation and load rating of an aging and impact damaged steel girder bridge: case study. *Innov Infrastruct Solut*. 2024;9(12):272. doi:10.1007/s41062-024-01770-5.

[5] Hasan MI, Yazdani N. An experimental study for quantitative estimation of rebar corrosion in concrete using ground penetrating radar. *J Eng*. 2016;2016(6):1–8. doi:10.1155/2016/8536850.

[6] Hong SX, Wiggenhauser H, Helmerich R, Dong BQ, Xing F. Long-term monitoring of reinforcement corrosion in concrete using ground penetrating radar. *Corros Sci*. 2017;114(2):123–132. doi:10.1016/j.corsci.2016.11.003.

[7] Narayanan RM, Hudson SG, Kumke CJ, Beacham MW, Hall DD. Detection of rebar corrosion in bridge decks using statistical variance of radar reflected pulses. In: *Proceedings of the Seventh International Conference on Ground Penetrating Radar*; 1998; Lawrence, KS, 601–605.

[8] Hubbard SS, Zhang J, Monteiro PM, Peterson JE, Rubin Y. Experimental detection of reinforcing bar corrosion using nondestructive geophysical techniques. *ACI Mater J*. 2003;100(6):501–510. doi:10.14359/12957.

[9] Lai WWL, Kind T, Wiggenhauser H. Using ground penetrating radar and time-frequency analysis to characterize construction materials. *NDTE Int*. 2011;44(1):111–120. doi:10.1016/j.ndteint.2010.10.002.

[10] Hong S, Lai WWL, Wilsch G, Helmerich R, Günther T, Wiggenhauser H. Periodic mapping of reinforcement corrosion in intrusive chloride contaminated concrete with GPR. *Construct Build Mater*. 2014;66:671–684. doi:10.1016/j.conbuildmat.2014.06.019.

[11] Hong S, Lai WWL, Helmerich R. Experimental monitoring of chloride-induced reinforcement corrosion and chloride contamination in concrete with ground-penetrating radar. *Struct Infrastruct Eng*. 2015;11(1):15–25. doi:10.1080/15732479.2013.879321.

[12] Lai WWL, Kind T, Stoppel M, Wiggenhauser H. Measurement of accelerated steel corrosion in concrete using ground-penetrating radar and a modified half-cell potential method. *J Infrastruct Syst*. 2013;19(2):205–220. doi:10.1061/(asce)is.1943-555x.0000083.

[13] Zhan BJ, Lai WWL, Kou SC, Poon CS, Tsang WF. Correlation between accelerated steel corrosion in concrete and ground penetrating radar parameters. In: *Proceedings of the International RILEM Conference on Advances in Construction Materials Through Science and Engineering*; 2011; Hong Kong, China.

[14] Liu H, Zhong J, Ding F, Meng X, Liu C, Cui J. Detection of early-stage rebar corrosion using a polarimetric ground penetrating radar system. *Construct Build Mater*. 2022;317(1):125768. doi:10.1016/j.conbuildmat.2021.125768.

[15] Raju RK, Hasan MI, Yazdani N. Quantitative relationship involving reinforcing bar corrosion and ground penetrating radar amplitude. *ACI Mater J*. 2018;115(3):449–457. doi:10.14359/51702187.

[16] Sossa V, Pérez-Gracia V, González-Drigo R, Rasol MA. Lab nondestructive test to analyze the effect of corrosion on ground penetrating radar scans. *Remote Sens*. 2019;11(23):2814. doi:10.3390/rs11232814.

[17] Senin SF, Hamid R, Ahmad J, et al. Damage detection of artificial corroded rebars and quantification using nondestructive methods on reinforced concrete structure. *J Phys: Conf Ser*. 2019;1349(1):012044. doi:10.1088/1742-6596/1349/1/012044.

[18] Faris N, Zayed T, Abdelkader EM, Fares A. Corrosion assessment using ground penetrating radar in reinforced concrete structures: influential factors and analysis methods. *Autom Constr*. 2023;156:105130. doi:10.1016/j.autcon.2023.105130.

[19] Ahmad S. Techniques for inducing accelerated corrosion of steel in concrete. *Arab J Sci Eng*. 2009;34(2C):95–104. doi:10.14359/18624.

[20] Ahmed SF, Maalej M, Paramasivam P, Mihashi H. Assessment of corrosion-induced damage and its effect on the structural behavior of RC beams containing supplementary cementitious materials. *Prog Struct Eng Mater*. 2006;8(2):69–77.

[21] Ha TH, Muralidharan S, Bae JH, et al. Accelerated short-term techniques to evaluate the corrosion performance of steel in fly ash blended concrete. *Build Environ*. 2007;42(1):78–85.

[22] Almusallam A. Effect of degree of corrosion on the properties of reinforcing steel bars. *Constr Build Mater*. 2001;15(8):361–368. doi:10.1016/s0950-0618(01)00009-5.

[23] Shahar N, Renan S, Speyer E, Gueta T, Alan R, David S. A factorial design experiment as a pilot study for non-invasive genetic sampling. *Mol Ecol Resour*. 2012. doi:10.1111/j.1755-0998.2012.03170.

[24] Minitab Inc. *Minitab Statistical Software*. State College, PA: Minitab Inc.; 1998.

[25] ACI Committee 318. *Building Code Requirements for Structural Concrete: (ACI 318-19) and Commentary (ACI 318R-19)*. Farmington Hills, MI: American Concrete Institute; 2018.

[26] ASTM International. *ASTM C231/C231M-17a: Standard Test Method for Air Content of Freshly Mixed Concrete by the Pressure Method*. West Conshohocken, PA: ASTM International; 2017.

[27] ASTM International. *ASTM C31: Standard Practice for Making and Curing Concrete Test Specimens in the Field*. West Conshohocken, PA: ASTM International; 2019.

[28] Abouhussien AA, Hassan AAA. Experimental and empirical time to corrosion of reinforced concrete structures under different curing conditions. *Adv Civil Eng*. 2014;2014(5):1–9. doi:10.1155/2014/595743.

[29] ASTM International. *ASTM A615/A615M-15a: Standard Specification for Deformed and Plain Carbon-Steel Bars for Concrete Reinforcement*. West Conshohocken, PA: ASTM International; 2015.

[30] El Maaddawy T, Soudki K. Effectiveness of impressed current technique to simulate corrosion of steel reinforcement

in concrete. *J Mater Civil Eng*. 2003;15(1):41–47. doi:10.1061/(asce)0899-1561(2003)15:1(41).
[31] Broomfield JP. *Corrosion of Steel in Concrete: Understanding, Investigation, and Repair*. 1st ed. London: E & FN Spon; 1997.
[32] Malumbela G, Moyo P, Alexander M. A step towards standardising accelerated corrosion tests on laboratory reinforced concrete specimens. *J South Afr Inst Civil Eng*. 2012;54(2): 78–85.
[33] ASTM International. *ASTM G1-03: Standard Practice for Preparing, Cleaning, and Evaluating Corrosion Test Specimens*. West Conshohocken, PA: ASTM International; 2011.
[34] GPR-SLICE. *Ground Penetrating Radar Imaging Software, Version 7 MT*. Houston: Geophysical Archaeometry Laboratory Inc.; 2021.
[35] Liu Y, Weyers RE. Modeling the time-to-corrosion cracking in chloride contaminated reinforced concrete structures. *ACI Mater J*. 1998;95(6):675–681. doi:10.14359/410.
[36] Vu KAT, Stewart MG, Mullard JA. Corrosion-induced cracking: experimental data and predictive models. *ACI Struct J*. 2005;102(5):719–726. doi:10.14359/14667.
[37] Daniels DJ. *Ground Penetrating Radar*. 2nd ed. London, UK: Institution of Engineering and Technology; 2004.
[38] Jol HM. *Ground Penetrating Radar Theory and Applications*. Amsterdam, Netherlands: Elsevier; 2009.
[39] Alani AM, Aboutalebi M, Kilic G. Applications of ground penetrating radar (GPR) in bridge deck monitoring and assessment. *J Appl Geophys*. 2013;97:45–54. doi:10.1016/j.jappgeo.2013.04.009.
[40] Dinh K, Gucunski N, Zayed T. Automated visualization of concrete bridge deck condition from GPR data. *Autom Constr*. 2018;89(1):120–128. doi:10.1016/j.ndteint.2018.11.015.
[41] Python Software Foundation. Python language reference, version 3.10; 2021. http://www.python.org.
[42] Sethuraman VS, Suguna K. Regression based analysis and visualization for identifying flexural behaviour of M60 beams under repeated compressive load based on observational data sets. *Procedia Comput Sci*. 2016;87:264–269. doi:10.1016/j.procs.2016.05.159.
[43] IBM Corp. *IBM SPSS Statistics for Windows, Version 27.0*. Armonk, NY: IBM Corp.; 2020.
[44] Tesic K, Baricevic A, Sedar M, Guucunski N. Quantifying the impact of parameters of chloride-induced reinforcement corrosion on the GPR signal. *Constr Build Mater*. 2023;399(20):132594. doi:10.1016/j.conbuildmat.2023.132594.
[45] Wong PT, Lai WW. Harmonising cross-system GPR wave amplitude for concrete diagnosis with machine learning. *J Nondestruct Eval*. 2023;42(4):73. doi:10.1007/s10921-023-01004-1.

BER the international journal of bridge engineering management and research

Load Testing and Rating of Simple-Span Prestressed Concrete Bridges with no Record Plans

Osman Hag-Elsafi[1*]; Jonathan Kunin[2] and Sreenivas Alampalli[3]

Submitted: 14 April 2026 **Accepted:** 24 June 2026 **Publication date:** 10 July 2026

DOI: 10.70465/ber.v3i3.91

Abstract: This paper introduces a pioneering approach for load testing and rating of simple-span prestressed concrete bridges when design information about the structure is not available. The paper uses the testing of a bridge in New York for illustration of the proposed approach. The bridge was built in 1961 and consisted of five simply supported 70-ft-long post-tensioned bulb-T beams. No documents or plans for the structure were available at the time of the testing. In 1970, the structure was posted for 12 tons. The absence of the bridge plans, coupled with the public's demand to accommodate school bus traffic on the bridge, prompted the load testing and rating. A plan based on an assumed design basis and investigation of bridge behavior under controlled truck loading was proposed to determine unknown design parameters and enable load rating of the structure. The bridge was then instrumented and load tested using trucks of known weights and configurations, positioned at specified locations on the deck to gradually increase their safe load effects on the structure. The results of the testing provided the required information about the bridge and allowed for load rating of the structure.

Author keywords: Prestressed concrete bridges; post-tensioned bridges; load testing; load distribution; bridge evaluation; load rating

Introduction

Bridge rating is routinely conducted by load rating engineers to evaluate and update the load carrying capacities of bridges. The rating process combines the knowledge gained during inspection cycles, which accounts for in-service condition, with appropriate analysis to determine load rating, namely, Inventory and Operating.[1] Load ratings based on the inventory level allow comparisons with the capacity for new structures and, therefore, result in a live load, which can safely utilize an existing structure for an indefinite period of time.[1] Load ratings based on the operating rating level generally describe the maximum permissible live load to which the structure may be subjected. Allowing unlimited numbers of vehicles to use the bridge at the operating level may shorten the life of the bridge.[1] Using these ratings, transportation agencies often apply their own policies to determine a structure's safe load-carrying capacity, which may result in allowing legal traffic on the bridge, posting a load limit on the structure, or restricting the bridge to certain types of permit loads. Most of the time there is a high degree of confidence in the parameters that influence the load-carrying capacity evaluation (such as the section properties of structural members, material strengths, and physical characteristics) to conduct an analytical rating. However, occasionally, these parameters cannot be adequately estimated/accounted for, and a test-based rating is warranted for a more realistic appraisal of the structure's load-carrying capacity. This is the typical situation for the application of testing for bridge load rating.[2–7] A more challenging situation arises when the bridge targeted for the load rating is a prestressed structure with no plans on record. An approach for load testing and rating of such structures is presented in this paper, using an actual load test performed on a bridge in New York State (NYS). Prestressed concrete bridges of unknown design records are not unique to any specific state and do exist in the inventory of many bridge owners all around the globe. This fact gives credence to the pioneering approach presented in this paper as a viable tool for all prestressed concrete bridge owners. This is especially true given that very few studies of this nature were conducted in the United States.[8–10] All these studies included approaches that combined a semi-theoretical basis for design with diagnostic or proof load testing. Texas Department of Transportation assigns HS-15 and HS-20 Inventory and Operating Ratings, respectively, for reinforced concrete bridges with no record plans that show no signs of structural stress. For bridges

*Corresponding Author: Osman Hag-Elsafi.
Email: Osman.Hag-Elsafi@dot.ny.gov
[1]Structure Management Bureau, Office of Structures, New York State Department of Transportation, 50 Wolf Road, Albany, NY 12232
[2]Technical Services Division, New York State Department of Transportation, 50 Wolf Road, Albany, NY 12232
[3]CEO, Alampalli Engineering, PLLC, 9 Stedman Way, Albany, NY 12211

Discussion period open till six months from the publication date. Please submit separate discussion for each individual paper. This paper is a part of the Vol. 3 of the International Journal of Bridge Engineering, Management and Research (© BER), ISSN 3065-0569.

older than 4 years that meet additional NBI ratings criteria, the structure may be load-posted at the Inventory level.[11] Oregon Department of Transportation assigns a rating factor of 1.0 for bridges in fair or better National Bridge Inventory (NBI) condition when long-term performance demonstrates their ability to carry legal loads. Inventory and Operating Ratings are estimated by considering the specific NBI condition ratings.[12]

The paper introduces a pioneering approach for the load rating of simple-span prestressed concrete bridges when there are no record plans. It discusses how load testing could be performed for load rating of simple-span prestressed concrete structures when there are no plans on record, using an actual bridge structure for illustration. It starts with background information on the structure, followed by a description of the preliminary analysis required for determining safe loads that could be applied during the testing, plans for instrumentation, load testing and results, load rating analysis, and conclusions.

Test Structure

The structure (Fig. 1) carried Dean's Mill Road over Hannacrois Creek near the Town of New Baltimore in Greene County, New York. The bridge was built in 1961 and made of 5 post-tensioned concrete bulb-T beams with 8-in. wide closure pours between the beams and an asphalt overlay riding surface.

In 1970, a load posting of 12 tons was placed on the bridge. No bridge plans or documentation of the load posting were available. Hence, preliminary analysis to estimate the capacity of the prestressed beams was performed using the 1961 edition of the AASHTO Standard Specifications for Highway Bridges.[7] Among the important revisions in this edition were the sections on Prestressed Concrete, which were based largely on the report of the Joint ASCE-ACI Committee on Prestressed Concrete of 1958 and used as Tentative Specifications for 2 years.

Instrumentation and load test plans were first developed, and the bridge was instrumented with strain gages in preparation for the load testing.

Preliminary Analysis

Analysis of the bridge structure conducted prior to the load testing targeted:

1. Identification of the beams' design parameters.
2. Estimation of ultimate and cracking moment capacities.
3. Determination of the maximum load that can be safely applied during the testing.
4. Estimation of expected strains under the maximum load determined above.

Identification of the design parameters was important to determine the tolerable stresses that will be used in the load rating equations. Ultimate and cracking moments are needed to determine the safe load to be applied during the testing, and the strain induced by this load is an important trigger to watch for during the testing. In the absence of the bridge plans, field measurements of the structure's critical dimensions could be made to determine section properties and estimate dead loads. The contribution of parapets, sidewalks, and other attachments to the stiffness of the structure could be ignored.

Beam Analysis

A typical beam was analyzed using Mathcad programming (Beam section in Fig. 1b). The analysis was performed assuming the beam was designed to satisfy the 1961 AASHTO requirements on initial and final stresses.[7] Section

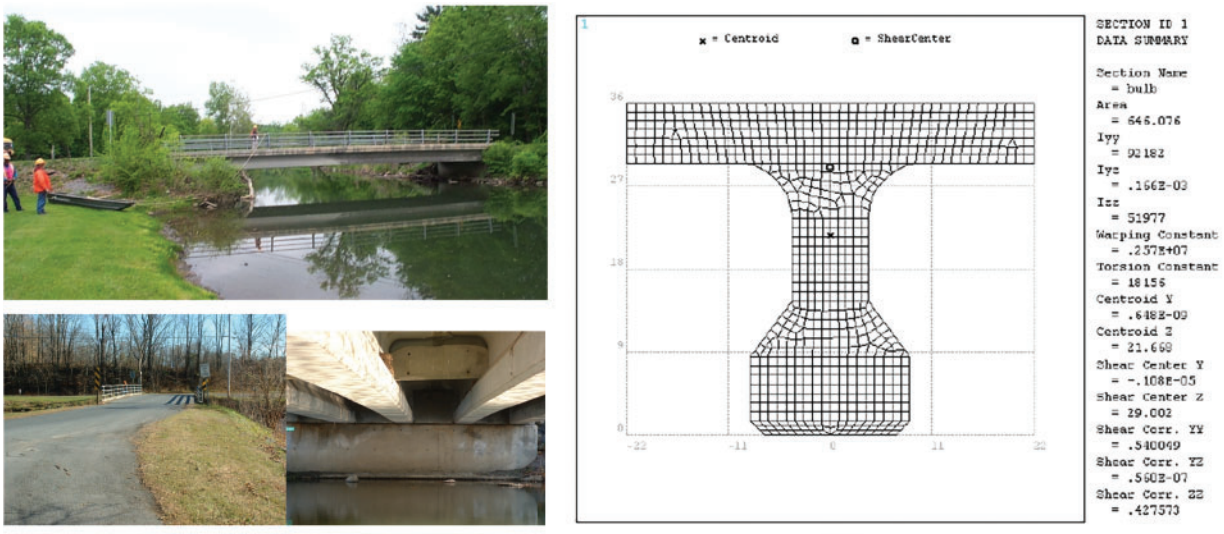

Figure 1. (a) Bridge views. (b) Typical beam section and properties

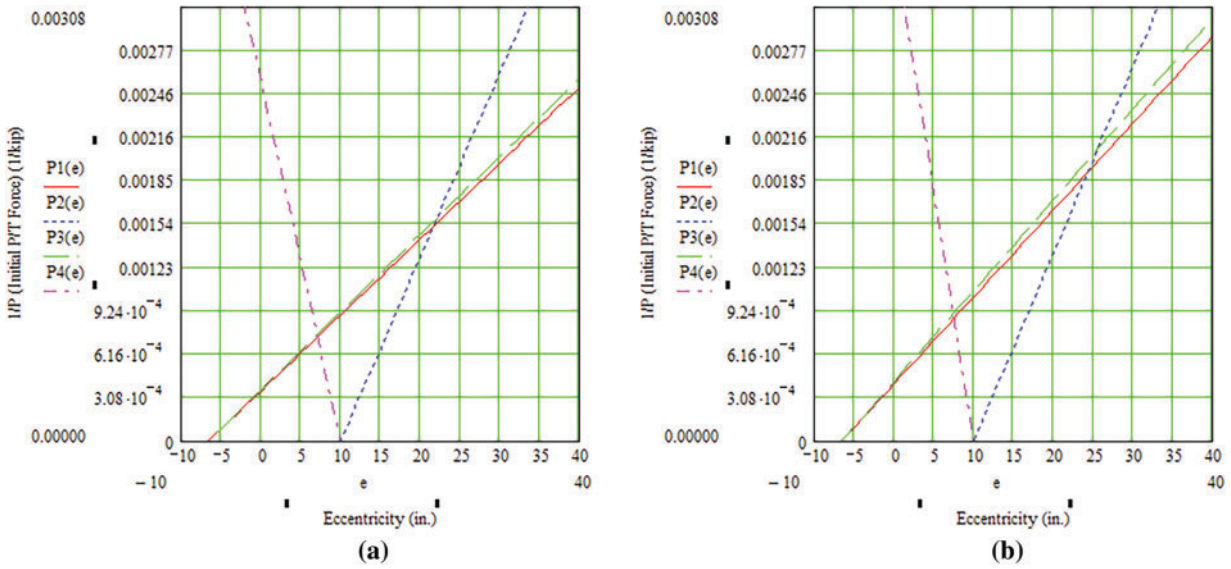

Figure 2. Feasible solution for AASHTO H-20 and HS-20 loading

properties were calculated based on measured beam dimensions. Dead load moment was calculated using the weight of the beam, closure pours, guide rails, and asphalt overlay (Total dead load moment M_{DL} = 522 kip-ft). Live load moment was calculated assuming the bridge was designed for an AASHTO HS-20 or H-20 loading, using a distribution factor of S/5, where S is the beam spacing (4 ft 4 in.), and an impact factor of 1.26 (respective design moments, $M_{HS\text{-}20}$ = 535.9 or $M_{H\text{-}20}$ = 384.9 kip-ft).[1,7,8]

Assumptions

The structure is assumed to meet the following minimum code requirements:

1. Compressive strength of concrete at 28 days f_c' = 5000 psi.
2. Compressive strength of concrete at time of initial prestress f_{ci}' = 4000 psi.
3. Modulus of elasticity of concrete $E_c = 57000\sqrt{f_c'}$.
4. Ultimate strength of post-tensioning steel f_s' = 240 ksi.
5. Nominal yield point stress of prestressing steel at 1% extension f_{sy} = 192 ksi.
6. Modulus of elasticity of steel E_s = 29000 ksi.

Allowable Stresses

The following allowable stresses were used in the program:

1. Temporary stresses in the steel before losses due to creep and shrinkage = 0.7 f_s'.
2. Steel stress at design load (after losses) = the smaller of 0.6 f_s' or 0.8 f_{sy}.
3. Temporary compressive stresses in concrete before losses due to creep and shrinkage = 0.55 f_{ci}'.
4. Temporary tensile stresses in concrete before losses due to creep and shrinkage = $3\sqrt{f_{ci}'}$
5. Concrete compressive stress after losses have occurred = 0.4 f_c'.
6. Concrete tensile stress after losses have occurred = 0.
7. Concrete cracking stress $f_{Cracking} = 7.5\sqrt{f_{ci}'}$.

Prestress Losses

Prestress losses were calculated based on:

1. Post-tensioning steel stress losses due to all causes except friction = 25 ksi.
2. Post-tensioning steel stress losses due to friction = 0.15 × 0.7 f_s'.

Ultimate Moment Capacity

The ultimate moment capacity of the beam was calculated by first confirming that the neutral axis was located inside the top flange. This is usually the case when the flange thickness calculated using $t_{flange} = 1.4\dfrac{d\rho f_{su}}{f_c'}$ is greater than the actual flange thickness t (t = 6.5 in.). The following equations:

$$M_u = A_{sr} f_{su} d\left(1 - 0.6\frac{A_{sr} f_{su}}{b'\,\mathrm{d}\,f_c'}\right) + 0.85 f_c'\left(b - b'\right)t\,(d - 0.5t) \quad (1)$$

where

$$A_{sr} = A_s - A_{sf} \quad (2)$$

is the steel area required to develop the ultimate compressive strength of the web.

$$A_f = 0.85 f_c'\left(b - b'\right)t / f_c' \quad (3)$$

Table 1. Beam analysis for selected P_i and e combinations

Parameter	HS-20		H-20	
	High P/T	Low P/T	High P/T	Low P/T
$1/P_i \times 10^{-4}$ (1/kip)	7.38	13.96	9.00	16.28
P_i (kip)	1355.00	716.50	1111.00	614.40
e (in.)	7.10	18.7	7.75	18.68
P_e (kip)	949.86	502.27	778.81	430.69
A_s (in.^{2})	8.07	4.27	6.61	3.67
$M_u \times 10^4$ (kip-in.)	2.65	3.14	2.27	2.62
$M_{Fact.} \times 10^4$ (kip-in.)	2.55	2.55	2.09	2.09
$M_{cr} \times 10^4$ (kip-in.)	1.55	1.52	1.34	1.31
$M_{Test} \times 10^3$ (kip-in.)	9.21	8.90	7.16	6.88
f_{Test} (ksi)	2.17	2.09	1.68	1.62
Δ (in.)	1.33	1.285	1.132	1.09

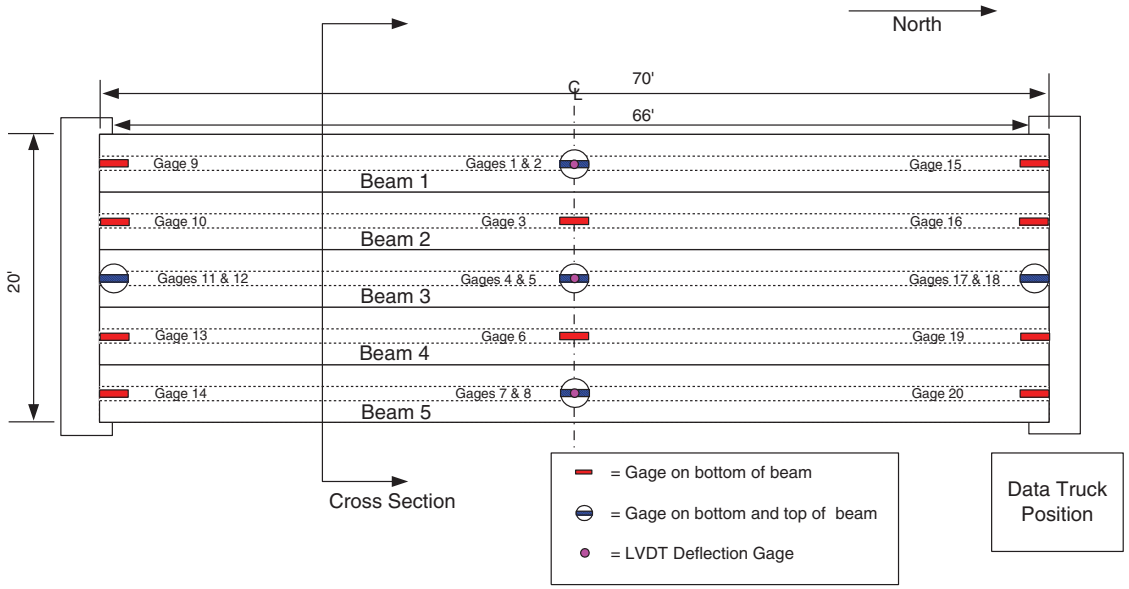

Figure 3. Instrumentation plan

is the steel area required to develop the ultimate capacity of the overhanging portion of the flange. The steel stress f_{su} is estimated using the following equation:

$$f_{su} = f_s' \left(1 - 0.5\frac{\rho f_s'}{f_c'}\right) \tag{4}$$

which is also subject to the condition that the effective prestress after losses is not less than 0.5 f_s'.

Cracking Moment

Cracking moment was calculated using

$$M_{Cracking} = S_b \left[P_e \left(\frac{1}{A} + \frac{e}{S_b}\right) + f_{Cracking}\right] \tag{5}$$

where S_b is the section modulus for the beam bottom, P_e is the effective prestress force, A is the beam cross-sectional area, e is the post-tensioning steel eccentricity, and $f_{Cracking}$ is previously defined.

Maximum and Minimum Steel Percentages

The maximum percentage of steel used in the analysis was 0.3 percent and the minimum percentage was calculated using

$$\rho_{\min} = A_{sr}\frac{f_{su}}{b' \, \mathrm{d} \, f_c'} \tag{6}$$

Feasible Solutions for Initial Prestress Force and Eccentricity

The analysis consisted of determining feasible solutions for the reciprocal of the initial prestressing force and eccentricity

using a linear programming approach. In this approach, the four inequalities relating the reciprocal of the initial post-tensioning force and eccentricity were first formulated, based on satisfying the code requirements for midspan top and bottom stresses under initial and service load conditions, and then plotted to determine the region of feasible solutions. The four inequalities were formulated as follows:

$$
\begin{aligned}
P1(e) &\geq \frac{1}{A \cdot \left(f_{bi} + \frac{M_{DL}}{S_b}\right)} + \frac{e}{S_b \cdot \left(f_{bi} + \frac{M_{DL}}{S_b}\right)} \\
P2(e) &\leq \frac{-1}{A \cdot \left(f_{ti} + \frac{M_{DL}}{S_t}\right)} + \frac{e}{S_t \cdot \left(f_{ti} + \frac{M_{DL}}{S_t}\right)} \\
P3(e) &\leq \kappa \left[\frac{1}{A \cdot \left(-f_{bf} + \frac{M_{Tot}}{S_b}\right)} + \frac{e}{S_b \cdot \left(-f_{bf} + \frac{M_{Tot}}{S_b}\right)} \right] \\
P4(e) &\geq \kappa \left[\frac{-1}{A \cdot \left(-f_{tf} + \frac{M_{Tot}}{S_t}\right)} + \frac{e}{S_t \cdot \left(-f_{tf} + \frac{M_{Tot}}{S_t}\right)} \right]
\end{aligned}
\tag{7}
$$

where P1(e) and P2(e), respectively, were based on satisfaction of midspan bottom and top stresses under initial prestressing force and before prestressing losses take place. P3(e) and P4(e), respectively, were based on satisfaction of midspan bottom and top stresses under final prestressing force and after prestressing losses take place. e is the prestressing steel eccentricity from the center of the beam, A is the beam cross-sectional area, and the rest of the variables have been previously defined. The resulting feasible solutions utilizing the above equations are given by the regions inscribed by the four lines in Fig. 2A and 2B, for the AASHTO HS-20 and H-20 truck loadings, respectively. The solutions in these figures are also bound by the physical constraint that the eccentricity e cannot exceed 18.68 in. (the distance from the neutral axis to the beam's bottom minus 3 in. cover). Two solutions were investigated to account for the possibility that the bridge was originally designed for either of the two AASHTO loads.[1,7,8]

Any combination of initial prestress force and eccentricity (P_i and e) falling in the feasible solution region should result in midspan stresses meeting the allowable stress limits. Using any such combination to calculate the stresses $f_{bi\_}$, $f_{ti\_}$, $f_{tf\_}$, and $f_{bf\_}$ in Eq. (8) below at midspan should result in stresses meeting the requirements of Section B3 on the respective stresses f_{bi}, f_{ti}, f_{tf}, and f_{bf}.

$$
\begin{aligned}
f_{bi\_} &:= \frac{P_i}{A} + \frac{P_i \cdot ec}{S_b} - \frac{M_{DL}}{S_b} \\
f_{ti\_} &:= -\frac{P_i}{A} + \frac{P_i \cdot ec}{S_t} - \frac{M_{DL}}{S_t} \\
f_{bf\_} &:= -\frac{\kappa \cdot P_i}{A} - \frac{\kappa \cdot P_i \cdot ec}{S_b} + \frac{M_{Tot}}{S_b} \\
f_{tf\_} &:= \frac{\kappa \cdot P_i}{A} - \frac{\kappa \cdot P_i \cdot ec}{S_t} + \frac{M_{DL}}{S_t}
\end{aligned}
\tag{8}
$$

Two initial prestress force and eccentricity combinations were selected from each of the solutions in Fig. 2. Analysis was then performed for each of those combinations to determine effective prestress force P_e, area of steel A_s, ultimate moment M_u, factored dead load and live load moments M_{Fact}, cracking moment M_{cr}, the moment available for testing M_{Test} and its resulting midspan stress f_{Test}, and the maximum deflection to be expected during the test Δ. The results of this analysis are shown in Table 1. Maximum deflections were calculated for a concentrated midspan load calculated using the test moment and assuming simply supported end conditions. From this analysis the following observations can be made:

1. As expected, the most economical designs, in terms of area of steel, include combinations of low prestressing forces and large eccentricities. One of those combinations was probably used in the bridge design.
2. All combinations resulted in ultimate moments exceeding factored dead load and live load moments. This makes the graphical solution for initial force and eccentricity combinations plausible.

Midspan instrumentation | Melted ice on day of testing

Figure 4. Mounting strain gages at midspan and a photo of the melted ice 1 week later

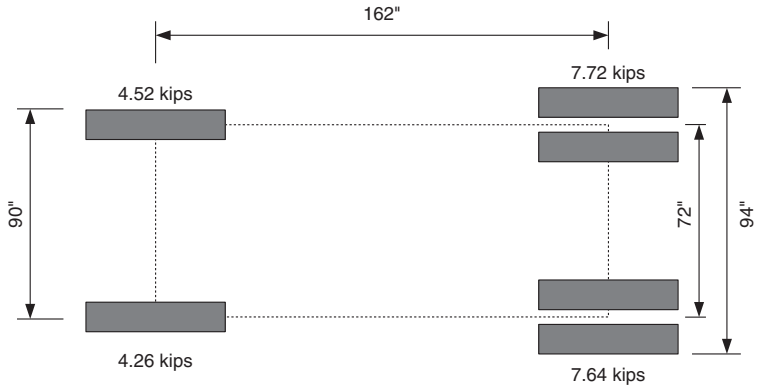

12-Ton Test Vehicle

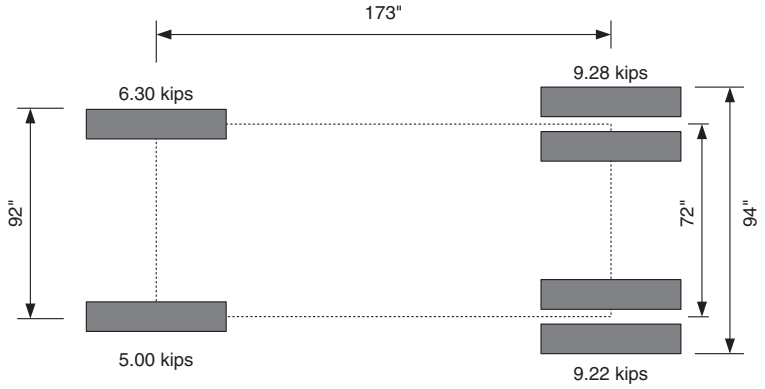

15-Ton Test Vehicle

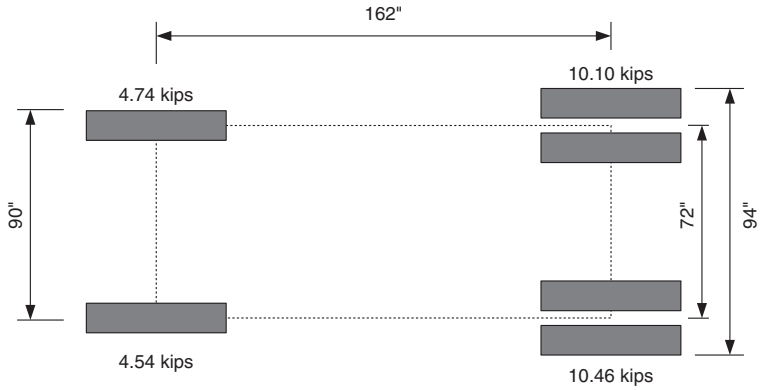

12-Ton Test Vehicle Raised to 15Tons

Test vehicle axle and gross weights

Test Vehicle	Front Axle Wt. (kips)	Rear Axle Wt. (kips)	Gross Vehicle Wt. (kips)
12-ton Truck	8.78	15.36	24.14
15-ton Truck	11.30	18.50	29.80
12-ton Raised to 15-ton	9.28	20.56	29.84

Figure 5. Test vehicle dimensions and wheel and axle loads

3. The lowest moment available for testing is 6.88×10^3 kip-in. (573 kip-ft). This is the moment that would crack a beam if it were fully applied during the testing.

In addition to the above observations, it was also noted that the code requirements on maximum and minimum prestressing steel percentages were satisfied for all four P_i and e combinations.[8]

Instrumentation

The bridge was instrumented at various locations to determine (1) midspan bottom flange stresses for all five beams, (2) level of fixity at the ends of all beams, (3) neutral axis location for the two fascia beams (Beams 1 and 5) and one interior beam (Beam 3), and (4) deflections at midspan of Beams 1 and 5 (fascia beams) and Beam 3.

Strain gages (manufactured by Bridge Diagnostics, Inc.) were used in the instrumentation. Three deflection gages were also planned for midspans of Beams 1, 3, and 5 but were not mounted due to logistics problems. A general-purpose strain gage measurement system, "System 6000" (manufactured by The Measurement Group), was employed for data acquisition. The complete instrumentation plan, including the location of strain gages and proposed LVDT deflection gages, is shown in Fig. 3.

Figure 6. Test vehicle moving into position

At the bridge crossing, the Hannacrois Creek is too deep to use ladders or waders to mount instrumentation at the beams' midspan locations. Additionally, the vertical clearance of the bridge is low. The low clearance combined with the 12-ton posting made use of an under-bridge inspection unit impossible. A decision was made to wait for the river to freeze and instrument the bridge from the ice surface. The thickness of the ice was monitored with an ice drill, and 20 strain gages were mounted on the structure at designated locations (Figs. 3 and 4) from the frozen ice surface. On the day of the testing, warm weather melted the ice and instrumenting the midspans of three girders with deflection gages (LVDTs) was not possible (Fig. 4).

Truck weights and dimensions

Prior to the testing, the test trucks were weighed and axle spacing measured for each truck. When loading the trucks with sand, care was taken to evenly distribute the load in the backs of the trucks. Two trucks were used in the testing—a 12-ton vehicle and a 15-ton vehicle. The loading of the 12-ton truck was increased to 15 tons for the second half of the testing. Dimensions and wheel loads are shown in Fig. 5, axle and gross vehicle weights are also summarized in Fig. 5, and a photo of a test vehicle is shown in Fig. 6. Each of the 15-ton trucks closely resembles an AASHTO H-15 truck.

Load Test Plans

The test plan is divided into four phases based on the loading scenario. Prior to the testing, each scenario was analyzed assuming the structure to be simply supported to determine expected strain levels during the testing. The structure was loaded incrementally by positioning the test trucks in a manner that would gradually increase midspan moment on the structure, while continually monitoring the strain gage readings.

Loading of the structure was calculated to remain below cracking. Inspection reports also did not show cracking in any of the beams. Throughout the load test, the structure was monitored for unexpected cracking, excessive deflection, abnormal strain readings, sensor issues, or other unusual behavior. If the structure did not behave as intended, the load test was stopped immediately. The strategy followed was to proceed to the next phase (increased loading) only when the preceding phase stresses were within expected limits. The following is a full description of the load test plan phases.

Phase 1

The first portion of the testing focuses one axle line of a 12-ton (the current posted weight limit) vehicle on each of the structure's five beams. The vehicle is to cross the bridge at crawl speed, stopping for readings when the rear axle is at each sixth point of the bridge (five readings per load sequence). All crossings begin at the south side of the structure. This phase is expected to reveal relative differences among the beams based on their response to similar loads. Lines indicating the beam centerlines and positions to place the rear axle were painted on the bridge prior to the test date. Illustrations of the truck paths are shown in Figs. 7 and 8. The beams will be tested in the order, Beam 1 through Beam 5. After each beam has been loaded, peak strain readings for each beam will be compared to the estimated safe strain and a decision will accordingly be made to continue with Phase 2 of the testing or not. At the end of this phase of testing, the 12-ton truck will return to a maintenance yard, and the gross weight of the vehicle will be increased to 15 tons.

Phase 2

Phase 2 of the testing uses a 15-ton vehicle that is planned to travel across the bridge at crawl speed stopping with the rear axle at the bridge sixth points for readings. The same

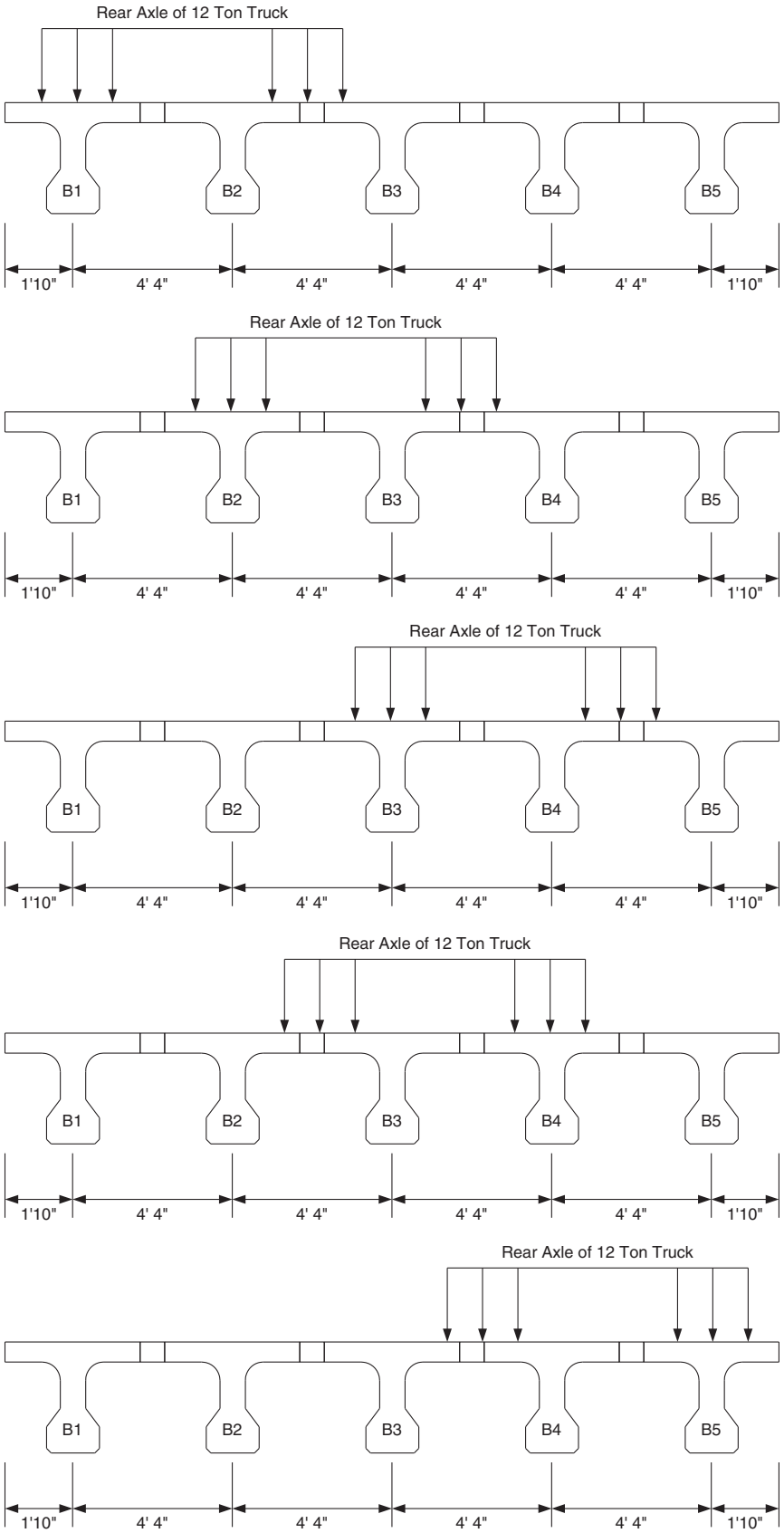

Figure 7. Wheel line locations for Phase 1 (not to scale)

vehicle will cross in the Northbound lane first and then in the Southbound lane. Both crossings begin on the south side of the structure. This phase will provide information on the structure's response for a load slightly higher than

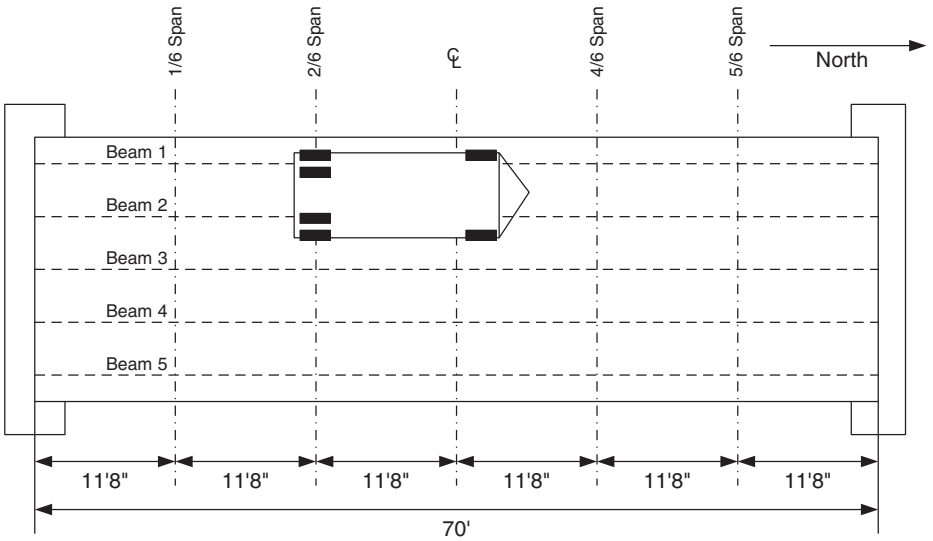

Figure 8. Phase 1 testing. A 12-ton vehicle with a wheel line on Beam 1 is shown stopping at marked locations on the bridge. This is repeated for each beam

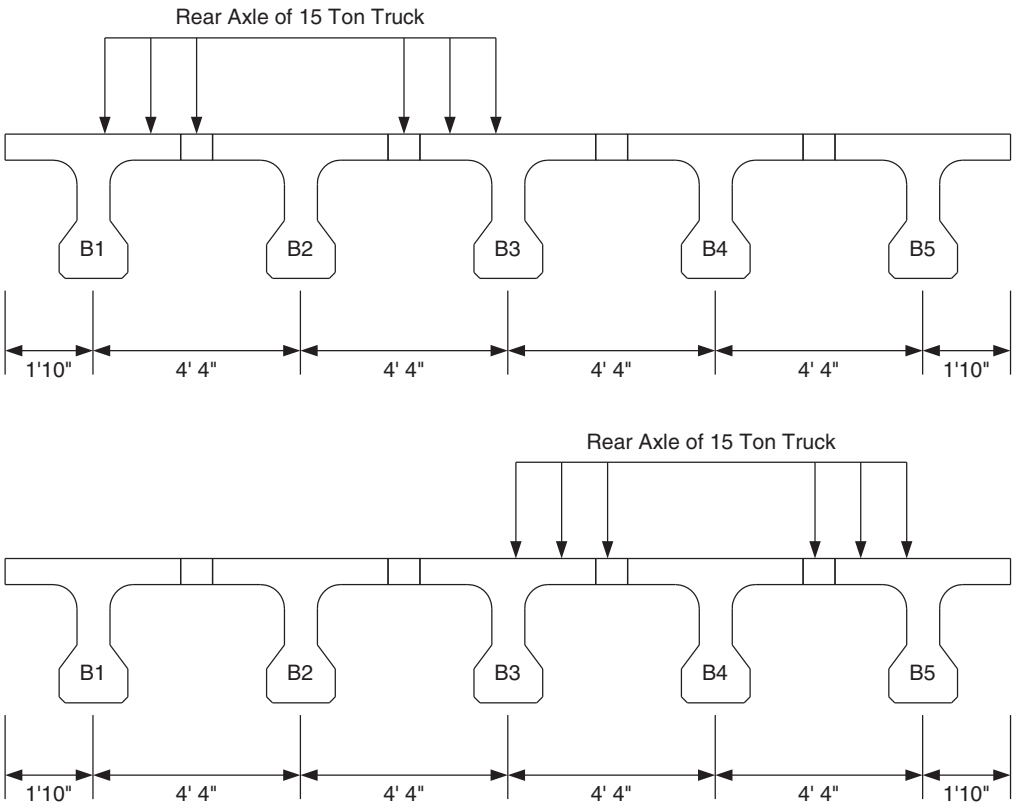

Figure 9. Fifteen-ton vehicle load paths

the posted. The truck paths are shown in Fig. 9. Strain data will be evaluated at each position and if the results are determined to be acceptable, the testing will be continued to Phase 3.

Phase 3

In Phase 3, two 15-ton trucks will be used. The two vehicles will follow each other across the bridge at crawl speeds, without stopping, keeping the following distance between the trucks at approximately 15 ft. The testing will be repeated in the Northbound lane first and then in the Southbound lane. Both crossings begin at the south end of the bridge. This phase will increase the loading on the structure by about 25 percent than that used in Phase 2. Strains will be continuously monitored to determine if the testing should be continued to Phase 4 or not.

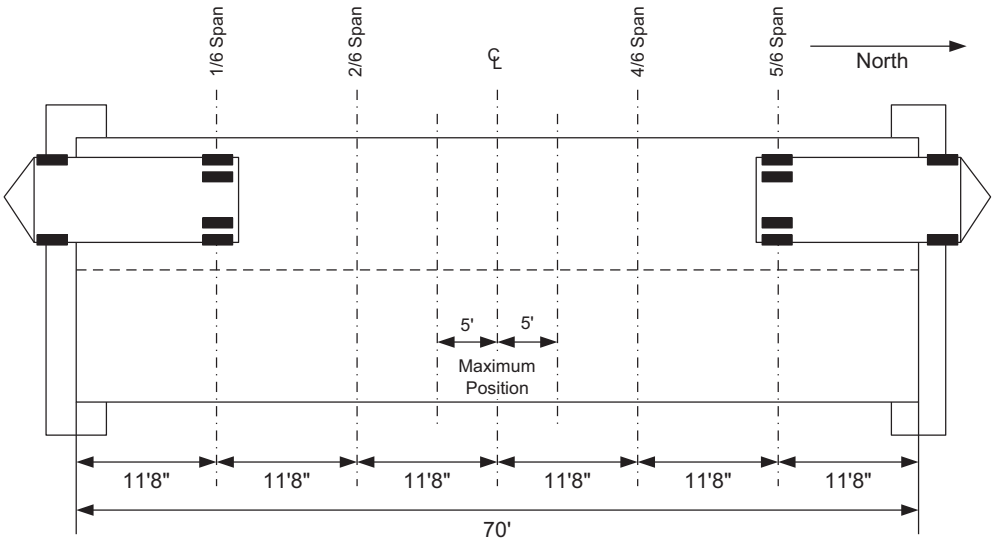

Figure 10. Two 15-ton vehicles back-to-back. (Testing repeated in Northbound lane)

Table 2. Estimated midspan moments and strains on beams during the testing, assuming simply supported end conditions

Test truck	Rear axle position	Predicted bridge moment (kip-ft)	Predicted beam moment (kip-ft)	Predicted strain (με)
12 ton	1/6 Point	197	85	59
12 ton	2/6 Point	319	137	96
12 ton	3/6 Point	365	157	110
12 ton	4/6 Point	223	96	67
12 ton	5/6 Point	93	40	28
15 ton	1/6 Point	246	106	74
15 ton	2/6 Point	398	171	120
15 ton	3/6 Point	456	196	137
15 ton	4/6 Point	287	123	86
15 ton	5/6 Point	117	50	35
Two 15 ton	Following	620	267	187
Two 15-ton back-to-back	1/6 Point	230	99	69
Two 15-ton back-to-back	2/6 Point	568	244	171
Two 15-ton back-to-back	Midspan	763	328	230

Phase 4

The two 15-ton vehicles will be placed back-to-back on the bridge. Testing will begin on the Northbound Lane with the rear axle of each vehicle at a sixth point of the bridge. Strains will be monitored at each step during the test, and if found to be acceptable, the trucks will be brought closer together to the 2/6 span markings, increasing the load effect of the bridge. If the strains at all steps are deemed to be acceptable, the trucks will be brought to a final back-to-back position at midspan to produce the maximum loading that will be applied during the testing. The Phase 4 back-to-back configuration will be repeated in the Southbound Lane. This phase of the testing will produce the highest loading on the structure because the limited bridge width does not allow for a side-by-side testing. The truck positions in this phase are shown in Fig. 10.

Estimated load effects

Prior to the testing, axle spacing for the test trucks was measured (164 in.) and the axle weights had to be estimated. For the 12-ton vehicle, a steering axle weight of 8 kips and a rear axle weight of 16 kips were assumed, and for the 12-ton truck, a steering axle weight of 10 kips and a rear axle weight of 20 kips were assumed. Using a simply supported finite element beam model, gross moments were calculated for each load case and then reduced to the beam level using the AASHTO distribution factor of 0.43. A modulus of elasticity was calculated for concrete based on a 5000-psi compressive strength. Using the estimated modulus, section

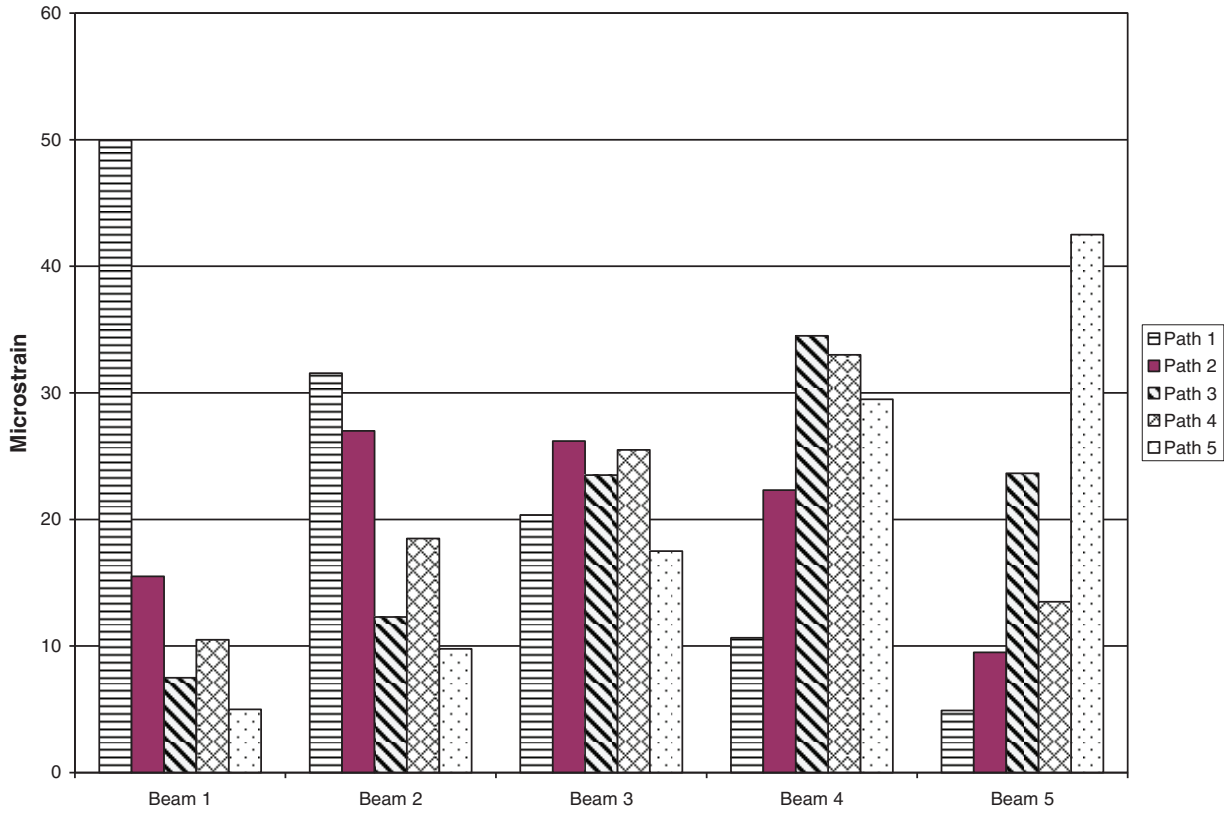

Figure 11. Midspan strain readings for the 12-ton crossings

Table 3. Distribution percentages for the 12-ton crossings

Path number	Beam number				
	1	2	3	4	5
1	42.5	26.9	17.3	9.1	4.2
2	15.4	26.9	26.1	22.2	9.5
3	7.4	12.1	23.2	34.0	23.3
4	10.4	18.3	25.2	32.7	13.4
5	4.8	9.4	16.8	28.3	40.8

properties, and estimated load effects, midspan strain for each load case in the testing was obtained as shown in Table 2.

Analysis of the Test Results

Load distribution

Phase 1 testing included a 12-ton truck aligning a wheel line with each of the five bridge beams. Fig. 11 shows the midspan strains recorded at the midspan point during each truck crossing. In most paths, the beams intentionally being loaded had the peak strain values. The exception is Path 3. In this passing, Beam 4 had the highest peak strain. For Paths 1, 2, and 3 crossings, the driver's side wheel line was placed directly on the beam. For the Paths 4 and 5 crossings, the passenger side wheel load was placed on the beam. Therefore, the Path 3 and Path 4 crossings apply similar loads on Beams 3 and 4. This can be seen in the Phase 1 test plan in Fig. 8. The peak strain in this portion of the testing was 50 με, which is significantly lower than the 110 με predicted in the preliminary analysis.

The percentage of the total moment on the bridge due to the test trucks is calculated by dividing each midspan gage reading by the sum of the five midspan gage readings, assuming all the beams have similar section moduli.

The percentages of the total truck moment carried by each of the beams during the truck crossings at the midspan point are shown in Table 3. As noted earlier, the similarity of Paths 3 and 4 crossings is reflected in the figure. After an on-site review of the low strains and the observed good load distribution, a decision was made to continue with the next phase of the testing.

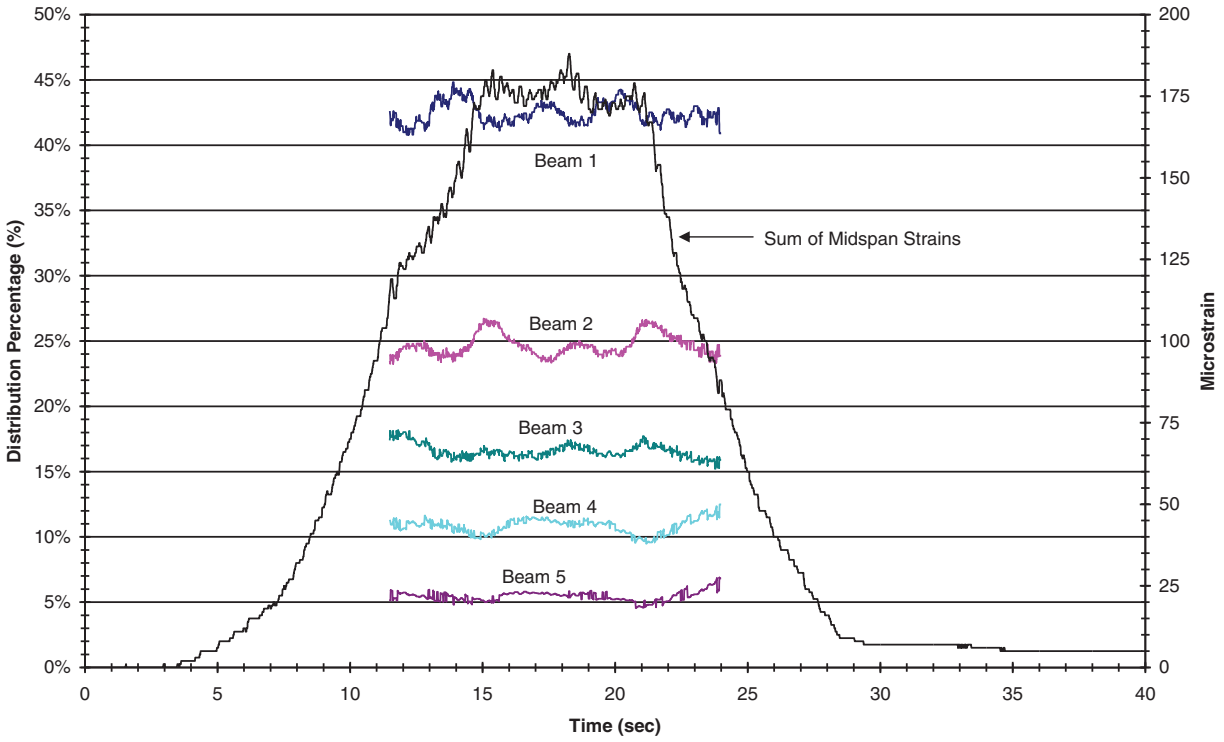

Figure 12. Continuous representation of load distribution percentages for two 15-ton trucks following each other on the upstream lane

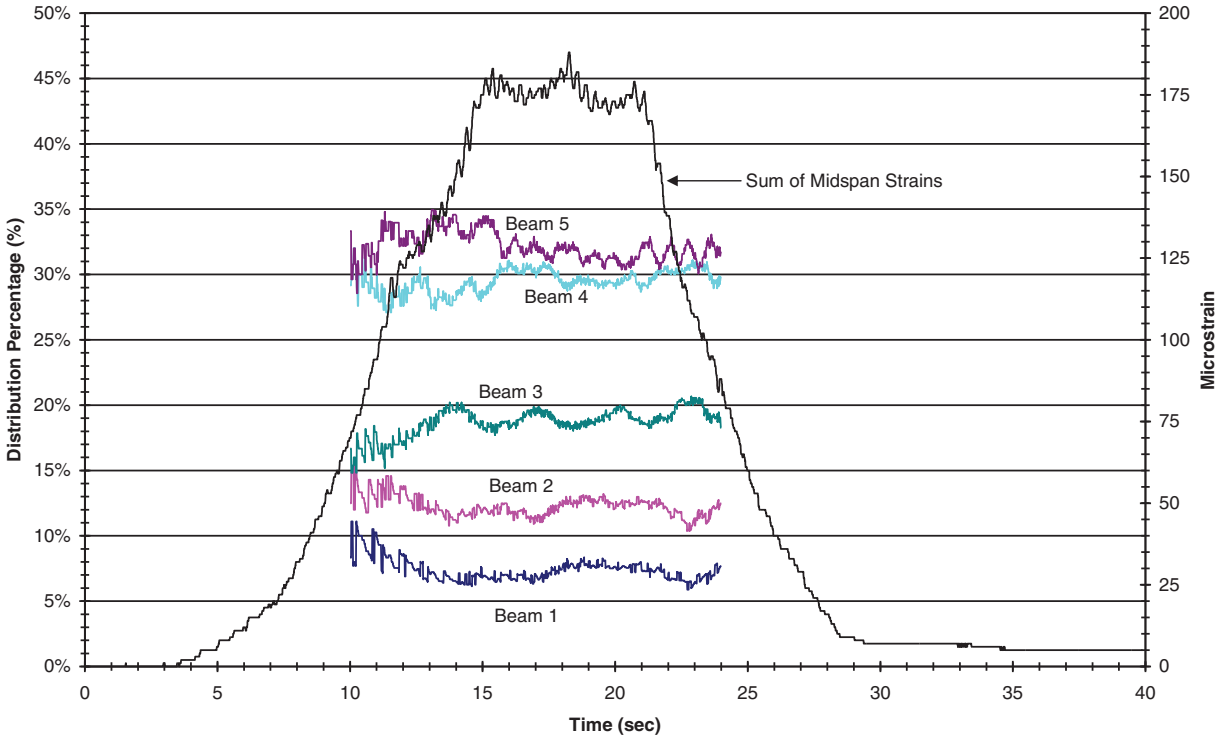

Figure 13. Continuous representation of load distribution percentages for two 15-ton trucks following each other on the downstream lane

Phase 2

The 15-ton truck traveled North twice on each of the upstream and downstream lanes of the structure in this phase. Again, after an on-site review of peak strain readings and the good load distribution between the bridge beams, a decision was made to continue with the next phase of the testing. This phase is intermediary, and for detailed results the reader may refer to.[8]

Figure 14. Icicles from water seeping between beams

Phase 3

This phase of the testing involved two 15-ton trucks following each other at crawl speed without stopping on the structure. The test was repeated on the upstream and downstream lanes, and the time histories for the midspan gages for the two lanes were recorded. Beam moment distribution percentages are obtained using peak strains and are shown in Figs. 12 and 13 using continuous representations. From these figures, Beam 1 is clearly the most loaded beam during the upstream lane crossing, while Beams 4 and 5 were the most loaded beams during the downstream crossing. There are noticeable differences when comparing the time histories and distribution percentages of the upstream and downstream following load cases. The strains under comparable loading measured on Beam 1 are higher than those measured on Beam 5. The highest load percentage calculated from this phase of the testing was also for Beam 1. Several factors could be responsible for these differences. First, the position of the trucks in the lane could have varied. The vehicles could have been very close to the curb near Beam 1 during the upstream crossing and further away from Beam 5 curb during the downstream crossing. Higher strain readings are sometimes indicative of a low section modulus or poor load distribution; however, these are unlikely based on the results of the previous phases. The joints on the sides of both fascia beams, along the closure pours, showed deterioration that allows for water seepage and formation of icicles (Fig. 14). Based on the low strain readings and good load distribution, the testing continued with positioning the two 15-ton trucks back-to-back as planned in Phase 4 testing.

Phase 4

This phase of the testing included loading of the structure on the upstream and downstream lanes, one lane at a time, with two trucks positioned back-to-back and moved in steps towards the bridge midspan. Midspan strain results are shown in Figs. 15 and 16 for the upstream and downstream lanes, respectively. The heaviest load case, "Mid" with the rear axles approximately 5 feet from midspan, places 763 kip-ft in a lane which is greater than an H-20 lane loading for a 66 ft span (clear span). The peak reading under this loading was 117 με and again, it was on Beam 1. Load distribution patterns for all the back-to-back load cases are similar to those found in the earlier testing.[7]

The strain results for the maximum loading position during this phase of testing were used to generate the comparative load percentage plots shown in Figs. 17 and 18, comparing midspan values to those recorded at the beam ends. The end span percentages are generally within 10 percent of those obtained for the midspan location.

Neutral axis location

Gages were placed on the bottom flange at all midspan beam locations, with additional top flange gages placed on Beams 1, 3, and 5. With the distance between the top and bottom gages known (29.5 in.), the neutral axis of the beam was calculated. The neutral axis of the beam estimated based on the beam's dimensions is 21.668 inches from the bottom. Using the data recorded from the static loadings, the average neutral axis locations for Beams 1, 3, and 5 were calculated in Table 4. Using the six back-to-back position results, the neutral axis locations were also calculated for Beams 1, 3, and 5.

Further analysis of the test results revealed that Beam 5 was about 10% weaker/of lesser stiffness than the remaining beams and that the maximum moment recorded during the load testing was about 50 percent of that estimated prior to the testing.[8] Since the beams are similar in geometry, deterioration of the top part of the beam would be a likely explanation of the reduced stiffness and lowered neutral axis location.

End fixity investigation

This was first investigated by studying how the recorded strains on each of the beams related to the truck moments on the structure, assuming simply supported and fixed end conditions. The results of this investigation showed that the beams were acting more like being fixed at their ends than being simply supported. Further investigation to determine the level of fixity at the beam's ends concluded that the bridge experienced 90 and 76 percent fixity at the south and north abutments, respectively.[8]

Load Rating Analysis

Based on the findings presented in the previous section, the following decisions were made:

1. Calculate live load moments using the AASHTO distribution factor (S/5, giving an equivalent percentage of about 43 percent) instead of that determined based on the test results (about 47 percent). The higher test distribution percentage was calculated by combining crossings to derive a percentage based on two lanes being loaded. The narrow bridge width does not allow for the presence of more than one large truck on the bridge. The AASHTO distribution factor agrees well with the field-measured distribution percentage with one lane loaded.

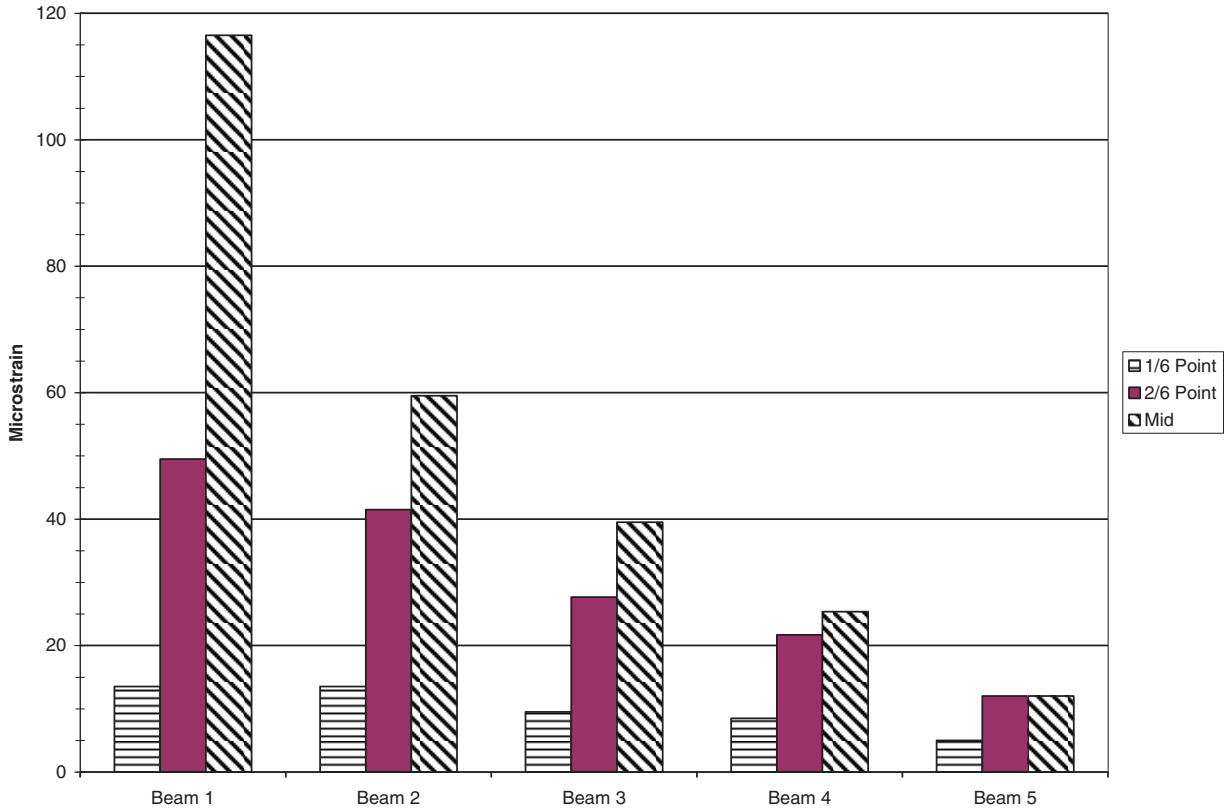

Figure 15. Upstream lane back-to-back midspan strain results

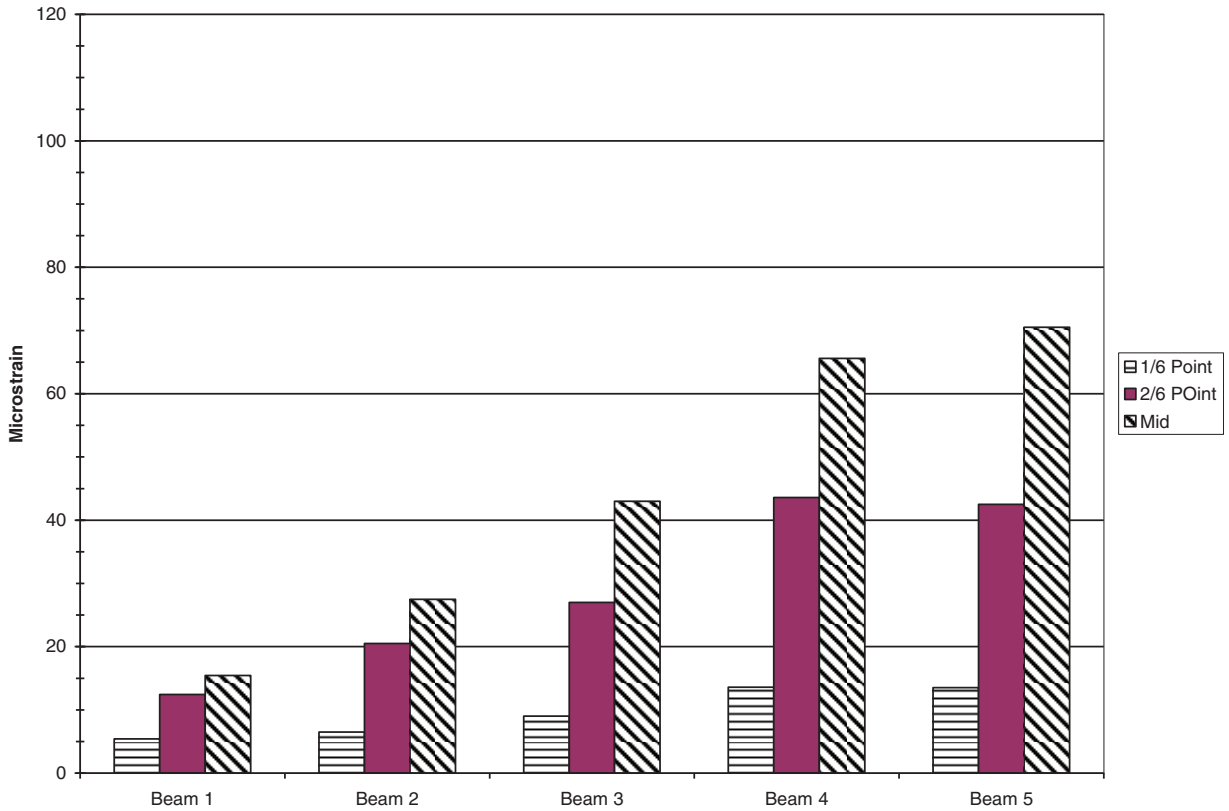

Figure 16. Downstream lane back-to-back midspan strain results

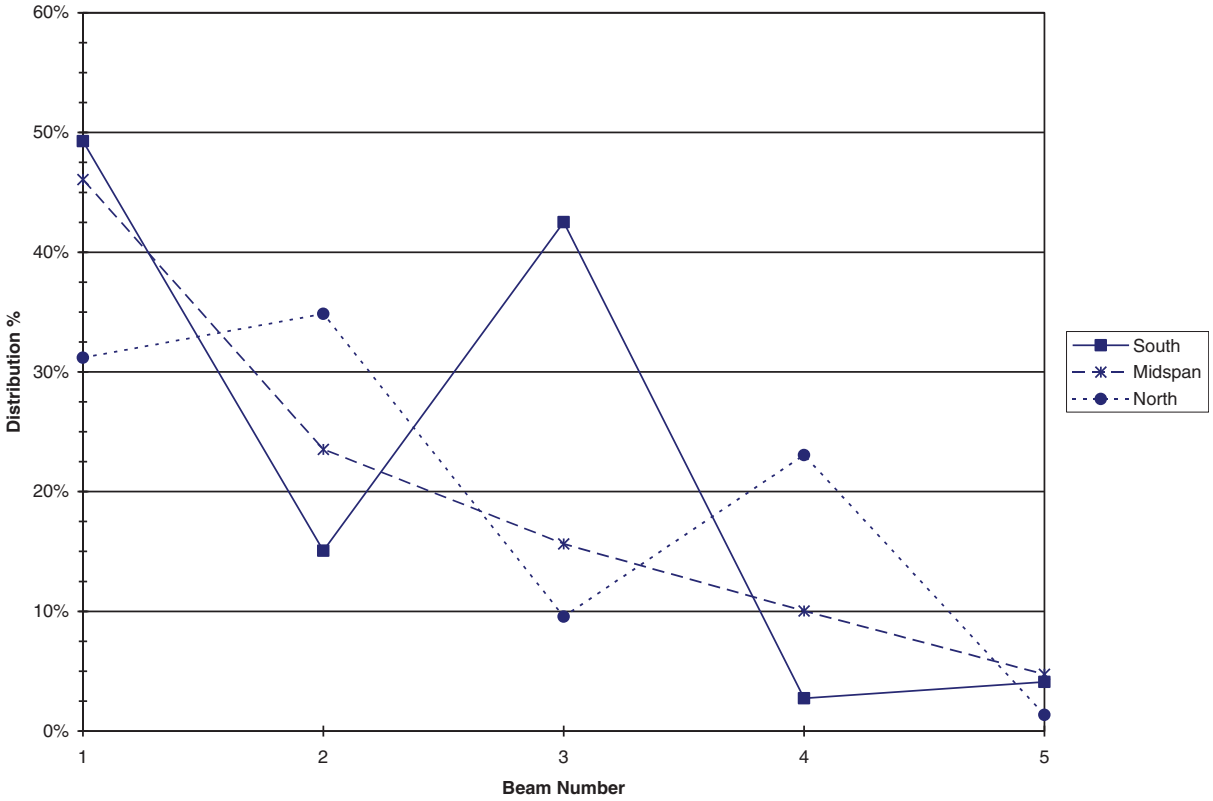

Figure 17. Load distribution percentages: Midspan versus ends for 15-ton truck back-to-back at maximum loading position on upstream lane

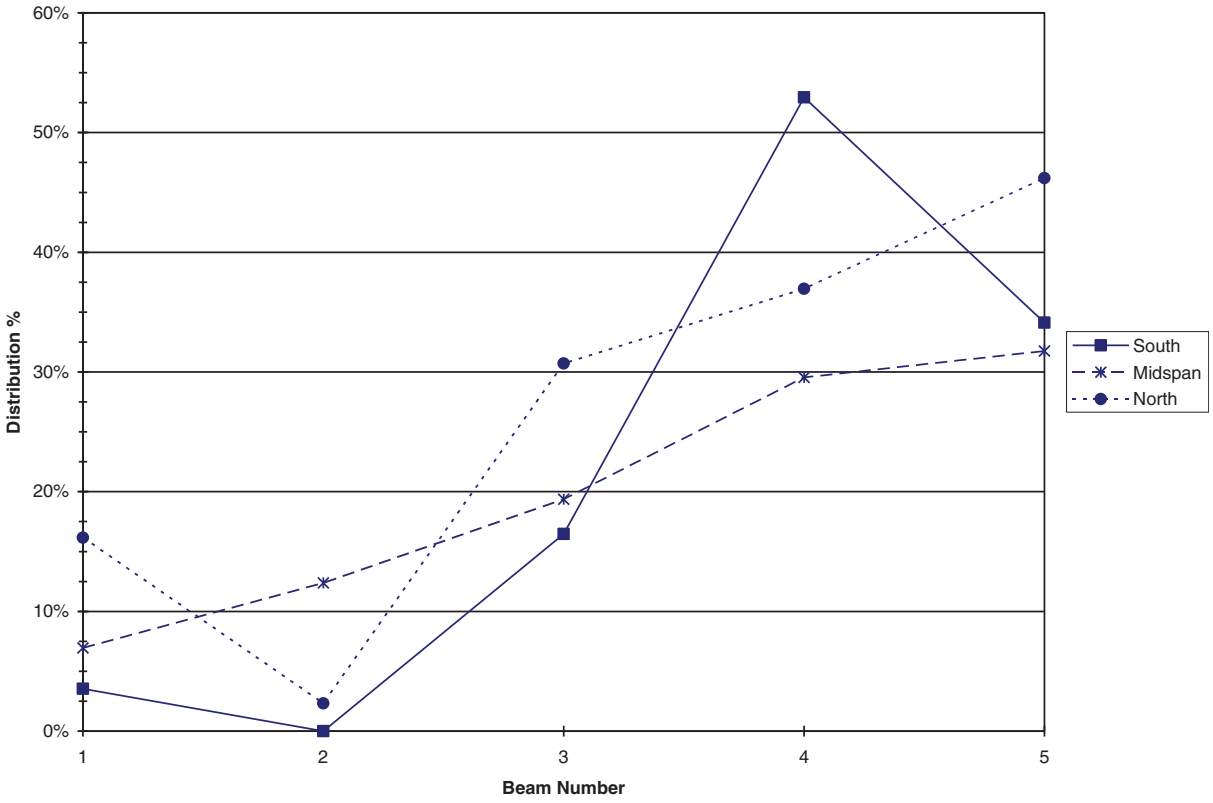

Figure 18. Load distribution percentages: Midspan versus ends for 15-ton truck back-to-back at maximum loading position on downstream lane

Table 4. Average midspan neutral axis locations (measured from beam bottom)

Beam number	Average midspan neutral axis location
1 and 3	22.8 in.
5	19.5 in.

2. Calculate stresses based on a typical (theoretical) section modulus, which is close to that based on the test results.
3. Conservatively ignore fixity in the rating analysis because there is uncertainty in the bridge design, and fixity assumptions may not remain valid at higher loads.

Load rating analysis performed based on the above and identified design parameters resulted in inventory and operating ratings of about 24.6 and 40.8 tons, respectively. The analysis was based on the AASHTO LFD method, including impact. Note that HS-20 and H-20 rating trucks were assumed in the load rating analysis, with each loading scenario accounting for the two possibilities of the bridge being designed using "High P/T" and "Low P/T". See Reference *8* for more information on high and low post-tensioning forces.

Based on the load rating results, the bridge owner was notified of the adequacy of the structure to carry the 15-ton school bus.

Conclusions and Recommendations

This paper introduces a pioneering approach for load rating existing simple-span prestressed concrete bridges with no record plans. To address the data knowledge gap, the approach assumes the structure was originally designed to the minimum AASHTO code requirements applicable at the time of construction. It then uses a linear programming solution to establish feasible combinations of prestressing force and eccentricity information. Finally, it utilizes the results in full-scale load testing to investigate the bridge response to loads and determine parameters for safe and reliable load rating of the structure. The documented approach serves as a proven evaluation tool and has already been validated in subsequent related studies.[9,13]

The paper showed how load testing could be planned and performed, despite the lack of design information about the structure. The incremental approach to the testing and the type of reasoning and analysis described in the paper could be replicated on any simple-span prestressed concrete structure with no plans on record.

The primary findings from the load testing can be summarized as follows:

- a. Load distribution on the structure was excellent and comparable with that estimated using the AASHTO equation.
- b. The theoretical beam section modulus was verified using results based on strain readings from gages mounted to determine neutral axis locations and again from moment-versus-strain results.
- c. The structure was about 90 percent fixed at the south end and about 76 percent fixed at the north end.
- d. An AASHTO LFD load rating was performed using a conservative approach, assuming the structure to be simply supported, the actual AASHTO distribution factor, and the theoretical section modulus, which was very close to that based on the test results.
- The recommended H inventory and operating ratings are 24.6 and 40.8 tons, respectively, and the recommended HS inventory and operating ratings are 40.3 and 67.7 tons, respectively
- e. The structure is more than adequate for carrying a15-ton school bus traffic.

Acknowledegments

Instrumentation and data collection for this project were conducted by George Schongar and Harry Greenberg, previously with the NYSDOT Research Bureau. The coordination and assistance of the Greene County Highway Department staff are gratefully acknowledged. All the views represented in this paper are those of the authors and not necessarily those of the NYSDOT.

References

[1] *Manual for Bridge Evaluation*. 3rd ed. Washington, D.C: American Association of State Highway and Transportation Officials; 2018.

[2] Alampalli S, Hag-Elsafi O. Sensors and instrumentation for bridge testing. *40th International Instrumentation Symposium, Instrumentation Society of America*; May 1994; Baltimore, Maryland, 485–496.

[3] Hag-Elsafi O, Kunin J, Alampalli S. Evaluating effectiveness of FRP composites for bridge rehabilitation through load testing. *Structural Materials Technology: An NDT Conference*; February–March 2000; Atlantic City, NJ, 434–439.

[4] Hag-Elsafi O, Alampalli S, Kunin J. In-service evaluation of a reinforced concrete T-beam bridge FRP strengthening system. *J Compos Struct, Elsevier Sci*. 2004;64(2):179–188. doi:10.1016/j.compstruct.2003.08.002.

[5] Alampalli S, Lund R. Field testing to determine the remaining fatigue life of patroon Island bridge. *ASNT Fall Conference & Quality Testing Show*; November 2004; Las Vegas, NV.

[6] Alampalli S, Hag-Elsafi O. Load testing of bridge FRP applications. *Chapter 40, International Handbook of FRP Composites in Civil Engineering*; September 2013; CRC Press.

[7] *Standard Specifications for Highway Bridges*. Washington, D.C: Association of State Highway and Transportation Officials; 1961.
[8] Hag-Elsafi O, Kunin J. *Load Testing for Bridge Rating: Dean's Mill Over Hannacrois Creek, Special Report 147*. Albany, NY: Transportation R&D Bureau, New York State Department of Transportation; February 2006.
[9] Aguilar CV, Jauregui DV, Newtson CM, Weldon BD, Cortez TM. Load rating a prestressed concrete double T-beam bridge without plans for field testing. In: *Transportation Research Record*. Washington, D.C: Transportation Research Board; 2015.
[10] Shenton HW III, Chajes MJ, Huang J, Load rating of bridges without plans. In: *Final Report DCT 195*. Delaware Center for Transportation, Dover; 2007.
[11] *Bridge Inspection Manual*. Austin, TX: Texas Department of Transportation (TxDOT); 2024.
[12] *ODOT LRFR Manual*. Salem, OR: Oregon Department of Transportation (ODOT); 2018.
[13] Jáuregui DV, Newtson CM, Weldon BD et al. Load rating bridges with no as-built plans or non-engineered bridges. In: *Report NM13STR-01*. 3035 S. Espina Street, Las Cruces, NM 88003: New Mexico State University, Department of Civil Engineering; June 2015.

BER the international journal of bridge engineering management and research

Theory and Application of a Method for Prioritizing Bridge Interventions

Alberto Contardi*

Submitted: 30 April 2026 **Accepted:** 29 June 2026 **Publication date:** 10 July 2026

DOI: 10.70465/ber.v3i3.93

Abstract: This article presents a calculation method developed by the company SINA with the aim of establishing a priority ranking for interventions involving the improvement, upgrading, or demolition and reconstruction of a set of bridges. As a measure of the urgency of an intervention, the "cost of postponement" for the community is proposed, defined as the increased risk associated with maintaining the current state of the structure for 1 year. Following the standard logic of risk analysis, this cost is estimated by multiplying the probability of bridge collapse, calculated over a 1-year period, by all the potential damages that such a collapse would cause.

Although the calculation is affected by several sources of uncertainty, the proposed procedure, based on the collection of a few essential data points and a limited number of simple steps, allows for sufficiently reliable comparisons between bridges. It highlights which characteristics most significantly influence risk and which can reasonably be neglected.

Author keywords: Risk analysis; failure costs; maintenance strategies; damages; aged bridges; priority ranking

Introduction

All calculation tools that enable a managing company to develop, in the most rational way possible, a program of maintenance or improvement interventions for the bridges within its road infrastructure, based on available knowledge of the structures, while minimizing economic resource consumption and maximizing user safety, are generally referred to as BMS (Bridge Management Systems).[1,2,3] The most recent examples of research in the field of BMS focus on the use of artificial intelligence for the preliminary classification of structures.[4–7]

When one of these evaluation methods is applied to the entire set of managed bridges, the result is always a more or less extensive list of bridges requiring intervention, along with an equally extensive list of various types of actions to be carried out on them. For example, in the case where the Italian Bridge Guidelines [CSLLPP[8]] are followed, at the end of the process of progressively increasing knowledge about the structures, a list of bridges classified as "Transitabili" (passable) is obtained. This refers to structures that require upgrading works so that they can be verified according to the currently applicable Technical Standards for Construction.

It should be noted that, in any case, regardless of the decision-making method adopted, the theoretical risk is minimized only when *all* the planned interventions are carried out *immediately*. However, when the workload is such that it makes the immediate execution of all interventions impossible, not only for economic reasons but also due to organizational and management constraints, it becomes necessary to determine which interventions can be postponed so that the associated increase in risk can be considered acceptable. A system is therefore needed to select the intervention program that represents the best compromise between risk reduction and operational management requirements.

This article presents the calculation method developed by the company SINA,[9] published in various papers and currently being tested,[10] with the aim of establishing a priority ranking for structures already classified as "Transitabili" according to the Italian Bridge Guidelines, that is, structures that must soon undergo repair, improvement, or demolition and reconstruction interventions. The method therefore serves as a necessary complement to the regulatory framework and is useful for estimating which structures (already identified for intervention) require more urgent action and which can reasonably tolerate a delay with an acceptable increase in risk.

General Considerations

The basic idea is that it is possible to estimate, for each bridge, the "cost of postponing" an intervention. This cost is represented by the increased risk associated with maintaining the current condition of the structure for another year instead of immediately carrying out the planned works. The higher the estimated cost, the greater the urgency of performing the improvement intervention without delay.

*Corresponding Author: Alberto Contardi.
Email: alberto.contardi@sina.it
SINA S.p.A., Milano, Italy

Discussion period open till six months from the publication date. Please submit separate discussion for each individual paper. This paper is a part of the Vol. 3 of the International Journal of Bridge Engineering, Management and Research (© BER), ISSN 3065-0569.

The estimate is developed by considering a finite number of risk scenarios against which protection is sought. For each scenario, it is necessary to identify a limit state that must not be exceeded, the probability that it may be exceeded within the considered time period, and the material damage to society that would result from exceeding that limit state. The cost of postponement for a single risk scenario is given by the product of the probability that the aforementioned limit state will be exceeded within 1 year and the corresponding theoretical economic damage, as expressed in Eq. (1):

$$C_d = \sum D_j \left(p_j - p_{0j}\right) \tag{1}$$

where C_d is the total cost of postponement, D_j represents the economic damage associated with exceeding the jth limit state, p_j is the probability that the structure in its current condition will exceed that limit state within 1 year, and p_{0j} is the probability calculated for the structure after the planned restoration intervention has been carried out immediately.

Risk Scenarios

The first step is therefore to appropriately select the risk scenarios to be considered. In order for the costs associated with individual scenarios to be simply summed, as in Eq. (1), it is necessary that the scenarios be statistically independent. For bridges with typical characteristics, a reasonable choice could be the following:

- Collapse of part of the deck due to traffic overload.
- Failure of a slab panel due to traffic overload.
- Collapse of one or more piers caused by an earthquake (or by wind, where more significant).
- Collapse of the structure caused by a hydrogeological event.

Further addressing the issue of the statistical independence of the events, it should be noted that, for each scenario, the structural components considered (girders, deck slab, piers, and foundations) are different; they were constructed at different times, using different materials, and, in some cases, by different personnel. Moreover, the external loads are also entirely independent. The only exception concerns the first two events, both of which are related to traffic loads. However, under ordinary conditions, the most critical actions for the verification of the entire deck are generally associated with global load models, such as Load Model 1 of the Eurocode. For deck slab verification, on the other hand, provided that the spacing between girders is not excessively large, the most critical results are more frequently associated with Load Model 2 or other concentrated loads. In other words, the traffic and loading configurations leading to collapse in the two scenarios are generally substantially different and, for the purposes of the proposed method, may reasonably be considered statistically independent. For bridges with very short design spans or with widely spaced girders, a case-specific assessment may be appropriate, and a single traffic-load scenario could be considered instead.

As is well known, the events that cause the greatest number of bridge collapses worldwide are hydrogeological in nature. Unfortunately, however, the literature does not currently provide sufficiently reliable formulations to estimate the probability of bridge collapse due to landslides or floods. Therefore, in this publication, hydrogeological events have not been considered. However, if a planned intervention does not affect the structural resistance to this type of event, it can be observed that the difference $p_j - p_{0j}$ in Eq. (1) for the hydrogeological scenario is equal to zero. Therefore, the cost component associated with hydrogeological events may reasonably be neglected. Conversely, if the set of interventions under comparison includes measures aimed at improving bridge performance with respect to hydrogeological hazards, the collapse probabilities associated with such scenarios should also be evaluated. In these cases, the relevant information available in the specialized literature should be consulted.

Probability of Collapse

Since this calculation is performed at a stage when the decision about which bridges require intervention has already been made, it is assumed that the results of structural assessments are available for traffic loads, as well as for seismic and wind actions. It should be noted that these assessments do not necessarily need to have been carried out using highly sophisticated calculation methods (e.g., finite element analysis). All that is required for the proposed method is, for each of the three considered risk scenarios, the value of the structural resistance R at the most critical section, to be compared with the maximum effect of external loads E at the same section.

It is therefore possible to estimate the probability of exceeding the limit state based on the aforementioned resistance and load effect data, as illustrated in a recent publication by SINA,[11] to which the reader is referred for further details and for the derivation of the formulas. The calculation of the reliability index β, which expresses the probability of exceedance, can be represented by the following relationship:[12]

$$\beta = \beta_C + ln\left(R/E\right)/\sigma \tag{2}$$

where the additional symbols have the following meaning:

- β_C is a constant representing the reliability index when resistance and load effect are exactly equal;
- σ is a parameter expressing the statistical variability of $ln\left(R/E\right)$.

The practical application of Eq. (2) varies depending on the specific risk scenario considered, as described in the following sections.

Since the time period considered is only 1 year and, under ordinary conditions, material deterioration does not progress significantly over such a short interval, the probability of collapse is assumed to remain constant over time and to depend solely on the structural assessments performed with respect to the current condition of the bridge. Conversely, if the deterioration process is progressing very rapidly, the bridge should be excluded from the present prioritization

procedure and immediate intervention should be undertaken without performing further analyses.

It should be noted that the choice of the time interval length—taken here, for convenience, as 1 year but potentially adjustable, provided that it remains within the range of short intervals and thus preserves the assumption that the evolution of the materials' condition state can be neglected—affects the absolute values of the collapse probabilities and, consequently, the final costs, but it does not affect the ranking of the bridges and is therefore not important for the purposes of the present method. It may be appropriate to set it equal to the frequency at which the calculations are periodically updated.

Failure due to traffic loads

In the case of global deck failure caused by traffic loads, the resistance R may be expressed as the bending moment capacity or shear capacity, calculated using the safety factors at the ultimate limit state required by current standards. Following the same logic, the maximum effect of external loads E may be represented by the corresponding bending moment or shear resulting from the most unfavorable traffic load configuration, including the relevant safety factors at the ultimate limit state, again according to current regulations. The section to be considered should clearly be the one yielding the lowest ratio R/E, selected among those of the main load-bearing structures, typically the beams or the entire deck in the case of box girder decks. In the case of local slab failure, the considered actions change, but the reasoning remains entirely analogous.

In calculating the resistance, material degradation must necessarily be taken into account. Since the time period considered for probability evaluation is very short, only 1 year, the deterioration of the bridge over time does not need to be modeled; it is sufficient to consider the current condition.

As for the constant β_C, since in this case the ratio R/E is equal to 1 when the structural resistance exactly meets the requirements of current standards, reference can be made to Eurocode 0,[13] Section B3.2, thus adopting $\beta_C = 3.8$ for a reference period of 50 years.

For the calculation of the statistical variability σ, reference is generally made to the previously mentioned SINA publication.[11] In brief, the parameter σ was calibrated to comply with the requirements of the Italian Bridge Guidelines, which prescribe reduced safety factors γ'_M, γ'_Q, and γ'_G when assessing a structure against a target reliability index of $\beta = 2.8$. Approximating R_d as $R_d \cong R_k/\gamma_M$, it can be demonstrated that the safety factor $(R/E)_{2.8}$ corresponding to a structure with $\beta = 2.8$ is such that $(R/E)_{2.8} \cong \gamma'_M(\gamma'_Q + \rho\gamma'_G)/(\gamma_M(\gamma_Q + \rho\gamma_G))$, where ρ denotes the ratio between permanent and variable loads. Since $\sigma = ln(R/E)/(\beta - \beta_C)$, by setting $\beta = 2.8$, it follows that $\sigma = -ln((R/E)_{2.8})$.

Formula (3) is therefore proposed, as it yields relatively low values and is thus highly conservative:

$$\sigma = -ln\left((1.1\,(1.2 + \rho \cdot 1.16))/(1.15\,(1.35 + \rho \cdot 1.25))\right) \quad (3)$$

Considering a variability of the ratio ρ between 0.5 and 2, the parameter σ ranges between 0.13 and 0.15. In the case of slab verification, ρ can be considered approximately equal to 0, resulting in $\sigma = 0.16$. Fig. 1 shows how the reliability index of the structure varies as a function of the ratios R/E and ρ.

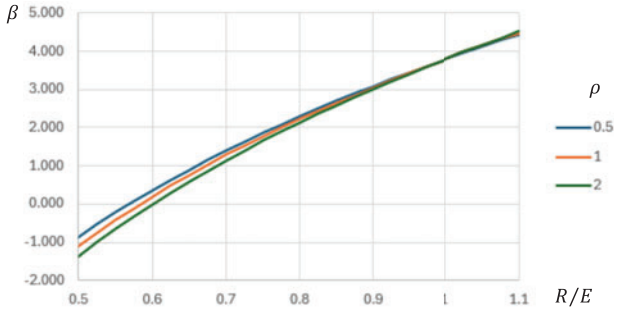

Figure 1. Reliability index as a function of the ratio between resistance and load effect

Recalling that $P = \Phi(-\beta)$, the variation in the probability of collapse, considering a reference period of 50 years, as a function of the ratio R/E is shown in Fig. 2.

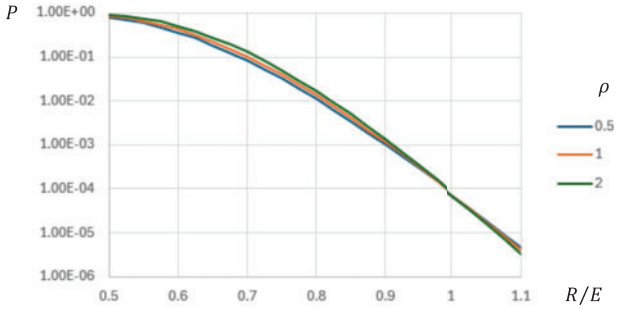

Figure 2. Probability of collapse (50 years) as a function of the ratio between resistance and load effect

The probability over 50 years P is then converted into the probability referring to a single year p using Eq. (4), based on the assumption that all years are equivalent (since only the current state of material degradation has been considered):

$$p = 1 - (1 - P)^{1/50} \quad (4)$$

As can be seen from the graphs and formulas, even a slight reduction in deck resistance leads to a significant increase in the probability of structural collapse, also due to the conservative value assigned to the standard deviation σ. For example, when the ratio R/E decreases from 0.9 to 0.85 (assuming $\rho = 1$), the annual probability of collapse increases from $2.3 \cdot 10^{-5}$ to $8.2 \cdot 10^{-5}$, effectively quadrupling. These values highlight how strongly the assessments presented in this article depend on the accuracy of the structural analyses: even minor approximations or simplifications made "on the safe side" can lead to a significant overestimation of the associated risk.

As an alternative to calculations performed using finite element models, where such models are not available and a

rapid assessment is required, the external load effects may also be estimated using simplified methods, for example, the Courbon method. Similarly, without precise knowledge of reinforcement details or actual thicknesses, the structural resistance may be assumed equal to the load effect corresponding to the requirements of the original design standards. However, when proceeding in this way, the standard deviation σ should be adjusted accordingly to account for the increased uncertainty in the calculation. Nevertheless, for the reasons discussed above and since this method is applied only after gaining sufficient knowledge of the bridges and defining the maintenance strategy, it is recommended not to rely on results that have not been obtained through accurate analyses when determining the ratio R/E.

Failure due to seismic action

In the case of failure of one or more piers caused by horizontal external actions, such as earthquakes or wind, many of the considerations already discussed remain valid. However, seismic actions require specific considerations. In particular, the calculation of the standard deviation σ differs because the uncertainty associated with the computational model is much more significant. Moreover, the standard deviation of ground acceleration is not a fixed value but varies depending on the location.

The total standard deviation can be expressed as the contribution of three main factors, as shown in Eq. (5):

$$\sigma = \sqrt{\sigma_R^2 + \sigma_M^2 + \sigma_a^2} \tag{5}$$

where

- σ_R represents the variability of the structural resistance,
- σ_M represents uncertainties related to mathematical modeling, and
- σ_a is the variability of peak ground acceleration.

Compared to the static case, the second and third contributions take on much higher values, making the first contribution almost negligible, which can be generally assumed as $\sigma_R = 0.1$. Italian standards provide ground acceleration values for their territory with $\sigma_a = 0.4 \div 0.6$. If the reliability of structures with respect to seismic loads must be on the order of $\beta = 3.8$, it can consequently be shown[11] that the modeling uncertainty should be $\sigma_M = 0.5 \div 1.0$, a variability that in design practice is represented by the behavior factor q. Using intermediate values $\sigma_a = 0.5$ and $\sigma_M = 0.75$, we obtain $\sigma = 0.9$, which is significantly higher than the value used for traffic loads. Assuming R/E as the result obtained from a seismic vulnerability analysis, that is, the ratio between the collapse acceleration of the structure and the peak ground acceleration, the variation in the probability of collapse, considering a reference period of 50 years, is as shown in Fig. 3.

It is nevertheless clear, similarly to the static case, how significant the role of uncertainties is.

It should be noted that in the static case the load effect E includes not only traffic loads but also permanent loads, whereas in the seismic case the external action is given solely by forces induced by the earthquake, so the trends shown in Figs. 2 and 3 can be considered similar.

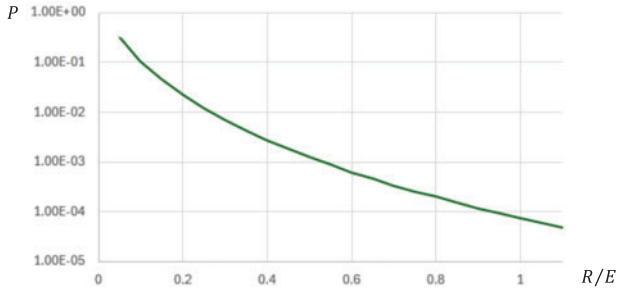

Figure 3. Probability of collapse (50 years) as a function of the ratio between accelerations

Damages

The analysis of damages suffered by society due to possible structural failures of a bridge has also been the subject of a dedicated publication,[14] to which the reader is referred for further details. In this article, only the main concepts are recalled, and above all the practical mathematical steps are presented that allow a credible estimate to be obtained starting from essential data about the structures. It should be noted that, in estimating damages, the aim is not to calculate their exact amount to the nearest unit; given the uncertainties involved, it is sufficient to capture their order of magnitude.

The figures presented in this chapter were calculated for Italy and refer to the year 2016. In particular, the values reported in Tables 1 and 2 may be affected by inflation and, of course, vary from country to country (and potentially also between regions with different economic conditions). For applications in countries other than Italy and in different time periods, it is recommended that the proposed values be adjusted using the international publications from which these data were derived.[15,16] However, for the sole purpose of bridge prioritization, these figures may be used without modification, since the effects of inflation and differing economic conditions are essentially the same for all bridges within a given infrastructure network and therefore do not affect the resulting priority ranking. Moreover, the uncertainties involved are such that corrections of only a few percentage points are unlikely to have a significant impact.

Equation (8), on the other hand, was derived empirically from the analysis of past bridge failure events in Italy. In different social contexts, particularly outside the European Union, where public perception and behavior may differ substantially, the psychological impact and reputational damage may be significantly different from those estimated herein. In such cases, a careful assessment is recommended before applying Eq. (8).

Only the most common cost items are reported here, as some types of damage are so specific that they would require case-by-case evaluation. Typically, when the interruption of the road crossing the collapsed bridge would isolate a town

Table 1. Hourly costs

	Light vehicles	Heavy vehicles
Short distances (<32 km)	13.7 €	56.1 €
Long distances (>32 km)	17.5 €	

Table 2. Congestion costs

	Flow-to-capacity ratio	Motorway	Other roads
Light vehicles	$r > 1.2$	0.223 €	0.452 €
	$1 < r < 1.2$	0.107 €	0.235 €
	$0.8 < r < 1$	0.044 €	0.105 €
Heavy vehicles	$r > 1.2$	0.936 €	1.572 €
	$1 < r < 1.2$	0.452 €	0.815 €
	$0.8 < r < 1$	0.185 €	0.365 €

Table 3. Probability of fatality as a function of height and velocity

v_m [km/h]	0	50	90	110
h [m]	Probability [%]			
2	0	5	63	93
5	1	8	72	95
10	3	18	83	98
15	9	33	90	99
20	18	50	95	100
25	33	66	98	100
30	51	78	99	100
35	66	87	100	100
40	79	94	100	100
45	88	97	100	100
50	94	99	100	100

or even an entire valley (a fortunately rare case), and considering that such an interruption may last several months, a specific study is required since the direct and indirect consequences can be extremely complex to estimate.

It should be noted that it is not necessary to include among the potential consequences those associated with the roadworks required to implement the proposed improvement measure. Since the comparison is made between the scenario in which the intervention is carried out immediately and the scenario in which the same intervention is postponed by 1 year, the construction site is assumed to be essentially identical in both cases. Consequently, any impacts associated with the works, whatever their nature, are the same in both scenarios and therefore do not affect the final result.

Finally, experience gained from analyzing numerous case studies shows that some types of damage, such as reconstruction costs and purely environmental damages, except in very particular cases, are numerically much less significant than the main ones; therefore, they will not be discussed in this article and can generally be neglected.

Estimation of the number of people involved

For obvious reasons, the first and most important evaluation when examining the consequences of a structural failure is the probability that loss of human life may occur in the event of a collapse.

According to the cited publications,[14] two different scenarios must be considered: the first is free-flowing traffic conditions, and the second is a situation in which the entire deck is occupied by stationary vehicles blocked in a queue or traffic jam. The free-flow scenario should be considered when the structural failure event is statistically independent of traffic conditions on the bridge: earthquakes, landslides, or floods do not depend on vehicular traffic and may occur at any time. Therefore, it is assumed that, at the moment the event occurs, traffic is in its most ordinary and typical condition.

Conversely, in the case of failure due to traffic overload, the event occurs (at least theoretically) when the vertical load on the structure is at its maximum. A queue of stationary vehicles, which may occur even on bridges with relatively low traffic volumes, represents the condition with the highest vehicle density and therefore the peak load. Unfortunately, it is also the condition with the greatest number of people present on the bridge.

In the free-flow traffic scenario, it is assumed that a number of vehicles equal to the average daily traffic travels over the bridge at an average speed (a good reference for speed is provided by travel times indicated by navigation systems for the specific road segment). The number of people involved in the collapse is given by Eq. (6):

$$n = ((L + d)/v_m)\,(1.2V_L + V_H)/(24 \cdot 60 \cdot 60) \qquad (6)$$

where L is the length of the portion of the structure involved in the failure, d is the stopping distance, v_m is the travel speed in m/s, V_{L} is the average daily number of light vehicles crossing the bridge, and V_{H} is the average daily number of heavy vehicles. Coefficient 1.2 represents the occupancy factor for light vehicles, while for heavy vehicles it is taken as 1. The stopping distance can be calculated as a function of the average speed by assuming a typical deceleration value of -6.5 m/s^2:[17] $d = v_m^2/13$.

To give a concrete example, the average daily traffic on Italian highways typically ranges between 10,000 and 30,000 vehicles per day. If $V_{\mathrm{L}} = 12000$, $V_{\mathrm{H}} = 3000$ and $v_m = 100\,km/h$, the number of people involved would be $n = 0.0073 \cdot L + 0.43$. For a collapsed length of 100 m, this corresponds to approximately 1.2 people, a relatively low number, despite the significant traffic volume and considerable length considered.

The same formula can be used to estimate the number of people involved when traffic passes beneath the structure rather than above it, as in the typical case of a highway overpass. In this case, L would represent the width of the overpass, generally a small value (usually $10 \div 15$ m).

The scenario involving a traffic queue on the bridge is entirely different. In this case, the empirical Eq. (7) is proposed, developed assuming one lane fully occupied by heavy vehicles (responsible for the overload) and the remaining lanes congested with passenger cars:

$$n = L/25 + 1.2\,(n_c - 1)\,L/10 \tag{7}$$

where, as before, L is the length of the portion of the structure involved in the failure and n_c is the number of lanes indicated by road markings. For roads with 1, 2, or 3 lanes, n is, respectively, $0.04\,L$, $0.16\,L$, and $0.28\,L$. It is clear that for large lengths, the number of people involved can become very significant.

Probability of fatalities

Once the most likely number of people involved has been estimated, it is necessary to determine what would happen to them, depending on the type of limit state considered. First, it should be clarified that in this publication the number of injured people is not calculated, since the associated damages can be considered negligible compared to those related to fatalities. Furthermore, in the case of local failures, such as slab collapse with a relatively small spacing between beams, given the limited extent of the damage, the possibility that such events could cause fatalities is excluded.

In general, it is assumed that, in the event of bridge collapse, the vehicles fall together with the structure. Consequently, the vertical impact velocity of the vehicles against the ground beneath is assumed to be equal to that of the bridge deck, neglecting the deceleration effect resulting from the interaction between the vehicles and the collapsing structure. To this vertical component, a horizontal component v_m is added, corresponding to the speed at which the vehicles were traveling at the instant the collapse began, assuming that the drivers had no time to brake.

For simplicity, by applying the free-fall equation in a vacuum, the impact velocity at ground level is given by $v = \sqrt{v_m^2 + 2gh}$, where h is the height of the bridge deck above ground level. For the scenario in which vehicles are stationary in a traffic queue, the same equation is used, with the assumption that $v_m = 0$.

It is then assumed that the consequences of impact are those indicated by a study published by the National Highway Traffic Safety Administration (NHTSA), part of the U.S. Department of Transportation for frontal vehicle collisions.[18] This is also an approximation, since during the fall each vehicle could overturn in various ways, but these results are considered reasonably applicable. See also[19] for other details. Table 3 and Fig. 4 show the probability that the fall is fatal as a function of velocity and height. The probability for the bridge under consideration can be obtained by interpolating the values in the table.

Let us now consider an example of application of the calculation just described. Consider a three-lane motorway viaduct, 20 m above ground level, consisting of three 30-m spans with a grillage of simply supported beams. Assume that the average daily traffic consists of 10,000 light vehicles and 2,000 heavy vehicles, and that the average speed is 110 km/h.

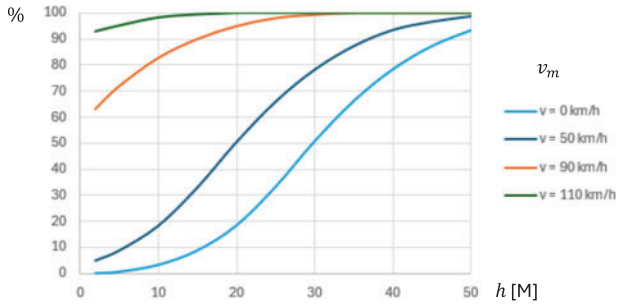

Figure 4. Probability of fatality as a function of height and velocity

For the limit state involving failure of a beam, the collapsed bridge length would be 30 m and the number of people involved would be: $n = 30/25 + 1.2\,(3-1)\,30/10 = 8.4$. Since stationary queued traffic is considered, there would be an 18% probability of fatality, resulting in a total of: $8.4 \cdot 0.18 = 1.5$ potential fatalities. If the bridge were higher, the probability would increase significantly, leading to a much higher expected number of victims. Conversely, traffic volume has no effect.

For the limit state involving collapse caused by an earthquake, it is assumed that the effect of horizontal actions is critical for both piers and therefore that the collapsed bridge length is the entire structure. Thus, $n = \left(\left(90 + 30.5^2/13\right)/30.5\right)(1.2 \cdot 10000 + 2000)/(24 \cdot 60 \cdot 60) = 0.86$. Although the probability of fatality is 100%, the expected number of victims remains approximately half that of the static case.

Finally, for the limit state involving slab failure, $n = 0$ is assumed.

Damages due to the presence of people on the bridge

In this section, an economic value is assigned to the loss of human lives. It is important to note that the aim is not to determine the value of human life, but rather to estimate *how much society is willing to pay* to avoid the risk of fatalities.

The total damage is given by the sum of a fixed compensation per victim and a contribution related to the psychological effect. This effect remains relatively limited when the number of victims is small, but increases exponentially when public perception of the bridge collapse shifts from a *tragic accident* to a *disaster*. The proposed empirical formula is given in Eq. (8), also illustrated in Fig. 5, and is based on experience from events that have occurred in Italy in the recent past:

$$\begin{cases} D = 3250000 \cdot n + 1000000 \cdot (3.523^n - 1) & \text{if } n < 5 \\ D = 3250000 \cdot n + 1000000 \cdot 1800 \log(n-3) & \text{if } n \geq 5 \end{cases} \tag{8}$$

The first part of the equation ($3250000 \cdot n$) was derived from the data published in the "European DG MOVE Handbook on External Costs of Transport".[15] The second part was determined by assigning a value of approximately €2.9

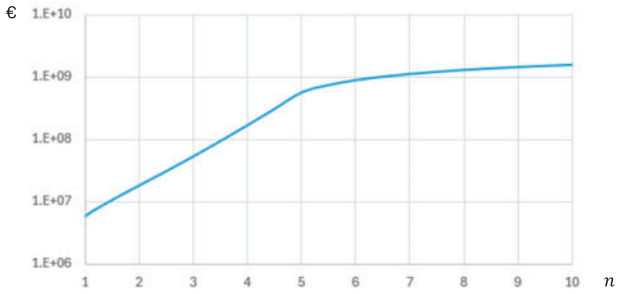

Figure 5. Damages as a function of the number of fatalities

billion to reputational damage—an estimate of the losses incurred by the concessionaire following the 2018 collapse of the Polcevera Viaduct;[20,21]—for $n = 43$, corresponding to the number of fatalities in that accident. Conversely, low values were assigned for $n < 3$, reflecting the observation that in all other bridge failure incidents involving at most two fatalities, no significant reputational damage was observed.

Returning to the previous example, $n = 1.5$ results in slightly more than 10 million euros in damages. From Fig. 5, it is clear that as the number increases, the calculated amount rapidly rises from millions to *billions* of euros, effectively making the postponement of improvement interventions inadvisable.

This effect makes the present method quite similar to what is proposed in Bulletin No. 80 of the FIB,[22] which suggests adopting a minimum reliability index of 2.8 for structures with short spans (less than about 30 meters) based solely on economic criteria, while the index increases rapidly for bridges with longer spans due to considerations related to the protection of human life.

Damages due to service interruption

As highlighted in the previous section, when a potential bridge collapse could result in numerous fatalities, the criterion of safeguarding human life becomes so important that all other considerations become secondary. When the size of the structure is smaller, however, damages caused by the interruption of the road service crossing the bridge also become significant.

Damages due to infrastructure interruption are typically calculated by estimating a daily cost and multiplying it by the duration of the service disruption. With regard to daily costs, the two main components are related to user delays (c_{del}) and traffic congestion (c_{con}), as expressed in Eq. (9):

$$D_{id} = T\,(c_{del} + c_{con}) \tag{9}$$

The time T during which the bridge is expected to remain closed was estimated on the basis of experience gained from past bridge failure events. In particular, it was observed that the total duration can be reasonably approximated as the sum of three distinct components:

- The first part is due to closure imposed by judicial authorities to allow investigations, only in cases where there are doubts about the causes of the collapse. It is proposed to consider 6 months for collapses caused by traffic overload and 0 months for seismic events (as well as hydrogeological events).
- The second part is required for the design of restoration or reconstruction works and for prefabrication of some structural elements. Assuming activities are organized to be completed as quickly as possible, a duration of 1 month is proposed.
- The third part concerns the execution of the works. Assuming maximum speed, the empirical Eq. (10) is proposed, where L is the length of the structure in meters:

$$t_w = 50\,log_{10}L \tag{10}$$

In the previously mentioned example of a motorway bridge 90 m long, the duration (assuming no additional bureaucratic delays) would be $T = 180+30+98 = 308$ days for traffic-related collapses and $T = 30 + 98 = 128$ days for seismic events.

Turning to the evaluation of daily costs, it is assumed that from the time of collapse until the bridge reopens, users will no longer be able to use the collapsed bridge and will have to take an alternative route, resulting in increased travel times and higher traffic on the alternative road. The proposed calculation approach considers these two effects separately; therefore, the increase in travel time is calculated independently of traffic congestion, to avoid double counting.

Drawing on the experience gained in the management of road infrastructure, we hypothesize that, when a road is unexpectedly closed for a short period, most drivers who would normally use it will follow the alternative route suggested by their navigation systems and will choose the same secondary road. For simplicity, it is also assumed that users already on the secondary road do not change their behavior and continue using the same route. This is particularly likely when the road crosses hilly or mountainous terrain, where alternative routes are very limited. However, even in flat areas, the road network is rarely dense enough to provide multiple substantially equivalent routes from which users can choose. As a result, traffic on the selected secondary road increases (being the sum of normal traffic and diverted traffic), while the impact on all other roads is negligible.

The damage due to increased travel time is calculated by summing the contributions of light and heavy vehicles, as shown in Eq. (11):

$$c_{del} = (D_L V_L + D_H V_H)\,(T - T_0) \tag{11}$$

where

- D_L is the hourly cost for a light vehicle (in euros),
- D_H is the hourly cost for a heavy vehicle (in euros),
- V_L is the average daily number of light vehicles crossing the bridge,
- V_H is the average daily number of heavy vehicles crossing the bridge,
- T is the travel time on the original route (before the collapse) (in hours), and
- T_0 is the travel time on the alternative route (before the collapse) (in hours).

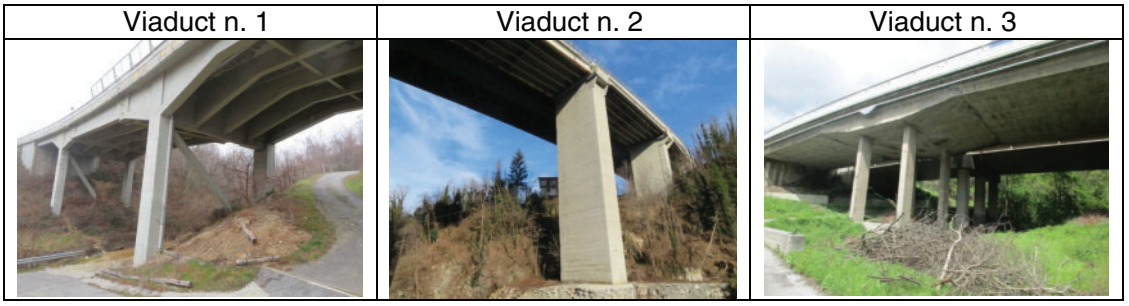

Figure 6. Case studies

Table 4. Congestion costs

				Bridge No. 1	Bridge No. 2	Bridge No. 3
Bridge characteristics						
	Deck length	L_D	[m]	56	508	53
	Maximum height above ground	H	[m]	16	45	16
Road section characteristics						
	Average daily traffic—light vehicles	V_L	[vehicles/day]	6340	8209	8028
	Average daily traffic—heavy vehicles	V_H	[vehicles/day]	1557	1848	1959
	Travel time (without interruption)	T_0	[min]	10	7	16
	Section length		[km]	13	11	17
	Average travel speed	v_m	[km/h]	78	94	64
Alternative route characteristics						
	Average daily traffic—light vehicles	V_{LS}	[vehicles/day]	4000	4000	6500
	Average daily traffic—heavy vehicles	V_{HS}	[vehicles/day]	500	500	550
	Travel time (without congestion)	T	[min]	18	14	24
	Section length	L_{AR}	[km]	13	12	16
	Traffic conditions during bridge closure	r		$> 1.0, < 1.2$	$> 1.0, < 1.2$	$r > 1.2$
		$c_{del} = (17.5V_L + 56.1V_H)(T - T_0)/(60 \cdot 1000)$				
	Delay cost	c_{del}	[k€/day]	26	29	33
		$\begin{cases} c_{con} = L_{AR}(0.235(V_L + V_{LS}) + 0.815(V_H + V_{HS}))/1000 & if\ 1 < r < 1.2 \\ c_{con} = L_{AR}(0.452(V_L + V_{LS}) + 1.572(V_H + V_{HS}))/1000 & if\ r > 1.2 \end{cases}$				
	Congestion cost	c_{con}	[k€/day]	53	57	168
Scenario No. 1: Deck collapse						
	Safety factor	R/E		0.51	0.83	0.69
	Ratio between loads	ρ		1.0	1.7	0.9
		$\beta = 3.8 - \ln(R/E)/\ln((1.1(1.2 + \rho \cdot 1.16))/(1.15(1.35 + \rho \cdot 1.25)))$				
	Reliability index	β		−1.00	2.41	1.19
		$p = 1 - (1 - \Phi(-\beta))^{1/50}$				

Table 4. (Continued)

				Bridge No. 1	Bridge No. 2	Bridge No. 3
	Annual probability of collapse	p		$3.6 \cdot 10^{-2}$	$1.6 \cdot 10^{-4}$	$2.5 \cdot 10^{-3}$
	Length of collapsed deck section	L	[m]	35	35	18
	Total number of lanes (excluding emergency lanes)	n_c		2	2	2
		$n = L/25 + 1.2\,(n_c - 1)\,L/10$				
	Number of people involved	n		5.60	5.54	2.94
	Estimated most probable number of fatalities (probability taken from Table 3)	n_f		0.58	4.85	0.31
		$\begin{cases} D = 3250 \cdot n_f + 1000 \cdot \left(3.523^{n_f} - 1\right) & \text{if } n < 5 \\ D = 3250 \cdot n_f + 1000 \cdot 1800 \log\left(n_f - 3\right) & \text{if } n \geq 5 \end{cases}$				
	Damages due to fatalities (including reputational damages)	D_f	[k€]	2900	463760	1010
		$\mathrm{T}_{SI} = 180 + 30 + 50\,log_{10} L_D$				
	Duration of service interruption	T_{SI}	[days]	297	345	296
		$D_{id} = \mathrm{T}_{SI}\,(c_{del} + c_{con})$				
	Service interruption cost	D_{id}	[k€]	23710	29757	59665
		$C_1 = \left(D_f + D_{id}\right) p$				
	Partial cost of postponement	C_1	[k€]	958	79	152
Scenario No. 2: Deck slab collapse						
	Safety factor	R/E		1.10	1.01	0.96
	Ratio between loads	ρ		0.10	0.10	0.12
		$\beta = 3.8 - \ln(R/E)/\ln\left((1.1\,(1.2 + \rho \cdot 1.16))/(1.15\,(1.35 + \rho \cdot 1.25))\right)$				
	Reliability index	β		4.40	3.87	3.55
		$p = 1 - (1 - \Phi(-\beta))^{1/50}$				
	Annual probability of collapse	p		1.1E-07	1.1E-06	3.9E-06
		$\mathrm{T}_{SI} = 180 + 30 + 60$				
	Duration of service interruption	T_{SI}	[days]	270	270	270
		$D_{id} = \mathrm{T}_{SI}\,(c_{del} + c_{con})$				
	Service interruption cost	D_{id}	[k€]	21554	23288	54424
		$C_2 = D_{id} p$				
	Partial cost of postponement	C_2	[k€]	0	0	0
Scenario No. 3: Piers collapse due to earthquake						
	PGA acceleration ratio	IR		0.53	1.32	1.14
		σ_a		0.44	0.44	0.44

Table 4. (Continued)

			Bridge No. 1	Bridge No. 2	Bridge No. 3
		$\beta = 3.8 - \ln(IR)/\sqrt{0.1^2 + \sigma_a^2 + (1.5\sigma_a)^2}$			
Reliability index	β		3.00	4.15	3.96
		$p = 1 - (1 - \Phi(-\beta))^{1/50}$			
Annual probability of collapse	p		2.7E-05	3.5E-07	7.7E-07
		$n = \left(\left(L_D + \left(v_m^2/13\right)\right)/v_m\right)(1.2V_L + V_H)/(24 \cdot 60 \cdot 60)$			
Number of people involved	n		0.45	2.90	0.58
Estimated most probable number of fatalities (probability taken from Table 3)	n_f		0.36	2.90	0.34
		$D = 3250 \cdot n_f$			
Damages due to fatalities (including reputational damages)	D_f	[k€]	1160	9410	1100
		$T_{SI} = 30 + 50\, log_{10} L_D$			
Duration of service interruption	T_{SI}	[days]	117	165	116
		$D_{id} = T_{SI}(c_{del} + c_{con})$			
Service interruption cost	D_{id}	[k€]	9340	14231	23382
		$C_3 = \left(D_f + D_{id}\right)p$			
Partial cost of postponement	C_3	[k€]	0	0	0
Total cost of postponement		**[k€]**	**958**	**79**	**152**

Using data available in the literature,[15,16] and assuming a traffic composition of 80% commuting/business and 20% personal travel, the proposed hourly costs are those shown in Table 1. Long-distance values should be used for motorway bridges, while short-distance values are more appropriate for local road bridges.

Travel times can be easily assessed using any navigation system by measuring the shortest travel time on the infrastructure under consideration and then forcing the route through the alternative secondary road.

On the selected secondary road, traffic volume increases, and therefore the speed of all vehicles decreases. In addition to the costs due to the longer route, the damage caused by the reduction in speed for all users must also be considered. The proposed formula, similar to the previous one, is Eq. (12):

$$c_{con} = L\left(C_L\left(V_L + V_{LS}\right) + C_H\left(V_H + V_{HS}\right)\right) \quad (12)$$

where

- L is the length of the congested road section (in km),
- C_L is the cost for a light vehicle (in euros),
- C_H is the cost for a heavy vehicle (in euros),
- V_{LS} is the average daily number of light vehicles normally using the alternative road, and
- V_{HS} is the average daily number of heavy vehicles normally using the alternative road.

For the calculation, the appropriate values should be selected from Table 2.

As an example, consider again the 90-m bridge. Assume that the alternative road onto which motorway traffic would be diverted is a 10-km secondary rural road, $V_{LS} = 3000$ and $V_{HS} = 300$, so that the resulting traffic would be more than congested. Also assume that travel times increase from 6 minutes to 15 minutes (the travel time on the uncongested secondary road under ordinary conditions). The resulting values would be: $c_{del} = (17.5 \cdot 10000 + 56.1 \cdot 2000)(15 - 6)/60 = 43080$€ and $c_{con} = 10(0.452(10000 + 3000) + 1.572(2000 + 300)) = 94916$€. Summing these costs, which are obtained under entirely ordinary conditions, and multiplying them by the reconstruction duration of 308 days, the total damage

exceeds 42 million euros. It is therefore clear that the reconstruction cost is, overall, negligible compared with the cost of service interruption.

Case Studies

The practical application of the method was tested through the classification of interventions on a significant number of real bridges. For the purposes of this paper, only the calculations performed for three bridges are presented for brevity shown in Fig. 6, as they are considered sufficiently representative.

All structures carry the same motorway and were built in the 1960s. Following the indications of the Italian guidelines, they were selected for rehabilitation interventions.

The first viaduct is a three-span reinforced concrete beam grillage, with the central deck section supported by Gerber hinges resting on cantilever brackets. The second is a larger bridge, both in terms of length and height, consisting of a grillage of post-tensioned prestressed concrete beams simply supported on the piers. The third bridge has only two spans and consists of a reinforced concrete box girder supported through Gerber hinges on the cap beam of the central pier.

Table 4 reports all calculation steps. The cells highlighted in gray contain the input data, whereas the remaining cells correspond to the calculations described in the previous sections. Given the context in which the bridges are located, environmental damages and damages to any underlying infrastructure were neglected.

For these three example bridges, it is evident that the parameter that most influenced the final ranking was not the exposure to risk, but rather the outcome of the structural assessment. In fact, the intervention on Bridge No. 2 is ranked as the least urgent, even though the consequences of a structural failure would be significantly greater than for the other two bridges. It can be observed that, if for this bridge the R/E ratio, equal to 0.83, were hypothetically 0.72 or lower, priority should instead be assigned to this structure.

It can also be seen that, in this case, the ranking was determined exclusively by the deck performance under traffic loads, whereas resistance to concentrated loads and seismic actions had no influence on the final classification.

Remarks

The estimation of the cost of postponement for each structure, obtained as described in the previous sections, makes it possible to establish a priority ranking of already planned improvement interventions, from the most urgent to those that can reasonably be deferred because the associated risk is sufficiently low.

It should always be remembered that the resulting monetary value has a purely conventional meaning. In other words, the estimated cost can be used in a relative sense to compare bridges with one another, but it cannot be used in an absolute sense to determine the actual cost to society of postponing an intervention. This issue arises not only from the uncertainties involved in estimating the consequences of bridge failure—particularly those related to psychological and social impacts—but, above all, from the choice of the design standards used for the structural assessment. Indeed, the primary requirement of a structural assessment report is that it be defensible, that is, capable of withstanding scrutiny by judicial or administrative authorities should the correctness of the engineer's work be challenged. For this reason, no engineer can disregard compliance with the applicable national regulations, even when less conservative assessment methods may be available in the scientific literature. The Eurocodes, as well as the national technical standards derived from them, were originally developed for the design of new structures rather than for the assessment of existing ones. Their application therefore tends to systematically underestimate the actual performance of existing bridges, as these standards incorporate numerous simplifications and assumptions made "on the safe side." As a consequence, the calculated probabilities of limit-state exceedance are generally much higher than the actual probabilities, and the associated estimated costs are correspondingly inflated.

As with any prioritization process, there is no absolute safety threshold that certifies risk acceptability; therefore, this method cannot be used to justify the decision not to carry out an intervention.

However, the proposed method has the advantage of not requiring projection of structural resistance into the future and therefore does not depend on knowledge of the evolution of material degradation over time. In fact, most bridges older than 50 years are periodically subject to maintenance interventions (such as concrete cover repairs, application of carbon fiber reinforcements, external prestressing, etc.), the long-term durability of which has not been adequately studied. For this reason, degradation models available in the literature, which typically consider only the original materials, are rarely applicable. By focusing solely on the probability of collapse over a 1-year period, the present method avoids these uncertainties.

The proposed procedure requires the collection of only a few essential data and a limited number of simple calculation steps. It enables sufficiently reliable comparisons between bridges, highlighting the characteristics that most strongly influence risk and those that can reasonably be neglected.

References

[1] Brighenti F, Caspani VF, Costa G, Giordano PF, Limongelli MP, Zonta D. Bridge management systems: a review on current practice in a digitizing world. *Eng Struct*. 2024;321:118971. doi:10.1016/j.engstruct.2024.118971.

[2] Brighenti F, Bado MF, Romeo F, Rebellato A, Zonta D. Ranking bridge intervention scenarios with a risk-based predictive decision support system. *Autom Constr*, 2025;180:106553. doi:10.1016/j.autcon.2025.106553.

[3] Diamantidis D, Tanner P, Holicky M, Madsen HO, Sykora M. On reliability assessment of existing structures. *Structural Safety*. 2025;113(2):102452. doi:10.1016/j.strusafe.2024.102452.

[4] Principi L, Morici M, Natali A, Salvatore W, Dall'Asta A. Preliminary fast assessment of bridge risk by neural network. *Int J Disas Risk Reduc*. 2025;116(3):105084. doi:10.1016/j.ijdrr.2024.105084.
[5] Bianchi S, Biondini F. Life-cycle assessment of deteriorating RC bridges using artificial neural networks. *J Infrastruct Syst*. 2022;28(2):686. doi:10.1061/(ASCE)IS.1943-555X.0000672.
[6] Principi L, Morici M, Leggieri V, Dall'Asta A. Mapping seismic risk of existing highway bridges at a regional scale using Artificial Neural Networks. *Int J Disas Risk Reduc*. 2026;132(3):105937. doi:10.1016/j.ijdrr.2025.105937.
[7] Casassa E, Gervasi V, Messina V, Del Carlo F, Natali A, Salvatore W. Data-driven approaches for predicting bridge defectiveness: a machine learning-based assessment of structural and contextual factors. International Conference on Experimental Vibration Analysis for Civil Engineering Structures, Cham: Springer Nature Switzerland; 2025. p. 369–378. doi:10.1007/978-3-031-96106-9_39
[8] Consiglio Superiore dei Lavori Pubblici. Linee Guida per la classificazione e gestione del rischio, la valutazione della sicurezza ed il monitoraggio dei ponti esistenti; 2020. https://cslp.mit.gov.it/circolari-e-linee-guida/linee-guida-la-classificazione-e-gestione-del-rischio-la-valutazione-della.
[9] Contardi A, Pasqualato G, Assessment as to the best strategies for the maintenance of existing bridges. In: *Life-cycle of structures and infrastructure systems*, pp. 2295–2302. London: CRC Press; 2023. doi:10.1201/9781003323020-280.
[10] Vozzi M, Costa G, Contardi A, Brighenti F, Zonta D, Limongelli MP. Decision making in bridge management: comparing the prioritization techniques of two Italian operators, (n.d.). Elsevier's Procedia Structural Integrity; 2026.
[11] Contardi A, Longarini N, Crespi P. Reliability index estimation for existing bridges. In: Cimellaro G P, Zhou Y, Cardoni A, Ansari F, eds. *Resilience, Earthquake Engineering and Structural Health Monitoring. ICONREM 2024. Lecture Notes in Civil Engineering*. Cham: Springer; 2025:770. doi:10.1007/978-3-032-08407-1_11.
[12] Zonta D, Zandonini R, Bortot F. A reliability-based bridge management concept. *Struct Infrastruct Eng*. 2007;3:215–235. doi:10.1080/15732470500315740.
[13] CEN. *EN 1990:2023 Eurocode: Basis of Structural and Geotechnical Design*. European Committee for Standardization; 2023. https://www.cencenelec.eu.
[14] Contardi A, La Fortezza F. Estimation of failure costs of a bridge in Italy. *Int J Bridg Eng Manag Res*. 2025;2. doi:10.70465/ber.v2i2.22.
[15] European Commission: Directorate-General for Mobility and Transport, Ricardo, INFRAS, CE Delft, TRT, Schroten A, Van Essen H, Van Wijngaarden L, et al. *Handbook on the External Costs of Transport: Version 2019*. Publications Office; 2019. https://data.europa.eu/doi/10.2832/27212.
[16] Ministero delle infrastrutture e dei Trasporti. Linee guida per la valutazione degli investimenti in opere pubbliche nei settori di competenza del Ministero delle infrastrutture e dei trasporti, Ministerial Decree 16/06/2017, n. 300; 2017. https://www.mit.gov.it/sites/default/files/media/notizia/2017-07/Linee%20Guida%20Val%20OO%20PP_01%2006%202017.pdf.
[17] Department for transport and driving standard agency. The Highway code; 1999. https://www.gov.uk/browse/driving/highway-code-road-safety.
[18] United States Department of Transportation. *Final Economic Assessment: Tire Pressure Monitoring System*. Washington DC: FMVSS n. 138. USDT, National Highway Traffic Safety Administration; 2002. https://www.nhtsa.gov/sites/nhtsa.gov/files/fmvss/TPMS-2005-FMVSS-No138.pdf.
[19] Wong SM, Onof CJ, Hobbs RE. Models for evaluating the costs of bridge failure. *Proc Instit Civil Eng-Bridge Eng*. 2005;158:117–128. Thomas Telford Ltd. United Kingdom. doi:10.1680/bren.2005.158.3.117.
[20] Autostrade per l'Italia. Relazione finanziaria annuale 2018. 2018. https://www.autostrade.it/documents/10279/4408513/RFA_2018_Gruppo_Autostrade_per_l%27Italia_Deloitte.pdf.
[21] Galvagni L. Atlantia: Chiusa l'epoca Autostrade, venduta a Cassa per 8,1 miliardi. Il Sole 24 Ore - Finanza e Mercati. May 06, 2022. https://www.ilsole24ore.com/art/atlantia-si-chiude-l-epoca-autostrade-venduta-cassa-depositi-81-miliardi-AEa8xfWB.
[22] FIB. *Partial Factor Methods for Concrete Structures*. Switzerland: Fédération internationale du béton; 2016. https://www.fib-international.org/publications/fib-bulletins/partial-factor-methods-for-existing-concrete-structures-detail.html.

BER the international journal of bridge engineering management and research

Transformer-Based Sequence Learning for Multi-Horizon Corrosion Initiation Probability Prediction in Reinforced Concrete Bridges

Yuzhong Huang and Wei Zheng*

Submitted: 04 May 2026 **Accepted:** 01 July 2026 **Publication date:** 10 July 2026

DOI: 10.70465/ber.v3i3.94

Abstract: Chloride-induced corrosion initiation is a major durability concern in reinforced concrete bridges. This study frames corrosion-initiation probability prediction as a multi-horizon sequence-learning problem motivated by the future use of deterioration records, laboratory studies, sensor histories, exposure variables, and published deterioration sequences for infrastructure forecasting.

Because compatible real-world deterioration sequence data are not yet fully organized for this task, a diffusion-based stochastic reliability framework is used to generate controlled simulator-derived corrosion-initiation probability trajectories. These trajectories provide a first-stage proof-of-concept testbed for evaluating whether a temporal fusion transformer (TFT) can organize scenario variables and historical sequence information to predict future probability trajectories.

The results show that the sequence-learning model closely follows the simulator-derived corrosion-initiation probability trajectory within the sampled scenario space and preserves the expected cover-depth ordering. Benchmark comparison under a common sliding-window task shows that gated recurrent units achieved the lowest numerical error in this smooth simulation setting, while TFT remained competitive and provided an interpretable and extensible multi-horizon forecasting structure. MC Dropout further provides an approximate model-level uncertainty estimate for the trained TFT predictor.

These findings support the feasibility of simulation-trained sequence learning for controlled corrosion-initiation probability trajectory prediction, but they do not constitute direct field validation. The contribution is a structured proof-of-concept workflow for organizing historical observations, covariates, future or scenario-defined inputs, benchmark evaluation, and approximate uncertainty quantification. Field validation using bridge inspection records, laboratory deterioration sequences, sensor histories, exposure histories, and maintenance records remains necessary before practical deployment.

Author keywords: Corrosion initiation; chloride ingress; reinforced concrete bridges; sequence learning; temporal fusion transformer; durability assessment

Introduction

Reinforced concrete (RC) bridge infrastructure forms a critical component of modern transportation systems. However, chloride-induced corrosion of embedded steel reinforcement remains one of the primary drivers of structural deterioration and life-cycle cost escalation. Long-term exposure to marine environments and de-icing salts leads to progressive chloride ingress through the concrete cover, eventually initiating corrosion, cracking, and loss of structural capacity.[1–3] Environmental factors such as atmospheric chloride deposition, aerosol transport, and long-term accumulation further influence chloride transport and corrosion development.[4–6] As a result, reliable estimation of corrosion-initiation probability is essential for durability assessment and maintenance planning of RC bridge structures.

Chloride transport in concrete is commonly described using diffusion-based models derived from Fick's second law.[7–9] While these models provide a useful first-order approximation, field observations indicate that long-term deterioration involves more complex interactions, including time-dependent diffusivity, microstructural changes, cracking, and environmental variability.[10,11] In addition, data-driven probabilistic approaches have been increasingly explored to capture environmental influences on deterioration processes.[12] These considerations highlight the limitations of purely diffusion-based formulations and motivate the need for modeling approaches that can account

*Corresponding Author: Wei Zheng. Email: j00411035@jsums.edu
Department of Civil and Environmental Engineering, Jackson State University, Jackson, MS, USA

for multiple sources of uncertainty. Recent developments in chemo-mechanical modeling further emphasize the coupled nature of corrosion-induced damage and transport processes.[13] For bridge-scale and network-level applications, repeated probabilistic evaluation under varying exposure and design conditions can become computationally demanding.

To address uncertainty in deterioration evolution, probabilistic reliability methods have been widely adopted to estimate time-dependent corrosion-initiation probability and structural performance.[14–17] These approaches incorporate uncertainties in material properties, environmental exposure, and structural geometry, and have been extended to include data fusion from inspection and monitoring systems.[18,19] Despite these advances, traditional reliability analyses often rely on repeated stochastic simulations for each scenario, which can limit their scalability for large-scale or network-level infrastructure assessments.[20,21]

Recent studies have emphasized the importance of integrating environmental variables and physical degradation mechanisms into predictive models for improved reliability forecasting.[22] Long-term exposure experiments and durability studies further demonstrate the need to explicitly account for environmental conditions and material behavior in deterioration modeling.[23] In infrastructure asset management, deterioration models play an important role in life-cycle cost analysis and maintenance planning, and system-level modeling frameworks have shown that incorporating probabilistic uncertainty propagation can improve prediction consistency and support decision-making processes.[24–27]

In parallel, data-driven and machine-learning approaches have been increasingly applied to infrastructure deterioration prediction. Neural network-based models and data-driven frameworks have demonstrated promising performance in predicting structural condition and long-term degradation trends.[28–30] Large-scale data analytics and multistate deterioration models further enable improved prediction of infrastructure performance under uncertainty.[31,32] However, many existing machine-learning studies focus on predicting condition states or degradation indicators, rather than directly representing reliability quantities such as corrosion-initiation probability, and they often face challenges related to data quality, interpretability, and generalization across varying environmental conditions.[33]

Advances in probabilistic machine learning and sequence modeling have created new opportunities for representing time-dependent deterioration processes. Techniques such as autoregressive probabilistic forecasting and recurrent neural networks enable distributional prediction under uncertainty.[34,35] More recently, Temporal Fusion Transformers (TFTs) have demonstrated strong capability in multi-horizon forecasting through attention mechanisms and interpretable feature selection.[36] These characteristics make TFT suitable for problems in which the target evolves over time and depends on both static and time-varying inputs.

Real deterioration-related sequence data already exist in bridge engineering practice and research, including inspection histories, component condition ratings, field chloride measurements, corrosion monitoring, structural-health-monitoring records, traffic records, weather and exposure histories, maintenance histories, long-term laboratory corrosion tests, and published experimental deterioration datasets. However, these sources are fragmented, heterogeneous, and not yet organized into a machine-learning-ready multi-horizon sequence format that separates historical deterioration states, static bridge/material/environmental covariates, observed historical external inputs, known or scenario-defined future inputs, and future deterioration targets.

The broader prediction problem motivating this work is long-term bridge deterioration forecasting from accumulated deterioration-status sequences and external impact variables. In future field applications, annual bridge inspection histories, component condition-state records, maintenance records, structural health monitoring histories, weather and climate histories, traffic histories, chloride or marine exposure records, and laboratory or literature-derived deterioration sequences can be organized as longitudinal training data. The present simulator-derived corrosion-initiation dataset is used as a controlled first-stage testbed for developing the sequence-learning structure before such heterogeneous real-world data are cleaned, aligned, and validated for model training.

Accordingly, the prediction accuracy reported in this study represents agreement between the trained sequence-learning model and the stochastic simulator, rather than validation against observed corrosion initiation in real bridges. Direct field validation requires structured data that include bridge identity, inspection dates, deterioration states, material and geometric properties, cover depth, exposure environment, chloride measurements or proxies, traffic and loading histories, maintenance histories, and observed corrosion or deterioration indicators.

Although diffusion-threshold reliability models can generate time-dependent corrosion-initiation probability trajectories, they do not by themselves provide a structured sequence-learning framework that separates historical observations, static bridge/material/environmental variables, known or scenario-defined future inputs, and future deterioration targets. Existing bridge deterioration studies have used inspection data, experimental data, physics-based models, Markov or semi-Markov models, and machine-learning methods, but much of this work focuses on condition ratings, corrosion rates, or state-transition probabilities. The remaining gap addressed here is the lack of a structured, interpretable, and uncertainty-aware multi-horizon sequence-learning framework for future corrosion-initiation probability trajectory prediction.

The TFT was selected because its architecture aligns with this forecasting structure. It separates static covariates, historical observed inputs, known or scenario-defined future inputs, variable-selection mechanisms, temporal attention, and multi-horizon outputs. This organization is useful for future bridge deterioration forecasting, where historical deterioration states, material properties, environmental exposure, traffic loading, and maintenance scenarios may need to be represented jointly. The value of TFT in this

study is architectural alignment with the intended real-data forecasting problem, not a claim of universal numerical superiority over gated recurrent units (GRU) or other sequence models.

Recent studies also show why a TFT-based deterioration forecasting framework requires careful positioning relative to related civil-engineering time-series work. TFT has been used for structural health monitoring and anomaly detection in heritage structures,[37] while Transformer or attention-based models have been explored for pavement skid, texture, and distress deterioration prediction.[38,39] These studies demonstrate growing interest in attention-based civil-infrastructure time-series modeling, but use of a TFT-style framework for scenario-based, multi-horizon bridge corrosion or deterioration probability forecasting remains limited. To the authors' knowledge, prior bridge deterioration studies have not yet widely developed a forecasting structure that explicitly separates long-term historical deterioration states, observed historical external inputs, static bridge or material attributes, known or expected future external inputs, and future deterioration probability outputs within one interpretable multi-horizon model.

Accordingly, this study is positioned as a controlled proof-of-concept sequence-learning framework. Beyond reproducing simulator-derived trajectories, the study evaluates whether a sequence-learning model can learn population-level corrosion-initiation probability trajectories, compares TFT with simpler baseline models under a common forecasting task, identifies dominant physical parameters through Sobol sensitivity analysis, and assesses approximate model-level uncertainty using MC Dropout. These additions clarify the methodological contribution while preserving the limitation that field validation remains future work.

Methodology

Chloride diffusion and stochastic reliability modeling

Chloride-induced corrosion initiation in RC can be formulated as a transport-driven limit-state problem, in which corrosion onset occurs when the chloride concentration at the reinforcement depth exceeds a critical threshold. The overall simulator-to-surrogate workflow used in this study is summarized in Fig. 1. Random material, environmental, and geometric inputs were first sampled to drive a chloride diffusion simulator. corrosion-initiation labels were then generated using a threshold-crossing criterion at the reinforcement depth, and the resulting realization-level labels were aggregated into population-level corrosion-initiation probability trajectories, $P_f(t)$, for surrogate-model training and evaluation.

Diffusion-based models derived from Fick's second law remain a widely used baseline for representing chloride ingress in concrete structures.[8] However, their direct applicability is limited because concrete is a reactive and heterogeneous medium, and the assumption of constant diffusivity is rarely satisfied over depth and time. Experimental and analytical studies further indicate that chloride transport is influenced by ionic interactions, binding effects, and electrochemical processes, motivating the use of effective diffusion parameters rather than intrinsic material constants.[9]

Let $C(x, t)$ denote the chloride concentration at depth x and time t. Corrosion initiation at the reinforcement depth x_{rebar} is described by the limit-state function

$$g(t) = C_{crit} - C(x_{rebar}, t), \tag{1}$$

where C_{crit} is the critical chloride concentration. Corrosion initiation is assumed to occur when

$$g(t) \leq 0. \tag{2}$$

The population-level corrosion-initiation probability is then defined as

$$P_f(t) = P(T_{init} \leq t) = P(g(t) \leq 0), \tag{3}$$

where T_{init} denotes the corrosion-initiation time. This formulation is consistent with probabilistic reliability frameworks for infrastructure systems, in which the temporal evolution of failure probability provides a more informative basis for engineering interpretation than a single deterministic estimate.

The present simulator focuses on chloride-induced corrosion initiation, defined as a threshold-crossing event when the chloride concentration at the reinforcement depth exceeds the critical chloride concentration. Therefore, post-initiation corrosion propagation, rust expansion, cracking, and spalling are not explicitly modeled. Chloride binding, wetting/drying cycles, and temperature-dependent transport are also not resolved explicitly; their potential influence is represented only indirectly through the apparent diffusion coefficient, surface chloride concentration, aging exponent, and stochastic variability of the input parameters.

In practice, chloride transport and corrosion initiation are influenced by multiple uncertain factors, including surface chloride concentration C_s, diffusion coefficient D, concrete cover depth x, and critical chloride threshold C_{crit}. These parameters may vary due to differences in material properties and environmental exposure conditions.

Model-form limitations and measurement uncertainty are acknowledged when interpreting the simulator-derived trajectories. Cracking and variability in material and exposure conditions can significantly affect initiation behavior relative to idealized uncracked assumptions.[11] In addition, uncertainty in chloride content assessment, including variability associated with semi-destructive testing and data processing, influences the calibration and interpretation of transport parameters.[19] These considerations motivate the use of stochastic reliability modeling as a physically grounded approach for generating consistent corrosion-initiation probability trajectories that serve as reference outputs for subsequent data-driven approximation.

Importantly, in the proposed framework, the simulated chloride concentration field $C(x, t)$ is used solely to generate

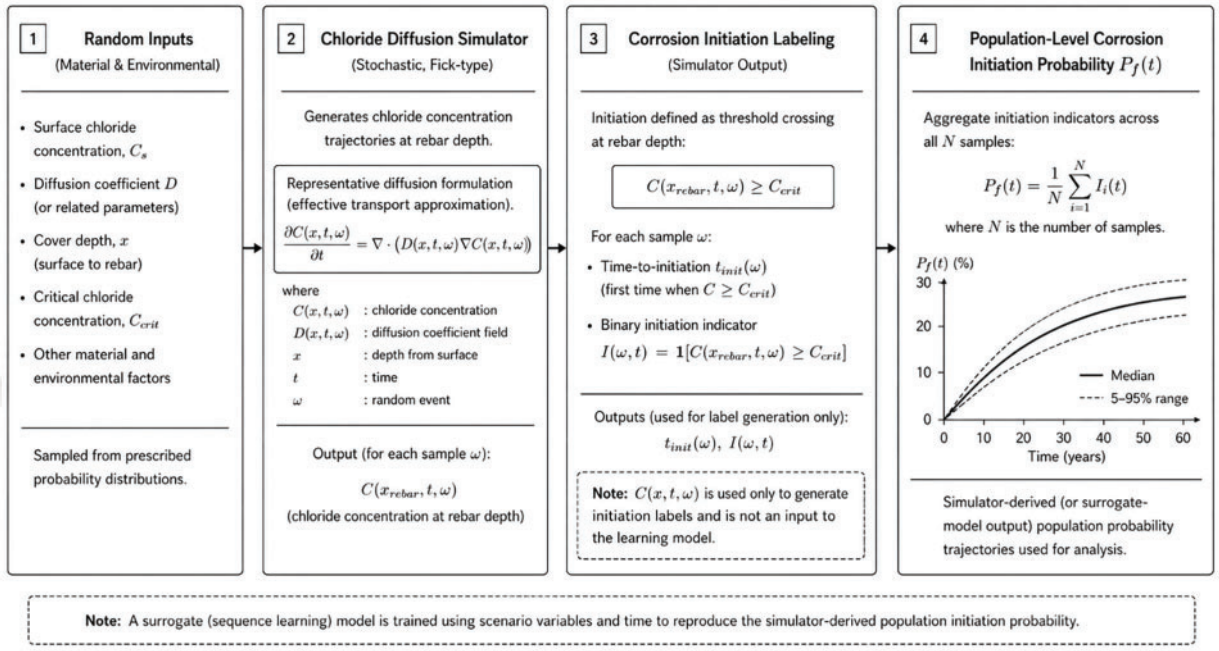

Figure 1. Schematic framework for generating simulator-derived corrosion-initiation probability trajectories $P_f(t)$

corrosion-initiation labels through the threshold condition in Eqs. (1) and (2) and is not provided as an input to the learning model. This design explicitly prevents circularity and ensures that the sequence-learning model learns to approximate population-level probability trajectories from scenario variables rather than reproducing simulator outputs through direct leakage.

Fig. 1 provides an overview of the modeling framework, illustrating the progression from stochastic input sampling to diffusion-based transport, corrosion-initiation labeling, and aggregation into population-level corrosion-initiation probability, $P_f(t)$. Within this framework, chloride concentration fields are generated by a stochastic transport simulator and used only to determine initiation events through the threshold criterion. The resulting simulator-derived probability trajectories define the reference outputs for training.

Any subsequent learning model is trained using scenario variables and time to reproduce this probability evolution, without directly using concentration fields as inputs. This separation between simulator outputs and learning inputs ensures consistency with the underlying reliability formulation and enables the development of a reusable sequence-learning approximation while preserving physically meaningful relationships (Table 1).

Stochastic population simulation

The population simulator generates ensembles of deterioration realizations by sampling uncertain input parameters and mapping each realization to a corrosion-initiation outcome over time. For each simulated element, a diffusion-based transport model produces $C(x_{\text{rebar}}, t)$ over the service-life horizon, and corrosion initiation is defined as the first time at which $C(x_{\text{rebar}}, t) \geq C_{\text{crit}}$. Aggregation across realizations yields an empirical estimate of the population-level corrosion-initiation probability, $P_f(t)$, expressed as the fraction of realizations that have initiated corrosion by time t.

In this study, the stochastic simulator is used as a controlled data-generation mechanism to construct reference probability trajectories for sequence-learning model development, rather than as a direct representation of field-observed corrosion behavior. The simulator-derived trajectories provide a consistent and physically grounded basis for evaluating whether a sequence-learning model can reproduce time-dependent corrosion-initiation probability under uncertainty.

The simulation inputs are sampled from prescribed probability distributions representing material properties, environmental exposure, and structural configuration. The simulation setup includes the service-life horizon, time discretization, number of realizations, and scenario configurations. These parameters are selected to ensure sufficient coverage of the input space while maintaining computational tractability. The full configuration of the simulation and dataset generation is summarized in Table 2.

In addition to representing uncertainty propagation, the simulation framework supports conditional evaluation across representative structural or exposure conditions. For example, stratification by concrete cover depth produces distinct reliability trajectories that reflect the sensitivity of corrosion-initiation probability to transport path length, a dependence that is well documented in chloride ingress design and durability assessment.[14] These stratified responses are used in subsequent sections to assess whether the sequence-learning model preserves physically meaningful relationships.

Table 1. Input variables used in the corrosion-initiation model

Variable	Description	Unit	Distribution	Range
C_s	Surface chloride concentration	kg/m^3	Lognormal	2–6 kg/m^3
D_{28}	Reference diffusion coefficient (28 days)	m^2/s	Lognormal	$1 \times 10^{-12} - 5 \times 10^{-12}$ m^2/s
m	Aging exponent	–	Normal	0.2–0.6
x	Concrete cover depth	mm	Uniform	40–110 mm
C_{crit}	Critical chloride concentration	kg/m^3	Lognormal	0.6–1.2 kg/m^3

Table 2. Simulation and dataset configuration

Item	Value
Service-life horizon	0–60 years
Time step	4 weeks (~0.077 years)
Number of scenario configurations	1000
Number of time steps per series	783
Total dataset size	783,000 rows
Train/validation/test split	700/150/150 series
Approximate row split	548, 100/117, 450/117, 450 rows
Cover-depth range	40–110 mm
Stratified groups	40–60, 60–80, 80–110 mm
Random seed	20250111

To ensure methodological consistency and avoid circularity, the simulator outputs are used only to generate corrosion-initiation labels and aggregated probability trajectories. The underlying chloride concentration field $C(x, t)$ is not used as an input to the learning model. Instead, the sequence-learning model is trained using scenario variables and time to approximate the resulting population-level probability evolution. This separation ensures that the learning task remains aligned with the reliability formulation and prevents information leakage from intermediate simulator states.

The simulator is formulated to remain consistent with both simplified reliability methods and full stochastic simulation-based approaches, which have been compared in corrosion modeling studies and motivate the use of learned approximations for repeated scenario evaluation.[20] By generating large ensembles of physically consistent trajectories, the simulation framework provides a reproducible and computationally tractable basis for training and evaluating sequence-learning models.

The dataset generated in this study consists of population-level corrosion-initiation probability trajectories, $P_f(t)$, associated with sampled input configurations. These trajectories are derived from simulator outputs and serve as reference responses for subsequent sequence-learning model development under uncertainty.

TFT sequence learning model

The learning task is formulated as multi-horizon prediction of simulator-derived population-level corrosion-initiation probability trajectories from historical sequence information and associated covariates. In the present proof-of-concept setting, the sequences are generated by a stochastic diffusion-threshold simulator. In the intended future real-data setting, the same forecasting structure could organize accumulated inspection histories, laboratory deterioration sequences, sensor histories, exposure variables, and maintenance or scenario-defined future inputs for predicting $P_f(t)$.

Within this formulation, the input–output structure distinguishes static variables, historical observed variables, known or scenario-defined future inputs, and future prediction targets. This distinction matters because infrastructure forecasting may require evaluating how future deterioration trajectories change under different exposure, traffic, weather, chloride, or maintenance scenarios. TFT is used because it is directly structured for this kind of multi-horizon forecasting task, although other architectures may achieve lower numerical error in simplified datasets.

This input-role separation is also important when comparing TFT with other sequence models. Markov and semi-Markov models remain useful for condition-state transition modeling, but they are less directly structured for preserving a full historical deterioration path together with time-varying historical and future external inputs. Recurrent models such as recurrent neural networks, GRUs, and long short-term memories can process ordered deterioration histories and remain useful benchmark architectures[40–42]; however, in very long deterioration records they compress past information into hidden states, which may limit retention, interpretation, or selective use of distant time steps.

General Transformer models improve long-range dependency modeling through attention mechanisms[43] and can be adapted to include external covariates. The advantage of TFT for the present research direction is not that other models cannot use such variables, but that TFT provides a forecasting-specific organization for static covariates, observed historical time-varying inputs, known future inputs, variable selection, gating, temporal attention, and multi-horizon outputs.

The model is trained to reproduce the simulator-derived trajectories $P_f(t)$ directly, rather than intermediate state variables such as chloride concentration. Consistent with the data-generation framework described in the previous section, the underlying chloride concentration field $C(x, t)$ is not used as an input to the model, thereby preventing information leakage and ensuring that the learning task remains aligned with the reliability formulation.

Although TFT provides a flexible architecture for interpretable and extensible multi-horizon reliability-trajectory learning, its use is not assumed to imply universal superiority over simpler models. Therefore, additional benchmark models, including pointwise Logistic Regression, Windowed multi-output linear/sigmoid regression, Windowed MLP, and GRU, were included to contextualize predictive performance under the present simulation setting. The benchmark is intended to evaluate the credibility of the forecasting formulation, not to establish that TFT is the best model for every deterioration dataset.

TFT architecture and temporal fusion rationale

The TFT architecture used in this study is based on the TFT framework.[36] TFT separates the forecasting problem into static covariates, historically observed inputs, known future inputs, and future prediction targets. This separation is important for bridge deterioration forecasting because future deterioration probability is not determined only by the past target trajectory; it may also depend on observed historical external conditions and known or scenario-defined future external conditions.

In the present forecasting formulation, the historical observed input window contains two distinct components. The first component is the historical state sequence, which represents the past evolution of the target deterioration or corrosion-initiation state. The second component is the observed historical external input sequence, which represents exogenous variables observed over the same historical period. In addition, the prediction horizon is associated with a known or scenario-defined future external input window. These future external inputs are conditioning variables over the prediction horizon and are not prediction targets. The output of the model is the future corrosion-initiation probability sequence over the forecast horizon.

The term temporal fusion refers to the model's ability to combine multiple categories of time-related information within a unified forecasting architecture. TFT separates static covariates, historical state information, observed historical external inputs, and known future external inputs according to their forecasting roles, and then fuses them through variable-selection networks, static covariate encoders, local temporal processing, static enrichment, interpretable temporal attention, and gated residual components. This design supports future bridge-deterioration applications in which past deterioration states, past external conditions, static attributes, and expected future weather, traffic, exposure, or maintenance conditions may jointly influence future deterioration probability trajectories.

Compared with a general Transformer, TFT is more directly designed for structured multi-horizon forecasting. A general Transformer can be adapted to include external covariates, but the distinction among static covariates, historical observed inputs, known future inputs, and future prediction targets must usually be imposed by the model developer. In contrast, TFT provides built-in mechanisms for this separation through variable-selection networks, static context encoding, recurrent local temporal processing, interpretable self-attention, and gated residual networks. Therefore, the use of TFT in this study is motivated by its forecasting-specific organization of state sequences and external input sequences, not by a claim that TFT is always numerically superior to other sequence models.

The resulting TFT input–output organization is illustrated in Fig. 2. In this study, each supervised sample uses a 52-step historical window and a 13-step prediction horizon. The 52-step historical window includes both the historical target-state sequence and the observed historical external input sequence. The 13-step future horizon includes known or scenario-defined external inputs that condition the forecast. The model then produces a 13-step future target-state sequence representing the predicted corrosion-initiation probability trajectory.

To ensure a fair comparison among the windowed and sequence-learning baselines, Windowed multi-output linear/sigmoid regression, Windowed MLP, GRU, and TFT were evaluated using the same sliding-window forecasting task. A common windowed dataset was constructed using a 52-step historical input window, a 13-step future prediction horizon, and a sliding stride of one time step. These models used the same physical covariates, cumulative corrosion-initiation target, scenario-level train/validation/test split, overlap-averaged inference procedure, population-level aggregation method, and mean absolute error/root mean square error (MAE/RMSE) evaluation metrics.

For benchmark interpretation, Pointwise Logistic Regression was retained only as a simple pointwise linear reference; it does not use a 52-step historical window to predict a 13-step future horizon. The Windowed multi-output linear/sigmoid regression baseline uses the same 52-step historical window and 13-step horizon but remains a fixed-window linear baseline. The Windowed MLP uses the same 52-step history after flattening it into fixed features and can capture nonlinear feature interactions, but it does not explicitly model temporal order through recurrence or attention. GRU processes ordered historical sequences through gated recurrent hidden states and can perform strongly on smooth, low-dimensional simulator trajectories. TFT explicitly separates static covariates, observed historical inputs, known

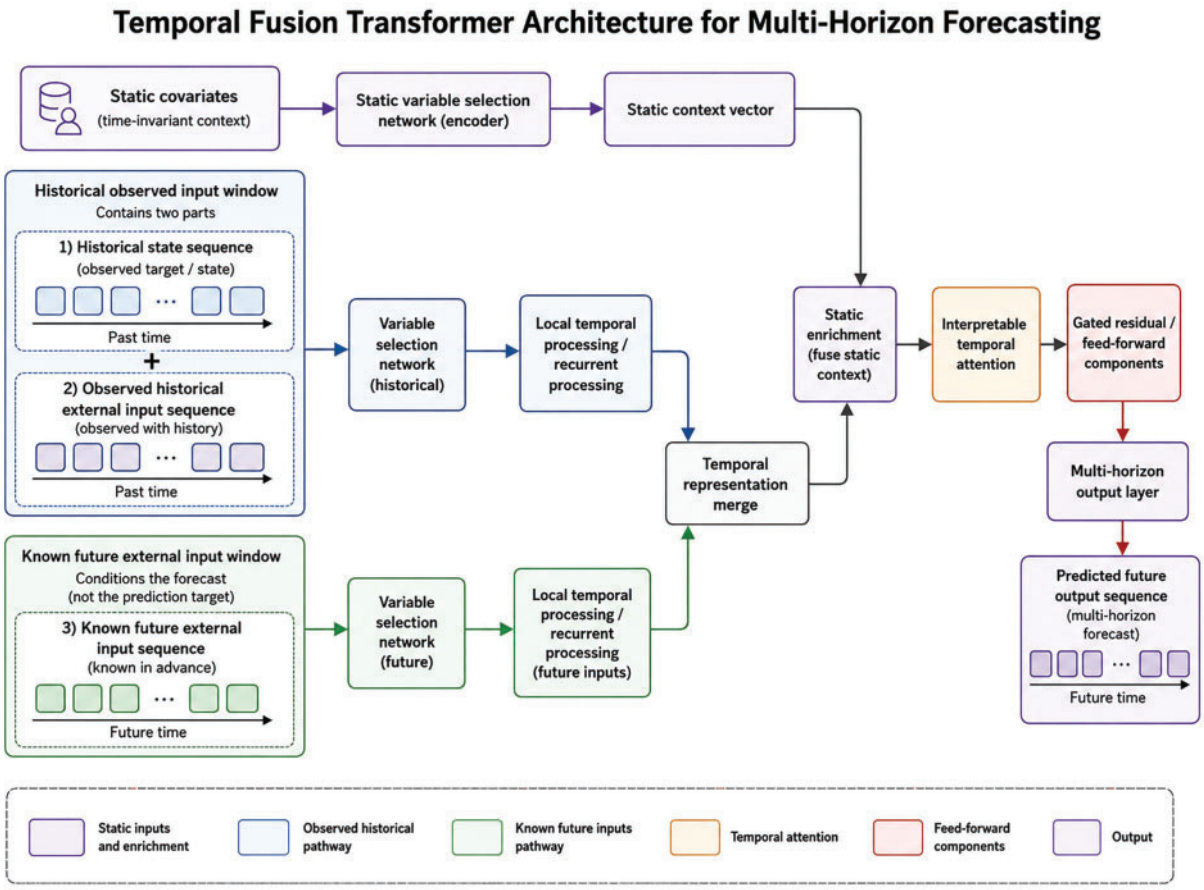

Figure 2. Temporal fusion transformer architecture for multi-horizon corrosion-initiation forecasting. The framework separates static covariates, historical observed inputs, known or scenario-defined future inputs, and multi-horizon probability outputs. Variable selection, temporal processing, static enrichment, attention, and gated residual components support structured sequence-to-sequence prediction

or scenario-defined future inputs, attention, gating, and multi-horizon outputs, which is why it remains structurally important for the intended real-data forecasting problem even when it is not the lowest-error model in this simulation dataset.

The model was trained using an independent series-level split of the simulated dataset, with early stopping based on validation loss to prevent overfitting. The detailed TFT training configuration, including encoder length, prediction horizon, hidden dimension, attention heads, dropout rate, batch size, optimizer, learning rate, number of epochs, and early stopping criterion, as well as train/validation split, is summarized in Table 3.

This setup ensures that the model learns generalizable temporal patterns rather than memorizing simulator outputs. The approach is consistent with probabilistic sequence modeling frameworks that learn conditional distributions for time series under uncertainty; including distribution-oriented forecasting approaches based on quantile representations.[34,35]

The role of physical modeling in this framework is reflected using simulator-generated targets derived from the diffusion-threshold reliability formulation, rather than through explicit enforcement of governing equations during training. In this sense, the sequence model acts as a data-driven approximation of simulator outputs, while remaining consistent with the underlying physical assumptions embedded in the transport-based reliability model. This distinction differentiates the present formulation from physics-informed neural network approaches that aim to infer transport fields directly.[44]

Training and loss design

The training data are constructed from simulated samples of the form $\left(\mathbf{x}, \mathbf{z}_{1:T}, P_f(1:T)\right)$, where $\mathbf{x}$ denotes static covariates, $\mathbf{z}_{1:T}$ represents time-varying covariates, and $P_f(1:T)$ corresponds to the simulator-derived population-level corrosion-initiation probability trajectory over the prediction horizon. Each sample therefore represents a complete trajectory associated with a given scenario configuration, rather than independent point-wise observations, which is consistent with the objective of learning time-dependent reliability evolution.

To explicitly define the learning task and avoid ambiguity regarding variable usage, the input-output structure of the sequence-learning model is summarized in Table 4. In particular, simulator-generated chloride concentration $C(x, t)$

Table 3. TFT model training configuration

Item	Value
Encoder length	52 time steps (∼4.0 years)
Decoder/prediction horizon	13 time steps (∼1.0 year)
Hidden dimension	32
Number of attention heads	4
Dropout rate	0.1
Batch size	32 training/64 inference
Optimizer	Adam
Learning rate	3×10^{-4}
Maximum epochs	10
Early stopping	Validation loss monitored; patience = 3
Data split	Independent series split: 700/150/150
Random seeds	20250111, 20250112, 20250113

Table 4. Input–output definition for the surrogate learning task

Component	Role in study	Used as TFT input?
Surface chloride concentration (C_s)	Environmental variable	Yes
Diffusion coefficient (D_{28})	Material parameter	Yes
Aging exponent (m)	Time-dependent parameter	Yes
Cover depth (x)	Structural variable	Yes
Time (t)	Sequence index	Yes
Chloride concentration $C(x, t)$	Simulator intermediate variable	No (label generation only)
Critical threshold C_{crit}	Initiation threshold	Yes
Population-level $P_f(t)$	Target variable	Predicted output

is used only for label generation and is not included as a model input, thereby preventing information leakage and ensuring that the model does not directly access intermediate simulator states.

The target variable $P_f(t)$ is bounded within [0, 1] and typically evolves smoothly and monotonically over time under fixed exposure conditions. Accordingly, the learning objective emphasizes reproducing stable trajectory patterns while reducing sensitivity to high-frequency fluctuations arising from finite-sample stochastic simulation, which are not directly relevant for population-level reliability assessment.

Model performance is evaluated using trajectory-level error measures, including MAE and RMSE, which quantify deviations between predicted and simulator-derived $P_f(t)$ trajectories. These metrics are adopted as first-stage fidelity measures because the primary objective is to approximate the simulator-defined reliability evolution rather than to perform full probabilistic calibration.

Although quantile-based loss formulations are widely used in probabilistic sequence modeling frameworks,[34,35] they are not explicitly implemented in the present study. Instead, such formulations are referenced only to indicate methodological compatibility, while the current implementation prioritizes deterministic trajectory approximation consistent with the simulator-fidelity objective.

The resulting trained model serves as a learned representation of the stochastic simulation process, providing a reusable approximation for repeated scenario evaluation while maintaining consistency with the probabilistic interpretation of corrosion-initiation trajectories derived from established durability modeling frameworks.[14,15] This formulation enables efficient evaluation across multiple exposure scenarios and structural configurations within the sampled parameter space and supports large-scale screening applications in bridge deterioration assessment.[20]

Experimental Design

Simulation scenario generation

The experimental design is based on a controlled generator of stochastic chloride-ingress scenarios intended to represent dominant sources of uncertainty in chloride-induced corrosion initiation in RC under representative marine aerosol and de-icing exposure conditions. In this study, the simulation framework is used as a controlled environment for evaluating the ability of a data-driven sequence-learning model to reproduce time-dependent reliability trajectories, rather than as a direct representation of field-calibrated deterioration

behavior. Corrosion initiation is formulated as a threshold-crossing event at the reinforcement depth, governed by the temporal evolution of chloride concentration at the bar location. Diffusion-based formulations derived from Fick's second law are used as a baseline representation; however, their underlying assumptions, including constant diffusivity and homogeneous transport, are not strictly satisfied in concrete. Accordingly, diffusion parameters are interpreted as effective transport quantities rather than intrinsic material constants.[8,9]

Each realization in the simulation is defined by a sampled set of material, environmental, and geometric variables. The diffusion model is used to generate chloride concentration histories at the reinforcement depth, which are subsequently used to determine corrosion initiation. In implementation, the scenario generator samples surface chloride concentration C_s, reference diffusivity D_{28} defined at 28 days, an aging exponent m controlling time-dependent diffusivity, concrete cover depth x, and a critical chloride threshold C_{crit}.

The effective diffusivity is modeled as a time-dependent quantity using a power-law aging function,

$$D(t) = D_{28}\left(\frac{t}{t_{\text{ref}}}\right)^{-m}, \tag{4}$$

which reflects the empirically observed reduction in transport rate over time under field conditions and is widely adopted in durability-oriented diffusion modeling.[8,9]

The chloride concentration at the reinforcement depth is evaluated over a discretized service horizon, 0–60 years, using the complementary error-function solution associated with one-dimensional diffusion under constant surface boundary conditions, with $D(t)$ treated as a time-dependent effective coefficient. This formulation provides an analytically tractable approximation while acknowledging model-form limitations and unresolved transport complexities in heterogeneous concrete systems.

Corrosion initiation is defined as the first time at which the computed chloride concentration at the reinforcement depth satisfies

$$C(x_{\text{rebar}}, t) \geq C_{\text{crit}}, \tag{5}$$

and for each realization the corresponding initiation time T_{init} is recorded. A time-dependent binary indicator is then constructed as

$$I(t) = 1(t \geq T_{\text{init}}), \tag{6}$$

where $1(\cdot)$ denotes the indicator function. The population-level corrosion-initiation probability $P_f(t)$ is estimated as the ensemble average,

$$P_f(t) = \mathbb{E}[I(t)], \tag{7}$$

which represents the fraction of realizations that have initiated corrosion by time t.

This probabilistic representation provides a consistent measure of time-dependent reliability for durability-oriented assessment, capturing uncertainty propagation across realizations rather than relying on a single deterministic estimate.[14,15] The formulation also reflects variability arising from heterogeneous transport conditions, cracking effects, and measurement uncertainty, which can influence apparent initiation behavior relative to idealized assumptions.[11] Importantly, the simulation framework preserves the expected monotonic relationship between cover depth and corrosion-initiation probability, providing a physically interpretable reference for subsequent sequence-learning evaluation.

Dataset construction

The learning task is formulated at the population level, while model training is performed using realization-level time series that collectively represent the underlying stochastic behavior of corrosion initiation. Each stochastic realization corresponds to one simulated structural element evaluated over a common discrete time grid associated with physical time t. This formulation allows the sequence-learning model to learn the evolution of population-level corrosion-initiation probability while remaining consistent with probabilistic reliability-based durability assessment frameworks.

For each realization, the dataset is constructed from sampled material, environmental, and geometric parameters, including surface chloride concentration C_s, reference diffusivity D_{28}, aging exponent m, concrete cover depth x, and the critical chloride threshold C_{crit}. These variables define the scenario configuration and are used as model inputs. The chloride concentration field $C(x_{\text{rebar}}, t)$ is generated by the diffusion-based simulator and is used solely to determine corrosion-initiation labels and reference trajectories; it is not included as an input to the learning model, thereby avoiding circularity in the mapping from inputs to outputs and preventing information leakage between the simulator and the sequence-learning model.

Corrosion initiation is represented through a binary indicator that is equal to zero prior to initiation and unity thereafter, and the corresponding population-level initiation probability $P_f(t)$ is obtained as the ensemble mean of this indicator across realizations at each time step, consistent with established probabilistic durability assessment practice.[14,15] The resulting dataset therefore consists of realization-level input variables and associated time-indexed initiation indicators, together with the aggregated population-level probability trajectory used as the reference target.

To examine whether the learned mapping preserves physically meaningful behavior, the dataset is interpreted through both aggregated and covariate-conditioned views. Aggregation across all realizations provides the overall population trajectory. Cover-depth conditioning is examined using finer 10-mm bands in Fig. 3 and summarized using broader intervals, 40–60, 60–80, and 80–110 mm, in Table 6. Because cover depth directly influences chloride transport path length, shallower cover is expected to lead to earlier corrosion initiation and higher values of $P_f(t)$ over a fixed horizon.[14] Preservation of this ordering is treated as a physical consistency check complementary to numerical error metrics.

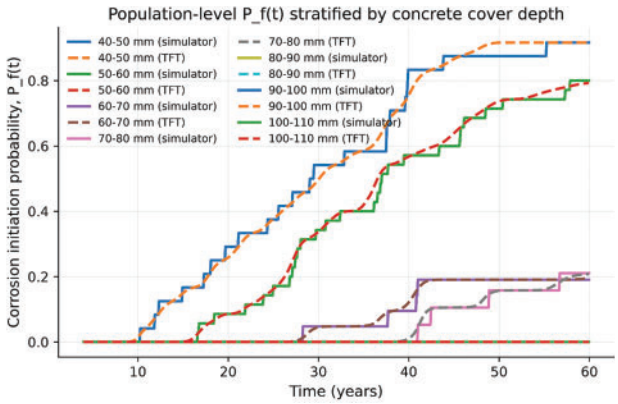

Figure 3. Cover-depth-stratified comparison between simulator-derived and TFT-predicted corrosion-initiation probability $P_f(t)$

Table 5. Population-level prediction accuracy metrics for $P_f(t)$

Metric	Value
Mean absolute error (MAE)	0.004543
Root mean squared error (RMSE)	0.006382
Maximum absolute error	0.024123
Year of maximum error	36.80 years
Final-year error (∼60 years)	0.001347

During inference, the sequence-learning model produces the probability of corrosion initiation at each time step for each realization. Because sequence models operate using sliding decoder windows, multiple predictions may be generated for the same realization-time pair. These overlapping predictions are combined through averaging to obtain a single pointwise estimate. The population-level predicted trajectory $P_{f,\text{pred}}(t)$ is then computed as the mean of these pointwise probabilities across realizations at each time step, mirroring the Monte Carlo estimator used to define the reference trajectory $P_{f,\text{true}}(t)$. This construction ensures that comparisons between predicted and reference curves are performed consistently at the level of the population-level reliability quantity, rather than being influenced by sequence-level prediction artifacts.

Evaluation metrics

Evaluation focuses on how accurately the sequence-learning model reproduces the simulator-defined population-level corrosion-initiation probability trajectory under the controlled proof-of-concept setting. Model accuracy is assessed by comparing the predicted trajectory with the reference trajectory over the full service-life horizon, with errors evaluated on the probability scale. These metrics should be interpreted as simulator-to-model fidelity measures, not as direct field-validation metrics.

MAE and RMSE are adopted as primary performance metrics to quantify trajectory-level agreement between predicted and reference probability curves. These metrics summarize deviations over the full time horizon and are consistent with standard practice when the quantity of interest is a time-indexed reliability function rather than a single endpoint estimate.[15]

To characterize the temporal distribution of discrepancies, the pointwise absolute error is defined as

$$e(t) = \mid P_{f,\text{pred}}(t) - P_{f,\text{true}}(t) \mid, \tag{8}$$

where $P_{f,\text{pred}}(t)$ denotes the model-predicted population-level corrosion-initiation probability and $P_{f,\text{true}}(t)$ denotes the simulator-derived reference trajectory. The temporal evolution of $e(t)$ is analyzed to identify regions where deviations are relatively large. Such localized discrepancies may arise from finite-sample Monte Carlo variability in the reference trajectory and increased sensitivity of $P_f(t)$ during periods of rapid change.

In addition to accuracy, computational performance is evaluated by comparing inference-time runtime between two evaluation procedures defined within the same simulation framework. The first corresponds to repeated stochastic simulation, in which corrosion-initiation probability is estimated through Monte Carlo sampling for each scenario configuration. The second corresponds to learned-model inference, where the trained model directly maps input variables and time to the probability trajectory without repeated simulation. The comparison therefore isolates differences between simulation-based evaluation and learned-model inference, rather than post-processing steps.

The computational comparison is interpreted as an inference-stage advantage, recognizing that model training incurs an upfront computational cost. Once trained, the trained model provides a consistent approximation to the simulator-defined mapping while enabling efficient evaluation across a large number of scenarios. This trade-off is particularly relevant for network-level screening and reliability assessment tasks that require repeated evaluation under diverse configurations.[20,21]

Taken together, the evaluation framework assesses trajectory fidelity, physical consistency, benchmark context, approximate model-level uncertainty, and conditional computational reuse. It does not establish universal acceleration over physics-based simulation or field-ready bridge deterioration prediction.

Global sensitivity analysis

To quantify the influence of major physical input parameters, a variance-based Sobol global sensitivity analysis was conducted using the same diffusion-threshold corrosion-initiation model and locked input distributions used for dataset generation. The analyzed parameters were C_s, D_{28}, m, concrete cover depth x, and C_{crit}. Saltelli sampling with a base sample size of 2,048 generated 14,336 model evaluations. Sensitivity indices were computed at 20, 40, and 60 years using the smooth limit-state margin $C_{rebar}(t) - C_{crit}$ as the primary response. A binary corrosion-initiation response

was also evaluated as a supplemental check. First-order S_1 and total-order S_T indices were reported.

Uncertainty quantification using MC Dropout

To quantify the predictive uncertainty of the trained TFT model, MC Dropout was used as a practical approximation for uncertainty quantification. Dropout was originally introduced as a regularization method for reducing overfitting in neural networks.[45] The theoretical foundation of MC Dropout is provided by Gal and Ghahramani, who showed that dropout can be interpreted as approximate Bayesian inference in deep neural networks.[46] During inference, dropout layers were kept active while the remaining model components were retained in evaluation mode. Under identical input conditions, repeated stochastic forward passes were performed using the trained TFT checkpoint. Because each forward pass uses a different dropout mask, the model produces a slightly different corrosion-initiation probability trajectory. The resulting ensemble of predictions was treated as an empirical predictive distribution of $P_f(t)$.

From this predictive distribution, the predictive mean, predictive standard deviation, empirical 2.5th percentile, empirical 97.5th percentile, approximate 95% predictive interval, and corresponding lower and upper predictive bounds were computed at each time step. In the present study, 50 stochastic forward passes were used for the main uncertainty estimation, and an additional 100-pass run was conducted to assess the of the predictive mean and standard deviation. The MC Dropout results should be interpreted as approximate model-level epistemic uncertainty within the simulation setting, not as exact Bayesian inference or fully calibrated physical, measurement, environmental, or field uncertainty.

Results

Population $P_f(t)$ prediction accuracy

The sequence-learning model reproduced the simulator-derived population-level trajectory with small error relative to the probability scale. As summarized in Table 5, the representative TFT checkpoint achieved an MAE of 0.004543 and an RMSE of 0.006382, with a maximum absolute error of 0.024123 and a final-year error of 0.001347. These results indicate close simulator-to-model fidelity within the sampled scenario space.

The results should be interpreted in the context of model-form uncertainty. Diffusion-based transport provides an effective representation of chloride ingress in concrete; however, it does not fully account for multi-ionic transport, binding effects, wetting and drying cycles, temperature effects, electrochemical coupling, corrosion propagation, cracking, or spalling. Within this context, the TFT is a learned approximation of the simulator-defined $P(t)$ trajectory, and its fidelity remains tied to the assumptions and sampled parameter ranges of the underlying simulator.

Cover depth reliability prediction

When population trajectories are stratified by concrete cover depth, the TFT preserves the expected ordering and separation of reliability curves. As shown in Fig. 3, shallower cover is associated with earlier and higher initiation probability, whereas deeper cover corresponds to delayed initiation and lower $P_f(t)$ over the same time horizon. This behavior reflects the fundamental role of transport path length in chloride ingress, where shorter diffusion distances accelerate the time required for chloride concentration to reach the reinforcement level.

The stratified trajectories in Fig. 3 demonstrate that the sequence-learning model captures conditional variation associated with structural covariates, rather than representing the population using a single aggregated trajectory. To further quantify this agreement, Table 6 reports the number of test series, final-year reference and predicted probabilities, and corresponding absolute errors for each cover-depth group.

The results indicate that prediction errors remain small across all cover-depth groups and that the monotonic ordering of initiation probability is consistently preserved. This ordering is a physically meaningful feature of diffusion-driven corrosion initiation and serves as an important physical consistency check for the sequence-learning model. The ability to reproduce such stratification supports the interpretation that the learned mapping respects the dominant transport-controlled mechanism embedded in the diffusion-threshold formulation, rather than merely fitting aggregate trends.

It is important to note that this agreement should be interpreted as consistency with the assumed physical model, rather than independent validation of corrosion mechanisms. The diffusion-threshold formulation provides a simplified representation of chloride ingress and does not explicitly account for additional processes such as multi-species transport or chemical binding. Nevertheless,

Table 6. Final-year population-level corrosion-initiation probability by broad cover-depth group on the held-out test set

Cover-depth group	Test series (N)	Final reference probability	Final predicted probability	Final absolute error
40–60 mm	59	0.847	0.843	0.004
60–80 mm	40	0.200	0.201	0.001
80–110 mm	51	0.000	0.000	0.000

Table 7. Sobol first-order and total-order sensitivity indices for the smooth limit-state margin $C_{rebar}(t) - C_{crit}$

Parameter	(S_1), 20 yr	(S_T), 20 yr	(S_1), 40 yr	(S_T), 40 yr	(S_1), 60 yr	(S_T), 60 yr
C_S	0.005	0.021	0.013	0.028	0.020	0.033
D_{28}	0.018	0.032	0.019	0.026	0.020	0.024
m	0.101	0.183	0.143	0.193	0.170	0.204
Cover depth	0.671	0.781	0.717	0.783	0.716	0.760
C_{crit}	0.092	0.092	0.037	0.037	0.025	0.025

preservation of the expected cover-depth dependence indicates that the model maintains coherence with the governing physical assumptions underlying the simulator.

More broadly, the observed stratified behavior aligns with the intended role of sequence models in learning covariate-conditioned temporal patterns. The TFT is designed for multi-horizon prediction with mixed covariates and includes mechanisms for covariate-dependent temporal modeling.[36] In this context, the ability to recover cover-depth-dependent trajectories can be interpreted as a learned approximation of simulator-defined responses across heterogeneous scenario groups. Such behavior is particularly relevant in civil infrastructure applications, where deterioration processes are governed by heterogeneous material, geometric, and environmental conditions, and stratified prediction provides a structured representation of variation across related groups.[32]

Sensitivity analysis of input parameters

The total-order index S_T of cover depth remained high across the three service times, with values of 0.781, 0.783, and 0.760 at 20, 40, and 60 years, respectively. The aging exponent was consistently the second most influential parameter, indicating that long-term diffusivity evolution also contributes to uncertainty in corrosion initiation. The remaining parameters, including C_s, D_{28}, and C_{crit}, had smaller but non-negligible effects depending on service time. The corresponding Sobol first-order and total-order sensitivity indices are summarized in Table 7.

These results indicate that, within the assumed diffusion-threshold framework, geometric protection provided by concrete cover has the strongest influence on corrosion-initiation risk. The increasing contribution of the aging exponent from 20 to 60 years further suggests that long-term diffusivity evolution becomes more influential as service time increases.

Time-dependent prediction error

The absolute error over time remains small relative to the probability scale and exhibits limited variation across the prediction horizon. As shown in Fig. 4, the error profile is not uniform and localized fluctuations are present; however, these variations do not introduce sustained bias in the predicted trajectory. This behavior is consistent with the nature of the learning target, which is derived from a finite-sample Monte Carlo estimate of a probability function. Even when the underlying transport process is deterministic under fixed parameters, the population-level reliability $P_f(t)$ reflects sampling variability, and localized irregularities may arise from stochastic labeling near the threshold-crossing region.

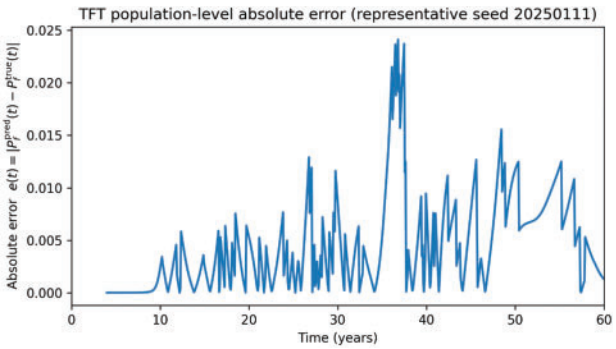

Figure 4. Time-dependent absolute error between TFT-predicted and simulator-derived population-level corrosion-initiation probability using the representative TFT checkpoint

The maximum absolute error over the full service-life horizon was 0.024123, occurring at approximately 36.80 years. The final-year absolute error was 0.001347, indicating that the long-term endpoint remained closely reproduced.

Such effects tend to be more pronounced in time intervals where initiation probability increases rapidly, as small differences in the implied initiation-time distribution can lead to larger instantaneous deviations in $P_f(t)$. As illustrated in Fig. 4, these discrepancies remain bounded and do not propagate into systematic divergence between predicted and reference trajectories.

Time-dependent reliability analysis typically relies on the evolution of $P_f(t)$ to support inspection scheduling and maintenance planning; therefore, preserving trajectory shape and avoiding sustained bias are more important than matching every localized finite-sample fluctuation exactly.

The observed error characteristics indicate that the TFT provides a stable learned approximation of the simulator-defined reliability trajectory for scenario-level evaluation within the sampled parameter space.

Computational efficiency

The computational comparison is interpreted cautiously. A single vectorized Monte Carlo simulation can be faster

Table 8. MC Dropout uncertainty summary

Metric	Value	Purpose/interpretation
Number of MC Dropout forward passes	50	Main stochastic inference setting
Predictive mean MAE	0.004616	Accuracy of MC Dropout mean relative to simulator-derived trajectory
Predictive mean RMSE	0.006503	Trajectory-level deviation of MC Dropout mean
Average predictive standard deviation over time	0.000461	Average spread among stochastic dropout predictions
Maximum predictive standard deviation over time	0.001682	Largest time-localized model-level uncertainty
Average 95% predictive interval width	0.001668	Average uncertainty-band width across service life
Maximum 95% predictive interval width	0.006213	Largest uncertainty-band width across service life
Year of maximum predictive interval width	59.95 years	When model-level uncertainty is largest
Final-year predictive mean	0.38564	Predicted corrosion-initiation probability at final service year
Final-year lower predictive bound	0.38309	Lower 2.5th percentile at final service year
Final-year upper predictive bound	0.38930	Upper 97.5th percentile at final service year
Average absolute change in predictive mean, 50 vs. 100 passes	3.77×10^{-5}	Stability check for predictive mean
Average absolute change in predictive standard deviation, 50 vs. 100 passes	2.73×10^{-5}	Stability check for uncertainty estimate
Maximum absolute change in predictive mean, 50 vs. 100 passes	2.47×10^{-4}	Worst-case convergence difference for the mean
Maximum absolute change in predictive standard deviation, 50 vs. 100 passes	2.40×10^{-4}	Worst-case convergence difference for the standard deviation
Prediction interval coverage probability, 50 passes	0.115	Empirical coverage of MC Dropout model-level prediction interval; not a calibrated field confidence interval.
Prediction interval coverage probability, 100 passes	0.114	Empirical coverage of MC Dropout model-level prediction interval; not a calibrated field confidence interval.

than neural-model inference in the present implementation, and model training requires an upfront cost. The practical value of the trained sequence model is therefore conditional: after training, it may support repeated scenario screening or future real-data forecasting workflows where many bridge, exposure, traffic, maintenance, or climate scenarios must be evaluated under a consistent learned mapping. Therefore, the reported runtime results should not be interpreted as a universal acceleration claim.

For a single simulation run, Monte Carlo evaluation is faster than TFT inference in the present implementation. The trained model becomes advantageous when it is reused across many scenario evaluations or embedded in larger screening workflows. Excluding training cost, the inference-time break-even point is approximately $612/5.35 \approx 115$ simulation-equivalent evaluations. Including the one-time training cost, the break-even point is approximately $(49,161 + 612)/5.35 \approx 9,303$ simulation-equivalent evaluations. Therefore, the reported computational benefit should be interpreted as a reusable inference-stage advantage for repeated large-scale scenario screening rather than as acceleration of a single simulation run.

Uncertainty quantification

From this predictive distribution, the predictive mean, predictive standard deviation, empirical 2.5th percentile, empirical 97.5th percentile, approximate 95% predictive interval, and corresponding lower and upper predictive bounds for $P_f(t)$ were computed at each time step. The resulting MC Dropout uncertainty metrics are summarized in Table 8.

Increasing the number of stochastic forward passes from 50 to 100 changed the predictive mean by 3.77×10^{-5} on average and the predictive standard deviation by 2.73×10^{-5} on average; the maximum absolute changes were 2.47×10^{-4} and 2.40×10^{-4}, respectively.

To clarify the benchmark comparison basis, Table 9 summarizes the input representation, historical input window, prediction horizon, target, and evaluation role of each surrogate model. Pointwise Logistic Regression was retained as a simple pointwise linear reference, whereas the Windowed multi-output linear/sigmoid regression, Windowed MLP, GRU, and TFT were evaluated using the same 52-step historical input window and 13-step prediction horizon.

Table 9. Benchmark design for surrogate model comparison

Model	Input representation	Historical input window	Prediction horizon	Sliding stride	Target	Evaluation role
Pointwise logistic regression	Pointwise covariates at each evaluation time	Not sequence-to-sequence	Pointwise prediction	Not applicable	Cumulative corrosion-initiation probability	Simple pointwise linear reference only
Windowed multi-output linear/sigmoid regression	Flattened 52 × 7 input window	52 time steps	13 time steps	1 time step	Same cumulative corrosion-initiation target	Fairer fixed-window linear baseline
Windowed MLP	Flattened 52 × 7 input window	52 time steps	13 time steps	1 time step	Same cumulative corrosion-initiation target	Fixed-window nonlinear baseline
GRU	Ordered 52-step sequence	52 time steps	13 time steps	1 time step	Same cumulative corrosion-initiation target	Recurrent sequence-learning baseline
TFT	Ordered 52-step sequence with structured covariates	52 time steps	13 time steps	1 time step	Same cumulative corrosion-initiation target	Interpretable multi-horizon sequence-learning model

Benchmark model comparison

To address the need for broader benchmark evaluation, Logistic Regression, Windowed multi-output linear/sigmoid regression, Windowed MLP, GRU, and TFT were compared using consistent target definitions, data splits, and population-level evaluation metrics. To improve benchmark fairness among fixed-window, nonlinear, and sequence-learning baselines, Windowed multi-output linear/sigmoid regression, Windowed MLP, GRU, and TFT were evaluated using the same sliding-window forecasting task. A common windowed dataset was constructed with a 52-step historical input window, a 13-step future prediction horizon, and a sliding stride of one time step. The Windowed multi-output linear/sigmoid regression and Windowed MLP baselines flattened the 52 × 7 covariate window into a fixed 364-dimensional input vector and used 13 future outputs, whereas GRU and TFT used ordered sequence inputs to predict the same 13-step horizon. All windowed models used the same physical covariates, cumulative corrosion-initiation target, scenario-level train/validation/test split, overlap-averaged inference procedure, population-level aggregation method, and MAE/RMSE evaluation metrics. Pointwise Logistic Regression was retained as a simpler linear reference using the same covariates and target at each evaluation time, but it was not treated as a fully equivalent sequence-to-sequence benchmark.

As summarized in Table 10, GRU achieved the lowest prediction error in the present low-dimensional simulation task, with an MAE of 0.001934 and an RMSE of 0.002931. TFT achieved the second-lowest error, with an MAE of 0.004542 and an RMSE of 0.006373, and outperformed the Windowed MLP, Windowed multi-output linear/sigmoid regression, and pointwise Logistic Regression baselines. Windowed MLP produced an MAE of 0.006975 and an RMSE of 0.009964. The Windowed multi-output linear/sigmoid regression baseline slightly improved over Pointwise Logistic Regression, reducing MAE from 0.020652 to 0.020212 and RMSE from 0.024271 to 0.023823, but remained much less accurate than Windowed MLP, GRU, and TFT. These results indicate that adding a historical window provides limited benefit to a linear model, while nonlinear and sequence-learning architectures provide additional predictive improvement. TFT should not be interpreted as universally superior, because GRU remained the most accurate model in this smooth simulator-derived dataset. Instead, TFT is retained as an interpretable and extensible multi-horizon architecture that is structurally aligned with future real-data deterioration forecasting, where historical deterioration states, static attributes, observed external inputs, and known or scenario-defined future external inputs may need to be modeled jointly.

Discussion and Guidelines for Applications

The results demonstrate simulator-to-model fidelity, physical consistency with the assumed diffusion-threshold

Table 10. Benchmark comparison of models under the common forecasting setup

Model	MAE	RMSE	Interpretation
Pointwise Logistic Regression	0.020652	0.024271	Pointwise linear reference; highest error
Windowed multi-output linear/sigmoid regression	0.020212	0.023823	Fairer fixed-window linear baseline
Windowed MLP	0.006975 ± 0.000843	0.009964 ± 0.001328	Fixed-window nonlinear baseline
GRU	0.001934 ± 0.000169	0.002931 ± 0.000207	Best numerical accuracy in the present simulation task
TFT	0.004542 ± 0.000261	0.006373 ± 0.000649	Interpretable multi-horizon sequence-learning model

Note: Pointwise Logistic Regression and Windowed multi-output linear/sigmoid regression are deterministic linear baselines and are reported without random-seed variability. Values for Windowed MLP, GRU, and TFT are reported as mean ± standard deviation across three random seeds: 20250111, 20250112, and 20250113.

mechanism, benchmark context, and approximate model-level uncertainty; they do not demonstrate universal TFT superiority, field validation, or complete physical uncertainty quantification. GRU achieved the lowest numerical error for the present smooth, low-dimensional simulation dataset, while TFT remains useful as an interpretable multi-horizon framework for future datasets that must separate static covariates, observed histories, known future or scenario-defined inputs, and future probability trajectories.

The MC Dropout analysis extends the TFT model from a deterministic predictor to an uncertainty-aware predictor. By retaining dropout during inference and repeatedly evaluating the trained model under identical input conditions, this procedure generates an approximate posterior predictive distribution for $P_f(t)$. The resulting distribution allows the model to report the predictive mean, predictive dispersion, and approximate 95% predictive interval, including lower and upper predictive bounds for $P_f(t)$.

However, this uncertainty estimate has important limitations. MC Dropout captures only approximate epistemic uncertainty associated with the trained sequence-learning model. It does not account for field measurement errors, environmental variability, chloride transport model assumptions, corrosion threshold uncertainty, or long-term deterioration mechanisms not included in the simulator. Therefore, the uncertainty estimates reported in this proof-of-concept study should be interpreted as model-level uncertainty indicators within the adopted simulation setting, rather than fully calibrated prediction intervals for real bridge deterioration.

The preceding results support a workflow in which physics-based stochastic reliability modeling provides traceable proof-of-concept targets, while sequence learning provides a structured forecasting formulation for organizing historical observations, covariates, and future probability trajectories. In the present study, this role remains simulation-based. Future extensions should test whether the same structure can be trained and validated using inspection records, laboratory deterioration sequences, sensor histories, exposure histories, maintenance records, and published deterioration datasets.

The framework may also be extended to settings where heterogeneous data sources are available and inspection or measurement uncertainty needs to be incorporated. Although the present results are derived from simulation-based reference trajectories, the underlying reliability formulation could be adapted to data-fusion applications in which monitoring or inspection data help constrain uncertainty in deterioration states and model parameters.[18] In practical applications, uncertainties in chloride measurements and semi-destructive testing may influence parameter calibration and should therefore be considered when transferring the sequence-learning model to field-oriented workflows.[19]

At the same time, the findings highlight that diffusion-based formulations should be interpreted with appropriate caution. Previous studies have documented the limitations of strict Fickian assumptions in concrete, particularly their inability to fully represent depth- and time-dependent transport behavior.[8,9] The sequence-learning model does not address these limitations directly; instead, it provides a computationally efficient approximation of the chosen reliability framework. From an engineering perspective, this distinction is important: while the approach improves scalability and facilitates systematic sensitivity analysis, the fidelity of the results remains tied to the adequacy of the underlying transport-initiation model and the representativeness of the sampled scenario space. Therefore, the applicability of the sequence-learning model should be interpreted within the scope of the adopted physical assumptions and parameter ranges.

Limitations

The present study should be interpreted as a first-stage concept demonstration of a physics-guided, simulation-trained sequence-learning framework for corrosion-initiation probability trajectory prediction. The reported agreement reflects simulator-to-model fidelity under the assumed stochastic diffusion-threshold reliability formulation, rather than

direct validation against field-observed bridge corrosion behavior.

Although field or laboratory validation is essential for practical deployment, a single external data point was not used as formal validation in this revision. Such a comparison would require compatible calibration of exposure conditions, cover depth, diffusion parameters, chloride measurement protocols, critical chloride threshold, and the definition of corrosion initiation. Without this compatibility, an isolated point comparison could be misleading and could overstate the level of validation. Future validation should therefore rely on structured datasets that support calibration and independent testing.

Corrosion initiation is represented as a threshold-crossing event at the reinforcement depth, which enables efficient population-level reliability evaluation. This simplified formulation was adopted to maintain a controlled proof-of-concept setting for simulator-to-model reliability-trajectory learning. It does not explicitly resolve chloride binding, wetting/drying cycles, temperature-dependent transport, corrosion propagation, rust expansion, or crack formation. Fully coupled treatment of these transport, electrochemical, and damage-evolution mechanisms would require additional material-specific, environmental, and field- or laboratory-calibrated parameters. These mechanisms should therefore be incorporated in future calibrated extensions rather than treated as fully resolved processes in the present simulation-based study.

The model was trained and tested within predefined parameter ranges; therefore, its predictions should be interpreted as interpolation within the sampled scenario space rather than reliable extrapolation beyond it. Outside these ranges, including unusually high surface chloride exposure, very low cover depth, extreme diffusivity, atypical critical chloride thresholds, or nonstationary environmental conditions, the learned mapping may become unreliable and the prediction error may increase. Extreme conditions may also change the governing deterioration mechanisms, making the diffusion-threshold assumptions less representative. Therefore, predictions outside the sampled domain should be treated as exploratory and verified through additional physics-based simulation, field calibration, or retraining with expanded parameter ranges.

In addition, the population-level corrosion-initiation probability is estimated from finite Monte Carlo realizations and therefore inherently contains sampling variability. This variability propagates into the training targets and may contribute to localized fluctuations in predicted probability trajectories, especially at later service times when uncertainty in initiation timing increases. Such behavior is consistent with the finite-ensemble nature of the reference data and should be interpreted within that context.

From a computational perspective, the efficiency advantage of the sequence-learning approach is primarily realized during inference. Model training requires non-negligible computational resources and depends on the quality and coverage of the training dataset. Furthermore, predictive stability can be influenced by hyperparameter selection and architectural design, which may require iterative calibration in practical implementations.

Although additional benchmark models were included in this revision, the comparison remains limited to a simulation-derived dataset. Future work should extend the benchmark evaluation to tree-based models, Gaussian process regression, larger datasets, and field-calibrated deterioration scenarios.

Finally, the current implementation focuses on corrosion-initiation probability rather than full deterioration progression or structural capacity loss. While initiation probability is a key durability indicator, its direct use in engineering decision-making requires integration with downstream models of damage evolution, structural performance, and life-cycle cost. Therefore, the applicability of the proposed sequence-learning framework should be interpreted within the scope of the adopted physical assumptions and the sampled scenario space.

Conclusion

This study presents a physics-guided, simulation-trained sequence-learning framework for multi-horizon forecasting of population-level corrosion-initiation probability trajectories in RC bridge systems. A stochastic diffusion-based simulator is used to generate controlled time-dependent reliability targets under uncertainty, and a TFT is trained to approximate the mapping from scenario variables, historical sequence structure, and time to the corresponding future probability evolution $P_f(t)$.

Within the controlled simulation setting, the results indicate that the sequence-learning model closely reproduces simulator-defined population-level reliability trajectories, preserves physically meaningful stratification across cover-depth groups, and maintains small bounded prediction deviations over the service-life horizon. The benchmark results further show that TFT should not be interpreted as universally superior, because GRU achieved the lowest numerical error in this smooth simulation dataset.

The contribution of this study lies in establishing a structured proof-of-concept workflow for sequence-based reliability trajectory prediction, benchmark comparison, sensitivity interpretation, and approximate model-level uncertainty quantification. The present simulation-generated dataset is a controlled first-stage substitute until real inspection, laboratory, sensor, exposure, maintenance, and published deterioration sequence data are structured for model training and field validation.

From an engineering perspective, the framework may support future scenario screening and deterioration forecasting once it is calibrated and validated with compatible real-world data. The current results demonstrate simulator-to-model fidelity only and should not be interpreted as readiness for direct bridge maintenance decision-making. Practical implementation requires future validation using bridge inspection records, laboratory deterioration sequences, field chloride profiles, sensor histories, exposure and traffic records, maintenance histories, and published deterioration datasets.

Recommendations for Future Work

Future work should extend the proposed framework beyond the current simulation-based setting. First, bridge inspection records, long-term laboratory corrosion measurements, field chloride profiles, structural health monitoring histories, exposure and traffic records, maintenance records, and published deterioration sequences should be cleaned, aligned, calibrated, and organized into machine-learning-ready sequence datasets. These data will support calibration of physical input distributions, external validation of prediction performance, and the transition from a simulator-based proof-of-concept to data-informed bridge deterioration forecasting.

Second, future work should extend the benchmark evaluation to additional model classes, larger datasets, and field-calibrated deterioration scenarios to determine whether the relative performance observed in the present simulation setting remains consistent under more complex conditions.

Third, the current formulation, which focuses on corrosion initiation, should be extended to incorporate subsequent deterioration stages such as corrosion propagation, cracking, section loss, and structural capacity degradation. Finally, the framework should be integrated with bridge management and life-cycle decision models so that predicted reliability trajectories can support inspection prioritization, maintenance planning, and scenario-based infrastructure assessment. These developments would enable the transition from a controlled simulation framework to data-informed and decision-oriented applications.

Acknowledgments

This work was supported in part by the Maritime Transportation Research and Education Center (MarTREC), a U.S. Department of Transportation University Transportation Center, under Contract No. 69A3552348331. The authors gratefully acknowledge this support.

Data Availability Statement

The data supporting the findings of this study are generated through simulation and are available from the corresponding author upon reasonable request. The code used to generate the simulation data and train the sequence-learning model can also be provided for research purposes.

Disclaimer

The contents of this paper reflect the views of the authors, who are responsible for the facts and accuracy of the information presented. The contents do not necessarily reflect the official views or policies of MarTREC, the U.S. Department of Transportation, or any affiliated institutions. This paper does not constitute a standard, specification, or regulation.

References

[1] Tang L, Boubitsas D, Huang L. Long-term performance of reinforced concrete under a de-icing road environment. *Cem Concr Res*. 2023;164:107039. doi:10.1016/j.cemconres.2022.107039.

[2] Khani S, Conciatori D, Chouinard L, et al. Chloride ingress in de-icing salt-exposed bridge: numerical modeling and field investigations. *Case Stud Constr Mater*. 2025:e05003. doi:10.1016/j.cscm.2024.e05003.

[3] Angst UM, Rossi E, Boschmann Käthler C, et al. Chloride-induced corrosion of steel in concrete. *Mater Struct*. 2024;57:56. doi:10.1617/s11527-024-02337-7.

[4] Liu J, Ou G, Qiu Q, Xing F, Tang K, Zeng J. Atmospheric chloride deposition in field concrete at coastal region. *Constr Build Mater*. 2018;190:1015–1022. doi:10.1016/j.conbuildmat.2018.09.118.

[5] Meira GR, Pinto WTA, Lima EEP, Andrade C. Vertical distribution of marine aerosol salinity in coastal area. *Constr Build Mater*. 2017;135:287–296. doi:10.1016/j.conbuildmat.2016.12.156.

[6] Meira GR, Ferreira PR, Andrade C. Long-term chloride accumulation on concrete surface in marine atmosphere zone. *Corros Mater Degrad*. 2022;3:349–362. doi:10.3390/cmd3030019.

[7] Angst UM, Geiker MR, Michel A, et al. The steel-concrete interface. *Mater Struct*. 2017;50:143. doi:10.1617/s11527-016-0907-5.

[8] Chatterji S. On the applicability of Fick's second law to chloride ion migration through Portland cement concrete. *Cem Concr Res*. 1995;25:299–303. doi:10.1016/0008-8846(94)00166-P.

[9] Zhang T, Gjørv OE. Diffusion behavior of chloride ions in concrete. *Cem Concr Res*. 1996;26:907–917. doi:10.1016/0008-8846(96)00073-5.

[10] Geiker M, Danner T, Polder R, Antonsen R, Hornbostel K. Long-term phase changes in cathodically protected marine reinforced concrete bridge. *Mater Struct*. 2025;58:168. doi:10.1617/s11527-024-02345-7.

[11] Konecny P, Lehner P. Effect of cracking and randomness of inputs on corrosion initiation of reinforced concrete bridge decks exposed to chlorides. *Fract Struct Integr*. 2017;11:29–37. doi:10.3221/IGF-ESIS.39.04.

[12] Zheng W, Qian F, Shen J, Xiao F. Probabilistic-based machine learning for bridge scour detection. *J Civ Struct Health Monit*. 2020;10:957–972. doi:10.1007/s13349-020-00424-5.

[13] Korec E, Jirásek M, Wong HS, Martínez-Pañeda E. Phase-field chemo-mechanical modelling of corrosion-induced cracking. *Theor Appl Fract Mech*. 2024;129:104233. doi:10.1016/j.tafmec.2023.104233.

[14] Vu KAT, Stewart MG. Structural reliability of concrete bridges including improved chloride-induced corrosion models. *Struct Saf*. 2000;22:313–333. doi:10.1016/S0167-4730(00)00018-7.

[15] Stewart MG, Mullard JA. Spatial time-dependent reliability analysis of corrosion damage and timing of first repair. *Eng Struct*. 2007;29:1457–1464. doi:10.1016/j.engstruct.2006.07.004.

[16] Li J, Guo X, Zhang X, Wu Z. Time-dependent reliability assessment and optimal design of corroded reinforced concrete beams. *Adv Struct Eng*. 2024;27:1313–1327. doi:10.1177/13694332231123456.

[17] Boonintra N, Tapsuphonkul K, Pheinsusom P, et al. Reliability assessment of RC bridge piers. *Case Stud Constr Mater*. 2025;23:e05610. doi:10.1016/j.cscm.2025.e05610.
[18] Wang B, Chen K, Wang B. Hierarchical Bayesian fusion of inspection and monitoring data for probabilistic bridge deterioration assessment. *Sci Rep*. 2026;16:5965. doi:10.1038/s41598-026-36808-4.
[19] Schoefs F, Awa Zahui Raissa K, Bonnet S, O'conor AJ. Uncertainty quantification of semi-destructive testing for chloride content assessment. *Front Built Environ*. 2023;9:1130066. doi:10.3389/fbuil.2023.1130066.
[20] Skrzypczak I, Halicka A, Słowik M. Modeling of chloride-induced corrosion in concrete bridge using simplified and full probabilistic methods. *Inż Bezp Obiektów Antropogenicznych*. 2023:35–45. doi:10.37105/iboa.194.
[21] Yehia A, Swei O. Probabilistic infrastructure performance models. *Transp Res Part C*. 2020;111:245–254. doi:10.1016/j.trc.2019.12.013.
[22] Qi L, Peng X, Yang Q, Xia K, Xu B. Prediction models for residual life of concrete structures. *Coatings*. 2025;15:693. doi:10.3390/coatings15060693.
[23] Bouteiller V, Marie-Victoire E, Bonnet A, et al. Reinforced concretes of tomorrow: corrosion behaviour according to exposure classes. *Proc DBMC*. 2023. doi:10.23967/c.dbmc.2023.027.
[24] Shen Y, Goodall JL, Chase SB. Condition state-based deterioration model at structure system level. *J Infrastruct Syst*. 2019;25:04018042. doi:10.1061/(ASCE)IS.1943-555X.0000482.
[25] Ibrahim A, Abdelkhalek S, Zayed T, Qureshi AH, Abdelkader EM. Key deterioration factors of concrete bridge decks: a review. *Buildings*. 2024;14:3425. doi:10.3390/buildings14113425.
[26] Anwar GA, Akber MZ, Ahmed HA, et al. Life-cycle performance modeling for sustainable and resilient structures. *Buildings*. 2024;14:3053. doi:10.3390/buildings14103053.
[27] Han D, Lee JH, Park KT. Deterioration models for bridge pavement materials for life cycle cost analysis. *Sustainability*. 2022;14:11435. doi:10.3390/su141811435.
[28] Medina PA, Gonzalez FJL, Todisco L. Data-driven prediction of long-term deterioration of RC bridges. *Constr Build Mater*. 2022;317:125790. doi:10.1016/j.conbuildmat.2021.125790.
[29] Althaqafi E, Chou E. Developing bridge deterioration models using artificial neural networks. *Infrastructures*. 2022;7:101. doi:10.3390/infrastructures7080101.
[30] Mia MM, Kameshwar S. Machine learning approach for predicting bridge component condition ratings. *Front Built Environ*. 2023;9:1254269. doi:10.3389/fbuil.2023.1254269.
[31] Chen CL, Hung CC, Zhang WY. Severe deterioration and maintenance rules of bridge components. *Case Stud Constr Mater*. 2025;22:e04907. doi:10.1016/j.cscm.2025.e04907.
[32] Zhang H, Marsh DWR. Multi-state deterioration prediction for infrastructure asset. *Inf Sci*. 2020;529:197–213. doi:10.1016/j.ins.2020.04.021.
[33] Faris N, Zayed T, Fares A. Review of condition rating and deterioration modeling approaches. *Buildings*. 2025;15:219. doi:10.3390/buildings15020219.
[34] Salinas D, Flunkert V, Gasthaus J, Januschowski T. DeepAR: probabilistic forecasting with autoregressive recurrent networks. *Int J Forecast*. 2020;36:1181–1191. doi:10.1016/j.ijforecast.2019.07.001.
[35] Gasthaus J, Benidis K, Wang Y, et al. Probabilistic forecasting with spline quantile function RNNs. *Proc AISTATS*. 2019.
[36] Lim B, Arik SO, Loeff N, Pfister T. Temporal fusion transformers for interpretable multi-horizon forecasting. *Int J Forecast*. 2021;37:1748–1764. doi:10.1016/j.ijforecast.2021.03.036.
[37] Carrara F, Falchi F, Girardi M, Messina N, Padovani C, Pellegrini D. Deep learning for structural health monitoring: an application to heritage structures. arXiv:2211.10351. 2022.
[38] Gao L, Din Z, Kim K, Senouci A. Time series transformer-based modeling of pavement skid and texture deterioration. arXiv:2507.01842. 2025.
[39] Tong S, Wu D, Liu X, Zheng L, Du Y, Zou D. STGAN: spatial-temporal Graph Autoregression Network for pavement distress deterioration prediction. arXiv:2503.01152. 2025.
[40] Hochreiter S, Schmidhuber J. Long short-term memory. *Neural Comput*. 1997;9:1735–1780.
[41] Cho K, van Merrienboer B, Gulcehre C, et al. Learning phrase representations using RNN encoder-decoder for statistical machine translation. arXiv:1406.1078. 2014.
[42] Bengio Y, Simard P, Frasconi P. Learning long-term dependencies with gradient descent is difficult. *IEEE Trans Neural Netw*. 1994;5:157–166. doi:10.1109/72.279181.
[43] Vaswani A, Shazeer N, Parmar N, et al. Attention is all you need. *Adv Neural Inf Process Syst*. 2017;30:5998–6008.
[44] Wu RJ, Xia Y, Xia J. Long-term prediction of surface chloride content using physics-informed neural networks. *Eng Struct*. 2025;329:119752. doi:10.1016/j.engstruct.2024.119752.
[45] Srivastava N, Hinton G, Krizhevsky A, Sutskever I, Salakhutdinov R. Dropout: a simple way to prevent neural networks from overfitting. *J Mach Learn Res*. 2014;15(56):1929–1958.
[46] Gal Y, Ghahramani Z. Dropout as a Bayesian approximation: representing model uncertainty in deep learning. *Proc 33rd Int Conf Mach Learn. PMLR*. 2016;48:1050–1059.